Computational Study of Interaction of an Elastic Plate with Laminar Flow Involving Large-scale Flow-induced Deformation

Submitted in partial fulfilment of the requirements
for the degree of
Doctor of Philosophy
of the
Indian Institute of Technology, Bombay, India
and
Monash University, Australia
by

Anup Kundu

Supervisors:
Prof. Rajneesh Bhardwaj (IIT Bombay)
Prof. Mark C. Thompson (Monash University)

The course of study for this award was developed jointly by
the Indian Institute of Technology, Bombay and Monash University, Australia
and given academic recognition by each of them.
The programme was administered by The IITB-Monash Research Academy.

March 2019

Acknowledgements

I would like to express my sincere gratitude, towards my guides Prof. Rajneesh Bhardwaj and Prof. Mark Thompson for providing me the opportunity for working with them. It has been a really great learning experience. I am also thankful to Prof. Amit Agrawal and Prof. John Sheridan for their time and suggestions and enlightening comments which have enhanced on the quality of my thesis.

The financial support by Prime Minister Fellowship Scheme for Doctoral Research is greatly acknowledged. I thank Prof. Mohan Krishnamoorthy for his efforts and guidance to apply Prime Minister Fellowship. I thank Prof. Murali Sastry, CEO of IITB-Monash research Academy for his support during my research. I thank Mr. Datta Kuvalekar, Director R&D Forbes Marshall Inc, Pune, India for providing the funding from Forbes Marshall Inc, Pune and support me to get Prime Minister Fellowship. I would also like to thank Mr. Shripad Kulkarni from Forbes Marshall Inc, Pune for his useful discussions about experimental setup.

Appreciation also goes to Kuheli Banerjee, Head- Finance and Legal Affairs, IITB-Monash Research Academy for administrative support.

I am thankful to all my teachers who have made me capable of reaching up to this point in life. I would like to thank my friends, especially, Dr. Atul Kumar Soti for his exciting and helpful comments on my research. I enjoyed long discussions with Mr. Hemanshul Garg about my research.

Declaration

I declare that this written submission represents my ideas in my own words and where others ideas or words have been included, I have adequately cited and referenced the original sources. I also declare that I have adhered to all principles of academic honesty and integrity and have not misrepresented or fabricated or falsified any idea/data/fact/source in my submission. I understand that any violation of the above will be cause for disciplinary action by the Institute and can also evoke penal action from the sources which have thus not been properly cited or from whom proper permission has not been taken when needed.

Notice 1

Under the Copyright Act 1968, this thesis must be used only under the normal conditions of scholarly fair dealing. In particular no results or conclusions should be extracted from it, nor should it be copied or closely paraphrased in whole or in part without the written consent of the author. Proper written acknowledgement should be made for any assistance obtained from this thesis.

Notice 2

I certify that I have made all reasonable efforts to secure copyright permissions for third-party content included in this thesis and have not knowingly added copyright content to my work without the owners permission.

Student Name
IITB ID:
Monash ID:

Abstract

Fluid-Structure Interaction (FSI) is central to several potential applications in engineering and biology. Specific examples include, fluttering of aerofoils, energy harvesting using thin piezoelectric plates, deformation of mitral valves in left ventricle, interaction of a blast wave with human eye, microelectronics cooling using thin elastic plates etc. The simulations of such problems are computationally challenging due to complex three-dimensional moving solid boundaries in the fluid domain and large-scale flow-induced deformation of the structure. In addition, geometric as well as material non-linearity and thickness of the structure should be accounted for accurate modeling. In the present thesis, we test and employ an in-house FSI solver to a thin, elastic plate undergoing large-scale deformation in laminar flow. The solver couples a sharp-interface immersed boundary method for the fluid dynamics with a finite-element method to treat the structural dynamics. The two solvers are implicitly (two-way) coupled using a partitioned approach.

First, we test the FSI solver with the benchmark data and validate the flow and structure solvers independently as well as module of large-scale flow-induced deformation. Although the flow solver has been extensively validated in the past, we carry out additional validations in the present thesis. The lift and drag coefficients and vortices in the wake of pulsatile flow past a circular cylinder placed in a channel are compared with the published results. For the structural solver, deflection of a cantilever beam under uniformly distributed impulse load is compared with the published results. In the present thesis, we revisit the validation of a FSI benchmark problem in which a thin elastic plate attached to a circular cylinder undergoes self-sustained oscillation. The difference in the displacement of the plate as compared to benchmark data is around 1%. In addition, we carry out the validation of a thin elastic plate attached to a square cylinder and the comparisons of the plate displacement and its vibration frequency with benchmark data are excellent.

Second, the response of an elastic splitter plate attached to a circular cylinder with the laminar pulsatile flow is studied. The cylinder and flexible splitter plate are contained within a narrow channel, and the Reynolds number is mostly restricted to $Re = 100$, primarily covering the two-dimensional flow regime. A power spectrum analysis of the time-varying plate displacement shows that the plate oscillates at more than a single

frequency for pulsatile inflow, compared to a single frequency observed for steady inflow. The multiple frequencies obtained for the former case can be explained by beating between the applied and plate oscillatory signals. The plate attains a self-sustained time-periodic oscillation with a plateau amplitude in the case of steady flow, while the superimposition of pulsatile inflow with induced plate oscillation affects the plateau amplitude. Lock-in of the plate oscillation with the pulsatile inflow occurs at a forcing frequency that is twice of the plate natural frequency in a particular mode, and this mode depends on the plate length. The plate displacement as well as pressure drag increases at the lock-in condition. The percentage change in the maximum plate displacement, and skin-friction and pressure drag coefficients on the plate, due to pulsatile inflow is quantified. The non-linear dynamics of the plate and its coupling with the pulsatile inflow are briefly discussed.

Third, we investigate the dynamics of an elastic thin splitter plate, attached to the lee side of a rigid circular cylinder, subjected to a laminar free stream. We examine a wide parameter space of mass ratio and bending stiffness of the plate. Numerical simulations show that the plate dynamics depend on mass ratio and bending stiffness at a given Reynolds number. The largest amplitude of the plate is found to be in the lock-in condition at which the natural frequency of the plate in a given fluid matches with the plate oscillation frequency. At lock-in, the natural frequency of the plate in a vacuum is lower than the oscillation frequency and thereby exhibiting strong added mass effect. These findings are consistent with those for classical vortex induced vibration of a rigid cylinder at the low mass ratio. The flapping boundary obtained from the simulations on mass ratio-reduced velocity plane is plotted and found to be consistent with previous available theories and data. We plot oscillation amplitude on the flapping map in order to show the lock-in condition and briefly discuss wake-structures and phase-plot in different cases of mass ratio and bending stiffness.

Fourth, we study the role of plate thickness on flapping dynamics of a thin elastic plate. Numerical simulations show that the plate dynamics depend on reduced velocity, bending stiffness and mass ratio at a given Re. The flapping of the plate starts at critical reduced velocity as well as mass ratio. The flapping boundary obtained from the simulations is plotted on a mass ratio-reduced velocity plane and is compared with prediction of a model. We show that the flapping boundary (or critical reduced velocity or mass ratio) depends upon the thickness of the plate.

Fifth, we investigate the dynamics of an inverted plate kept behind the circular cylinder in a uniform steady flow in an open domain. Numerical simulations suggest that the deformation of the inverted flag depends on its position as shown in Fig. 6.6, density ratio, and Young's modulus. The instability in the shear layer is completely taken place at critical distance. Shedding vortex from circular cylinder fall on the tip of the plate

which gives fluid force to the plate and consequently large plate deformation occurs.

Finally, we study augmentation of heat transfer by large-scale, flow-induced deformation of two elastic plates mounted in a cross-flow configuration in a channel with pulsating flow. The interaction between twin elastic plates, flow field, and temperature field as function of distance between the plates are discussed. The interaction of wake vortices between the deforming plates increases the mixing of the fluid in the channel and thereby increase the convective heat transfer from the heated channel walls due to reduction in thermal boundary layer thickness. The local Nusselt number increases by order of magnitude at specific locations on the channel wall, explained by the interaction of wake vortices with the wall. The numerical results show nearly 38% improvement of time-averaged wall Nusselt number as compared to a channel without any bluff body.

The findings of the present thesis provide fundamental insights into the interaction of an elastic plate with laminar flow in different configurations and will be useful for designing several applications such as energy-harvesting devices, cooling microelectronics by thin flexible plates and artificial valves for cardiovascular flows.

Contents

List of Figures

List of Tables

Nomenclature

Symbols	Definitions
D^*	Diameter of the cylinder [m]
L^*	Plate length [m]
μ^*	Dynamic viscosity [pa-s]
I^*	Moment of inertia of the plate cross-section $[b^*{h^*}^3/12]$ $[m^4]$
U_∞^*	Velocity of fluid [m/s]
ρ_f^*	Density of fluid [kg m^{-3}]
ρ_s^*	Density of solid [kg m^{-3}]
b	Dimensionless plate width $[b^*/D^*]$
E	Dimensionless Young's Modulus $[E^*/\rho_f^* {U_\infty^*}^2]$
h	Dimensionless plate thickness $[h^*/D^*]$
M	Dimensionless mass ratio $[\rho_s h^*/\rho_f L^*]$
K_b	Dimensionless bending stiffness per unit width $[K_b = Eh^3/(12L^3)]$
Re	Reynolds number $[\rho_f^* u^* D^*/\mu^*]$
Y_{tip}	Dimensionless maximum Y-displacement of the tip $[Y_{tip}^*/D^*]$
$A_{Y,\ tip}$	Dimensionless amplitude of Y-displacement of the tip $[A_{Y,\ tip}^*/D^*]$
C_{LP}	Lift coefficient of plate$[2{F^*}_{LP}/\rho_{f^*}{U_\infty^*}^2 D^*]$
$f_{ni,\ AM} = St_{ni,AM}$	Natural frequency of plate with added mass $[{f_{ni,AM}}^* D^*/U_\infty^*]$
$f_{ni} = St_{ni}$	Natural frequency of plate without added mass$[{f_{ni}}^* D^*/U_\infty^*]$
$f_p = St_p$	Frequency of plate $[{f_p}^* D^*/U_\infty^*]$
$R_1 = f_p/f_{ni}$	frequency ratio without added mass
$R_2 = f_p/f_{ni,\ AM}$	frequency ratio with added mass

Symbols	Definitions
μ^*	Dynamic viscosity [Pa-s]
ρ	Density ratio [$\rho = \rho_s/\rho_f$]
U_R	Reduced velocity [$U_R = \sqrt{M/K_b}$]
St_{ni}	Strouhal number(f^*D^*/u^*)
Nu	Nusselt number

Subscripts

s	Solid
f	Fluid
p	Plate
c	Cylinder
ni	natural frequency of ith order
$n1$	First natural frequency
$n2$	Second natural frequency
$n3$	Third natural frequency
AM	Added mass

Superscript

$*$	Dimensional quantity

Acronym

FSI	Fluid-structure interaction
2D	Two dimensional
3D	Three dimensional

Chapter 1

Introduction

Many interesting problems are associated with coupled motions of a structure with a surrounding fluid. Modeling the coupled dynamics of the fluid and the structure is very challenging. In most cases, especially with highly flexible structures, we deal with strongly coupled systems in which neither fluid nor structure dynamics can be neglected, and to understand the fluid effects on the structure and similarly the structural forces on the fluid, we need to study the detailed interaction between the fluid and the structure by solving their coupled behavior. In some cases, the interactions have significant effects on the dynamics of the fluid as well as the structure and together determine the system behavior. Essentially, when a fluid interacts with a structure, pressure forces act on the structure causing a deformation. This deformation of the structure changes the kinematic constraints in the flow field and thus, modifies the flow. Similarly, bodies moving in a flow field impose time-dependent kinematic boundary conditions at their interface. This interaction of a deformable or a moving structure with an associated flow field is called fluid-structure interaction referred to as FSI, hereafter.

1.1 Applications of Fluid-Structure Interaction (FSI)

Strong coupling between fluid and structure is considered in almost all parts of nature and in most engineering problems. Examples of fluid-structure interaction (FSI) problems are categorized below :

- Engineering fields: Typical examples include the failure of the Tacoma Narrows bridge because of large galloping responses in high winds, flow interaction with flexible pipes causing garden-hose and fire-hose instabilities, and fluttering motion in blades of aircrafts, wind turbines, helicopters and aeroelastic deformation (Rogers et al. (2006); Gordnier (2009)), mechanical vibration (Terracol et al. (2005)).

- Energy harvesting: The FSI has numerous applications in engineering field such

as energy harvesting (Li and Lipson (2009), Shoele and Mittal (2014)),Tang et al. (2009); Dunnmon et al. (2011) and microelectronics cooling.The thin flexible structures can be used as engineering application in energy-harvesting devices (Fig. 1.1, 1.2).

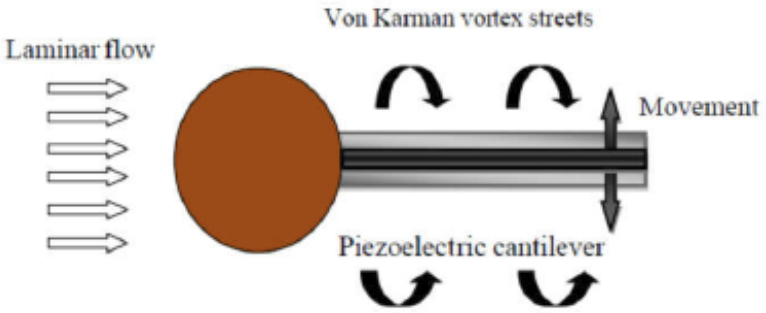

Figure 1.1: Schematic of the piezo-aeroelastic power harvester patch by Buffeting (Rostami)

- Thermal augmentation: The response of an elastic plate subjected to a laminar fluid flow also has important applications in thermal augmentation (Soti et al. (2015); Joshi et al. (2015)) via elastic deformation.

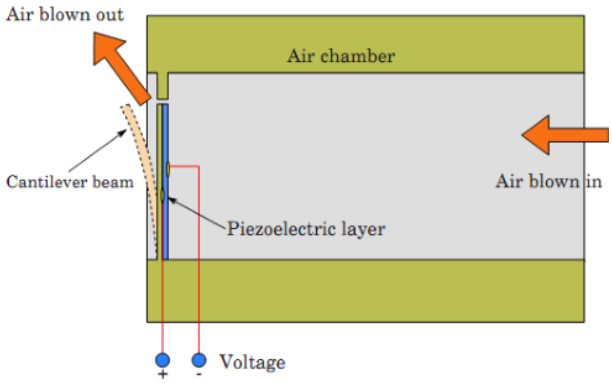

Figure 1.2: Flow induced self excited wind power generator (Çevik et al. (2011))

.

- Bio-medical: FSI with large-scale flow-induced structure deformation has potential applications in complex biomedical, biological systems and blood transport by heart valve of the human heart (Razzaq et al. (2010)). For instance, the non-linear dynamic response of a soft structure subjected to pulsatile flow is useful for understanding cardiac hemodynamics (Vigmostad et al. (2010); Choi et al. (2014); Mittal et al. (2016); Shoele and Mittal (2014)).

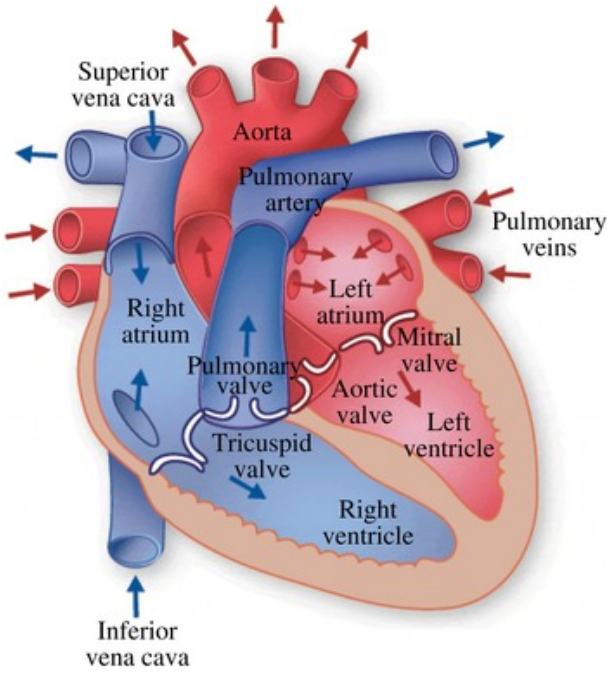

Figure 1.3: Schematic description of the heart functioning. Picture adapted from www.texasheart.org. via.(Meschini et al. (2018))

.

The interaction between flexible arterial walls and blood flow and its relation to the formation of aneurysms, beating patterns of healthy and diseased human heart muscles, fluid dynamics within flexible heart valves (Fig. 1.3) and human snoring (Tetlow and Lucey (2009)) are examples in this category.

- Bio-locomotion: wing fluttering (Tang et al. (2003)) and fish swimming (Liao et al. (2003)) are the example of FSI in biological locomotion systems.

The FSI of an elastic plate attached to a circular cylinder has been studied extensively numerically. The effects of pulsatile flow are more interesting when the vortex shedding frequency and pulsatile flow frequency are close to the natural frequency of the structure, also known as 'lock-in,' resulting in the large amplitude of vibrations. From the safety point of view, an engineer tries to avoid lock-in from happening by keeping the system natural frequency far from the vortex shedding frequency. On the other hand, the lock-in is desired for the energy harvesting purpose because the energy output depends on the vibration amplitude.

A relatively new study of an inverted plate dynamics kept behind a circular cylinder is also promising. Vortex shedding from a circular cylinder affects the inverted plate dynamics. As a result, plate vibrates with higher amplitude. The motion of the plate can be used to harvest energy.

The FSI of the inverted elastic (Fig. 1.4)plate has numerous applications in engineering field such as energy harvesting (Beeby et al. (2006); Kim et al. (2013); Sader et al.

(2016)), microelectronics cooling and biological systems. Leaf motion and the dynamics of hair follicles are also the same configurations of an inverted plate. In conventional plate configuration, leading is clamped and trailing edge is free, but inverted plate configuration, it is reversed the clamped position from a leading edge to trailing edge which completely changes the behavior of an inverted plate.

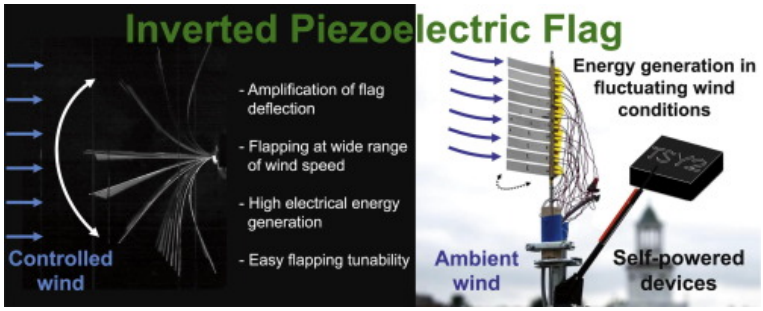

Figure 1.4: Harvesting ambient wind energy (Orrego et al. (2017))

.

The FSI of twin flexible structures in cross-flow can also be used for enhancing heat transfer. The deformation of the structures promotes mixing in the fluid and thereby improves heat transfer. One example of heat transfer enhancement via FID is shown in Fig. 1.5. A flexible wing is mounted on a heated surface, and a pulsating flow is applied at the inlet. The flexible wing undergoes periodic deformation cycles due to the pulsating nature of the incoming flow. The up and down motion of the wing directs the flow towards the heated surface which results in enhanced heat transfer as shown by the time-averaged Nusselt number in Fig. 1.5.

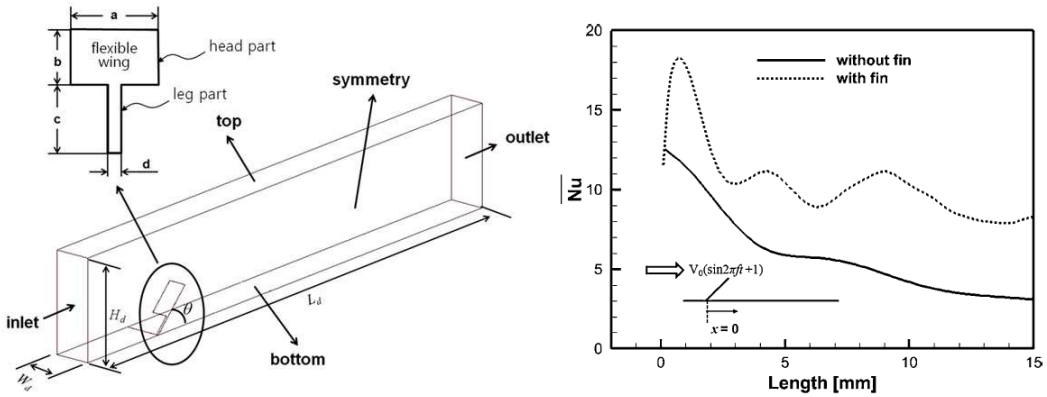

Figure 1.5: Flexible wing mounted on a bottom of a rectangular channel (left side). The bottom surface is heated and pulsating flow was incorporated. Thermal augmentation achieved by improving the Nusselt number (right side)(Park et al. (2013)).

The application of twin like structures in cross-flow in the microchannel can also be used for enhancing heat transfer. Microchannel with structure surface promotes mixing inside the channel and thereby heat transfer enhancement occurs.

1.2 Objectives of the present thesis

The primary focus of the present thesis is to investigate the coupled dynamics of flow-induced flapping of an elastic plate and application of FSI to heat transfer systems.

The more specific objectives of the present thesis are given below:

- First, we investigate the effect of the pulsatile flow on the flow-induced deformation of a thin, elastic structure of an inline flow configuration. To achieve this, the FSI benchmark case proposed by Turek and Hron (2006) is extended to account for the pulsatile inlet flow, and is used to investigate the coupling of the forcing flow frequency as well as amplitude with the frequency of the oscillating plate.

- Second, we investigate the effect of the mass ratio (M) and bending stiffness (K_b) on the flow-induced plate dynamics of an elastic plate attached to a cylinder in a free-stream laminar flow with a high-fidelity numerical model. The plate dynamics are implicitly coupled to an immersed-boundary method based flow solver. We consider a wide range of M = [0.143, 20], K_b = [0.0008, 0.0435] and reduced velocity (U_R) = [2.562, 30.0], at Reynolds number (Re_D) = 100, where Re is based on cylinder diameter and mean velocity of inflow.

- Third, we investigate critical reduced velocity and critical mass ratio for plate flapping. We also examine plate flapping for different thicknesses of the plate as flapping dynamics is the function of critical reduced velocity and critical mass ratio of the plate. We consider a wide range of M = [0.9, 19.5], K_b = [0.0009, 0.017] and U_R = [10, 40.0], at Reynolds number (Re_L) = 100, where Re_L is based on plate length and mean velocity of inflow to identify flapping boundary.

- Fourth objective is to investigate an inverted elastic plate dynamics kept behind circular cylinder with a specific gap. We investigate the effect of the gap between the circular cylinder and inverted plate to obtain maximum plate deformation. We also study the effect of mass and Young's modulus by keeping the fixed gap between the circular cylinder and the inverted plate on the plate dynamics.

- Finally, we study the large flow-induced deformation of two thin, parallel, insulated elastic plate in a channel with pulsating cross inflow. We also investigate the interaction between twin elastic plates dynamics, flow field, and heat transfer enhancement by varying distance between two plates.

1.3 Organization of the thesis

The rest of the thesis is organized into eight chapters. Chapter 2 presents benchmarking a fluid-Structure interaction solver. Chapter 3 reports the response of an elastic splitter plate attached to a cylinder with the laminar pulsatile flow. Chapter 4 provides the flow induced dynamics of elastic splitter plate. Chapter 5 presents the effect of the thickness of an elastic plate on the flow-induced flapping of an elastic plate. Chapter 6 provides the dynamics of an inverted elastic plate at the rear side of a cylinder. Chapter 7 presents a numerical study of thermal augmentation by twin plates in a laminar channel flow. Chapter 8 represents the conclusions and the future work.

Chapter 2

Benchmarking a Fluid-Structure Interaction Solver

An in-house fluid-structure interaction solver consists of a sharp-interface immersed boundary method for the fluid dynamics solver and a finite-element method to treat the structural dynamics solver. The structural solver is implicitly (two-way) coupled with the flow solver using a partitioned approach. The large-scale flow-induced structural deformation can be solved by FSI solver. The FSI solver was developed by Mittal and co-workers Zheng et al. (2010); Mittal et al. (2008); Seo and Mittal (2011); Mittal et al. (2011), and later further developed for large-scale flow-induced deformation by Bhardwaj and Mittal Bhardwaj and Mittal (2012). Details of FSI solver and coupling between flow and structure solver are discussed. Flow solver and structure solver have been validated independently. We perform flow solver validation against the pulsatile flow over cylinder and structure solver validation using freely vibration a cantilever beam. Next, we validated the large-scale flow-induced deformation module as part of the in-house fluid-structure interaction Solver (FSI). We consider two cases to validate FSI solver – (a) an elastic plate attached behind the circular cylinder (b) an elastic plate attached to the square cylinder. The comparison between our results and published result are matching well.

2.1 Introduction

IBM was first introduced by Peskin (1972) for the simulation of fluid-structure interaction of the blood flow in a beating human heart. The method is widely used to solve the complex fluid problem. Based on a variety of methods for implementing a boundary condition on an immersed surface, Immersed boundary methods can be classified broadly two categories (Mittal and Iaccarino (2005)).

In the first category of methods continuous forcing term is added to the continuous NavierStokes equations before discretization (Peskin (1972); Goldstein et al. (1993); Saiki

and Biringen (1996)). Implementation of forcing term is easy and independent of the spatial discretization, but it produces a diffuse boundary. The boundary condition on the immersed surface is not satisfied precisely at its actual location but within a localized region around the boundary. In the second category, the discrete forcing term is either explicitly or implicitly applied to the discretized NavierStokes equations (Udaykumar et al. (1999); Ye et al. (1999a); Fadlun et al. (2000); Kim et al. (2001); Gibou et al. (2002); You et al. (2003); Balaras (2004); Marella et al. (2005); Ghias et al. (2007) and others.). In this category, forcing scheme is very much dependent on the spatial discretization. In the specific formulations, they allow for a sharp representation of the immersed boundary.

For moving boundary problems, IBM is generally known to suffer from the generation of pressure oscillations on the surface of a moving immersed body (Lee et al. (2011); Seo and Mittal (2011)). Lee et al. (2011) identified two sources of the pressure oscillations in a discrete-forcing IBM. One source is related to the spatial discontinuity related to fresh cells, which were previously inside an immersed body and became fluid cells due to body motion. The other one is associated with the temporal discontinuity related to dead cells, which were fluid cells and now turn into solid cells with body motion. Some extrapolation techniques (Yang and Balaras (2006); Yang and Stern (2012)) and mass source/sink methods (Seo and Mittal (2011), Lee and You (2013a)) are used to reduce spurious force oscillations.

Yang and Balaras (2006) proposed a non-boundary-conforming formulation for simulating moving boundaries on fixed Cartesian grids. The finite-difference solver for incompressible NavierStokes equations is based on a second-order fractional step method on a staggered grid. The velocity field at the grid points near the interface is reconstructed using momentum forcing without smearing the sharp interface to satisfy the boundary conditions on an arbitrary immersed interface. The concept of field-extension is also introduced to treat the points emerging from a moving solid body to the fluid.

Kim et al. (2001) proposed an immersed-boundary method for simulating flows over or inside complex geometries by introducing a mass source/sink as well as a momentum forcing. They used a finite-volume approach on a staggered mesh together with a fractional-step method. Both momentum forcing and mass source are applied on the body surface or inside the body to satisfy the no-slip boundary condition on the immersed boundary and also to satisfy the continuity for the cell containing the immersed boundary. In the immersed-boundary method, the choice of an accurate interpolation scheme satisfying the no-slip condition on the immersed boundary is important because the grid lines generally do not coincide with the immersed boundary. Therefore, a stable second-order interpolation scheme for evaluating the momentum forcing on the body surface or inside the body is proposed.

Yang et al. (2008) presented an embedded-boundary formulation that applies to fluid-

structure interaction problems. The NavierStokes equations for incompressible flow are solved on a fixed grid, and the body is tracked in a Lagrangian reference frame. A strong-coupling scheme is presented, where the fluid and the structure are treated as elements of a single dynamical system, and all of the governing equations are integrated simultaneously and interactively in the time domain. The NavierStokes equations for incompressible flow are solved on a Cartesian grid which is not aligned with the boundaries of a body that undergoes large-angle/large-displacement rigid body motions through the fixed grid. A strong-coupling scheme is adopted, where the fluid and the structure are treated as elements of a single dynamical system, and all of the governing equations are integrated simultaneously and interactively in the time domain. A demonstration of the accuracy and efficiency of the method is given for a variety of fluid-structure interaction problems.

The formulation given by Mittal and co-workers (Mittal et al. (2008); Zheng et al. (2010); Seo and Mittal (2011); Mittal et al. (2011)) is based on the calculation of the variation on ghost-cells inside the body such that the boundary conditions are satisfied precisely on the immersed boundary. In their formulation, no ad-hoc constants and momentum forcing terminals are employed in any of the fluid cells. Consequently, the method results in a sharp representation of the immersed boundary. This implies that the boundary conditions on the immersed boundary are imposed at the precise location of the immersed body and there is no spurious spreading of the boundary forcing into the fluid as what usually occurs with diffuse interface methods (Mittal and Iaccarino (2005)). Unlike the ghost-fluid method (GFM) (Gibou et al., 2002), the interpolation scheme used here stays well-conditioned in all cases, and there is no need to resort to lower-order fixes for ill-conditioned situations. Furthermore, unlike GFM where interpolations are performed along the Cartesian directions, the interpolation operators in the current method are constructed in a direction normal to the immersed boundary, and this significantly simplifies the implementation of the Neumann boundary conditions on the immersed boundary. Finally, in comparison to the previous cut-cell based sharp interface methods (Udaykumar et al., 1999) the current method provides the same spatial order of accuracy but is easily extended to complex 3D geometries. Seo and Mittal (2011) significantly improves the mass conservation and reduces spurious force oscillations with a combination of a sharp-interface IBM and a cut-cell technique.

The FSI modeling with large-scale flow-induced structural deformation involves complex 3D geometries, moving structural boundaries in the fluid domain, and geometric and/or material nonlinearity of the structure. The coupling of the governing equations of the fluid with those of the structure brings additional non-linearity to the governing equations. In order to address these complexities, an in-house FSI solver is employed. The solver is based on a sharp-interface immersed boundary method, in which the governing equations of the flow domain are solved on a fixed Cartesian (Eulerian) grid while the

movement of the immersed structure surfaces is tracked within a Lagrangian framework. As reviewed by Mittal and Iaccarino (2005), the Immersed Boundary Method (IBM) is designed to treat 3D moving boundaries but using a simple and efficient Cartesian grid. Since the governing equations are solved on a body non-conformal Cartesian grid, there is no need for remeshing to treat deforming or moving structure boundaries in the fluid domain, provided spatial resolution is adequate. The FSI solver employed in the present chapter was developed by Mittal and co-workers (Mittal et al. (2008); Zheng et al. (2010); Seo and Mittal (2011); Mittal et al. (2011)), and later further developed for large-scale flow-induced deformation by Bhardwaj and Mittal (2012). Details of Ghost-Cell based immersed boundary (IB) method, and fluid and structure solvers coupling are discussed in section 2.2 and section 2.4.

2.2 Ghost-Cell based IB method

Ghost-cells based finite difference method, given by Mittal et al. (2008) and Bhardwaj and Sharma (2017), will be described here in details. Consider a 3D unsteady incompressible flow with constant properties which is governed by Navier-Stokes equation, written in tensor notation as:

$$\frac{\partial u_i}{\partial x_i} = 0, \tag{2.1}$$

$$\frac{\partial u_i}{\partial t} + \frac{\partial u_i u_j}{\partial x_j} = -\frac{1}{\rho}\frac{\partial p}{\partial x_i} + \nu \frac{\partial}{\partial x_j}\left(\frac{\partial u_i}{\partial x_j}\right), \tag{2.2}$$

where i and j varies from 1 to 3. u_i are the Cartesian velocity components, p is the pressure and ρ and ν are fluid density and kinematic viscosity respectively. Above equations can be solved by various methods. In Mittal et al. (2008) these equations were discretized on a collocated grid where all variables are stored at cell centres. Apart from cell-centre velocity u_i, the face-centre velocities U_i are required in collocated grid formulation. Fractional step method of Van Kan (1986) is used for time integration. In the first step, momentum equation is solved for intermediate velocity U^* using Adams-Bashforth and Crank-Nicolson schemes for convective and diffusion terms respectively

$$\frac{u_i^* - u_i^n}{\Delta t} + \frac{1}{2}\left(3C_i^n - C_i^{n-1}\right) = -\frac{1}{\rho}\frac{\delta p^n}{\delta x_i} + \frac{1}{2}\left(D_i^* + D_i^n\right), \tag{2.3}$$

where $C_i = \frac{\delta}{\delta x_j}\left(U_j u_i\right)$ and $D_i = \nu \frac{\delta}{\delta x_j}\left(\frac{\delta u_i}{\delta x_j}\right)$.

Note that both convective and diffusion term are discretized using a second order central difference scheme. Fig. 2.1 shows a representative cell. Intermediate face-centre velocities are obtained by averaging the intermediate cell-centre velocities as follows

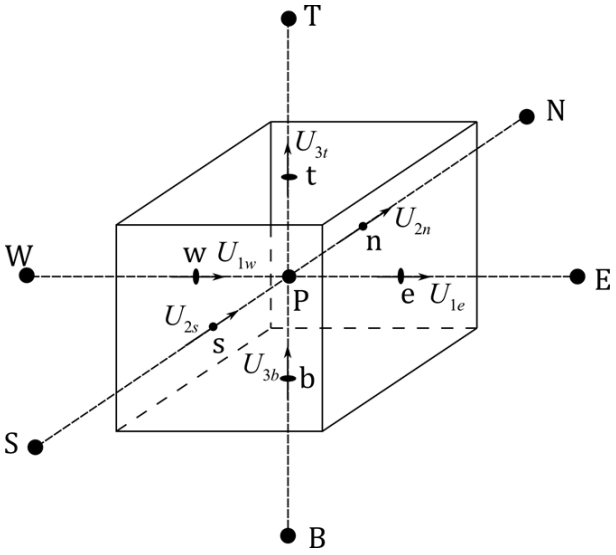

Figure 2.1: A representative cell.

$$\tilde{u}_i = u_i^* + \Delta t \frac{1}{\rho} \left(\frac{\delta p^n}{\delta x_i} \right)_{cc}, \tag{2.4}$$

$$\tilde{U}_{1w} = \gamma_w \tilde{u}_{1P} + (1 - \gamma_w)\tilde{u}_{1W}; \tilde{U}_{1e} = \gamma_e \tilde{u}_{1P} + (1 - \gamma_e)\tilde{u}_{1E}, \tag{2.5}$$

$$\tilde{U}_{2s} = \gamma_s \tilde{u}_{2P} + (1 - \gamma_s)\tilde{u}_{2S}; \tilde{U}_{2n} = \gamma_n \tilde{u}_{2P} + (1 - \gamma_n)\tilde{u}_{2N}, \tag{2.6}$$

$$\tilde{U}_{3b} = \gamma_b \tilde{u}_{3P} + (1 - \gamma_b)\tilde{u}_{3B}; \tilde{U}_{3t} = \gamma_t \tilde{u}_{3P} + (1 - \gamma_t)\tilde{u}_{3T}, \tag{2.7}$$

$$U_i^* = \tilde{U}_i - \Delta t \frac{1}{\rho} \left(\frac{\delta p^n}{\delta x_i} \right)_{fc}, \tag{2.8}$$

In eq. 2.5, 2.6 and 2.7 $\gamma_w, \gamma_e, \gamma_s, \gamma_n, \gamma_b$, and γ_t are the weights for linear interpolation at west, east, south, north, bottom and top faces respectively. Also, 'fc' and 'cc' stands for face-centre and cell-centre. Next, following Poisson equation is solved for pressure correction

$$\frac{1}{\rho} \frac{\delta}{\delta x_i} \left(\frac{\delta p'}{\delta x_i} \right) = \frac{1}{\Delta t} \frac{\delta U_i^*}{\delta x_i}, \tag{2.9}$$

Again central difference scheme is used for discretization. Neumann boundary conditions are applied for pressure correction at all boundaries. In third and final step, intermediate velocity and pressure are updated as follows

$$p^{n+1} = p^n + p', \tag{2.10}$$

$$u_i^{n+1} = u_i^* - \frac{\Delta t}{\rho} \left(\frac{\delta p'}{\delta x_i} \right)_{cc}, \tag{2.11}$$

$$U_i^{n+1} = U_i^* - \frac{\Delta t}{\rho} \left(\frac{\delta p'}{\delta x_i} \right)_{fc}, \tag{2.12}$$

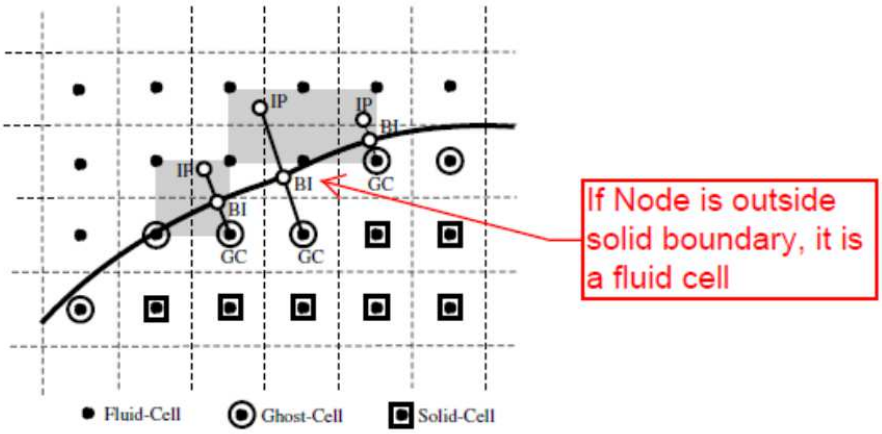

Figure 2.2: Immersed boundary and labelling of computational cells (taken from (Mittal et al., 2008)).

This completes the solution procedure for one-time step. IB can be represented by verity of ways such as level set field and unstructured mesh. To account for the presence of IB, proper boundary conditions should be applied at the location of IB.

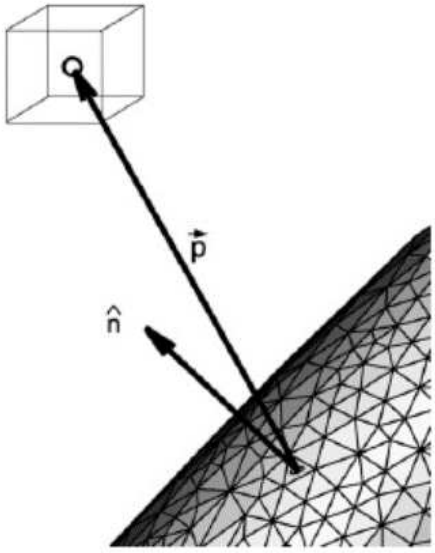

Figure 2.3: Procedure for labelling the computational cells (taken from (Mittal et al., 2008)).

For this purpose, computational cells are divided into following categories a) Fluid cells, b) Solid cells and c) Ghost cells. Cells whose center lies outside the IB are labeled as 'fluid cells,' and others are labeled as 'solid cells.' Further solid cells whose at least one neighbor out of 6 (4 in 2D) is a fluid cell is relabelled as 'ghost cell.' Fig. 2.2 (taken from (Mittal et al., 2008)) shows an IB in a Cartesian grid with different kind of cells. If IB is represented using a level set field (signed distance function in particular), then fluid

cells will have positive value of the level set field. For IB represented by an unstructured mesh, a procedure was suggested in Mittal et al. (2008). As shown in Fig. 2.3 (taken from (Mittal et al., 2008)), to determine whether a node is inside or outside the IB one finds a surface element on the IB which is closest to the node and then takes the dot product of two vectors p and n where p is a vector originating from the nearest surface element of IB and pointing towards the node and n is the surface normal vector. If the dot product is positive, then cell lies outside the IB and is labeled as fluid cell and vice-versa. Note that for stationary IB this labeling needs to be done only once in the start of the solution procedure, but for moving IB we need to repeat this labeling procedure after each time step. Once all cells are labelled, next job is to find appropriate values of different variables at the ghost cells such that boundary conditions are satisfied at the location of IB. For this a normal is drawn on to the IB from ghost cell which cuts the IB at a point called the 'boundary intercept' (BI) and extends into the fluid region up to a point called the 'image point' (IP). IP is chosen such that BI is midpoint of IP and ghost cell centre. After determining the IP for a ghost cell, a trilinear (bilinear in 2D) interpolation is used to interpolate the value of any variable, let us say ϕ, at IP. Any variable ϕ can be expressed by the following expression in the neighbourhood of 8 (4 in 2D) cells which surrounds the IP

$$\phi(x, y, z) = c_1xyz + c_2xy + c_3yz + c_4xz + c_5x + c_6y + c_7z + c_8, \tag{2.13}$$

There are eight unknown coefficients in eq. 2.13 which can be determined by the fact that ϕ is known at 8 neighbouring cells

$$\phi_i = c_1(xyz)_i + c_2(xy)_i + c_3(yz)_i + c_4(xz)_i + c_5x_i + c_6y_i + c_7z_i + c_8; \forall i = 1, 2, ...8. \tag{2.14}$$

Above equation can be written in matrix form as

$$\{\phi\} = [V]\{c\}, \tag{2.15}$$

where V is the Vandermonde matrix given by

$$[V] = \begin{pmatrix} (xyz)_1 & (xy)_1 & (yz)_1 & (xz)_1 & x_1 & y_1 & z_1 & 1 \\ (xyz)_2 & (xy)_2 & (yz)_2 & (xz)_2 & x_2 & y_2 & z_2 & 1 \\ \vdots & \vdots & \vdots & \vdots & \vdots & \vdots & \vdots & \vdots \\ (xyz)_8 & (xy)_8 & (yz)_8 & (xz)_8 & x_8 & y_8 & z_8 & 1 \end{pmatrix} \tag{2.16}$$

Equation 2.15 gives the value of coefficients

$$\{c\} = [V]^{-1}\{\phi\}, \tag{2.17}$$

After determining the coefficients, eq. 2.15 can be used to find the value of ϕ at IP as

$$\phi_{IP} = \sum_{i=1}^{8} \beta_i \phi_i, \tag{2.18}$$

In eq. 2.18 β_i are function of coefficients c_i and the coordinates of IP. As discussed in Mittal et al. (2008), sometimes one cell out of 8 neighbours of IP can be the ghost cell itself. In that situation the row corresponding to the ghost node in eq. 2.17 is replaced by the boundary condition at BI. In the case when Neumann boundary condition is specified at the immersed boundary, we need to find gradient of ϕ at BI as follows

$$\begin{aligned} \left.\frac{\partial \phi}{\partial n}\right|_{BI} &= (\nabla \phi)_{BI} \cdot \vec{n}_{BI} \\ &= c_1(n_1 yz + n_2 xz + n_3 xy) + c_2(n_1 z + n_2 x) + c_3(n_2 z + n_3 y) \\ &+ c_4(n_1 z + n_3 x) + c_5 n_1 + c_6 n_2 + c_7 n_3, \end{aligned} \tag{2.19}$$

In eq. 2.19 n_1, n_2 and n_3 are components of unit normal at BI. Also x, y and z are coordinates of BI.

Now the value of ϕ is available at IP, a linear extrapolation is used along the normal from ghost cell to IB to find the value of ϕ at ghost cell centre. For example, consider the Dirichlet boundary condition for velocity at IB. Since BI is midway between IP and ghost cell, we have

$$\phi_{BI} = \frac{1}{2}\left(\phi_{IP} + \phi_{GC}\right), \tag{2.20}$$

In an implicit solution procedure all the neighbouring values of ϕ are not known hence above equation is written as

$$\phi_{GC} + \sum_{i=1}^{8} \beta_i \phi_i = 2\phi_{BI}, \tag{2.21}$$

For Neumann boundary condition for pressure on IB following central difference scheme is used

$$\left(\frac{\delta \phi}{\delta n}\right)_{BI} = \frac{\phi_{IP} - \phi_{GC}}{\Delta l}, \tag{2.22}$$

Here Δl is the distance between ghost cell centre and IP and n stands for normal direction. Again above equation is written as

$$\phi_{GC} - \sum_{i=1}^{8} \beta_i \phi_i = -\Delta l \left(\frac{\delta \phi}{\delta n}\right)_{BI}, \tag{2.23}$$

Equations 2.21 and 2.23 are solved with 2.3 and 2.9 for all fluid cells. When IB is moving then so-called 'fresh cells' are being created in the fluid domain. Fresh cells are those cells which were labeled as the solid cell in the previous time step but become a fluid cell for

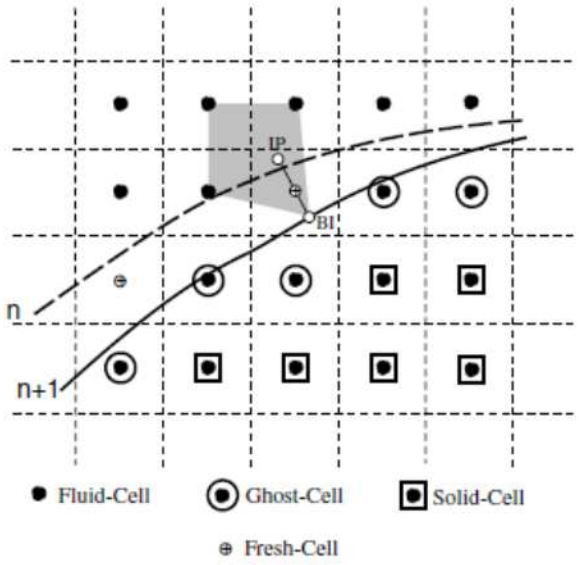

Figure 2.4: Moving IB and fresh cells treatment (taken from Mittal et al. (2008)).

the current time step due to the motion of IB. An example is shown in fig. 2.4 (taken from Mittal et al. (2008)) for 2D problem. The problem is that values of flow variables, such as velocities and pressure, are not available from previous time steps for fresh cells since these were in the solid domain. A solution to this problem was proposed in Ye et al. (1999b). During the solution procedure for next time step, intermediate velocities for fresh cells are interpolated from their neighbouring cells using a similar trilinear interpolation procedure that was used for ghost cells. As shown in fig. 2.4 (taken from Mittal et al. (2008)), a normal is drawn to the IB from fresh cell center which cuts the IB at point called boundary intercept 'BI.' Then image point 'IP' is found such that fresh cell lies midway between IP and BI. 8 (4 in 2D) neighbours of IP are identified, among which one is the fresh cell itself. Finally fresh cell intermediate velocities are interpolated from 7 neighbours of IP (fresh cell is excluded) and BI. After obtaining the intermediate velocities and pressure, pressure correction for fresh cells is obtained by solving pressure correction eq. 2.9 and final velocity and pressure are obtained by eq. 2.10 to 2.12.

2.3 Structural dynamics solver

The governing equations for the structure, Navier equations (momentum balance equation in Lagrangian form), are written as follows,

$$\rho_s \frac{\partial^2 d_i}{\partial t^2} = \frac{\partial \sigma_{ij}}{\partial x_j} + \rho_s f_i \tag{2.24}$$

where i and j range from 1 to 3, ρ_s is the structure density, d_i is the displacement component in the i direction, t is the time, σ_{ij} is the Cauchy stress tensor and f_i is the body force component in the i direction. The displacement vector $\mathbf{d}(\mathbf{x}, t)$ describes the motion of each point in the deformed solid as a function of space $\mathbf{x}$ and time t. The deformation gradient tensor F_{ik} can be defined in terms of the displacement gradient tensor $\frac{\partial d_i}{\partial x_k}$ as follows:

$$F_{ik} = \delta_{ik} + \frac{\partial d_i}{\partial x_k}, \tag{2.25}$$

where δ_{ik} is the Kronecker delta, defined as follows,

$$\delta_{ik} = \begin{cases} 1, i = k \\ 0, i \neq k \end{cases} \tag{2.26}$$

The right Cauchy green tensor is defined in terms of the deformation gradient tensor as follows:

$$C_{ij} = F_{ki} F_{kj} \tag{2.27}$$

The invariants of the right Cauchy green tensor are defined as follows:

$$\begin{aligned} I_1 &= \lambda_1 + \lambda_2 + \lambda_3 \\ I_2 &= \lambda_1\lambda_2 + \lambda_2\lambda_3 + \lambda_3\lambda_1 \\ I_3 &= \lambda_1\lambda_2\lambda_3 \end{aligned} \tag{2.28}$$

where λ_i are eigenvalues of the right Cauchy green tensor. In the present study, the structure is considered as Saint Venant-Kirchhoff material which considers geometric non-linearity for the large-scale deformation of a linear elastic material. The elasticity of the material is characterized by the Young Modulus (E) and the Poisson ratio (ν_s). For large deformations, the constitutive relation between the stress and the strain is based on Green-Lagrangian strain tensor $\boldsymbol{E}$ and second Piola-Kirchhoff stress tensor $\boldsymbol{S(E)}$ as a function of $\boldsymbol{E}$. The second Piola-Kirchhoff stress tensor can be expressed in terms of the Cauchy stress tensor $\boldsymbol{\sigma}$ as follows

$$\mathbf{S} = \mathbf{J}\mathbf{F}^{-1}\boldsymbol{\sigma}\mathbf{F}^{-\mathbf{T}}, \tag{2.29}$$

where J is the determinant of the deformation gradient tensor $\mathbf{F}$. The Green-Lagrangian strain tensor $\mathbf{E}$ is defined as

$$\mathbf{E} = \frac{1}{2}(\mathbf{F}^{\mathbf{T}}\mathbf{F} - 1), \tag{2.30}$$

The Navier equations are solved by Galerkin finite-element (FE) method for spatial discretization, implemented in Tahoe, an open-source, Lagrangian, three-dimensional, finite-element solver Tahoe (Tahoe). It yields the following system of ordinary differential

equations for the nodal displacement vector **d**, given by Hughes (1987),

$$M\ddot{d}_{n+1} + C\dot{d}_{n+1} + Kd_{n+1} = F_{n+1} \tag{2.31}$$

where M is the lumped mass matrix, C is the damping matrix and K is the stiffness matrix. For temporal discretization, Newark method is used, which is a family of integration formulae that depends on two parameters β and γ Tahoe (Tahoe):

$$\begin{aligned} d_{n+1} &= d_n + \Delta t\dot{d}_n + \tfrac{\Delta t^2}{2}\{(1-2\beta)\ddot{d}_n + 2\beta\ddot{d}_{n+1}\} \\ \dot{d}_{n+1} &= \dot{d}_n + \Delta t\{(1-\gamma)\ddot{d}_n + \gamma\ddot{d}_{n+1}\} \end{aligned} \tag{2.32}$$

With $\beta = 0.25$ and $\gamma = 0.5$, an unconditional stable and second order scheme results which used trapezoidal rule. Since Newark method does not account for numerical damping, undesired or spurious high-frequency oscillations are not handled effectively by this method ((Hughes, 1987), Negrut et al. (2007)). In the present paper, we employ Hilber-Hughes-Taylor (HHT) time integration scheme (or α-method) developed by Hilber et al. (1977) and this method accounts for the numerical damping with a parameter α in the governing equation such that Tahoe (Tahoe),

$$M\ddot{d}_{n+1} + (1+\alpha)C\dot{d}_{n+1} - \alpha C\dot{d}_n + d\sigma + (1+\alpha)Kd_{n+1} - \alpha Kd_n = F(t_{n+\alpha}) \tag{2.33}$$

$$t_{n+\alpha} = (1+\alpha)t_{n+1} = t_{n+1} + \alpha\Delta t \tag{2.34}$$

If α, β and γ are selected such that $\alpha \in$ [-1/3, 0], γ = (1 - 2α)/2 and β = (1 - α)^2/4, an unconditionally stable, second order accurate scheme results (Tahoe). Decreasing α increases the amount of numerical damping and $\alpha = 0$ corresponds to the Newark method. In the present simulations, we use α = -0.30, β = 0.4225 and γ = 0.80, allowing for the maximum numerical damping in the finite element model.

2.4 Fluid-structure interaction coupling

The incompressible flow solver (section 2.3) and structural solver (section 2.3.1) are coupled using the implicit partitioned approach. Note that an in-house incompressible flow solver Mittal et al. (2008) was coupled with the structural dynamics solver Tahoe (Tahoe) by Bhardwaj and Mittal (2012) and we implement the implicit coupling reported in Bhardwaj and Mittal (2012), in the present work. The solvers are coupled such that they exchange data at each time step (Fig. 6.1). The flow solution is marched by one time step with the current deformed shape of the structure and the velocity of the fluid-structure interface act as the boundary condition in the flow solver (Fig. 6.1).

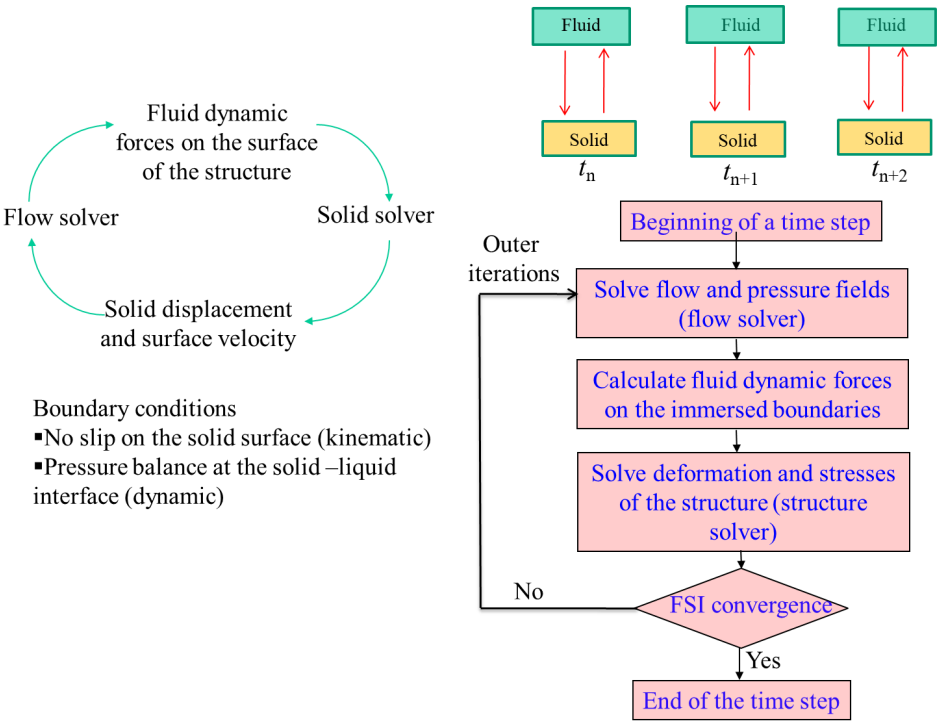

Figure 2.5: Coupling of flow and structure solver

Boundary conditions

The boundary condition representing the continuity of velocity at the interface (or no slip on the structure surface) is as follows,

$$u_{i,f} = \dot{d}_{i,s} \tag{2.35}$$

where subscripts f and s denote the fluid and structure, respectively. The pressure loading on the structure surface exposed to the fluid domain is calculated using the interpolated normal fluid pressure at the boundary intercept points via a trilinear interpolation (bilinear interpolation for 2D), as described by Mittal et al. (2008). This boundary condition represents continuity of the traction at the solid-fluid interface and is expressed as follows,

$$\sigma_{ij,f} n_j = \sigma_{ij,s} n_j \tag{2.36}$$

where n_j is the local surface normal pointing outward from the surface. The structural solver is marched by one-time step with the updated fluid dynamic forces. The convergence is declared after the L_2 norm of the displacement of the fluid-structure interface reduces below a preset value Bhardwaj and Mittal (2012). In order to ensure the numerical stability of the FSI solver at low structure-fluid density ratio, under-relaxation of the displacement and the velocity of the fluid-structure interface is implemented, as discussed by Bhardwaj and Mittal (2012). The details of in-house, validated FSI solver are given

in Kundu et al. (2017), Garg et al. (2018) and Kumar Soti (2018).

2.5 Code validation

The flow solver has been extensively validated by Mittal et al. (2008) against several benchmark problems, such as flow past a circular cylinder, sphere, airfoil, and a suddenly accelerated circular cylinder and a normal plate. First, we validate structure solver. In this section, additional qualitative and quantitative validations are also performed for the flow past a circular cylinder with pulsatile inflow boundary condition applied at the channel inlet. The large-scale flow-induced deformation module in the in-house FSI solver was previously validated by Bhardwaj and Mittal (2012), and this is briefly described here for completeness.

2.5.1 Pulsatile inflow past a stationary cylinder

Vortical wake structures for pulsatile flow past a circular cylinder placed in a channel are qualitatively compared. This flow problem was considered previously by Al-Sumaily and Thompson (2013). The computational domain is $23D \times 4D$, where D is the cylinder diameter, and the center of the cylinder is positioned at $(8D, 2D)$. A fully developed pulsatile flow velocity profle given in Al-Sumaily and Thompson (2013) as flows,

$$u^*(t) = u_0^*(1 + Asin(2\pi f^* t^*)) \tag{2.37}$$

Where $u^*(t)$, u_0^*, f^*, t^* are horizontal velocity component (m/s), horizontal fluid velocity at the inlet of the channel (m/s), pulsating frequency (Hz) and time (s). Note that A is dimensionless oscillating amplitude of axial inlet velocity. The dimensionless mean velocity in the channel of dimensionless height H is u_m. u_m and t can be expressed as $u_m = u^*(t)/u_0^*$ and $t = t^*\ u_0^*/D^*$. The length and velocity scale used for non-dimensionalization are cylinder diameter (D^*) and mean velocity ($u^*{}_m$), respectively. Note that the superscript $*$ and subscript m denote dimensional variable and mean value, respectively. Eq. (3.1)can be written as non-dimensionless from as

$$u_m = 1 + Asin(2\pi f^* \frac{tD^*}{u^*}) \tag{2.38}$$

A fully developed dimensionless pulsating flow velocity $u(t)$ is applied at the inlet of the channel and is expressed as follows Al-Sumaily and Thompson (2013),

$$u = 1 + A_f sin(2\pi St\ t) \tag{2.39}$$

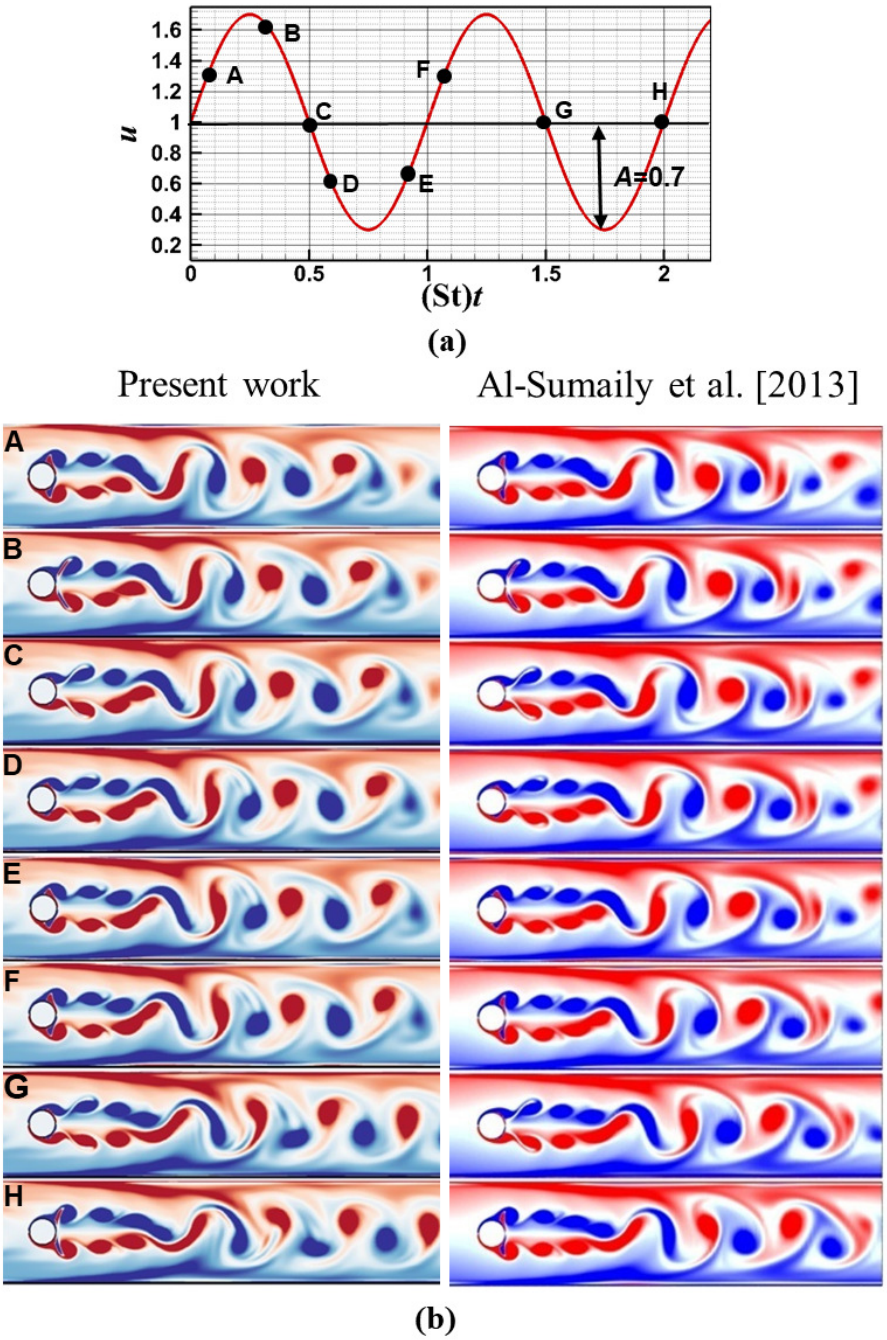

Figure 2.6: Validation against the wake structure of Al-Sumaily and Thompson (2013) for the pulsatile flow past a circular cylinder placed in a horizontal channel. Left: present wake vorticity predictions, Right: vorticity fields from Al-Sumaily and Thompson (Adapted with permission from Al-Sumaily and Thompson (2013)). In both cases St= 0.8, Re = 250 and A_f =0.7.

where A_f, St and t are the amplitude of the pulsatile inflow, Strouhal number and time respectively. No-slip boundary conditions at the top and bottom walls, and an outflow boundary condition at the right boundary are enforced for the simulation. The computed vorticity contours obtained by using the same parameters in our FSI model (St_f = 0.8)

Table 2.1: Comparison between flow quantities for steady flow past a circular cylinder at $Re = 100$ with published data (Li et al. (2010); Behr et al. (1995))

Flow quantities	Present work	Li et al. (2010)	Behr et al. (1995)
Maximum lift coefficient	0.3354	0.3630	0.3743
Average drag coefficient	1.3801	1.3415	1.3836
Strouhal number	0.1639	0.1678	0.1641

are plotted in the left column of Fig. 2.6.

These contours are compared with those of Al-Sumaily and Thompson (2013) plotted in the right column of this figure, at a series of different time instances. A good agreement in the vorticity field predictions is observed, notably, in terms of both vortex strength and shape, thereby providing confidence in the implementation of oscillating flow boundary conditions. Quantitatively the flow model is validated for predicting the flow past a circular cylinder under steady flow and pulsatile flow with non-zero mean velocity (Li et al. (2010); Behr et al. (1995)). The computational domain is $16D \times 30.5D$ where D is cylinder diameter, and the center of the cylinder is at ($8D$, $8D$). The dimensionless inflow velocity in the channel is expressed as,

$$u = 1 + A_f sin(2\pi f_t t) \tag{2.40}$$

where A_f, f_t and t are flow amplitude, frequency of the pulsatile inflow and time, respectively. A good agreement is obtained for predictions of maximum lift coefficient, average drag coefficient and Strouhal number for the steady flow ($A_f = 0$), as given in the Table 2.1.

Quantitatively the flow model is validated for predicting the flow past a circular cylinder under steady flow and pulsatile flow with non-zero mean velocity Li et al. (2010); Behr et al. (1995). The computational domain is $16D \times 30.5D$ where D is cylinder diameter, and the center of the cylinder is at ($8D$, $8D$). The dimensionless inflow velocity in the channel is expressed as,

$$u = 1 + A_f cos(2\pi f_t t) \tag{2.41}$$

where A_f, f_t and t are flow amplitude, frequency of the pulsatile inflow and time,

respectively. A good agreement is obtained for predictions of maximum lift coefficient, average drag coefficient and Strouhal number for the steady flow ($A_f = 0$), as given in the Table 2.1. Results for the pulsating flow past a stationary cylinder at $Re = 100$ were compared with those of Li et al. (2010). The forcing frequency was taken as natural vortex shedding frequency ($f_f = 0.1639$). The first and second frequency of the lift coefficient signals, obtained by FFT analysis, at different forcing amplitudes are given in Table 2.2. The comparisons between the frequencies are good and validate our flow model.

Table 2.2: Comparison of dominant frequencies in lift signals at different forcing amplitude (A_f) for pulsatile flow past a circular cylinder at $Re = 100$ with those reported by Li et al. (2010). All these frequencies are dimensionless.

cases	Present work		Li et al. (2010)	
	First frequency	Second frequency	First frequency	Second frequency
$A_f = 0.05$	0.1645	0.3215	0.1678	0.3357
$A_f = 0.08$	0.1647	0.3312	0.1602	0.3281
$A_f = 0.1$	0.1639	0.3279	0.1526	0.3204
$A_f = 0.4$	0.1647	0.3246	0.1678	0.3357

2.5.2 Free vibration of a cantilever beam

We describe only one validation case here to demonstrate the nonlinear structural solver's accuracy. For this purpose, the dynamic vibration of a cantilever beam is considered. As shown in Fig. 2.7, a cantilever beam under uniformly distributed impulse load is analyzed using Tahoe solver. The material of the cantilever is assumed to be isotropic and elastic with geometrical nonlinearity (i.e., large displacement) incorporated. The parameter values in the setup are given in Fig. 2.7(a). Fig. 2.7(b) shows displacement of cantilever beam D/L which is good agreement with Tian et al. (2010).

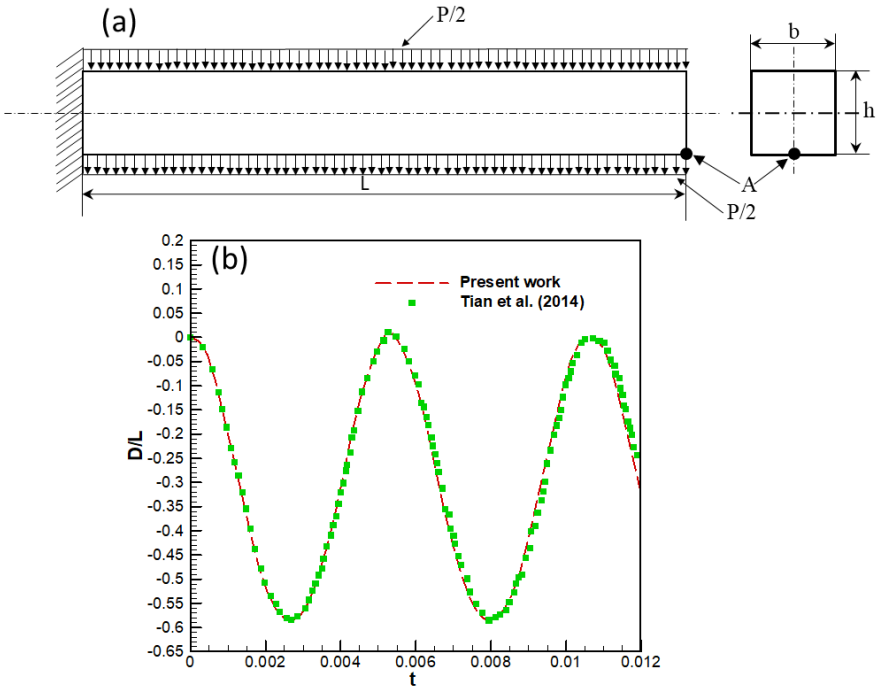

Figure 2.7: (a) Cantilever beam under an impulse load, where L=10 in., b = 1 in., E = 12000 lbf/in^2, ν_s=0.2, $\rho_s = 10^6$ $lbfs^2/in^4$, and $P = 2.85lbf/in^2$. (b) Comparison of the time-varying vertical displacement of the free end, D/L with Tian et al. (2010)

2.5.2.1 Structural grid size convergence study

We performed a structural grid convergence study with four different triangular finite elements, under steady inflow for flow past an elastic splitter plate behind a cylinder. All other simulation setup parameters are given in section 2.6.3.1 in the thesis. The finite triangular elements are listed in Table 3.1. The tip deflection (Y_{tip}) signals obtained from the different triangular elements are compared in Fig. 2.9 showing the minor differences observed in peak amplitude for the different sizes of finite element grids.

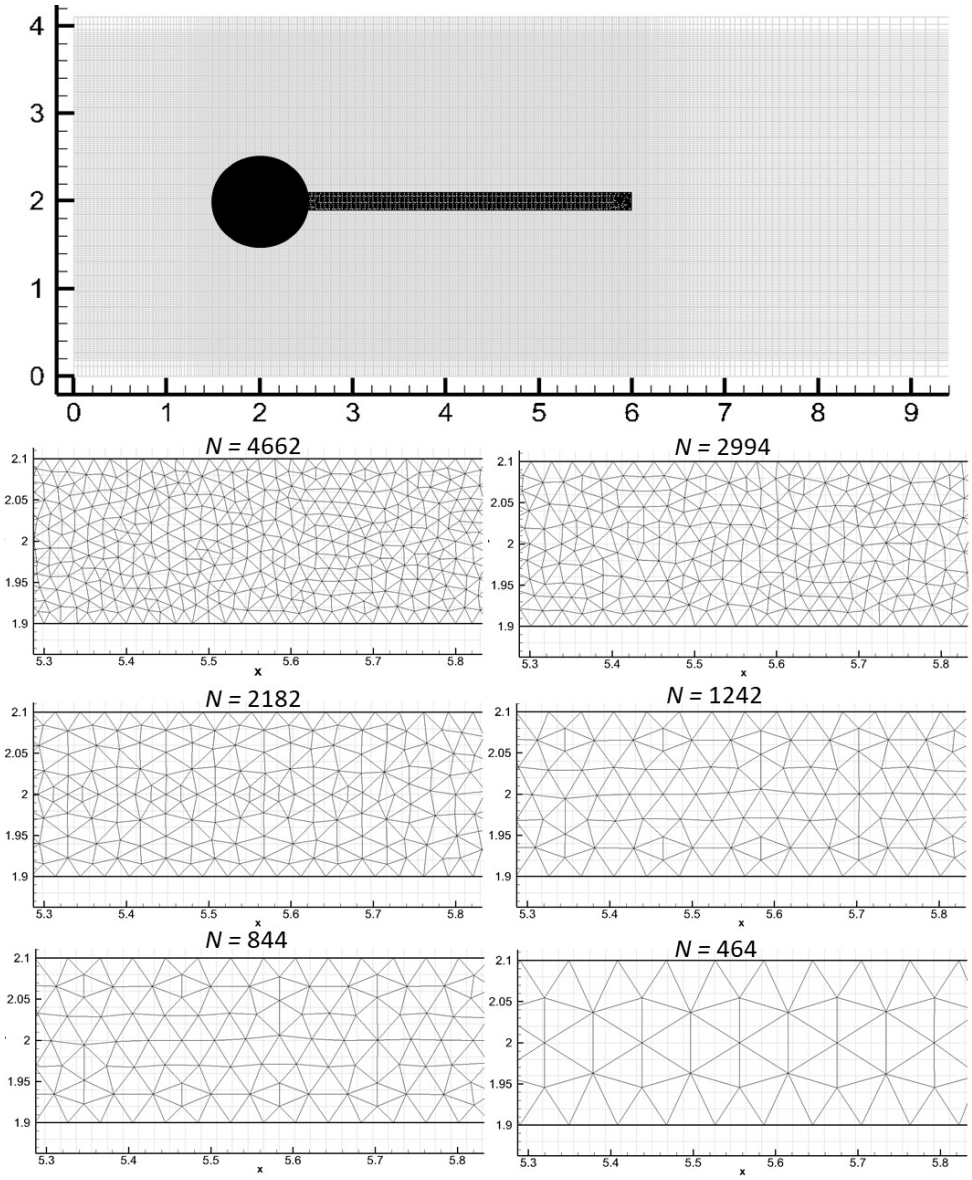

Figure 2.8: (A) Structural mesh immersed in non-uniform Cartesian grid in the computational domain. (B-E) Zoomed in view of the structural grid immersed in a uniform grid of Cartesian mesh for different cases. Uniform grid is used in the region in which the plate is expected to move and non-uniform grid stretching is used from this region to the wall.

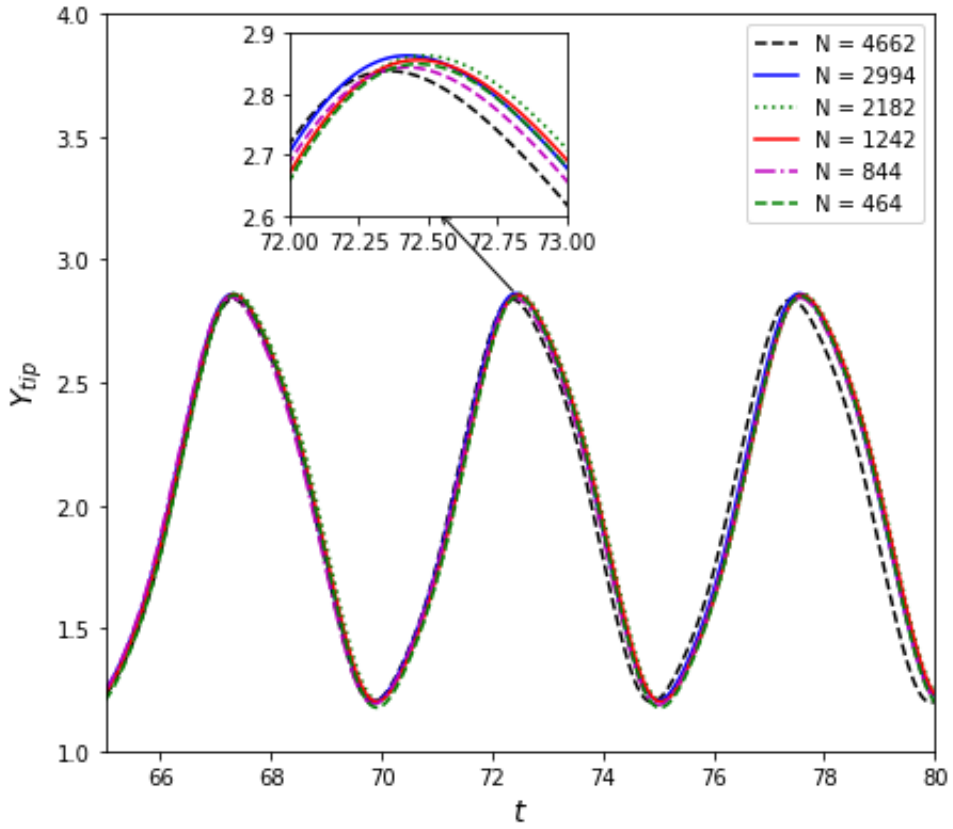

Figure 2.9: Structure Grid size convergence study: comparison of the time-varying cross-stream displacement of the plate tip (Y_{tip}). Note that Cartesian grid sizes are same for each cases.

The errors with respect to finest finite triangular elements, are listed in Table 3.1. Since the relative error for 2182 numbers of triangular finite element mesh, as shown in Table 3.1, is one order of magnitude smaller. 2182 numbers of triangular finite element mesh were selected for the simulations.

Table 2.3: Grid size convergence study. Error in the maximum plate tip deflection (Y_{tip}) for different grids with respect to the finest grid examined.

Cases	triangular finite elements	Y_{tip}	Relative error in Y_{tip}
1	464	0.821	1.68 %
2	844	0.828	0.84%
3	1242	0.829	0.71%
4	2182	0.829	0.71%
5	2994	0.832	0.35%
6	4662	0.835	-

2.5.3 Large-scale flow-induced deformation

In this section, we present validations for two cases of large-scale flow-induced deformation. Two cases have been considered to validate FSI solver – (a) an elastic plate attached behind the circular cylinder in section 2.5.3.1 and (b) an elastic plate attached to the square cylinder in section 2.5.3.2

2.5.3.1 Splitter plate attached to a circular cylinder

The large-scale flow-induced deformation module as part of the in-house FSI code was validated by Bhardwaj and Mittal (2012) against the FSI benchmark problem proposed by Turek and Hron (2006). In this benchmark problem, a cylinder with a $3.5D \times 0.2D$ thin elastic plate with specified material properties attached at its rear is placed inside a channel of width $4.1D$, where D is the cylinder diameter (Fig. 2.10). The fluid is taken to be Newtonian and incompressible. The plate is considered to consist of Saint Venant-Kirchhoff material, which accounts for geometric nonlinearity for a linear elastic material (Fung (1965)). Geometric nonlinearities is not a material type. St. Venant-Kirchhoff model considers geometric nonlinearities. This model is more suitable for large scale elastic structure deformation where linear elastic solid models fail to describe the structure behavior. The boundary conditions for the benchmark problem are illustrated in Fig. 2.10A. No-slip boundary conditions are applied at the channel walls and immersed structure boundary. Zero Neumann boundary condition is applied for the velocity at the channel outlet.

At the inlet, a fully developed, parabolic, steady velocity profile is applied, expressed in dimensionless form as follows Turek and Hron (2006),

$$u_{steady} = 6u_m(\frac{y}{H})(1 - \frac{y}{H}) \tag{2.42}$$

such that the dimensionless mean velocity in the channel of dimensionless height H is u_m. The length and velocity scale used for non-dimensionalization are cylinder diameter (D^*) and mean velocity ($u^*{}_m$), respectively. The Height used for non-dimensionalization is cylinder diameter (D^*). Here dimensionless height (H) is H^*/D^*. Note that the superscript $*$ and subscript m denote dimensional variable and mean value, respectively. The Reynolds number (Re) and dimensionless Young's modulus (E) are defined as follows,

$$Re = \frac{\rho_f^* U^*{}_m D^*}{\mu^*} \tag{2.43}$$

$$E = \frac{E^*}{\rho_f^* U^*{}_m{}^2} \tag{2.44}$$

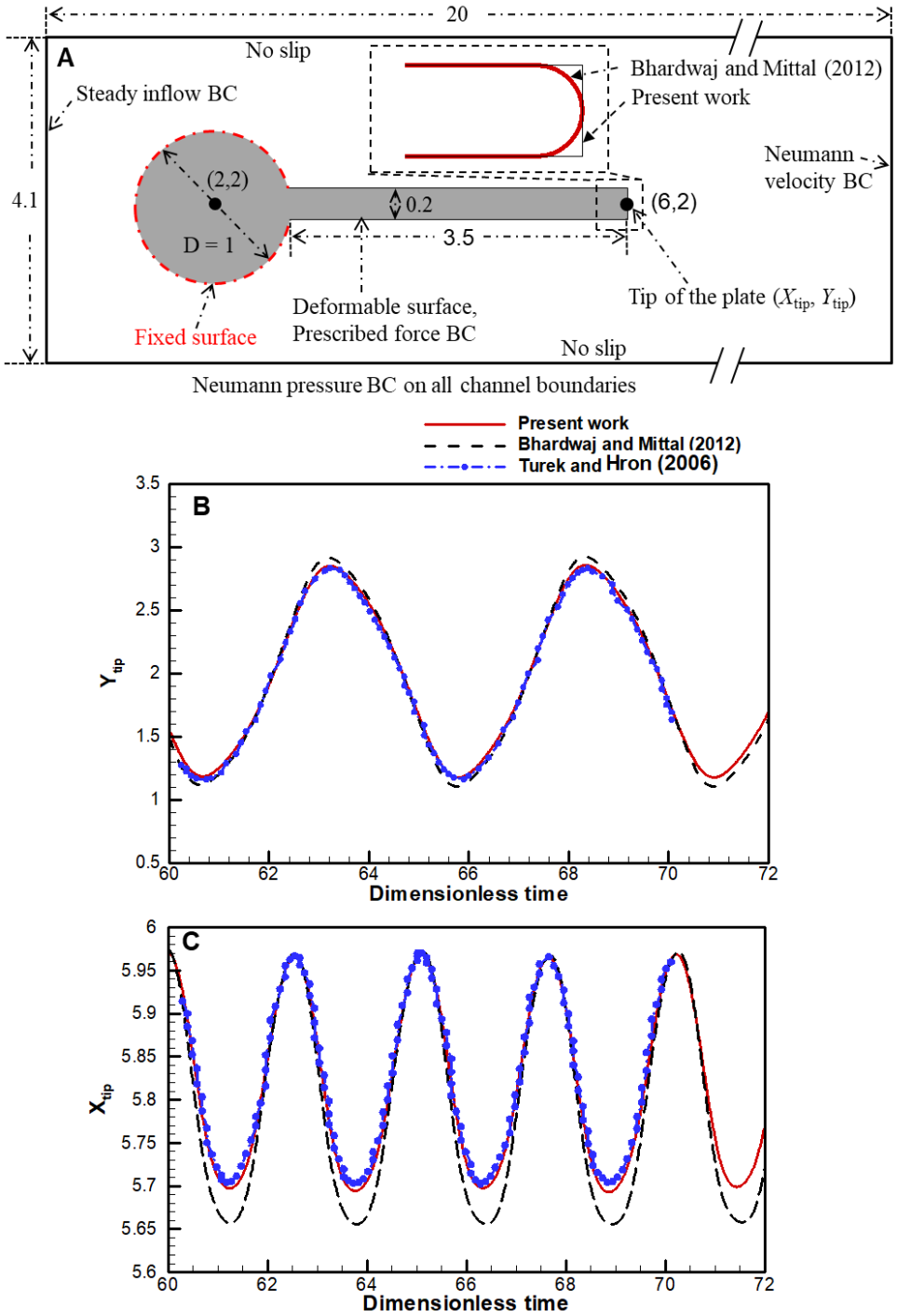

Figure 2.10: (A) Schematic of the computational domain with boundary conditions (BC) considered for the FSI benchmark. The benchmark was first proposed by Turek and Hron (2006) and later considered by Bhardwaj and Mittal (2012). In Ref. Bhardwaj and Mittal (2012), the plate was considered with rounded corners (shown in the inset of Fig. 2.10A). In the present case we consider that plate is reactangular shape. (B) Comparison of computed time-variation of Y_{tip} position with published results (C) Comparison of computed time-variation of X_{tip} with the published results.

where ρ_f^*, μ^*, E^* are dimensional fluid density, dynamic viscosity and Young's mod-

ulus, respectively, and subscript f denotes fluid. The dimensionless structure density is expressed as,

$$\rho_s = \frac{\rho_s^*}{\rho_f^*} \tag{2.45}$$

where subscript s denotes structure.

Table 2.4: Comparison of results for different shapes of corner, mesh type of plate and kinematic boundary condition.

Cases	Mesh Type	Y_{tip}	$\%error$
Turek and Hron (2006)	Body fitted	0.83	-
Bhardwaj and Mittal (2012)	Quadrilateral	0.92	10.84
Single body circular corner of free end of elastic plate (circular section fixed)	Triangle	0.8976	8.14
Single body sharp corner of free end of elastic plate (circular section fixed)	Triangle	0.8373	0.89
Two body circular corner of free end of elastic plate	Triangle	0.8946	7.78
Two body sharp corner of free end of elastic plate	Triangle	0.8276	-0.29
Two body sharp corner of free end of elastic plate (without shear force)	Triangle	0.845	1.81
Two body small circular corner of free end of elastic plate	Triangle	0.85	2.41
Single body circular corner of free end of elastic plate (only surface node fixed)	Triangle	0.919	10.72
Two body circular corner of free end of elastic plate	Quadrilateral	0.8955	7.89
Two body sharp corner of free end of elastic plate	Quadrilateral	0.8210	1.08

In the FSI benchmark, the following values are considered for the simulation setup Turek and Hron (2006): $u_m = 1$, $D = 1$, $Re = 100$, $E = 1.4\times10^3$, $\rho_s = 10$. The Poissons ratio is taken as 0.4 in the structural solver. The validation by Bhardwaj and Mittal (2012) was conducted for the time-varying cross-stream position of the plate tip (Y_{tip}) and its oscillation frequency (St_p), after the plate has reached a self-sustained periodic oscillatory state. In Ref. Bhardwaj and Mittal (2012), St_p was in excellent agreement while the difference in Ytip was around 11%, as compared to the benchmark data of Turek and Hron (2006). In the present chapter, we investigated the source of this difference and it is attributed to the following factors. In Ref. Bhardwaj and Mittal (2012), the plate was considered with rounded corners (shown in the inset of Fig. 2.10A) and the simulation did not include the contribution of shear force in traction boundary condition at the fluid-

structure interface. These factors contributed around 8% and 3% difference with respect to the values of Turek and Hron (2006), respectively. Fig. 2.11 shows the different mesh and shape of the plate. Three different kinds of mesh such as circular corner, sharp corner and small circular corner of plate trailing edge shown in Fig. 2.11, are taken to perform the simulation. Fig. 2.11A, B and C show one body configuration (cylinder and plate are together one body), two body configuration (cylinder and plate are two separate bodies, the plate is attached behind cylinder) with a sharp corner and two body configuration with small corner respectively. Details of

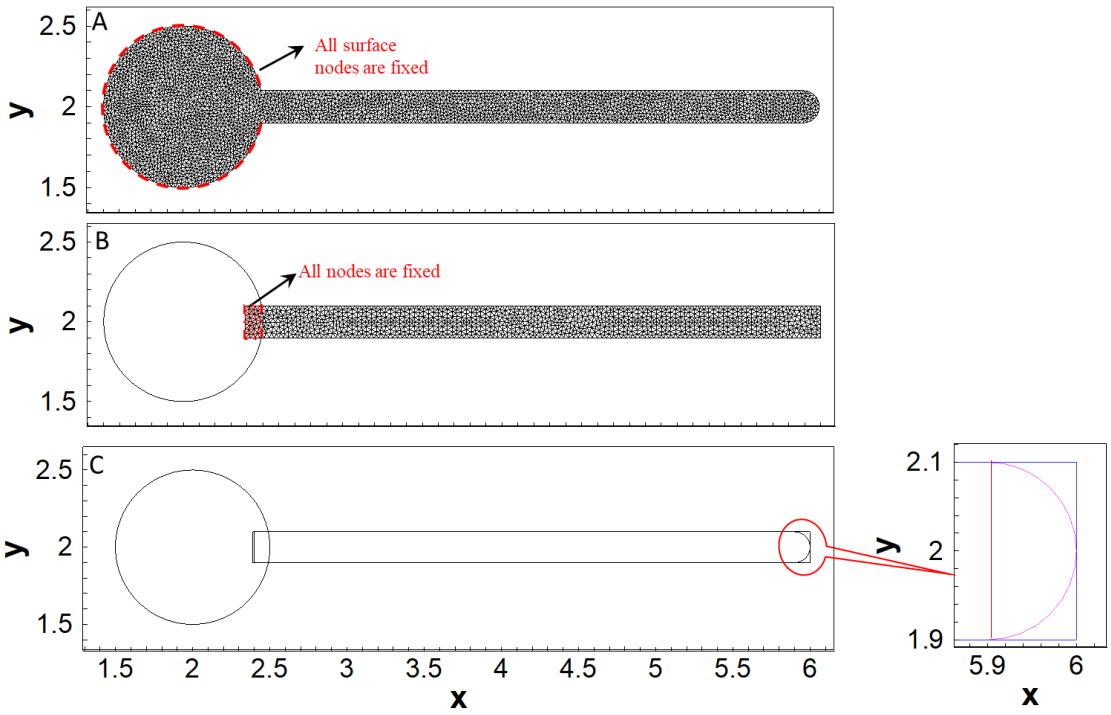

Figure 2.11: Schematic of the different shape of a free end of the elastic plate and kinematic boundary nodes as shown in the red mark : (a) circular corner (b) sharp corner (c) small circular corner

corner effect of elastic plate, mesh type and % error with respect to Turek and Hron (2006) benchmark problem, are given in Table 2.4. Two body sharp corner of free end of triangular mesh elastic plate gives the lowest error (0.29 %) which is good agreement with Turek and Hron (2006) result.

The natural frequencies (St_{ni}) of the plate in first three modes calculated using the modal analysis are also listed in Table 2.5. Using Euler-Bernoulli beam model, the natural frequency (St_{ni}) of the vibration of a cantilever beam in dimensionless form is given by Furquan and Mittal (2015); Thomson (1996)

$$St_{ni} = \frac{{k_i}^2}{2\pi}\sqrt{\frac{EI}{\rho_s A L^4}} \tag{2.46}$$

where EI is the dimensionless flexural rigidity of the beam, $i = 1, 2, 3$ represents frequency modes of the plate and k is the respective constant for the modes. ρ_s, A and L are dimensionless density, cross-sectional area and length of the plate respectively. The values of k are 1.875, 4.694 and 7.855 for first, second and third mode of the natural frequency, respectively.

Table 2.5: Simulation results for different cases considered for steady inflow. The Reynolds number (Re), structure-fluid density ratio (ρ_s) and plate length (L) are varied. The Young's Modulus and plate thickness are 1400 and 0.2, respectively, in all cases. The natural frequencies of the plate in first three modes (St_{ni}) calculated using eq. 3.2 are also listed for all cases.

Cases	Re	ρ_s	L	Y_{tip}	St_p	St_{n1}	St_{n2}	St_{n3}	Remarks
1	100	10	3.5	0.83	0.19	0.03	0.20	0.55	$Y_{tip} \cong St_{n2}$
2	200	10	3.5	0.89	0.20	0.03	0.20	0.55	$Y_{tip} \cong St_{n2}$
3	100	5	3.5	0.45	0.23	0.04	0.28	0.78	$Y_{tip} \cong St_{n2}$
4	100	10	1	0.37	0.35	0.38	2.40	6.71	$Y_{tip} \cong St_{n1}$

The time-varying Y_{tip} and X_{tip} obtained in the revised simulation performed in the present work are compared with the respective results in Refs. Turek and Hron (2006); Bhardwaj and Mittal (2012)] and are Fig. 2.10B and Fig. 2.10C, respectively. The plate displacement as well as frequency is in excellent agreement with the published results of Turek and Hron (2006) in the present work. The computed values of St_p and Y_{tip} are listed in Table 2.5 along with the values reported in the published studies (Turek and Hron (2006); Bhardwaj and Mittal (2012); Lee and You (2013b); Furquan and Mittal (2015); Tian et al. (2010)).

2.5.3.2 Splitter plate attached to a square cylinder

We further validate the large-scale flow-induced deformation module against the benchmark problem, proposed by Wall and Ramm (1998). In this problem, a thin elastic splitter plate is attached to a rigid square cylinder, as shown in Fig. 2.12(a). The reference length is taken the side of the square cylinder, and reference velocity is taken as inlet velocity. The Reynolds number based on these reference values is $Re = 333$. The material parameters are taken as follows: Poisson ratio = 0.35, dimensionless Young's modulus $E = 8.1 \times 10^5$ and the solid to fluid density ratio, $\rho = 84.7$. The inlet flow conditions and boundary conditions are illustrated in Fig. 2.12(a). A non-uniform Cartesian mesh same as earlier validation has been taken for this simulation with non-dimensional time step $\Delta t = 7.5 \times 10^{-3}$. The plate reaches to a self-sustained periodic state, similar to the case of an elastic plate attached to a circular cylinder as shown by the time history of the tip displacement (Y_{tip}) is plotted in Fig. 2.12(b).

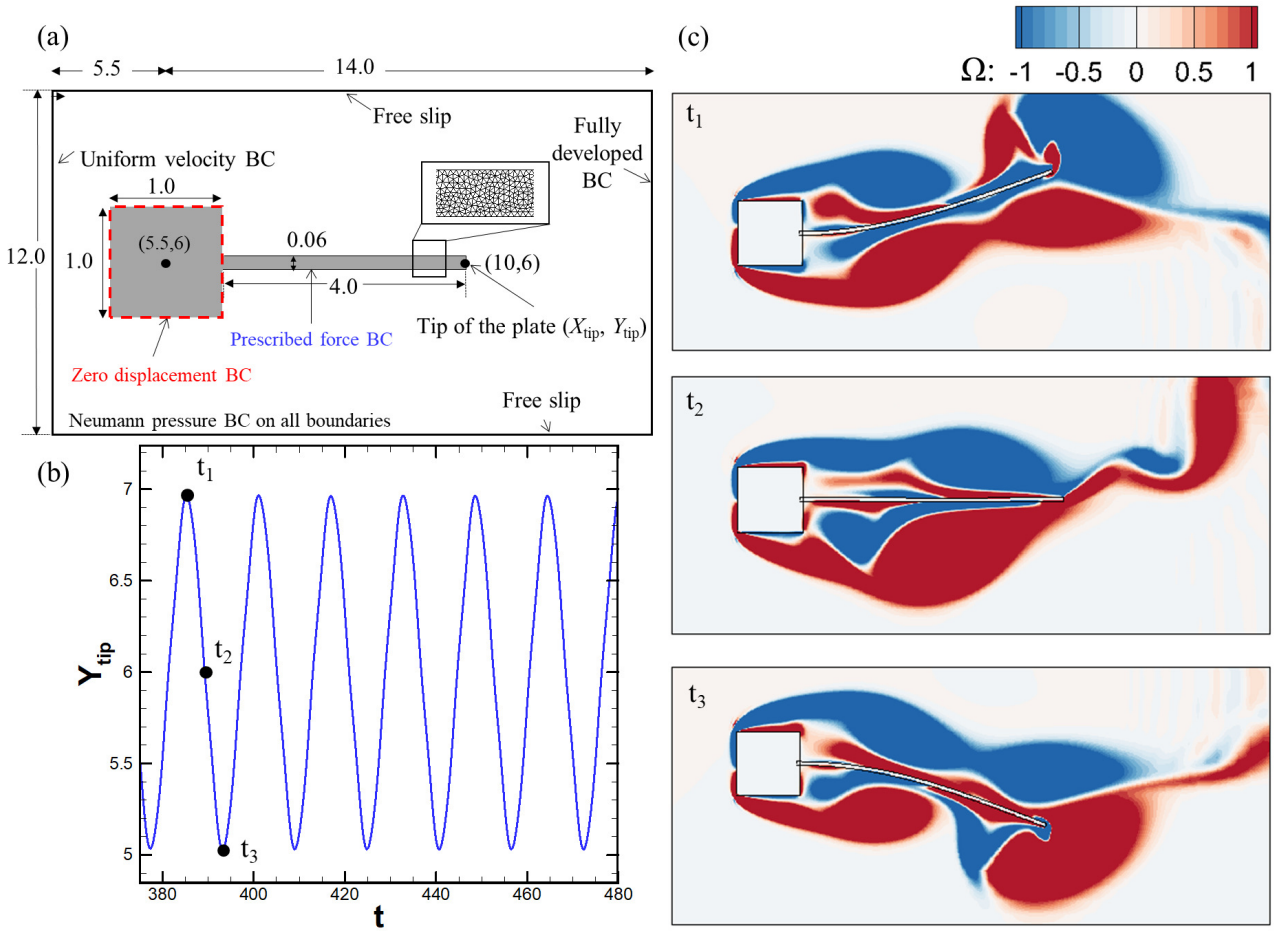

Figure 2.12: (a) Schematic of FSI benchmark problem for square cylinder with thin plate (b) The tip displacement at steady state (c) The vorticity contours at three different locations as shown in (b).

Table 2.6: Comparison between flow quantities for steady flow past a circular cylinder at $Re = 100$ with published data Comparison of Y_{tip} of plate deformation of various cases for Square Cylinder-flag

Study	f_p	Y_{tip}
Present work	0.0637	0.97
Olivier et al. (2009)	0.0617	0.95
Habchi et al. (2013)	0.0634	1.02
Wall and Ramm (1998)	0.058	1.22

The computed plate frequency, as well as tip displacement along with published results, are listed in Table 2.6. We found an excellent agreement between the present and published result, which validates present simulations. At the maximum tip displacement, contours of vorticity are shown at different time instances in Fig. 2.12 (c). These time-instances are shown by dots in Fig. 2.12(b). As noted from the vorticity field, vortices shed alternatively at the top and bottom of the deforming plate.

2.6 Closure

The in-house fluid-structure interaction (FSI) solver is based on a sharp-interface immersed boundary method. The flow solver is strongly-coupled with an open-source **structural dynamic** solver using a partitioned approach. In the present chapter, We have validated flow solver and structure solver independently. We have performed flow solver validation against the pulsatile flow over cylinder and structure solver validation using freely vibration a cantilever beam. Then, we have validated the large-scale flow-induced deformation module as part of the in-house fluid-structure interaction Solver (FSI). We have considered two cases to validate FSI solver – (a) an elastic plate attached behind the circular cylinder (b) an elastic plate attached to the square cylinder. The comparison between our results from FSI solver and published result are good agreement, and we have validated our solver. This solver is used to understand flow-induced dynamics and FSI application which are described in **subsequent** chapter.

Chapter 3

Response of an elastic splitter plate attached to a cylinder to laminar pulsatile Channel flow

The flow-induced deformation of a thin, elastic splitter plate attached to the rear of a circular cylinder and subjected to laminar pulsatile inflow is investigated. The cylinder and elastic splitter plate are contained within a narrow channel and the Reynolds number (Re) is mostly restricted to Re = 100, primarily covering the two-dimensional flow regime. An in-house fluid-structure interaction code is employed for simulations, which couples a sharp-interface immersed boundary method for the fluid dynamics with a finite-element method to treat the structural dynamics. The structural solver is implicitly (two-way) coupled with the flow solver using a partitioned approach. This implicit coupling ensures numerical stability at low structure-fluid density ratios. A power spectrum analysis of the time-varying plate displacement shows that the plate oscillates at more than a single frequency for pulsatile inflow, compared to a single frequency observed for steady inflow. The multiple frequencies obtained for the former case can be explained by beating between the applied and plate oscillatory signals. The plate attains a self-sustained time-periodic oscillation with a plateau amplitude in the case of steady flow, while the superimposition of pulsatile inflow with induced plate oscillation affects the plateau amplitude. Lock-in of the plate oscillation with the pulsatile inflow occurs at a forcing frequency that is twice of the plate natural frequency in a particular mode and this mode depends on the plate length. The plate displacement as well as pressure drag increases at the lock-in condition. The percentage change in the maximum plate displacement, and skin-friction and pressure drag coefficients on the plate, due to pulsatile inflow is quantified. The non-linear dynamics of the plate and its coupling with the pulsatile flow are briefly discussed.

3.1 Introduction

Deforming thin structures are potentially useful for energy-harvesting devices, and recent studies have demonstrated thermal augmentation via flow-induced deformation of thin elastic plates (Soti et al. (2015); Joshi et al. (2015)). In the following sub-sections, we review previous studies on flow past rigid as well as flexible structures

3.1.1 Studies on pulsatile inflow past a rigid cylinder

Through investigations of the effect of pulsatile inflow perturbations on flow past a stationary cylinder, previous numerical studies have shown lock-in behavior (also referred to as phase-locking or synchronization), in which the vortex shedding frequency shifts to be commensurate with the pulsatile forcing frequency at inflow (see review by Griffin and Hall (1991)). Measurements of the flow past a circular cylinder (Barbi et al. (1986); Armstrong et al. (1986)) showed that lock-in occurred for pulsatile frequencies at approximately twice the vortex-shedding frequency. Meneghini and Bearman (1995) plotted the lock-in range for different pulsatile frequencies and amplitudes. Guilmineau and Queutey (2002) numerically studied the flow over an in-line oscillating cylinder with 20% oscillation amplitude of the cylinder diameter and for Reynolds number, $Re = 185$. They showed that the shed vortices switch from one side of the cylinder to the other, as the pulsatile flow frequency increases to a limiting value. Konstantinidis et al. (2003) confirmed the lock-in characteristics observed in previous measurements (Barbi et al. (1986); Armstrong et al. (1986)), and showed that the wavelength of the vortex street varies with the pulsatile flow frequency but the flow amplitude does not alter vortex spacing. More recently Leontini et al. (2013) further quantified the lock-in behavior of a circular cylinder undergoing forced streamwise oscillations as a function of forcing frequency and amplitude, characterizing the wake response over a wide range of control parameters in the two-dimensional laminar regime.

3.1.2 Studies on steady or pulsatile inflow past flexible thin structures

In the context of steady inflow past flexible or elastic thin structures, previous studies documented the effects of the material properties of the structure and flow conditions on the response of the structure. While proposing a FSI benchmark for flow-induced deformation of elastic thin structures, Turek and Hron (2006) showed that the flow past an elastic splitter plate attached to lee side of a rigid cylinder in two-dimensional laminar channel flow results in a self-sustained oscillation of the plate. Bhardwaj and Mittal (2012) quantified the effect of Reynolds number, material properties and geometric non-linearity

on the plate displacement as well as its frequency in the FSI benchmark proposed by Turek and Hron (2006). They showed that the oscillation frequency of the plate varies linearly with dilatational wave speed inside the plate (or its natural oscillation frequencies). Lee and You (2013b) showed that the plate length influences vibration modes of the splitter plate, and the plate displacement is a function of the Young's Modulus and its natural frequencies. Furquan and Mittal (2015) investigated flow past two side-by-side square cylinders with flexible splitter plates and observed lock-in for the plate frequency closer to its first natural frequency. Shoele and Mittal (2016b) proposed stability curves for a flexible plate in an inviscid channel flow and showed that the plate oscillation frequency as well as its stability depends on the channel height. Shukla et al. (2013) experimentally studied the effects of flexural rigidity as well as plate length on the response of the plate in the wake of a circular cylinder and found that the plate displacement collapses on a single curve for different cases of dimensionless bending stiffness. The FSI of elastic, inextensible filaments attached to a cylinder was also reported in previous studies. Bagheri et al. (2012) showed that a hinged flexible filament attached on a cylinder generates a net lift force without increasing drag on it, due to symmetry-breaking instability of the filament which oscillates in upper or lower part of the cylinder wake. Extending work of Bagheri et al. (2012), Lācis et al. (2014) showed the symmetry-breaking instability is similar to the instability of an inverted pendulum. Note that these studies considered very low values of structure-fluid density ratio ((0.1)) as well as flexural rigidity ((0.001)−(0.1)), which is two-three orders of magnitude lesser than the values used in the present chapter. An attached filament on a cylinder also helps in reducing mean drag as well as fluctuations of lift on the cylinder, as reported by Wu et al. (2014). Very few studies are reported in the context of pulsatile inflow past flexible or elastic thin structures in the literature. For instance, Razzaq et al. (2012) studied the FSI interaction of the elastic walls of an aneurysm with an implanted stent structure subjected to pulsatile flow. Habchi et al. (2013) studied twin elastic thin plates mounted in cross-flow configuration at a distance and subjected to the pulsatile flow. They reported that the plates oscillate in opposite-phase and in-phase for larger and smaller value of Young's modulus of the plate, respectively.

3.1.3 Objectives of the present chapter

While the effect of the pulsatile flow on oscillating rigid structures is well-documented and understood, previous reports (Razzaq et al. (2012); Habchi et al. (2013)) available for the pulsatile inflow past flexible, deformable structures did not investigate the effects of forcing frequency and flow amplitude. In addition, the response of the structure for different material properties is poorly reported. The non-linear interaction of the pulsatile flow with the moving structure leads to complex system behavior, such as lock-in and beating.

Such effects have not been investigated to the best of our knowledge. The objective of the present chapter is to investigate the effect of the pulsatile flow on the flow-induced deformation of a thin, elastic structure for an inline flow configuration. To achieve this, the FSI benchmark case proposed by Turek and Hron (2006) is extended to account for the pulsatile inlet flow, and is used to investigate the coupling of the forcing flow frequency as well as amplitude with the frequency of the oscillating plate. The FSI model employed to tackle this problem is discussed in section 2.5.3 and results are presented in section 3.2.

3.2 Results and discussion

In this section, we investigate the effect of pulsatile inflow on the flow-induced deformation and associated wake flow for the flow past a cylinder with a thin trailing elastic plate attached (Fig. 2.10A). The boundary conditions are same as those described in section 2.5.3.1 and are shown in Fig. 2.10A, except at the left channel boundary. A fully-developed pulsatile inflow velocity at the left boundary is prescribed and is expressed in non-dimensional form as follows,

$$u_{pulsatile} = u_{steady}(1 + Ksin(2\pi St_f t)) \tag{3.1}$$

where u_{steady}, St_f and t are dimensionless steady component of the velocity given by eq. 2.42, Strouhal number and time, respectively. The parameters used for the non-dimensionalization for eq. 3.1 are same as the ones used in section 3.1.2. The inflow velocity in eq. 3.1 is superimposition of the steady inflow (u_{steady}) and pulsatile inflow ($u_{pulsatile}$), where K is a constant in range of [0, 1] and controls the fraction of the unsteady component in the total inflow. A typical mesh used in the simulation in the present chapter is shown in Fig. 3.1.

A non-uniform Cartesian grid with stretching is employed in the computational domain as shown in Fig. 3.1A. Zoomed-in views of the grid in the vicinity of the immersed boundary and downstream are shown in Fig. 3.1B and 3.1C, respectively. A uniform grid is used in the region in which the plate is expected to move and non-uniform grid stretching is used from this region to the wall (Fig. 3.1B). In the present section, we use the plate with rounded corners as shown in Fig. 3.1B. The remainder of this section is organized as follows:

- First, grid convergence and domain independence studies are presented in section 3.2.1.
- Second, the effect of plate length and structure-fluid density ratio is discussed on the plate oscillation in case of steady state inflow in section 3.2.2.

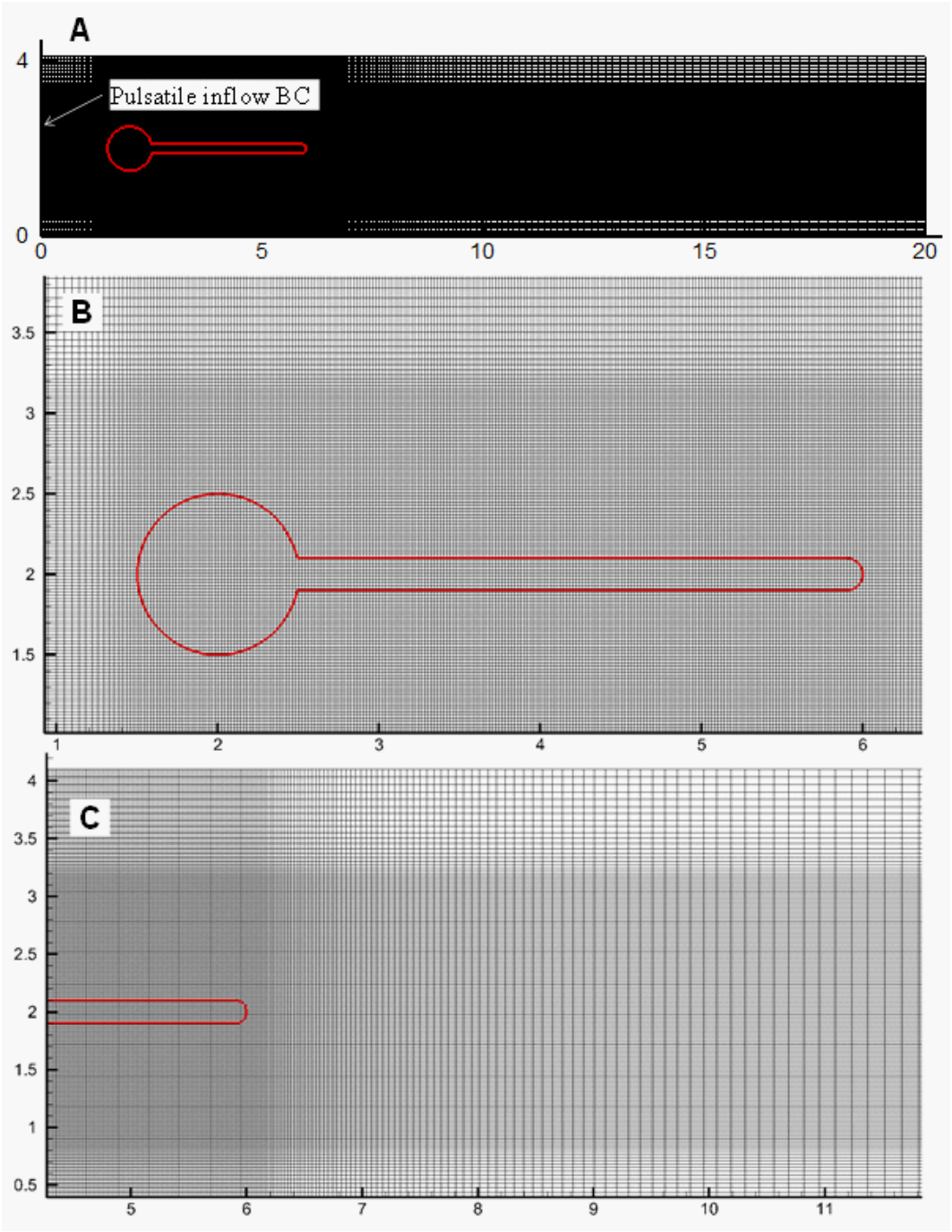

Figure 3.1: (A) Non-uniform Cartesian grid in the computational domain. (B) Zoomed in view of the grid in the vicinity of the immersed boundary. Uniform grid is used in the region in which the plate is expected to move and non-uniform grid stretching is used from this region to the wall. The immersed boundary (fluid-structure interface) is shown in red. (C) Zoomed in view of the grid in the downstream with grid stretching used away from the tip of the plate.

Table 3.1: Grid size convergence study. Error in the maximum plate tip deflection (Y_{tip}) for different grids with respect to the finest grid examined.

Cases	Grid	Δx_{min}	Δy_{min}	Relative error in Y_{tip} with respect to case 3
1	256 × 160	0.03	0.020	-0.075 %
2	384 × 160	0.02	0.020	-0.002%
3	480 × 224	0.015	0.014	-

- Third, the effect of the pulsatile flow frequency (St_f) on the flow-induced deformation and associated flow fields are compared in section 3.2.3. . The flow frequency is varied between 0.1 and 1.0, while keeping the flow amplitude constant ($K = 0.4$).

- Fourth, the effect of the flow amplitude (K) on the plate dynamics and flow fields are investigated in section 3.2.4. The flow amplitude (K) is varied between 0.0 and 1.0, while keeping the flow frequency constant ($St_f = 0.4$).

- Finally, a parameter map is presented in section 3.2.5 to specify the lock-in region and plate response based on the data obtained from several simulation sequences.

3.2.1 Grid and domain size convergence study

We performed grid convergence study with three different non-uniform Cartesian grids, 256 × 160, 384 × 160 and 480 × 224, under pulsatile inflow ($K = 0.4$, $St_f = 0.2$) for flow past an elastic splitter plate behind a cylinder. The time-step was set to $\Delta t = 0.01$. All other simulation setup parameters are given in section 2.5.3. The minimum grid sizes in x and y direction, $\Delta x_{min} = 0.02$ and $\Delta y_{min} = 0.02$ respectively, are listed in Table 3.1. The tip deflection (Y_{tip}) signals obtained for the different grids are compared in Fig. 3.2A, with the inset showing the minor differences observed in peak amplitude for the different grids. The errors with respect to the finest grid are listed in 3.1. Since the relative error for 384 × 160 grid, as shown in 3.1, is one order of magnitude smaller than that for 256 × 160 grid, the 384 × 160 grid ($\Delta x_{min} = 0.02$ and $\Delta y_{min} = 0.02$) was selected for all simulations presented in present chapter.

The domain independence study was conducted with four domains of sizes $20D \times 4.1D$, $25D \times 4.1D$, $30D \times 4.1D$, $40D \times 4.1D$. The steady inflow was considered and simulation parameters are given in section 3.2.2. The tip displacement (Y_{tip}) signals obtained from four different domains considered are compared in Fig. 3.2B. The inset of Fig. 3.2B shows the minor differences observed in peak amplitude for the different domains considered. The error with respect to the longest domain considered are listed in Table 3.2. Since the error for $20D \times 4.1D$ domain is lesser than 1%, this domain size is considered for all simulations presented in this chapter.

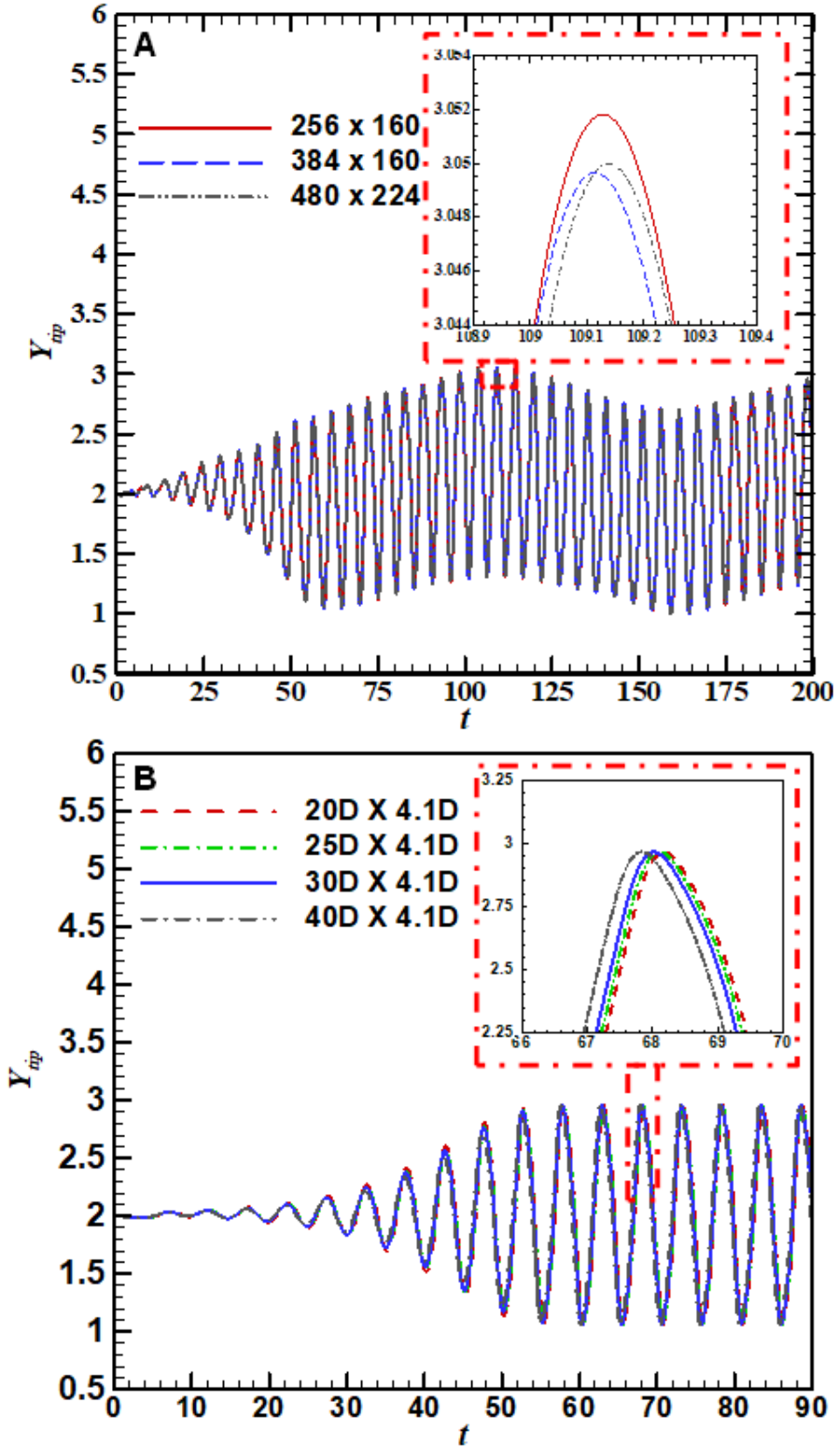

Figure 3.2: (A) Grid size convergence study: comparison of the time-varying cross-stream displacement of the plate tip (Y_{tip}) as a function of grid resolution of the immersed boundary method solver. (B) Domain size independence study: comparison of the time-varying cross-stream displacement of the plate tip (Y_{tip}) for different domains.

Table 3.2: Domain size independence study. Error in the maximum plate tip deflection (Y_{tip}) for different domain sizes with respect to the longest domain size examined

Cases	Domain size	Relative error in Y_{tip} with respect to case 4
1	$20D \times 4.1D$	0.042%
2	$25D \times 4.1D$	0.021%
3	$30D \times 4.1D$	0.010%
4	$40D \times 4.1D$	-

3.2.2 Steady inflow

In this section, we investigate the effect of problem parameters on the plate oscillation frequency in FSI benchmark described in section 2.5.3. We vary Reynolds number (Re), structure-fluid density ratio (ρ_s) and plate length (L), keeping all other parameters same in cases 2, 3 and 4 listed in Table 2.5, respectively. The maximum computed displacement (Y_{tip}) and oscillation frequency (St_p) in all cases are summarized in Table 2.5. The natural frequencies (St_{ni}) of the plate in first three modes calculated using the modal analysis are also listed in Table 2.5. Using Euler-Bernoulli beam model, the natural frequency (St_{ni}) of the vibration of a cantilever beam in dimensionless form is given by Furquan and Mittal (2015); Thomson (1996)

$$St_{ni} = \frac{{k_i}^2}{2\pi}\sqrt{\frac{EI}{\rho_s A L^4}} \tag{3.2}$$

where EI is the dimensionless flexural rigidity of the beam, $i = 1, 2, 3$ represents frequency modes of the plate and k is the respective constant for the modes. ρ_s, A and L are dimensionless density, cross-sectional area and length of the plate respectively. The values of k are 1.875, 4.694 and 7.855 for first, second and third mode of the natural frequency, respectively. In the FSI benchmark (case 1 in **Table 2.5**, $L = 3.5D$), the plate initially exhibits small deformation and reaches a periodic self-sustained oscillation with a constant amplitude, displaying a sinusoidal-like wave pattern of the time-varying displacement of the tip of the plate Bhardwaj and Mittal (2012) (Fig. 2.10B). The superimposed shapes of the deformed plate at different time instances are shown in Fig. 3.4A(left).

In this case, the plate oscillation frequency is close to the natural frequency in the second mode ($St_p \cong St_{n2}$, case 1 in **Table 2.5**). In cases 2 and 3 in **Table 2.5**, we vary $Re = 200$ and $\rho_s = 5$, respectively, keeping all parameters same and the simulated plate frequency St_p is again close to the second mode of the natural frequency ($St_p \cong St_{n2}$). In case 4, we vary plate length to $L = D$ and the plate oscillates with the frequency close to the first mode of natural frequency ($St_p \cong St_{n1}$). The superimposed shapes of the deformed plate at different time instances for this case are shown in Fig. 3.4B.

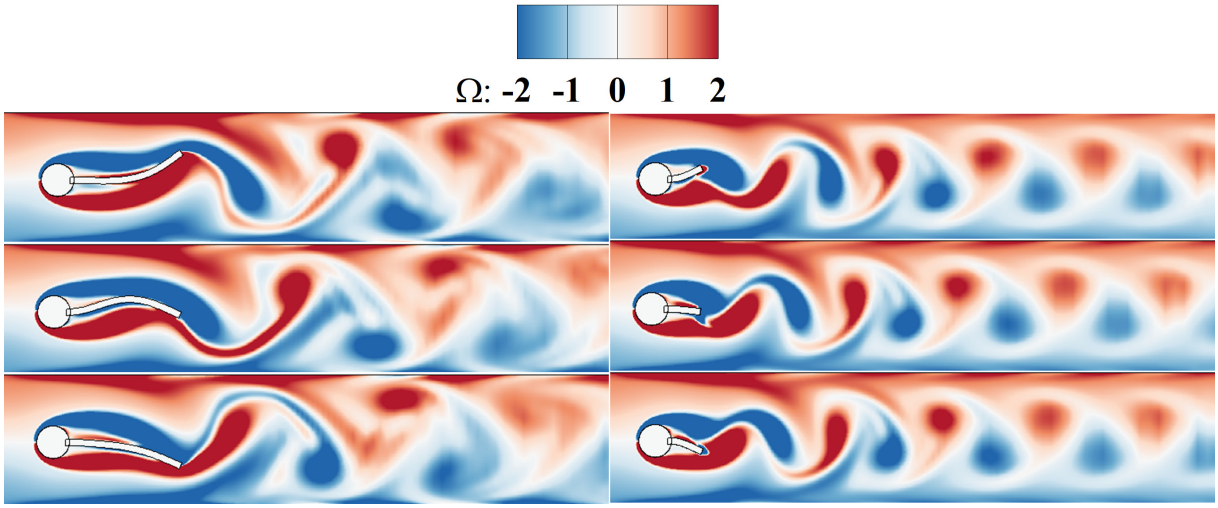

Figure 3.3: Vorticity contour for steady inflow at the inlet for different plate lengths. (left) $L = 3.5D$ (right)$L = D$. Other parameters used in both cases are $E = 1400$, $Re = 100$ and $\rho_s = 10$.

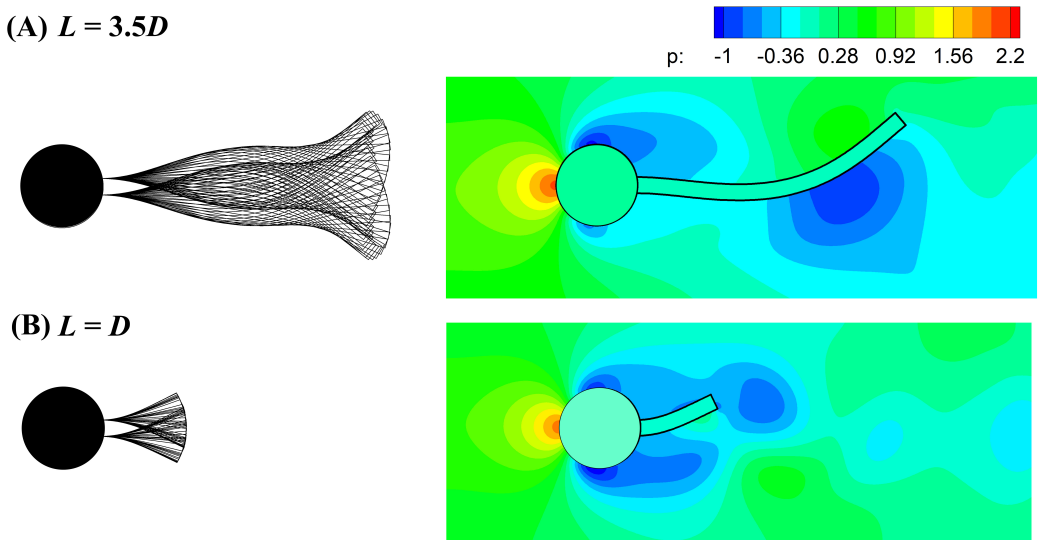

Figure 3.4: Superimposed deformed shapes of the plate at several time instances for the plate length (left) and pressure contours (right) for steady inflow at the inlet for different plate lengths. (A) $L = 3.5D$ (B)$L = D$. Other parameters used in both cases are $E = 1400$, $Re = 100$ and $\rho_s = 10$.

Fluid-structure interaction of a cylinder with attached elastic splitter plate is a coupled system. Vortex sheds from cylinder roll over the plate and sheds behind the tip of the plate and plate oscillate in the case of the larger elastic plate, as shown in Fig. 3.3. For small elastic splitter plate, vortex shedding behavior is different from the large elastic plate as shown in Fig. 3.3 because vortex comes from the cylinder and falls at the tip of the plate. Plate natural frequency depends on material properties. When Vortex shedding frequency of the plate matches with plate natural frequency, lock-in occurs, and plate vibrates with

a particular mode. Thus, the plates with length $L = 3.5D$ and $L = D$ oscillate with second and first mode of the natural frequency, respectively. This can be explained by the fact that the flow past cylinder creates regions wherein the pressure on one side of the plate is greater than that on the other side. This pressure differential translates to non-uniformly distributed load applied to the structure, which produces plate deformations The pressure loading on the longer plate is non-uniformly distributed as compared to that on the shorter plate. The non-uniform loading results in larger bending and consequently the plate vibration is closer to that in the second mode. A qualitative comparison of the pressure distribution at the instance of maximum plate deformation is shown in Fig. 3.4 (right column) and confirms this hypothesis. Note that these observations are consistent with those given by Lee and You (2013b).

3.2.3 Effect of pulsatile inflow frequency

In this section, we discuss the effect of pulsatile inflow on the plate oscillation. In pulsatile inflow case, the forcing frequency interacts with the natural oscillation frequency of the plate, which results in beating and lock-in signals. The effect of the pulsatile inflow frequency (St_f) is studied by varying it within the range [0.0, 1.0], while keeping the flow amplitude constant at $K = 0.4$. The time-varying tip displacement of the plate (Y_{tip}) is shown in the left column of Fig. 3.5 and Fig. 3.6 .

The power spectra of these signals are shown in the middle column, indicating the dominant frequencies in the signals. Note that the difference in the applied flow frequency (St_f) and the oscillating plate frequency (St_{n2}) generates beating between these frequencies, clearly evident in the tip displacement evolutions. For instance, at $St_f = 0.1$, 0.2 and 0.4, the plate oscillates with $\mid St_f \pm kSt_{n2} \mid$ and kSt_{n2} (k = integer), as shown in the power spectra, plotted in middle column of Fig. 3.5. Lock-in (phase-locking, synchronization) is a phenomenon in which the vortex shedding frequency of plate changes (and locks) to match the natural frequency of plate. In the present case, vortex shedding frequency of plate ($St_{v,p}$) is equal to plate oscillation frequency (St_p). The natural frequency of the plate depends on material properties, and when the natural frequency of the plate matches with plate vortex shedding frequency, lock-in occurs. Plate vibrates with natural plate frequency. Here material properties are fixed ($E = 1400$ and $\rho = 10$) and plate always oscillates in the second mode.When two frequency matches with each other, only resonance occur, there is no change in frequency, and external frequency does not play any role to trigger higher Structural natural frequencies. Lock-in condition occurs with pulsatile flow for $St_f = 0.4$, for which $St_f \sim St_{n2}$, which results in the largest plate displacement . For the lower frequencies$St_f = 0.1$ - 0.5, the vorticity contours at the instance of maximum plate deformation, plotted in the right column of Fig. 3.5 show that the shear layers at the top and bottom of the plate roll up to form strong positive and

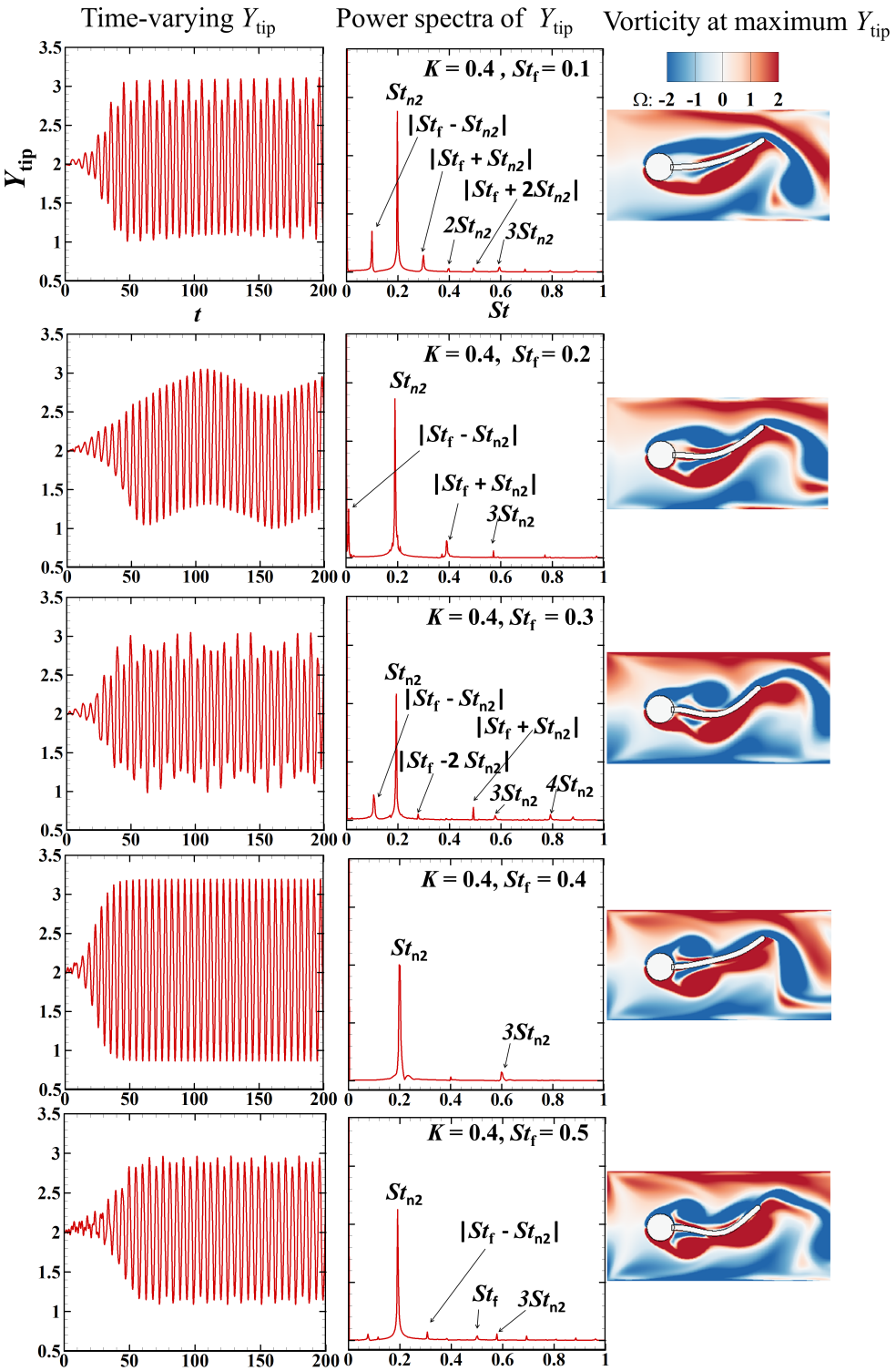

Figure 3.5: Time-varying tip displacement varying with amplitude (K) and frequency (St_f). Note that $K = 0$, $St_f = 0$ corresponds to non-pulsatile flow. Power spectra of Y_{tip} displacement of elastic plate (middle figure). Vorticity distribution of pulsatile flow (right).

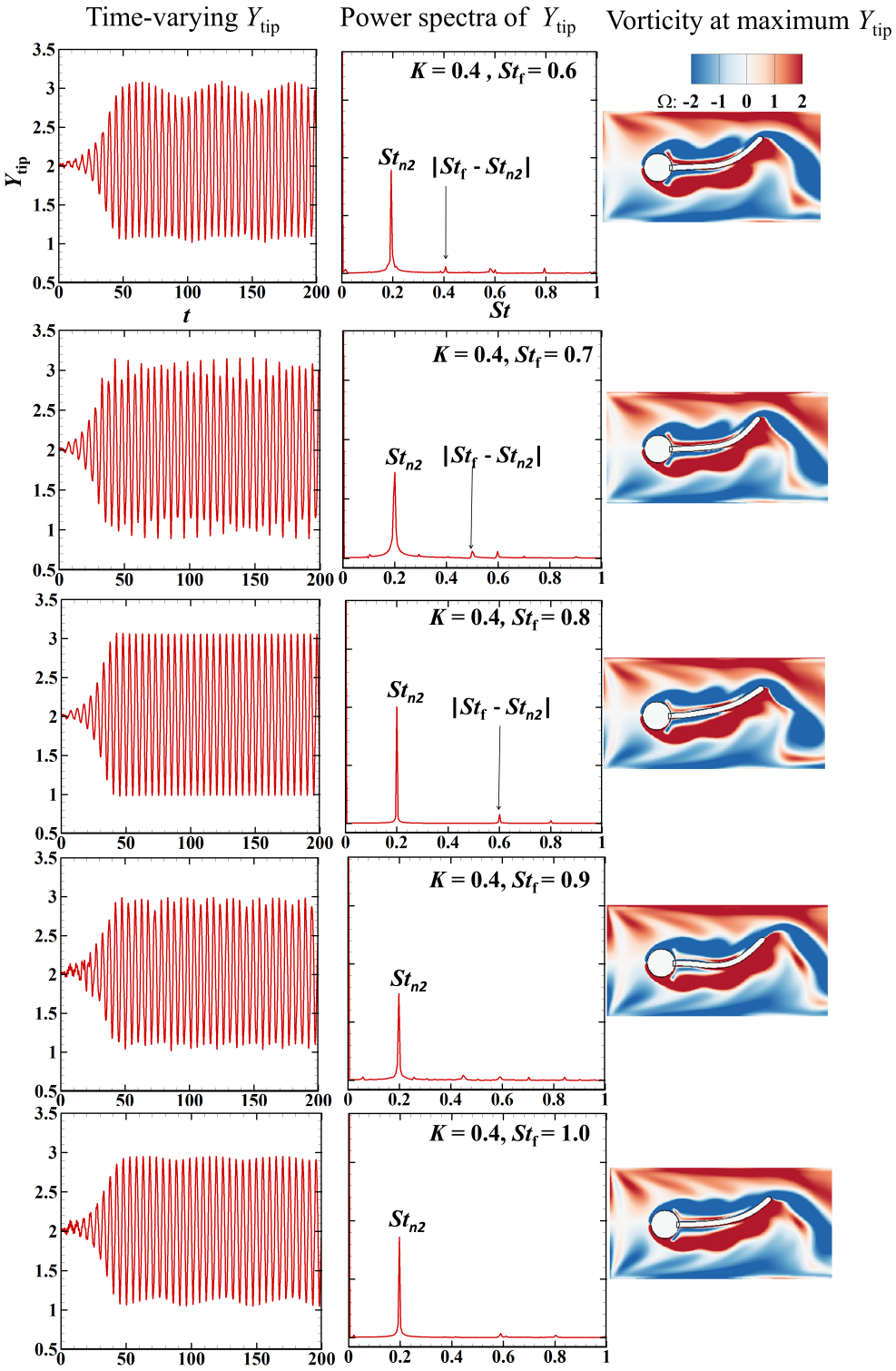

Figure 3.6: Continuation of Fig. 3.5

negative vortices, resepctively. At higher frequencies ($St_f > 0.5$), the shear layer shows the formation of the two or more smaller vortices of the same sign on each side of the plate, showing the strong effect of pulsatile flow on the wake. We quantify the effect of pulsatile flow in terms of the drag coefficients for the plate, defined as,

$$C_{DP} = \frac{2{F^*}_{DP}}{\rho_f^* {U^*_m}^2 D^*} \tag{3.3}$$

$$C_{DS} = \frac{2{F^*}_{DS}}{\rho_f^* {U^*_m}^2 D^*} \tag{3.4}$$

$$C_D = C_{DP} + C_{DS} \tag{3.5}$$

where C_{DP}, C_{DS} and C_D are pressure, skin-friction and total drag coefficient of the plate, respectively. ${F^*}_{DP}$ and ${F^*}_{DS}$ are the pressure and shear force per unit span-wise length on the plate, respectively.

In order to quantify the influence of pulsatile inflow on the drag on the plate and its components, we plot the time-variation of Y_{tip}, C_{DP}, C_{DS} and C_D for steady inflow and two cases of pulsatile inflow in Fig. 3.7A and 3.7B, 3.7C, respectively. The vorticity distribution at different time instances is shown in the insets. The plots of the pulsatile inflow are presented for lock-in condition ($K = 0.4$, $St_f = 0.4$) in Fig. 3.7B. In Fig. 3.7A for the steady inflow, the maximum pressure drag as well as skin friction drag occurs at the maximum plate displacement (at $t \sim 186$ and 189). The contribution of the skin-friction drag in the total drag is around 13% at these instances. The maximum pressure drag is attributed to blockage of the flow created by the deformed plate in the channel at the instance of the maximum deformation. As expected, the total drag and its components are the lowest at the instance of the mean position of the tip ($t \sim 187.5$). In case of the pulsatile inflow (Fig. 3.7B), the maximum pressure drag as well as skin friction drag also occurs at the maximum plate displacement (at $t \sim 187.5$ and 190). However, the contribution of the skin friction drag in the total drag is 33%, around three times larger than that in the case of the steady inflow in Fig. 3.7A. Interestingly, the skin friction drag is negative at the instance of the mean position of the tip ($t \sim 189$). This observation may be attributed to the formation of shear layers along the plate length due to the pulsatile inflow and is described as follows. As shown in the inset of Fig. 3.7B, at the instance of the maximum tip displacement at $t \sim 187.5$ ($t \sim$190), a shear layer of negative (positive) vorticity at the top (bottom) of the plate roll up to form strong negative (positive) vortex near the cylinder and another negative (positive) vortex which is about to shed in the downstream. On the other hand, at the mean position of the tip ($t \sim$189), a shear layer of positive vorticity dominates along the plate length, which corresponds to negative skin friction drag at this instance.

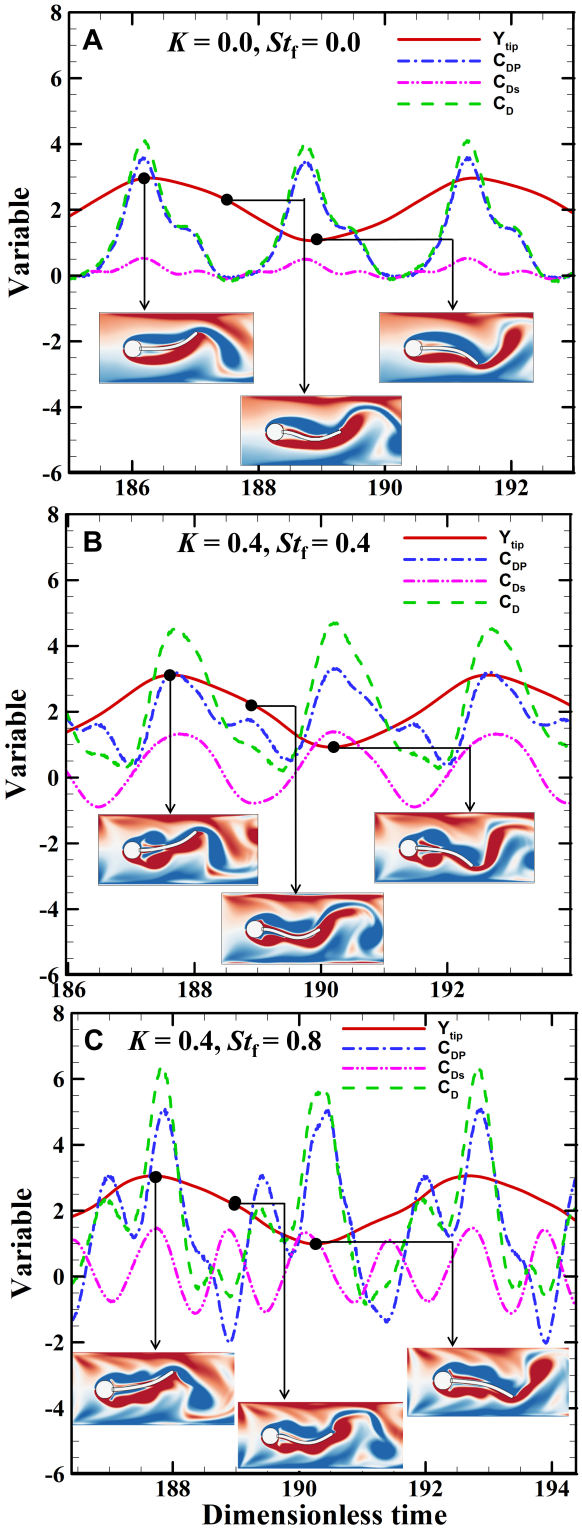

Figure 3.7: Comparison among time-varying displacement of the tip of the plate (Y_{tip}), pressure drag coefficient (C_{DP}), skin friction drag coefficient (C_{DS}) and total drag coefficient (C_D). (A) Steady inflow, $K = 0.0$, $St_f = 0.0$ (B) Pulsatile inflow, $K = 0.4$, $St_f = 0.4$, (C) Pulsatile inflow, $K = 0.4$, $St_f = 0.8$. Vorticity distribution at different time-instances is shown in insets and the vorticity scale is same as in Fig. 3.5 (third column).

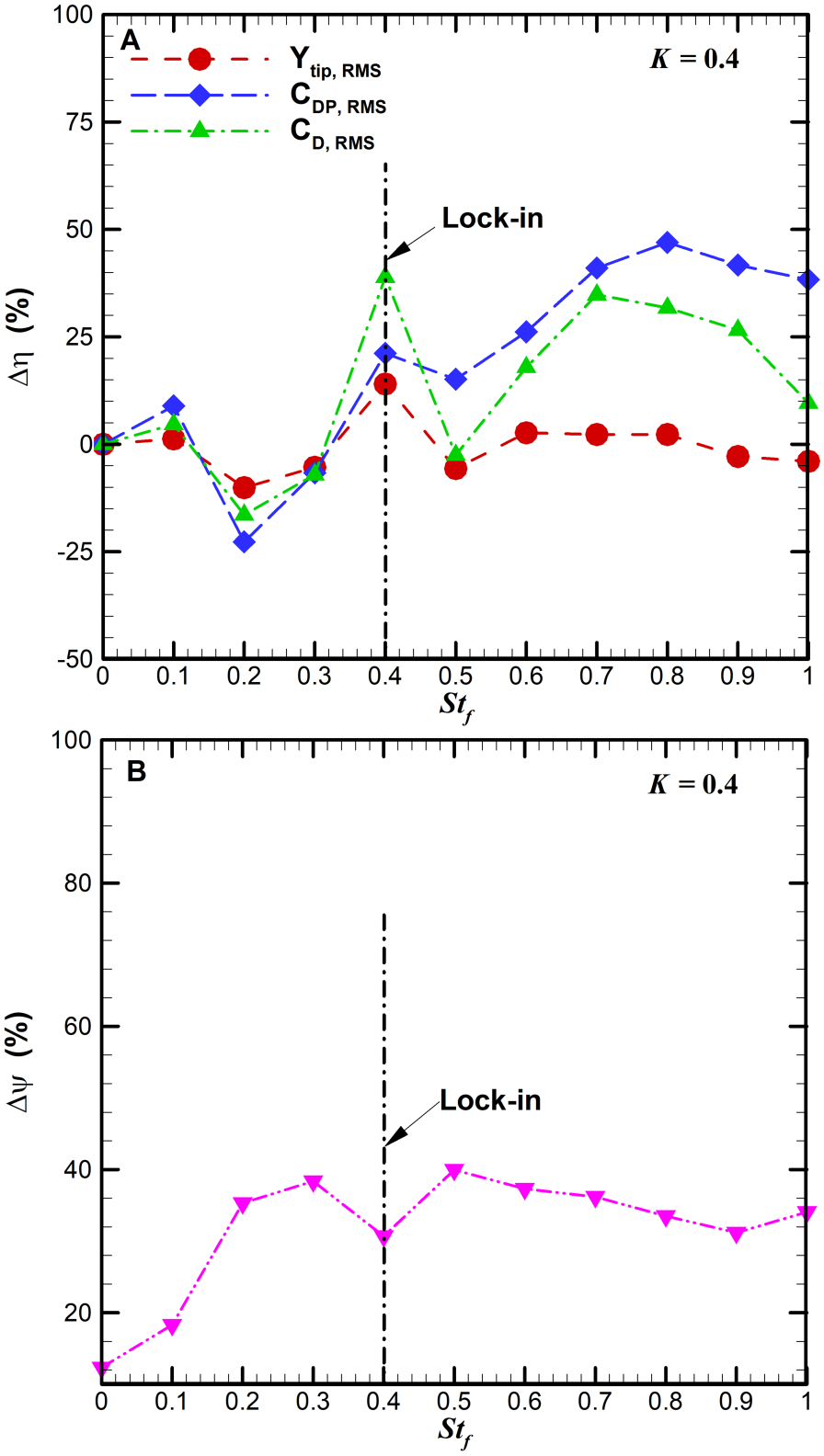

Figure 3.8: Percentage change in RMS values of deformation of plate (Y_{tip}), pressure drag coefficient (C_{DP}) and total drag coefficient (C_D), relative to results for steady inflow, as a function of pulsatile inflow amplitude (K). The inflow frequency was fixed at $St_f = 0.4$. (B) Contribution of the RMS skin friction drag with respect to RMS total drag.

Similarly, the time-variations of Y_{tip}, C_{DP}, C_{DS} and C_D at larger forcing frequency ($K = 0.4$, $St_f = 0.8$) are plotted in Fig. 3.7C. Due to increased forcing frequency, the tendency to roll the vortices over the plate as well as their strength decreases (as seen in the insets in Fig. 3.7C) and it results in larger pressure perturbations near the structure. Therefore, the maximum pressure drag at the instance of the maximum displacement at $St_f = 0.8$ is around 50% larger than that in $St_f = 0.4$. To further quantify the effect of the pulsatile flow frequency, it is useful to define the percentage change in a flow quantity with respect to the steady inflow,

$$\eta = \frac{\eta_{pulsatile} - \eta_{steady}}{\eta_{steady}} \times 100\% \tag{3.6}$$

where $\eta_{pulsatile}$ and η_{steady} are the flow quantities for the pulsatile and steady inflow, respectively. Fig. 3.8A plots Y_{tip} for RMS values of Y_{tip}, C_{DP} and C_D as a function of pulsatile flow frequency, St_f. $\Delta\eta$ for $C_{DP,RMS}$ and $C_{D,RMS}$ scales non-monotonically with Y_{tip}, RMS for Y_{tip} [0.1, 0.5]. The total drag and pressure drag contribution show a significant increase at the lock-in condition ($St_f \sim 2St_{n2}$), due to a 16 % larger plate displacement. Similarly, C_{DP}, and C_D show decrease of around 15-25% in Fig. 3.8A due to decrease in RMS value of Y_{tip} at $St_f = 0.2$ since Y_{tip} shows a strong variation with time due to the beating in the Fig. 3.5A (second row). At higher frequencies, $St_f \in$ [0.6, 1.0], Y_{tip} for $C_{DP,RMS}$ is significantly larger (∼25-40%) in Fig. 3.8A. As explained earlier, this is due to the decrease in strength of the rolling vortices over the plate (see insets of Fig. 3.7C) which results in larger pressure perturbations near the structure and increases pressure drag. Thus, the pressure drag is larger for $St_f \in$[0.6, 1.0] and the total drag also shows similar characteristics except at $St_f = 1.0$. The total RMS drag at $St_f = 1.0$ reaches to a value, comparable to that computed in the steady inflow case and is around 10% larger due to increase in the shear drag on the plate, explained in the following paragraph. The flow field at $St_f = 1.0$ becomes qualitatively similar to that in the steady inflow case, due to the decaying strength of the rolling vortices at the top and bottom of the plate. The vorticity field at the instance of the maximum displacement shown in the inset of Fig. 3.5B (last row) is qualitatively similar to that for the steady inflow, in the inset of Fig. 3.7A, except in close proximity to the surface of the plate. In order to quantify the contribution of the skin-friction drag, we define percentage of the skin-friction drag coefficient with respect to total drag coefficient $\Delta\psi$, as follows,

$$\Delta\psi = \frac{C_{DS,RMS}}{C_{D,RMS}} \times 100\% \tag{3.7}$$

As plotted in Fig. 3.8A, $\Delta\psi$ is more than 30% for $St_f \in$ [0.2, 1.0]. The increase in the skin-friction drag is attributed the formation of shear layers along the plate length due to pulsatile inflow, as explained earlier (see insets of Figs. 3.7B and 3.7C). A slight dip in

$\Delta\psi$ at lock-in is explained by shedding of rolled vortices over the plate, which pushes the shear layer along the plate length. Overall, the total drag is significantly larger (20%-50%) for the pulsatile flow cases as compared to the steady inflow case for $St_f \in [0.4, 1.0]$ and $K = 0.4$.

3.2.4 Effect of pulsatile inflow amplitude

In this section, the effect of the forcing flow amplitude on the flow-induced deformation of the splitter plate at constant pulsatile inflow frequency, $St_f = 0.4$, is examined. The time-varying plate displacement (Y_{tip}), power spectra of Y_{tip} and vorticity contours at instance of maximum Y_{tip} are plotted in the left, middle and right columns of Fig. 3.9, respectively. The flow amplitudes investigated are $K \in [0.0, 1.0]$ and $K = 0.0$, $St_f = 0.0$ corresponds to the steady inflow at the inlet. Since $St_f = 0.4$ corresponds to the lock-in frequency, as simulated in section 3.2.3, the beating is not observed in the simulated cases shown in Fig. 3.9, in contrast to many of the cases examined in section 3.2.3. Indeed, the power spectra of Y_{tip}, plotted in Fig. 3.9, show lock-in at all flow amplitudes. The vorticity contours are plotted in the right column of Fig. 3.9, showing that the vortices on the top and bottom sides of cylinder surface roll up increasingly tightly and are clearly identifiable as discrete entities as they move along the plate, as the forcing amplitude increases.

As in section section 3.2.3, Fig. 3.10A shows the percentage change in various system characteristics with respect to the steady inflow: the maximum plate deformation ($Y_{tip,RMS}$), total drag ($C_{D,RMS}$) and pressure drag ($C_{DP,RMS}$) for the flow amplitudes tested for the lock-in condition. $C_{D,RMS}$ and $C_{DP,RMS}$ show almost a linear increase due to increase in $Y_{tip,RMS}$, implying increased blockage of the flow by the deformed plate in the channel at the instance of the maximum deformation. The maximum percentage increase in the total pressure drag ($C_{D,RMS}$) is approximately 75% and the plate deformation increases by 31%, both at $K = 1$. The contribution of the skin friction drag with respect to total drag ($\Delta\psi$, (3.7)) with respect to flow amplitude K is plotted in Fig. 3.10B. In general, we note a linear increase in $\Delta\psi$ with K and the largest value 50% occurs at $K = 1$. The increase in shear drag with flow amplitude is due to the increasing strength of the rolling vortices and shear layers along the plate length. The vorticity signatures at the instance of the maximum plate deformation, plotted in the insets of Fig. 3.9, verify this hypothesis. Overall, the total drag is significantly larger (20% to 75%) for the pulsatile flow cases as compared to the steady inflow case for $K \in [0.4, 1.0]$ and $St_f = 0.4$.

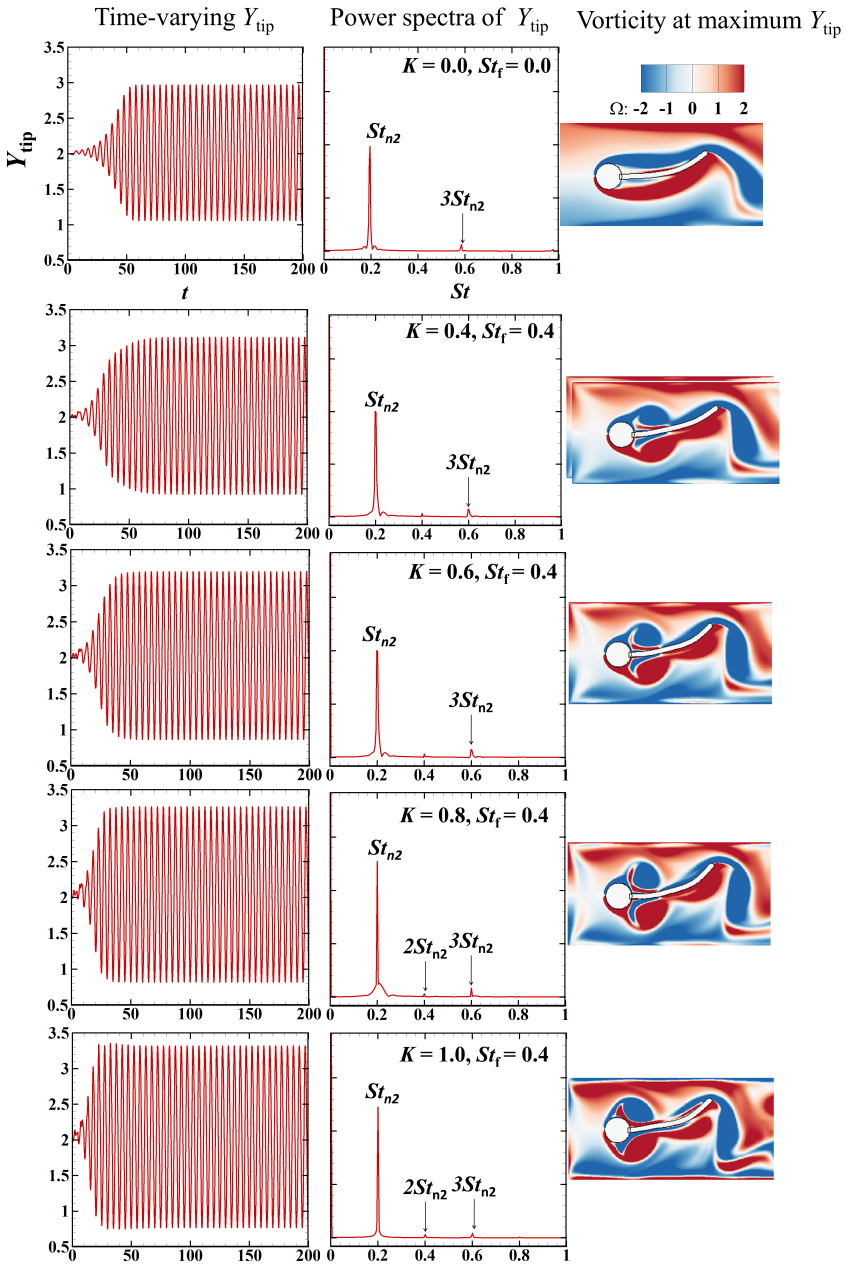

Figure 3.9: Time-varying Y-displacement of the tip of the plate varying with amplitude (K) for constant frequency $St_f = 0.4$. Note that $K = 0$, $St_f = 0$ corresponds to steady flow at the inlet. Effect of amplitude on elastic plate (left figure). Power spectra of Y_{tip} displacement of elastic plate (middle figure). Vorticity distribution of pulsatile flow (right).

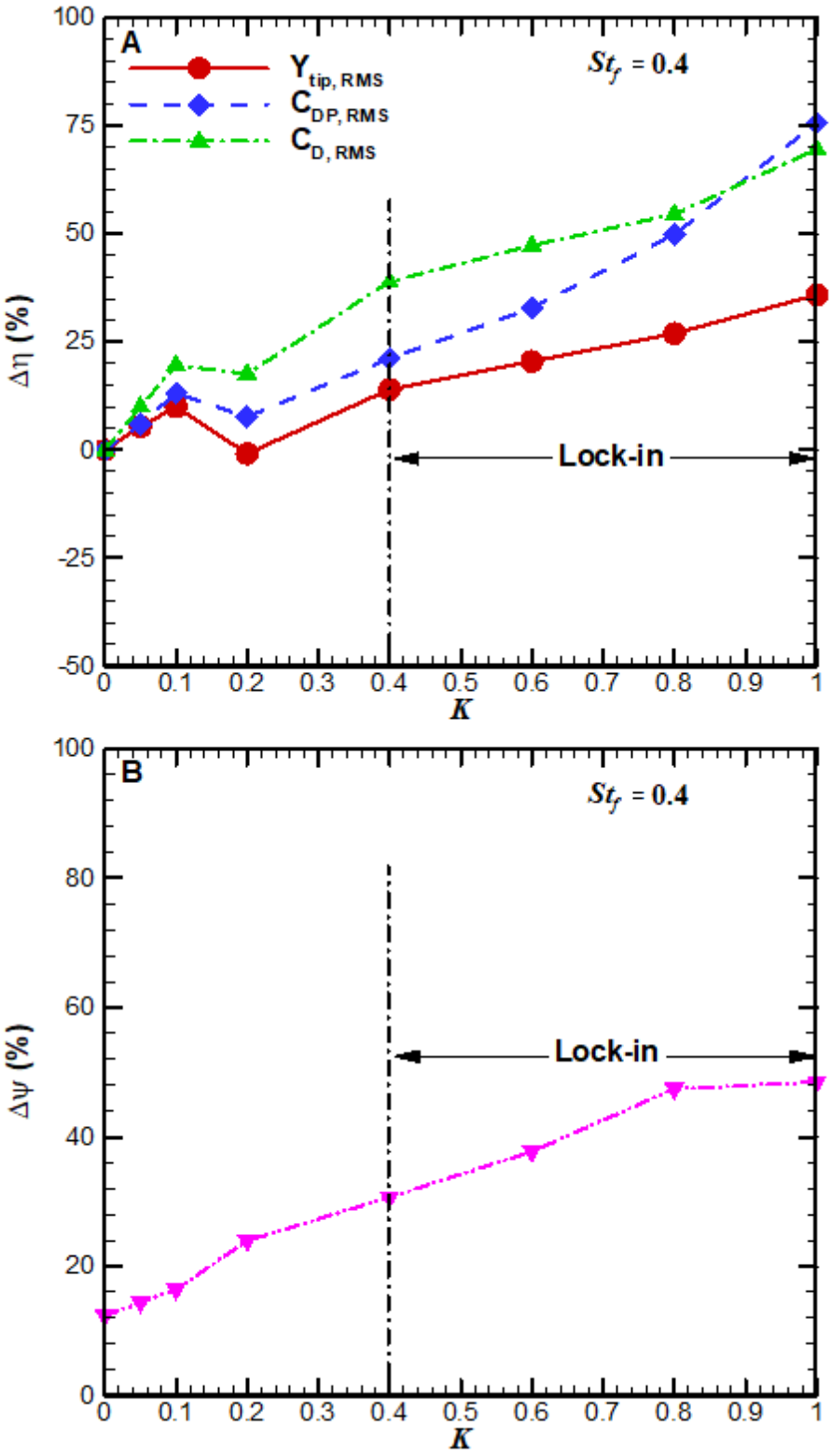

Figure 3.10: Percentage change in RMS values of deformation of plate (Y_{tip}), pressure drag coefficient (C_{DP}) and total drag coefficient (C_D), relative to results for steady inflow, as a function of pulsatile inflow amplitude (K). The inflow frequency was fixed at $St_f = 0.4$. (B) Contribution of the RMS skin friction drag with respect to RMS total drag.

3.2.5 Lock-in condition

As explained in section 3.1, in the absence of deformation of the splitter plate, lock-in (phase-locking, synchronization) is a phenomenon in which the vortex shedding frequency changes (and locks) to match the applied flow perturbation frequency. Extending this to deformable plates, lock-in occurs if beating does not occur in the Y_{tip} signal and the plate frequency synchronizes to the forcing frequency. This situation leads to maximum plate deformation. Fig. 3.11A summarizes the simulations performed, plotting beating and lock-in cases as a function of forcing frequency (St_f) for different applied forcing flow amplitudes (K). The natural frequencies of the plate for the first three modes (St_{n1}, St_{n2} and St_{n3}) are also plotted. The lock-in occurs for the flow amplitude, $K \geq 0.4$ and at a forcing frequency, $St_f = 0.4$, twice of the splitter plate oscillation frequency as well as its natural frequency in the second mode, i.e., $St_f \cong 2St_p \cong 2St_{n2}$. The natural frequencies are calculated using eq. (3.2) and are listed for first three modes in **Table 2.5**). Note that the simulations at $St_f = 0.35$ and 0.45 at different flow amplitudes show beating patterns. In Fig. 3.11B, the increase in the plate displacement (Y_{tip}) at lock-in is quantified by plotting percentage change in it with respect to the steady inflow (eq. (3.7)) as a function of the forcing flow amplitudes. $\Delta\eta$ for Y_{tip} linearly increases with the flow amplitude and reaches to around 35%, at $K = 1$, as plotted in Fig. 3.11B. Superimposed shapes of the deformed plate at different time instances are shown in the inset of Fig. 3.11B for a typical lock-in case. The effects of the lock-in on the plate motion are quantified by comparing the phase plane plot of the trajectory of the plate tip (X_{tip}, Y_{tip}) for the steady inflow and pulsatile inflow ($St_f = 0.4$, $K = 0.4$) in Fig. 3.12. Around 20 plate oscillation cycles are plotted for both cases after plate reaches self-sustained oscillation with plateau displacement. Results shows that the plate oscillates about a mean position in both cases and Y_{tip} is around 15% larger in pulsatile flow case due to lock-in condition. The influence of lock-in on the associated wake structures is shown by qualitatively comparing vorticity contours at different instances in a typical cycle in insets in Fig. 3.12. The right insets for pulsatile inflow case show that the shear layers at the top and bottom of the plate roll up to form strong positive and negative vortices at the instance of maximum plate deformation. In order to quantify the effect of structure-fluid density ratio (ρ_s) on the lock-in and beating conditions, we performed additional simulations by varying it to $\rho_s = 5$ and keeping all other parameters same ($E = 1400, Re = 100, L = 3.5D$) in the cases considered in section 3.2.3 and section 3.2.4. The beating and lock-in cases are plotted in Fig. 3.13 for several values of forcing frequency (St_f) and forcing amplitude (K). The lock-in occurs for all flow amplitudes, $K > 0$ and at a forcing frequency, $St_f = 0.46$, roughly twice of the natural frequency in the second mode ((3.2)), i.e., $St_f \cong St_p \cong 2St_{n2}$. Superimposed shapes of the deformed plate at different time instances are shown in the inset of Fig. 3.13A for a typical lock-in case.

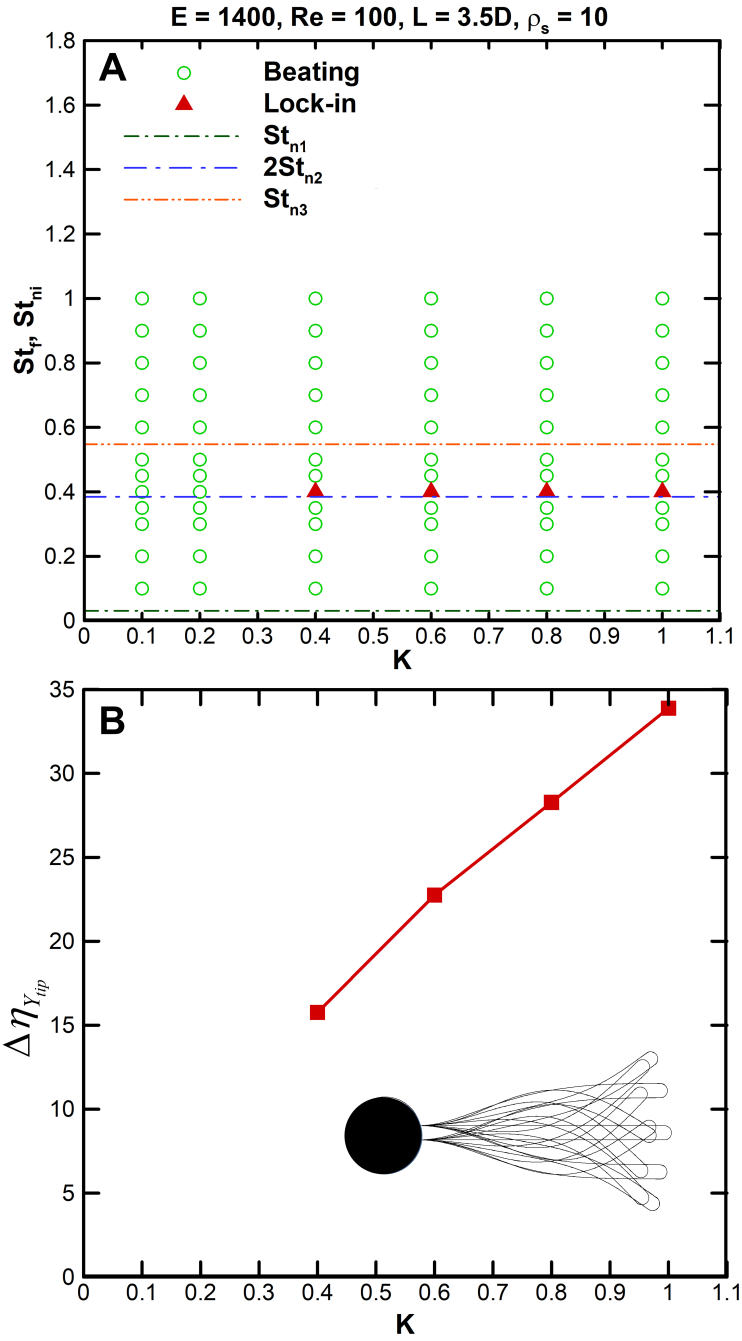

Figure 3.11: (A) Lock-in and beating plotted as a function of forcing amplitude (K) and forcing frequency (St_f). The first three modes of natural frequency of the plate (St_{n1}, St_{n2} and St_{n3}) are plotted as lines. The lock-in occurs if the forcing frequency is twice of the second mode of natural frequency ($St_f \cong St_p \cong 2St_{n2}$). (B) Percentage increase in the tip displacement of the plate at lock-in condition with respect to steady inflow. The maximum plate oscillation amplitude occurs at lock-in, when the forcing frequency is twice the plate oscillation frequency. The different points (filled squares) correspond to different forcing amplitudes. The inset shows superimposed deformed shapes of the plate at several time instances for a typical lock-in case.

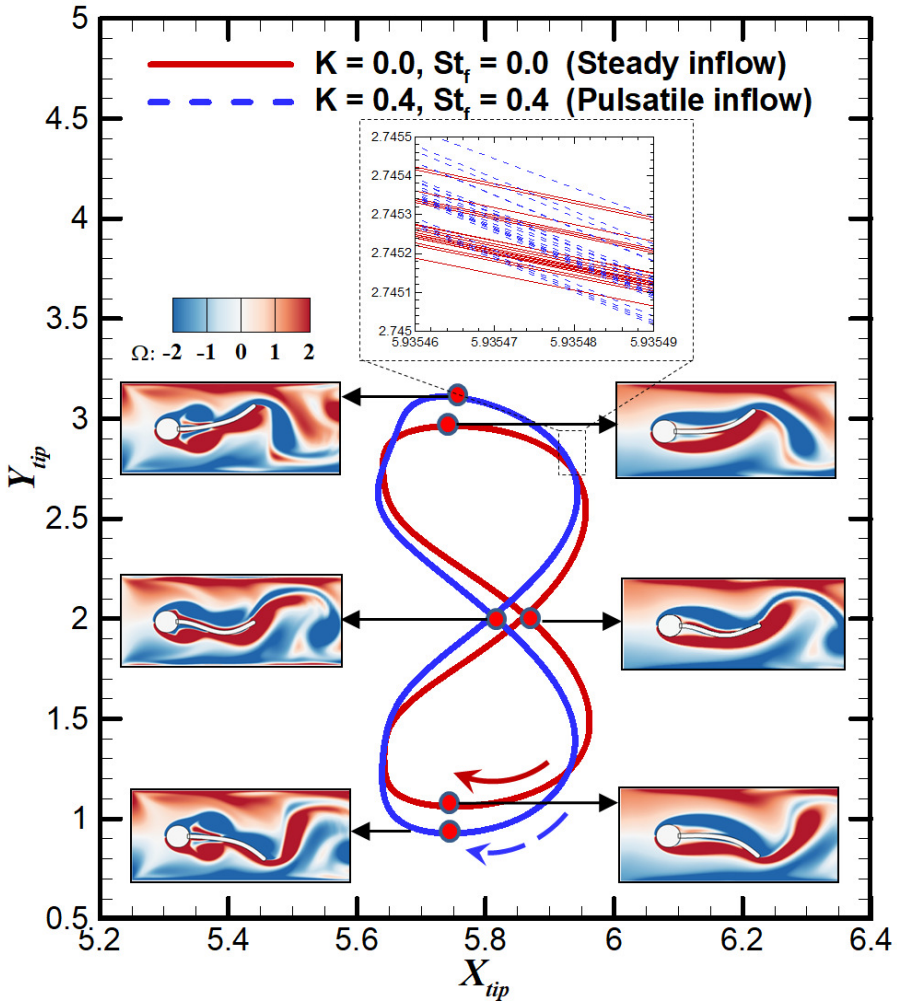

Figure 3.12: Comparison between the phase plane plots of the trajectories of the plate tip are for pulsatile and steady inflow. Around 20 plate oscillation cycles are plotted for both cases, shown in the top inset. Insets on the left and right show the corresponding vorticity contours at critical points in the cycle

Finally, we vary the plate length to L = D for plotting the lock-in and beating cases. The other parameters are kept same as in sections 3.2.3 and 3.2.4 ($E = 1400, \rho_s = 10$). The Reynolds number, $Re = 200$ is used in these simulations since the plate displacement for $L = D, Re = 100$ is too small (on the order of 0.01) to evaluate the lock-in and beating conditions. The lock-in and beating cases are plotted in Fig. 3.13B as function of forcing frequency (St_f) and forcing amplitude (K). The inset in the figure shows the superimposed shapes of the deformed plate at different time instances. The lock-in occurs for flow amplitude, $K \geq 0.2$ and at a forcing frequency, $St_f = 0.76$, twice of the natural frequency in the first mode ((3.2)) i.e., $St_f \cong St_p \cong 2St_{n1}$. Therefore, in all three cases considered (Fig. 3.11A, Fig. 3.13A and Fig. 3.13B), the lock-in occurs when the applied oscillation frequency is around twice of the natural frequency in a particular mode. The mode of the natural frequency depends on the plate length, as discussed in section 3.2.2.

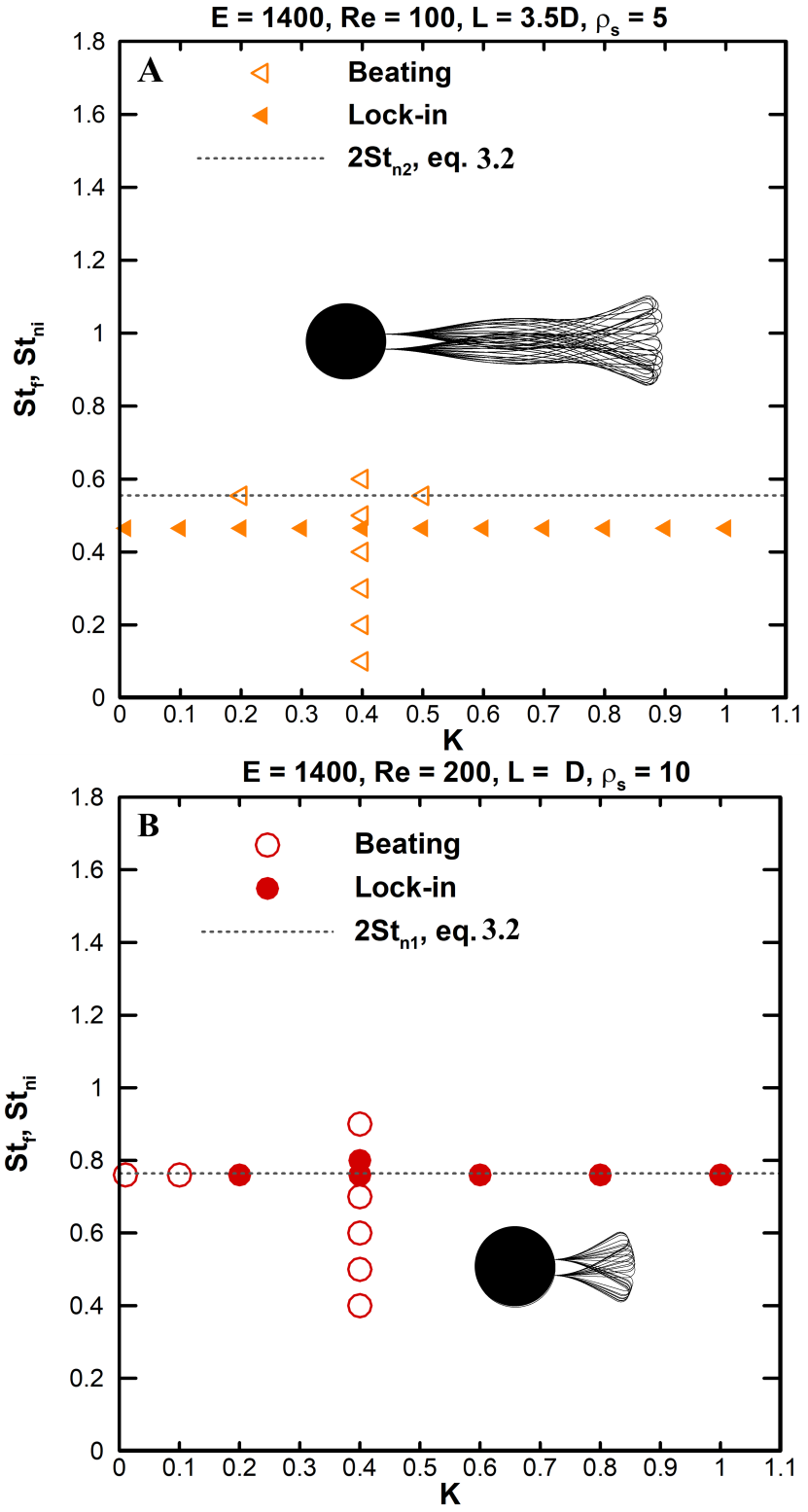

Figure 3.13: Lock-in and beating plotted as a function of forcing amplitude (K) and forcing frequency (St_f). (A) The structure-fluid density ratio is varied to $\rho_s = 5$. The twice natural frequency is second mode (St_{n2}) is plotted as a broken line. The lock-in occurs if the forcing frequency is twice of natural frequency in second mode ($St_f \cong St_p \cong 2St_{n2}$) (B) The plate length is varied to, $L = D$. The second mode of natural frequency (St_{n1}) is plotted as broken lines. The lock-in occurs if the forcing frequency is twice of natural frequency in second mode ($St_f \cong St_p \cong St_{n1}$)

3.3 Closure

The effect of the pulsatile inflow on the flow-induced deformation of an elastic plate inside a channel is simulated numerically by combining a sharp-interface immersed boundary method flow solver and an open-source finite-element based structural solver. The coupling is accomplished using an implicit iterative approach to improve the stability properties of the combined solver. The plate exhibits small deformations initially, asymptoting to a periodic self-sustained oscillation at longer times for the steady inflow. In the case of the pulsatile inflow, the plate experiences strong forcing from vortices that form from the separating shear layers from the cylinder and subsequently advect downstream over the surfaces of the plate. Despite the tendency of the vortices to form and shed symmetrically because of the applied longitudinal forcing, the coupling with the allowable cross-stream oscillation mode of the plate leads to substantially increase cross-stream oscillation amplitude relative to the unforced case in general. The maximum plate displacement is observed when the applied oscillation frequency is twice the natural plate oscillation frequency in a particular mode ($St_f \cong 2St_{ni}$), corresponding to the resonant or lock-in case. The mode of the natural frequency depends upon the plate length. For applied frequencies away from this condition, beating is observed due to the superposition of the applied and natural oscillatory signals. The plate deformation response, and drag of the plate and its components, are quantified for forcing flow amplitudes $K \leq 1$, and for forcing frequencies $St_f \leq 1$. The total drag on the plate is found to be significantly larger relative to the steady inflow, at forcing frequencies equal or larger than lock-in frequency, at a given flow amplitude. For lock-in cases, the plate displacement, total drag, pressure as well as skin friction drag increases with the forcing flow amplitude. The present chapter provide fundamental insights into lock-in with pulsatile inflow of an elastic splitter plate attached to a rigid circular cylinder in a rectangular channel. Elastic plate vibrates with larger amplitude which could be useful to the design of piezoelectric beam for energy harvesting and thermal augmentation applications.

Chapter 4

Flow-induced Dynamics of an Elastic Splitter Plate attached to a Cylinder Subjected to Free-stream Flow

We investigate the flow-induced dynamics of an elastic splitter plate, attached to the rear of a rigid circular cylinder, subjected to uniform laminar free-stream flow. An in-house fluid-structure interaction solver is employed, which couples a sharp-interface immersed boundary method for the fluid dynamics with a finite-element method to treat the structural dynamics. An implicit partitioned approach is utilized to couple the fluid and structural solvers. A rigid splitter plate suppresses the vortex shedding behind the cylinder. Depending on the plate and flow properties, vortex shedding can occur in case of a flexible plate. We investigate a wide range of mass ratio and bending stiffness of the plate at a cylinder Reynolds number of $Re = 100$. At a given Re, numerical simulations show that the plate dynamics effectively depend on only those two parameters. The largest amplitude of the plate is found to occur in the lock-in region, where the vortex shedding frequency of the coupled fluid-structure system is close to the natural frequency of the splitter plate. At lock-in, the oscillation frequency is lower than the natural frequency of the plate in a vacuum and thereby exhibits a strong effective added-mass effect. These findings are consistent with those for classical vortex-induced vibration of a rigid cylinder at a low mass ratio. The flapping boundary obtained from the simulations is plotted on the mass-ratio-reduced-velocity plane. In addition, we plot oscillation amplitude on this flapping map in order to show the lock-in condition and to briefly discuss wake structures and phase plots for different cases of mass ratio and bending stiffness. The present results could be useful to the design of flexible plates that exhibit large oscillation amplitudes for energy-harvesting applications.

4.1 Introduction

The interaction of a fluid flow with a flexible structure may lead to large-scale flow-induced vibration due to resonant forcing of the structure caused by periodic vortex shedding. Several previous studies (Connell and Yue (2007); Deivasigamani et al. (2013); Alben (2015); Akcabay and Young (2012); Gurugubelli et al. (2014); Liu et al. (2014)) have defined two important dimensionless parameters that govern the dynamics of the plate–the bending stiffness (K_b) and the mass ratio (M). These are given by

$$K_b = \frac{E^*}{\rho_f^* {U_\infty^*}^2} \frac{{h^*}^3}{12 {L^*}^3}, \tag{4.1}$$

$$M = \frac{\rho_s^* h^*}{\rho_f^* L^*}, \tag{4.2}$$

where the superscript * denotes a dimensional variable. Here, E^*, ρ_f^*, U_∞^*, h^*, L^*, ρ_s^* are the Young's modulus of the plate, fluid density, free-stream velocity, plate thickness, plate length and plate density, respectively. Note that K_b is defined per unit spanwise width of the plate in eq. 4.1. Physically, K_b represents the ratio of restoring force produced by stiffness and the loading on the structure by the fluid. The parameter M represents the ratio of the density of the structure to that of the fluid, which is often referred to as the mass ratio. In addition, the reduced velocity U_R is another important parameter, defined as ratio of the characteristic time scale of the structure to that of the fluid (Tang et al. (2007)) and is given by

$$U_R = \sqrt{\frac{M}{K_b}}. \tag{4.3}$$

The dynamics of a thin, flexible plate subjected to oscillations in a free-stream flow has been reported in several studies. Watanabe et al. (2002) studied the flutter of a paper sheet using an analytical method and reported high flutter modes at low M. Argentina and Mahadevan (2005) proposed a critical speed for the onset of flapping and estimated the flapping frequency based on scaling analysis. Tang et al. (2007) investigated the dynamics of a flexible plate using the Euler-Bernoulli model coupled with an unsteady lumped-vortex model. They investigated the flutter boundary and the post-critical behavior of this fluid-structure system. They obtained the flutter boundary in the form of the critical flow velocity versus the length of the flexible plate. They observed that the critical flow velocity is sensitive to short plate lengths. Connell and Yue (2007) proposed a regime map of flag flutter based on their FSI simulations. They proposed the following three categories of plate dynamics: fixed-point stability, limit-cycle flapping, and chaotic flapping. Fixed-point stability occurs when the flag aligns with the flow. As the flow velocity is increased, limit-cycle flapping takes over, characterized by single-frequency

repeating flag oscillations. Chaotic flapping occurs as the flow velocity is further increased. A comprehensive review of such flapping states was provided by Shelley and Zhang (2011). Lee et al. (2014) examined the flapping dynamics of a flexible flag in a uniform flow. They found three different flapping states such as regular flapping, irregular flapping and irregular flapping with violent snapping by varying M and K_b. Alben and Shelley (2008) simulated the nonlinear dynamics of a flexible sheet in a 2D inviscid fluid. They characterized the behavior of flapping flags at large amplitudes and over many flapping periods, and demonstrated a transition from a periodic to a chaotic flapping as the bending rigidity was decreased. They also found that the stability boundary of the flow-aligned state for a flag within the two-dimensional parameter space of dimensionless flag inertia and bending rigidity. Eloy et al. (2007) studied the linear stability of a flexible plate immersed in an axial flow. The found that a finite-span plate is more stable than infinite-span plate. Eloy et al. (2008) addressed the linear stability of rectangular plate in a uniform flow and incompressible axial flow by varying aspect ratio. They identified critical velocities for the instability transitions as a function of system parameters, showing good agreement with their data. Akcabay and Young (2012) examined the dynamic response and stability of piezoelectric beams in viscous and axial flows. They showed that a heavy beam undergoes flutter in a light fluid when the fluid inertial forces are in the balance with the solid elastic restoring forces, and for a light beam in a heavy fluid, flutter occurs when the fluid inertial force dominates the solid inertial force. Tian (2013) studied the hydrodynamic interaction between flag/flags and surrounding fluid. They found that the sustained flapping in the convectively instable wake can be produced in nonzero mass but the mass is unimportant condition for absolutely instable wake. The unsteady flapping can occur with zero mass. Previous studies also addressed the flow-induced dynamics of an elastic splitter plate attached to a cylinder. Turek and Hron (2006) showed self-sustained oscillation of an elastic plate attached to a rigid cylinder in a confined channel. The frequency scales as the dilatational wave speed inside the plate, as shown by Bhardwaj and Mittal (2012). Using the same configuration of Turek and Hron (2006), Kundu et al. (2017) studied the effect of Reynolds number and plate length on the flapping frequency. They showed that the simulated frequency scales with the natural frequency of a vibrating cantilevered plate (f^*_{ni}) in vacuum, i.e. obtained using the Euler-Bernoulli beam model, and is given by Kundu et al. (2017); Thomson (1996) as

$$f^*_{ni} = \frac{k_i^2}{2\pi}\sqrt{\frac{E^*I^*}{\rho^*_s A^* L^{*4}}}, \tag{4.4}$$

where $i = 1, 2, 3$ represents the frequency modes of the plate, E^*I^* is the dimensional flexural rigidity of the beam and k_i are the respective constants for the modes. The values of k are 1.875, 4.694 and 7.855 for the first, second and third mode of the natural

frequency, respectively. Also ρ_s^*, A^*, and L^* are the structure density, cross-sectional area, and length of the plate, respectively. Using eqs. 4.1 and 4.2, the non-dimensional form of eq. 5.1 is expressed as follows

$$f_{ni} = \frac{k_i^2}{2\pi L}\sqrt{\frac{K_b}{M}}. \tag{4.5}$$

Note that the natural frequency of a cantilevered plate expressed by eq. 4.5 in the presence of a fluid is modified due to the added-mass effect, especially at low M, and the is given as follows Sader et al. (2016)

$$f_{ni,AM} = \frac{k_i^2}{2\pi L}\sqrt{\frac{K_b}{M+1}}, \tag{4.6}$$

where subscript AM indicates added mass. This assumes a potential added mass coefficient of $C_A = 1$. Shukla et al. (2013) experimentally showed that the amplitude of the oscillation of a hinged splitter plate attached to a circular cylinder increases with Reynolds number (Re_D) based on the cylinder diameter and they reported a plateau oscillation amplitude at $Re_D > 4000$. Recently, Furquan and Mittal (2015) numerically studied two side-by-side flexible splitter plates attached to square cylinders. They observed that lock-in occurs when the plate frequency is close to its natural frequency. Most of the previous investigations (Connell and Yue (2007); Liu et al. (2014); Lee et al. (2014); Xu et al. (2016); Shoele and Mittal (2016b)) ignored internal stresses in the plate. The ratio of thickness to length, K_b and M were restricted to $O(0.01)$, $O(10^{-3})$ and $O(1)$, respectively. The objective of the present chapter is to investigate the effect of M and K_b on the flow-induced plate dynamics of an elastic plate attached to a cylinder in a free-stream laminar flow with a high-fidelity numerical model. We resolve the internal stresses for an elastic plate of finite thickness and the plate dynamics is implicitly coupled to an immersed-boundary-method based flow solver. We consider a wide range of $M = [0.143, 20]$, $K_b = [0.0008, 0.0435]$ and $U_R = [2.562, 30.3]$, at $Re_D = 100$. The chapter is organized as follows. We discuss the effect of M, K_b and U_R on the fluid-induced deformation of the plate in sections 4.2.1, 4.2.2 and 4.2.3, respectively. We show that the plate dynamics only depends on M, K_b and U_R in section 4.2.4. Finally, based on all simulation results, we plot a *flapping map* in the $1/M$–U_R plane in section 4.2.5. Some additional numerical simulation is performed to understand the effect of shape of bluff-body on flow-induced deformation of an elastic plate, given in Appendix A. In this chapter, we choose circular cylinder to study flow-induced dynamics of an elastic splitter plate.

4.1.1 Grid-size and domain-size independence study

As a precursor to the main study, we investigated grid convergence of uniform inflow past a flexible splitter plate behind a cylinder in a nominally open domain for three different

grids with sizes of 384 ×192, 481 × 256, and 512 × 256. Note that length of the splitter plate is $4D$. The time-step is set to $\Delta t = 0.01D/U_\infty$. The minimum cell sizes in the x and y directions are listed in Table 4.1. Neumann boundary conditions are applied at the outlet and a uniform flow velocity set at the inlet. Free slip is applied at the side boundaries. The tip deflection (Y_{tip}) signals obtained for the grids are compared in Fig. 4.1(a), with the inset showing the minor differences observed in peak amplitude for the different grids. The errors relative to the finest grid are listed in Table 4.1. Since the relative difference of the maximum tip displacement for the 384 × 192 grid, as shown in Table 4.1, is less than one percent and is similar to the 481× 257 grid, the 384 × 192 grid is selected for all the simulations in the present chapter.

Table 4.1: Variation in the maximum plate tip deflection for different grid sizes relative to the finest grid.

Cases	Grid points	Δx_{min}	Δy_{min}	Relative error in the maximum Y_{tip} from case 3
1	384 ×192	0.03	0.02	0.095%
2	481 ×257	0.02	0.02	0.082%
3	513 ×257	0.0154	0.1375	–

Three domains of sizes of $19.5D \times 12D$, $30D \times$ 12D and $40D \times 12D$ are used to address domain independence. The tip displacement (Y_{tip}) signals obtained from the three different domains are compared in Fig. 4.1(b). The inset of Fig. 4.1(b) shows the minor differences observed in peak amplitude for the different domains. The error concerning the $19.5D \times 12D$ domain is listed in Table 5.3 and is less than 2%. Therefore, the $19.5D \times 12D$ domain is subsequently used for all further simulations. In the present chapter, a 384 × 192 non-uniform Cartesian grid with $\Delta x_{min} = 0.02$ and $\Delta y_{min} = 0.02$ is considered for open domain. High resolution of grid is incorporated into the region where the plate movement is expected. For the structural solver, a total of 4662 finite quadrilateral elements are used for the plate. The finite-element grid used to represent the plate is shown in the inset of Fig. 4.2.

Table 4.2: Variation in the maximum plate tip deflection for different domain sizes relative to the largest domain size.

Cases	Domain size	Relative error in maximum Y_{tip} from case 3
1	19.5 ×12	0.14%
2	30 ×12	0.09%
3	40 ×12	–

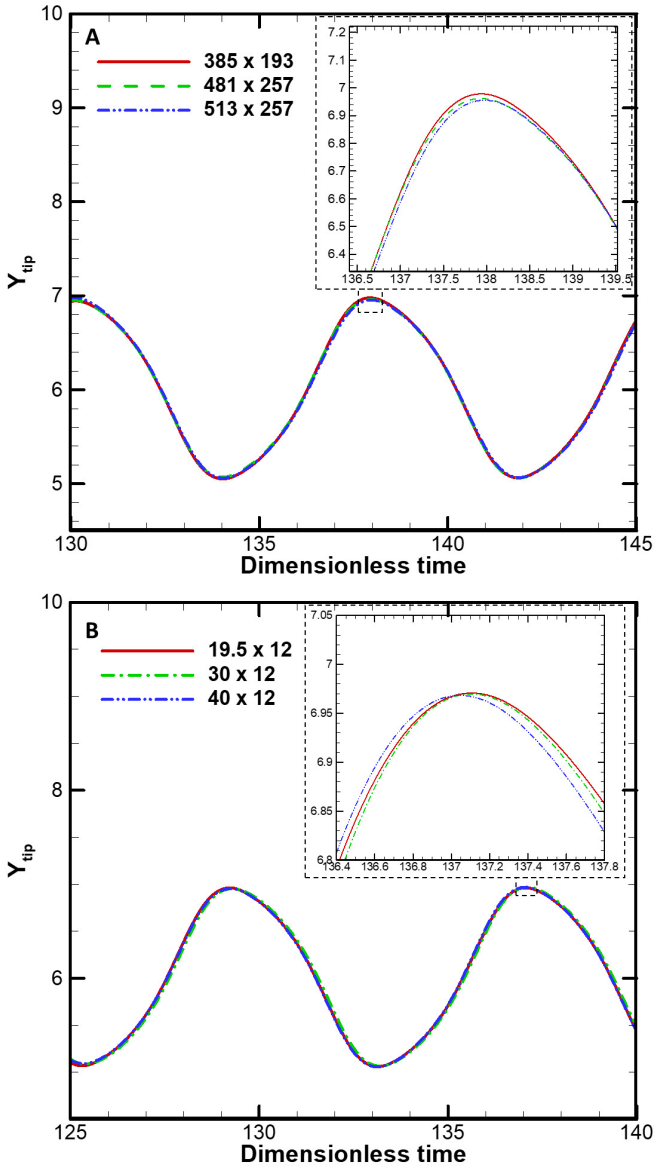

Figure 4.1: (a) Grid size convergence study: comparison of the time-varying cross-stream displacement of the plate tip (Y_{tip}) as a function of grid resolution used with the immersed boundary method solver. (b) Domain size independence study: comparison of the time-varying cross-stream displacement of the plate tip (Y_{tip}) for three different domain sizes. Note that length of the elastic splitter plate is $4D$.

4.2 Results and Discussions

Numerical simulations are performed using the same parameters of the flexible splitter plate as discussed in the previous section 2.5.3.1. The domain size is taken as follows: $S_1 + S_2 = 19.5D$ and $S_3 = 12.0D$, as shown in Fig. 4.2(a).

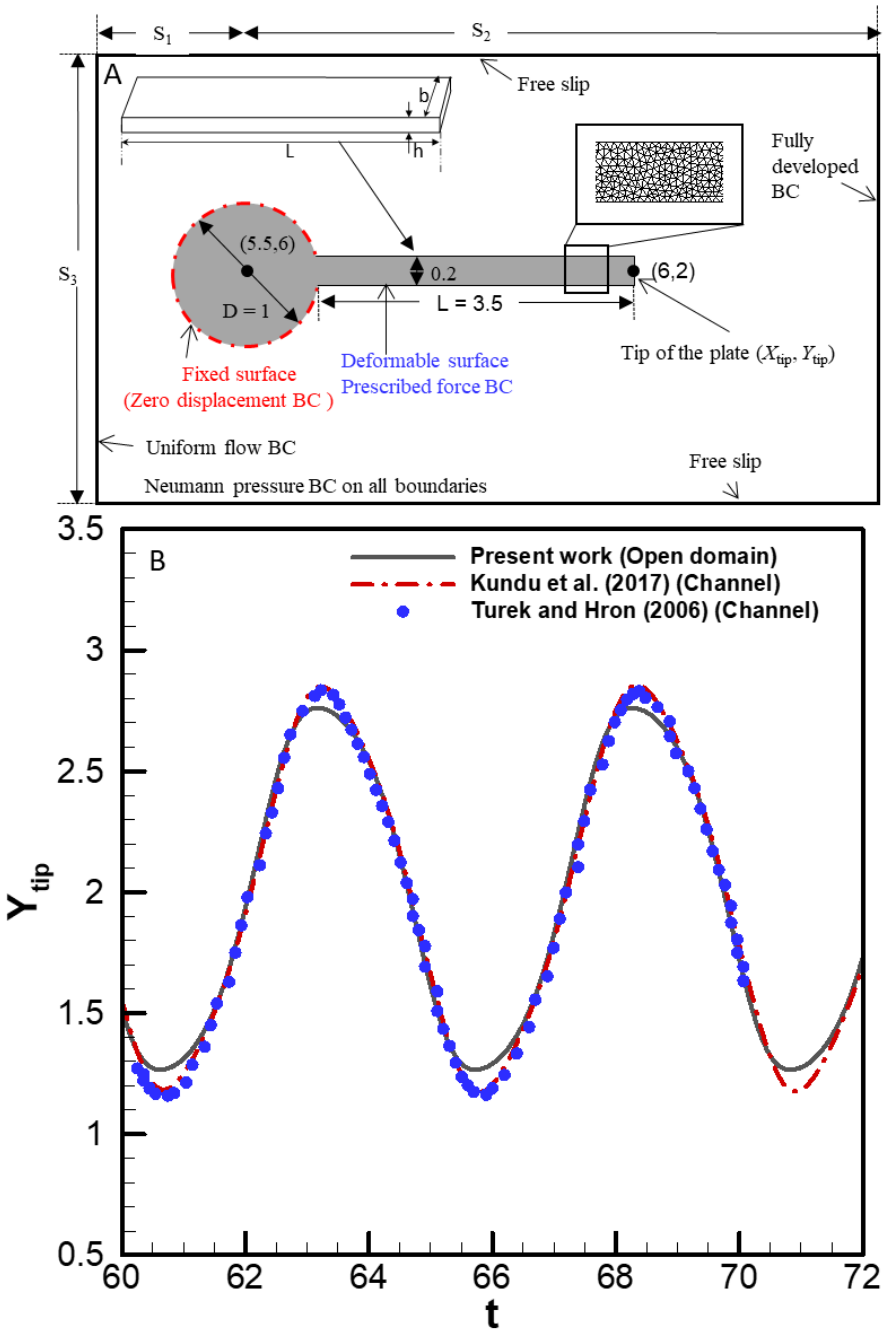

Figure 4.2: (a) Schematic of the computational domain with details of the boundary conditions (BC). (b) Comparison of the tip displacement in the Y-direction of the thin elastic splitter attached to the cylinder; previous validation was accomplished by Kundu et al. (2017) against the benchmark results of Turek and Hron (2006) using an in-house code.

Table 4.3: Input parameters for the set of simulations studying the effect of mass ratio (M) for fixed bending stiffness K_b.

Case number	E	h	ρ	M	K_b	U_R
1	1400	0.2	2.5	0.143	0.022	2.562
2	1400	0.2	5.0	0.286	0.022	3.623
3	1400	0.2	7.5	0.429	0.022	4.437
4	1400	0.2	10.0	0.571	0.022	5.123
5	1400	0.2	15.0	0.857	0.022	6.275
6	1400	0.2	20.0	1.143	0.022	7.246
7	1400	0.2	25.0	1.429	0.022	8.101
8	1400	0.2	30.0	1.714	0.022	8.874
9	1400	0.2	35.0	2.000	0.022	9.585
10	1400	0.2	40.0	2.286	0.022	10.247
11	1400	0.2	45.0	2.571	0.022	10.869
12	1400	0.2	47.0	2.686	0.022	11.107
13	1400	0.2	48.0	2.743	0.022	11.225
14	1400	0.2	48.5	2.771	0.022	11.283
15	1400	0.2	49.0	2.800	0.022	11.341
16	1400	0.2	50.0	2.857	0.022	11.456
17	1400	0.2	60.0	3.429	0.022	12.550
18	1400	0.2	75.0	4.286	0.022	14.031
19	1400	0.2	90.0	5.143	0.022	15.370
20	1400	0.2	100.0	5.714	0.022	16.202
21	1400	0.2	125.0	7.143	0.022	18.114
22	1400	0.2	150.0	8.571	0.022	19.843
23	1400	0.2	200.0	11.429	0.022	22.913
24	1400	0.2	250.0	14.286	0.022	25.617
25	1400	0.2	300.0	17.142	0.022	28.062
26	1400	0.2	350.0	20.0	0.022	30.3109

Note again that we use an open domain instead of a channel. The dynamics of the elastic plate as a function of a mass ratio (M), bending stiffness (K_b) and reduced velocity (U_R) of the plate are discussed. We vary M, K_b and U_R in the ranges: [0.143, 14.286], [0.0008, 0.0435] and [2.562, 30.0], respectively. The simulation cases are also given in Table 4.3-4.6 and are shown in the Fig. 4.3 on the $1/M - U_R$ plane. In this present study, the response of plate oscillation is limit-cycle flapping. Symmetric plate displacement is observed and vortex is shedding from tail of the plate. A von Kármán vortex street, consisting of a continuous series of alternately signed vortices is observed. Same scenario is observed in Connell and Yue (Connell and Yue, 2007).

Table 4.4: Input parameters for the set of simulations studying the effect of bending stiffness K_b for fixed M.

Case number	E	h	ρ	M	K_b	U_R
26	50	0.2	10.0	0.571	0.0008	27.111
27	100	0.2	10.0	0.571	0.0016	19.170
28	150	0.2	10.0	0.571	0.0023	15.652
29	250	0.2	10.0	0.571	0.0039	12.124
30	350	0.2	10.0	0.571	0.0054	10.247
31	560	0.2	10.0	0.571	0.0087	8.101
32	700	0.2	10.0	0.571	0.0109	7.246
33	933	0.2	10.0	0.571	0.0145	6.276
4	1400	0.2	10.0	0.571	0.0218	5.123
34	1866	0.2	10.0	0.571	0.0290	4.438
35	2800	0.2	10.0	0.571	0.0435	3.623
36	196.00	0.20	48.0	2.743	0.0030	30.000
37	282.00	0.20	48.0	2.743	0.0044	25.011
38	441.00	0.20	48.0	2.743	0.0069	20.000
39	967.90	0.20	48.0	2.743	0.0150	13.500
40	783.00	0.20	48.0	2.743	0.0122	15.010
41	1128.00	0.20	48.0	2.743	0.0175	12.505
42	1277.68	0.20	48.0	2.743	0.0199	11.750
43	1400.00	0.20	48.0	2.743	0.0218	11.225
44	1764.00	0.20	48.0	2.743	0.0274	10.000
45	2177.78	0.20	48.0	2.743	0.0339	9.000
46	2756.25	0.20	48.0	2.743	0.0429	8.000
47	3133.00	0.20	48.0	2.743	0.0487	7.504
48	4150.00	0.20	48.0	2.743	0.0645	6.520
49	5750.00	0.20	48.0	2.743	0.0894	5.539

Table 4.5: Input parameters for the set of simulations studying the effect of K_b and M in keeping the reduced velocity (U_R) constant.

Case number	E	h	ρ	M	K_b	U_R
50	175	0.2	1.25	0.071	0.0027	5.123
51	350	0.2	2.5	0.143	0.0054	5.123
52	700	0.2	5.0	0.286	0.011	5.123
4	1400	0.2	10.0	0.571	0.022	5.123
53	2100	0.2	15.0	0.857	0.033	5.123
54	2800	0.2	20.0	1.143	0.044	5.123
55	4200	0.2	30.0	1.714	0.065	5.123
56	5600	0.2	40.0	2.286	0.087	5.123

Table 4.6: Input parameters for the set of simulations with fixed U_R, K_b and M.

Case number	E	h	ρ	M	K_b	U_R
57	175	0.4	5	0.571	0.022	5.123
58	716.8	0.25	8	0.571	0.022	5.123
4	1400	0.2	10	0.571	0.022	5.123
59	3318	0.15	13.33	0.571	0.022	5.123

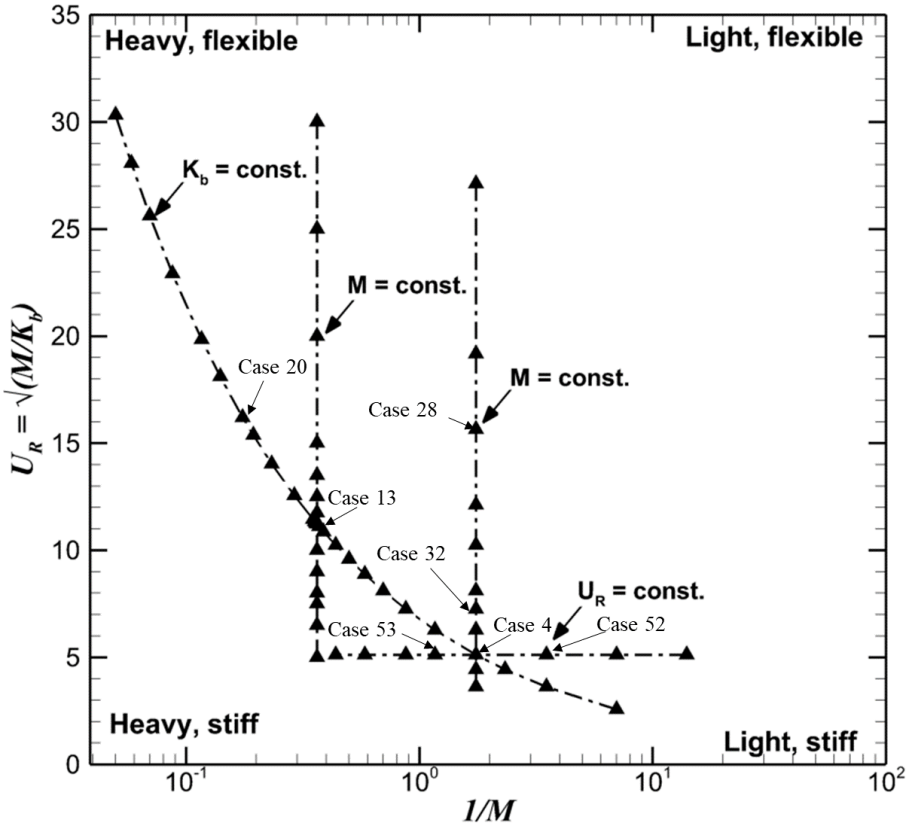

Figure 4.3: Reduced velocity (U_R) as a function of mass ratio (M). Triangles are the simulation point for present chapter in an open domain.

4.2.1 Effect of mass ratio (M)

We discuss the effect of M on the elastic splitter plate displacement (Y_{tip}), oscillation frequency (f_p) and wake structure, keeping K_b constant. Simulations are presented for M = [0.143, 20] and $K_b = 0.022$, with simulation parameters given in Table 4.3 and plotted in Fig. 4.3. Fig. 4.4(a) plots f_p as a function of M. The natural frequencies of first three modes are also plotted, without the added mass (f_{n2}, eq. 4.5), and with the added mass ($f_{n2,\ AM}$, eq. 4.6), as a function of M in Fig. 4.4(a). It can be seen that f_p decreases with M due to the larger inertia of plate. At lower M ($0.143 < M < 1.71$), f_p lies between $f_{n2,AM}$ and f_{n2}, and matches with the $f_{n2,\ AM}$ curve for $1.71 < M < 2.79$. The f_p curve

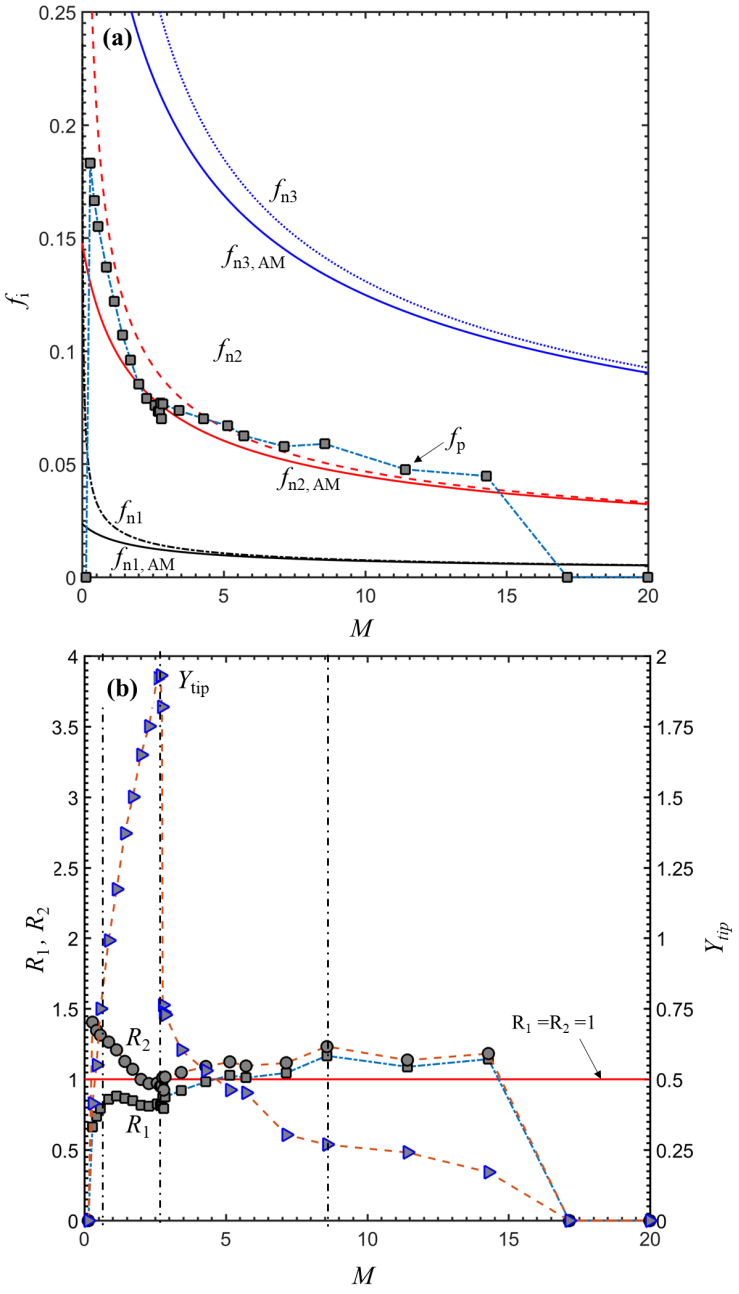

Figure 4.4: Comparison of: (a) simulated plate oscillation frequency (f_p) and plate natural frequency f_{ni} and $f_{ni,AM}$ without or with the added mass correction as a function of the mass ratio M. Dotted and solid lines represents the f_{ni} and $f_{ni,AM}$ variations, respectively. Square symbols show results for simulated f_p; (b) plate amplitude (Y_{tip}), and frequency ratios R_1 and R_2 without or with the added mass correction as a function of the mass ratio M. Solid square, solid circle and triangle symbols show R_1, R_2 and Y_{tip} variations, respectively. Three simulations for $M = 0.57$, 2.74 and 5.71 are represented by vertical dashed line. Note that $K_b = 0.022$ is fixed for all cases.

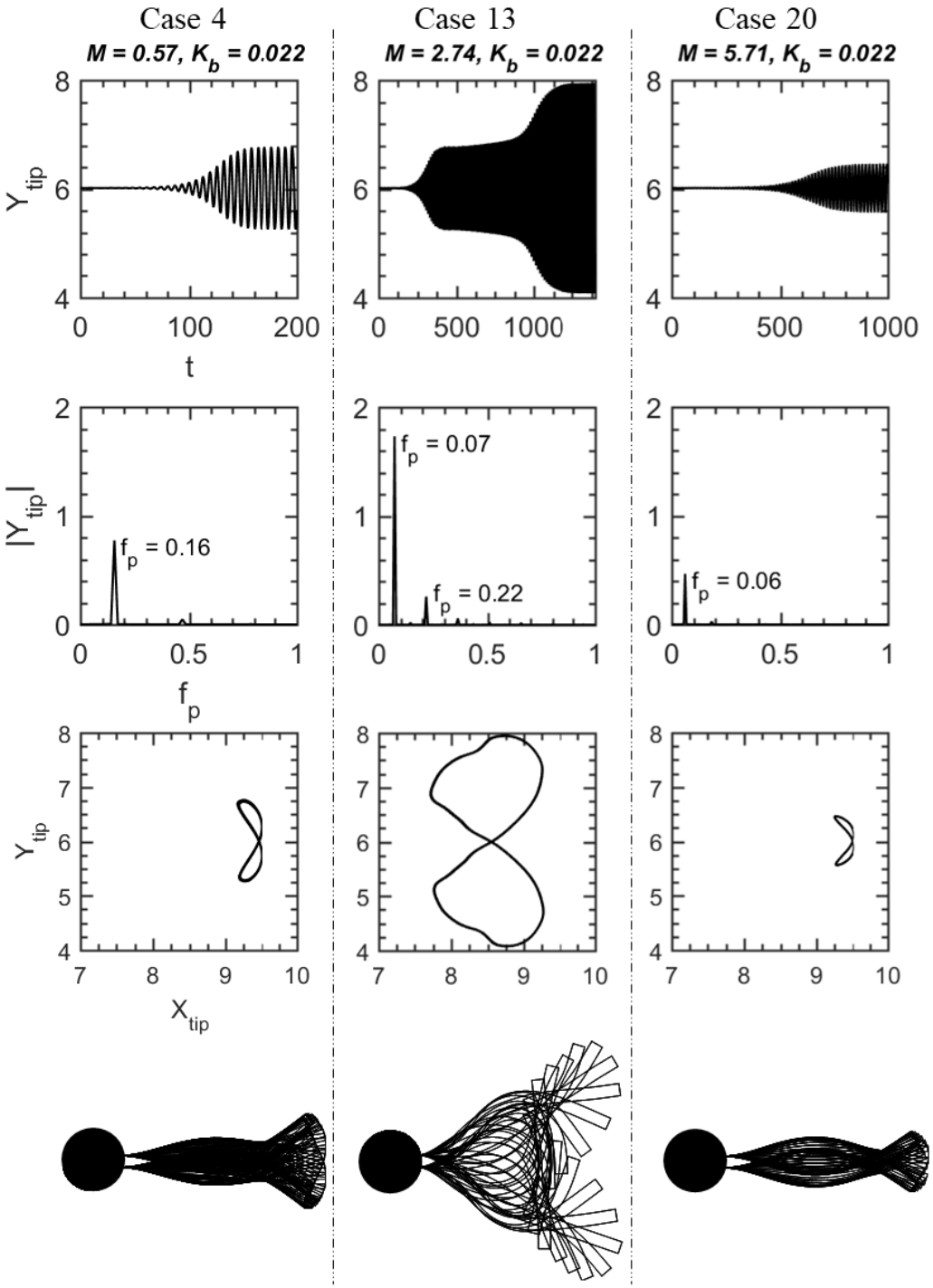

Figure 4.5: Comparison of tip displacement Y_{tip} (top row), power spectra (second row), and phase-plane plots (third row) are for three different mass ratios. The superimposed views of the deflection mode of the elastic splitter plate are shown in the bottom row. These three cases belong to the dashed vertical line in Fig. 4.4(b). Note that for these cases $K_b = 0.022$ is fixed, with the mass ratio (M) varied.

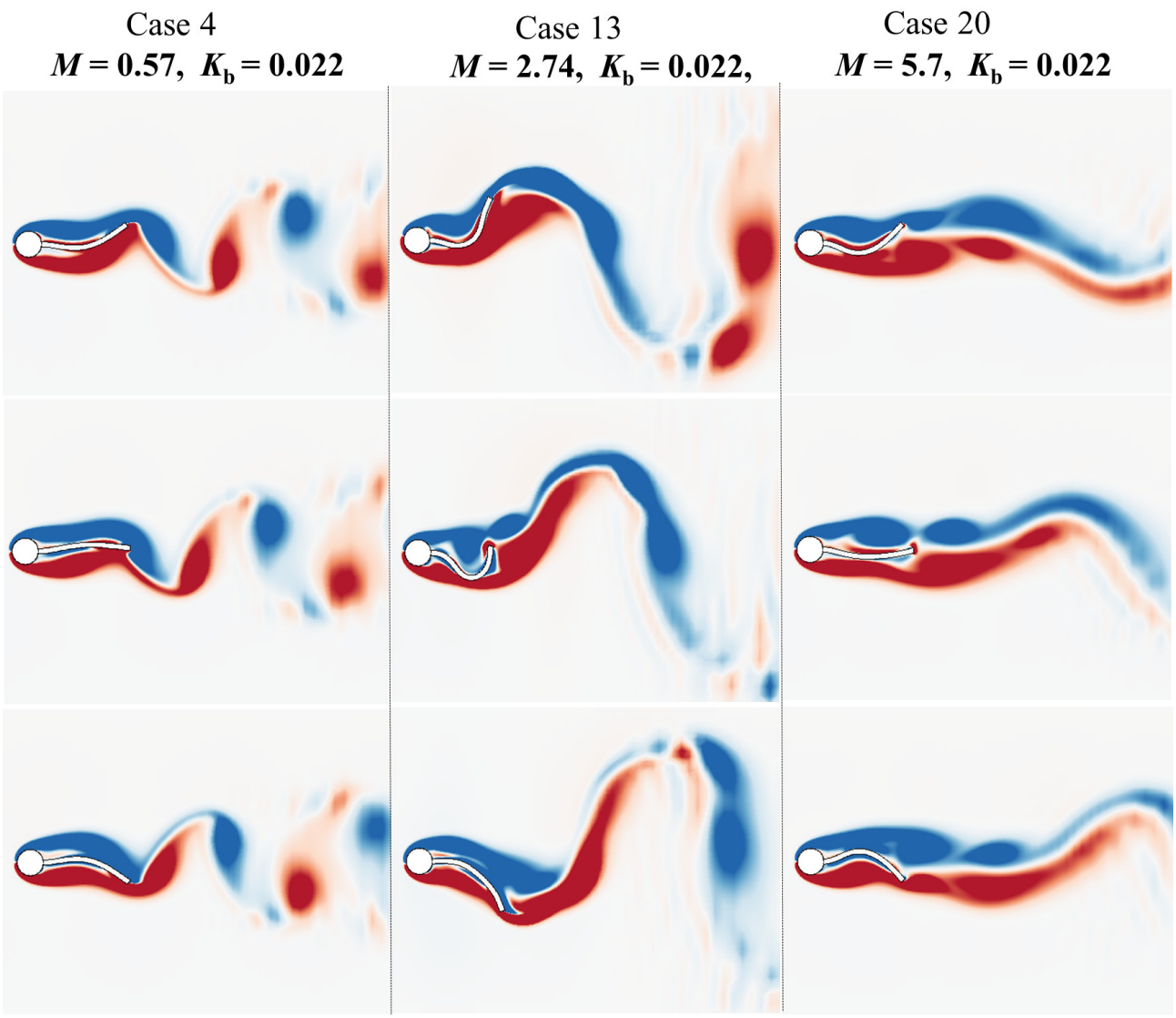

Figure 4.6: Comparison of vorticity field at different time instances for three different mass ratios. These three cases belong to the dashed vertical line in Fig. 4.4(b). The color map range is [-1, 1]; the same as shown in Fig. 5.1.

starts to deviate from the $f_{n2,AM}$ curve to match the f_{n2} curve over the mass ratio range $3.43 < M < 5.71$. Also, f_p is closer to f_{n2} or $f_{n2,\ AM}$ for $M > 5.71$. Fig. 4.4(b) plots Y_{tip}, and the frequency ratios $R_1 = f_p/f_{ni}$ and $R_2 = f_p/f_{ni,\ AM}$ as a function of M. We also plot a solid red line to denote the resonance condition where R_1 and $R_2 = 1.0$. Fig. 4.4(b) shows that Y_{tip} increases with M for $0.285 < M < 2.74$, reaching a maximum at $M = 2.74$ and then decreases with M in the range $2.74 < M < 14.286$. The frequency ratios R_2 and R_1 increase and decrease, respectively, as M decreases. Fig. 4.4(b) shows that large amplitude oscillation occurs for the cases where $f_p = f_{n2,\ AM}$, i.e. R_2 is very close to unity for $1.71 < M < 3.43$ and it is called lock-in region. Lock-in occurs if the vortex shedding or plate oscillation frequency is close to the natural frequency for any mode, and then the plate oscillates with larger amplitude. We note that large amplitude

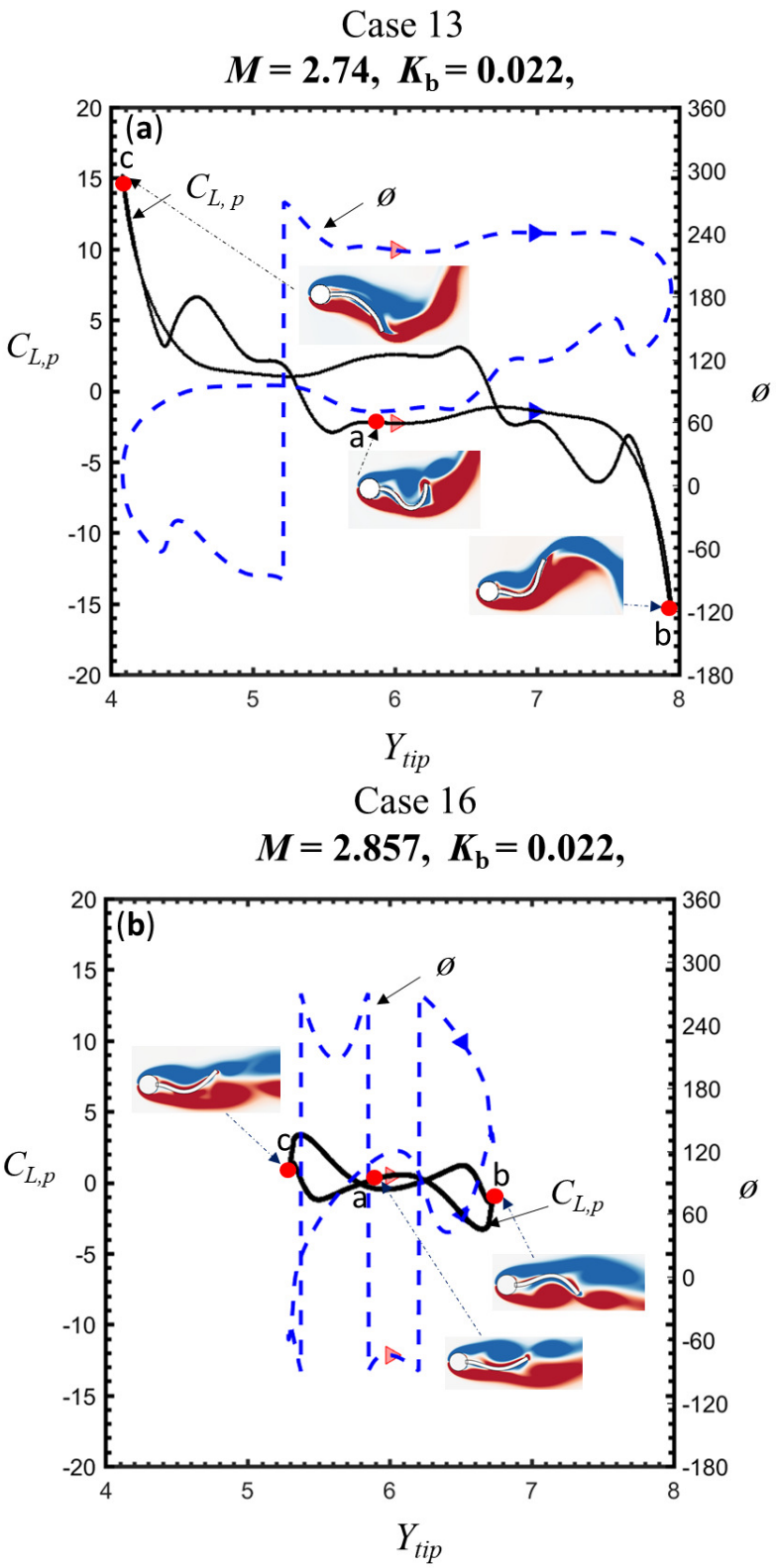

Figure 4.7: Lift coefficient (C_{LP}) and phase difference (ϕ) are the function of the vertical displacement of the tip for two different mass ratios. Note that $K_b = 0.022$ is fixed for these cases. Black solid line and blue dotted line represents the lift coefficient and phase difference respectively. The motion of vertical displacement of the tip is from point a to point b and then point c, which is shown in red circle. Inset shows the corresponding vorticity contours at the critical point of vertical displacement of the tip.

oscillation occurs at $M = 2.74$, for which $R_2 = 1$ and $Y_{tip} = 1.93$. By contrast, R_1 matches well with the line where R_1 is close to unity for $4.1 < M < 5.9$. In Fig. 4.4(b) the plate deformation increases for $0.143 < M < 2.57$, reaching a maximum at $M = 2.74$, and then decreases with M. Y_{tip} is significantly larger for $1.71 < M < 2.74$ due to lock-in with the added mass effect at which R_2 coincides with the lock-in line. This can be explained as follows. The lock-in occurs if the following three frequencies coincide: the structural vibration frequency (f_s), the vortex shedding frequency (f_v) and the natural frequency in a vacuum (f_n) or $f^* = f_v/f_n \approx 1$. This is valid for large mass ratio M =O (100); however, for a lower mass ratio of M =O(10), f^* deviates from unity (Khalak and Williamson (1997, 1999)). In the latter case, $f_s = f_v = f_{n,AM}$, where $f_{n,AM}$ is the natural frequency in a fluid including the potential added mass. Of course, this is true for the high mass ratio case, noting that the added mass is then small enough to be ignored. Similar charateristics are observed during vortex-induced vibration (VIV) of a rigid cylinder (Khalak and Williamson (1997, 1999)).

Fig. 4.7 shows that the lift coefficient (C_{LP}) and phase difference (ϕ) are the function of the vertical displacement of the tip of the plate for two different mass ratios. Note that $K_b = 0.022$ is fixed for these cases. Black solid line and blue dotted line represents the lift coefficient (C_{LP}) and phase difference (ϕ) respectively. The motion of vertical displacement of the tip of the plate is from point (a) to point (b) and then point (c), which are shown in the red circle. Inset shows the corresponding vorticity contours at the critical point of vertical displacement of the tip. When plate motion is from point (a) to point (b) in the case 13 (M = 2.74), the phase difference is constant and above 180°. The motion of the plate and the force acting on the plate is the same phase, as a result, maximum plate displacement is observed. Positive vortex (shown in the inset of right side Fig. 4.7) is attached near the plate which creates low pressure and accelerates the plate motion. On the other hand, in the case 16 (M = 2.857), the phase difference is rapidly decreasing with plate deformation. The motion of plate and the force acting on the plate is gradually changing to opposite phase which gives minimum plate displacement. We plot three cases with mass ratios $M = 0.57$, 2.74 and 5.71 in Fig. 4.4. These are represented by vertical dashed lines in Fig. 4.4(b). These cases are case 4, case 13 and case 20 of Table 4.3, and are also shown in Fig. 4.3. Fig. 4.5 (first row) compares the time-varying Y_{tip} for mass ratios 0.57, 2.74 and 5.7, and the maximum plate amplitude values recorded are 0.75, 1.93 and 0.48, respectively. These cases are shown in Fig. 4.3. The heavier plate takes longer to reach a self-sustained periodic state due to the larger inertia. Fig. 4.5 (second row) shows the FFT of Y_{tip} for the three cases. The dominant f_p for mass ratios 0.57, 2.74 and 5.7 are 0.154, 0.079 and 0.061, respectively, which are closer to $f_{n2,AM}$ of the plate as discussed earlier. Fig. 4.5 (second row) shows that the plate with largest deformation for $M = 2.74$ vibrates with more than one frequency. One

frequency component is closer to a dominant second mode, and other is a third harmonic of the dominant frequency. The phase plots in the third row of Fig. 4.5 show the axial

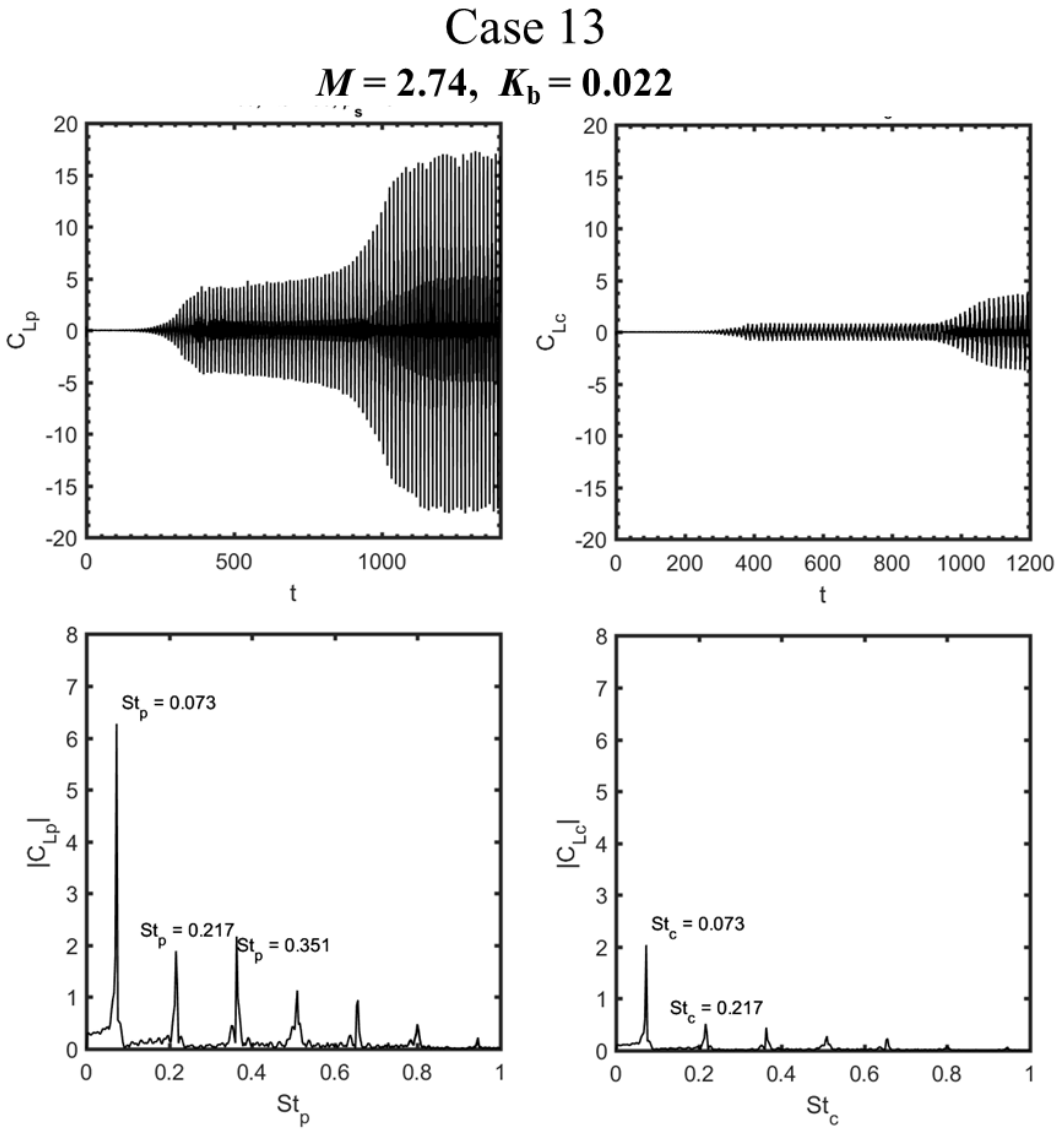

Figure 4.8: Time varying lift coefficient of (a) the plate and (b) the cylinder for mass ratio (M) = 2.74. FFT of lift coefficient is shown in (c) for the plate and (d) for the cylinder for same mass ratio.

and lateral movement of the plate tip, which are larger for $M = 2.74$ than other mass ratios because of lock-in. As a result, the phase plots are wider at $M = 2.74$. Snapshots of the plate deformation shape over one cycle for the three cases are shown in Fig. 4.5 (fourth row). Flow over a rigid cylinder with an attached splitter plate ($L/D = 3.5$) is stable and does not show any vortex shedding. Vortex shedding frequency is negligible. Both Cylinder and plate lift frequency is zero. For the case of flow over a rigid cylinder with an attached flexible splitter plate (L/D=3.5), vortex shedding frequency is equal to plate oscillation frequency. Cylinder and plate lift frequency is equal to plate oscillation

frequency. Fig. 4.8 and 4.9 shows the time-varying lift coefficient of plate and cylinder and their FFT analysis. The magnitude of lift coefficient of the plate higher than the cylinder for both case.

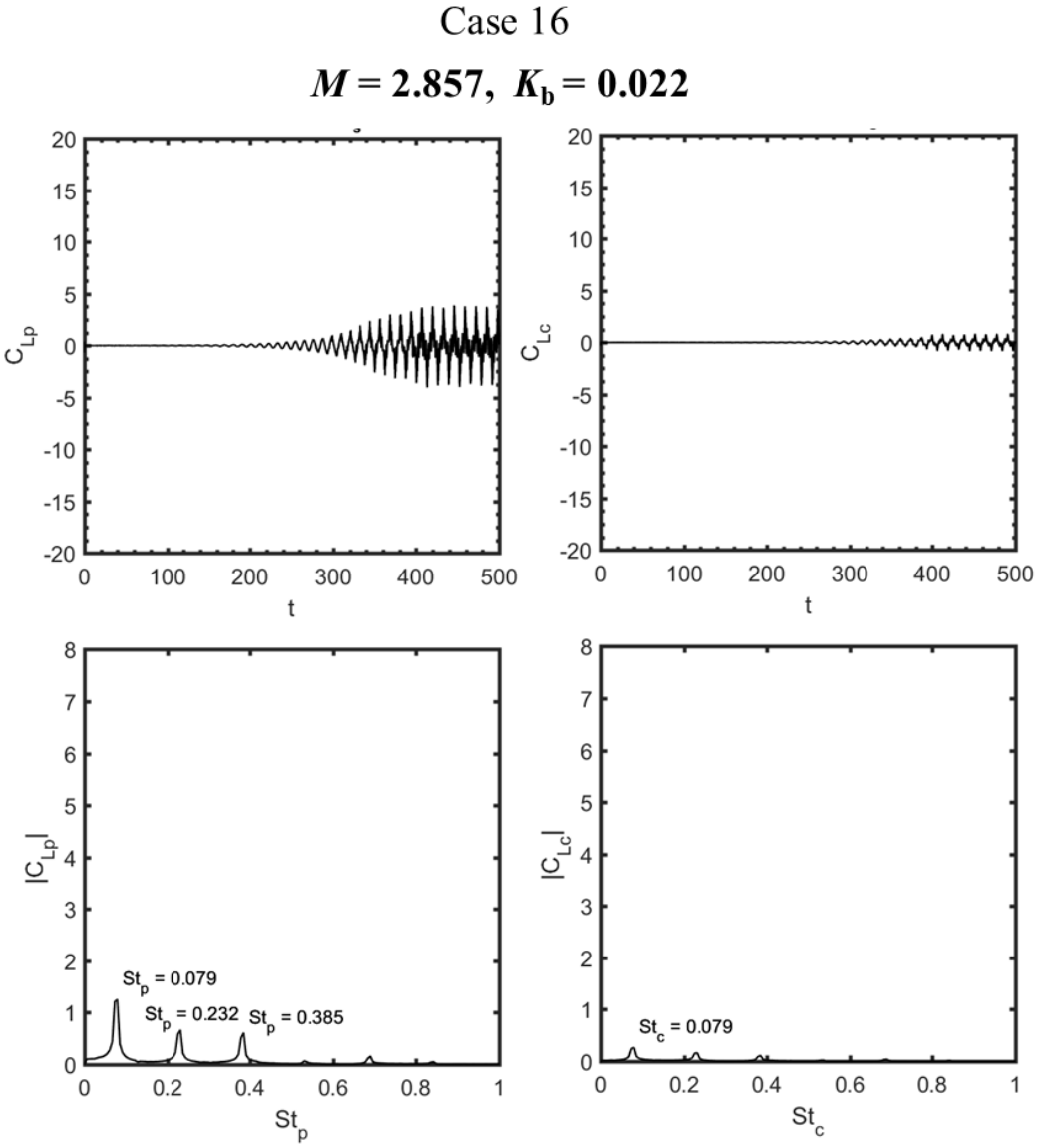

Figure 4.9: Time varying lift coefficient of (a) the plate and (b) the cylinder for mass ratio (M) = 2.74. FFT of lift coefficient is shown in (c) for the plate and (d) for the cylinder for same mass ratio.

The magnitude of lift coefficient of the plate for the case of mass ratio, $M = 2.74$ is higher than the case of mass ratio, $M = 2.857$ because of the higher amplitude of Y_{tip} of the plate. Fig. 4.8(c and d) show the FFT analysis of the plate and cylinder lift coefficient signal. From the FFT analysis, it is observed that the lift signal has multiple frequencies. One is the dominant frequency which is same as plate frequency, and other frequencies are the odd harmonic of dominant frequency. The similar observation is

noticed in VIV of a cylinder. Fig. 4.6 depicts the instantaneous vorticity field around the plate. Three different positions covering the maximum, minimum and central positions at three different instances are plotted in Fig. 4.6. For $K_b = 0.022$ and $M = 0.57$, the elastic splitter plate is in its self-sustained oscillation state and vortices are shedding alternately (see the first column of Fig. 4.6). The vortex shedding flow pattern is a typical 2S mode (one vortex sheds from each side of the plate in a cycle)(Govardhan and Williamson (2000)). For $K_b = 0.022$ and $M = 2.74$, the elastic plate bends to a greater degree compared to the $M = 0.57$ plate. As a result, longer vortex shedding from the elastic plate is observed, and it tends to be split into two small vortices, which are not completely separated immediately but later separate into two individual vortices. This vortex shedding flow pattern is typically similar to the 2P mode (two vortices shed from each side of the plate each time) (Govardhan and Williamson (2000)). For $K_b = 0.022$ and $M = 5.7$, two positive and two negative vortices are shedding alternatively. Therefore, the vortex-shedding pattern depends on plate amplitude.

4.2.2 Effect of bending stiffness (K_b)

The effect of K_b on the flow-induced deformation of the elastic splitter plate is examined in this section. We take $K_b = [0.0008, 0.0435]$ keeping the mass ratio $M = 0.571$ constant, as shown in the Fig. 4.3. The parameters of these simulation cases are also given in Table 4.4. Note U_R decreases with K_b. We plot f_p and f_{ni} of first three modes with and without added mass as a function of K_b in Fig. 4.10(a). The dotted and solid lines show f_{ni} and $f_{ni,AM}$, respectively. The square symbols show the simulated f_p values. These values decrease with K_b up to $K_b = 0.0016$ and subsequently, they then generally increase with K_b. Fig. 4.10(a) shows that a plate with a larger $K_b > 0.004$ oscillates with second natural frequency; however, at low $K_b = 0.0016$, f_p falls on the $f_{n3,AM}$ curve.

Fig. 4.10(b) shows that the plate deformation (Y_{tip}), and frequency ratios R_1 and R_2, as a function of K_b. Both R_1 and R_2 decrease with K_b. Fig. 4.10(b) shows that the plate displacement is negligible at low K_b and plate displacement decreases with K_b. We also plot the line where $R_1 = R_2 = 1$. Large amplitude occurs for the case $f_p \simeq f_{n2,AM}$ at $K_b = 0.0023$ in Fig. 4.10(b), i.e. a point close to the $R_1 = R_2 = 1$ line. At $K_b = 0.0016$, the f_p point lies on lock-in line ($f_p = f_{n2,AM}$) but plate displacement is not maximum due to plate flexibility. Other points lie away from the lock-in line, so the plate displacement is lower than at $K_b = 0.0023$.

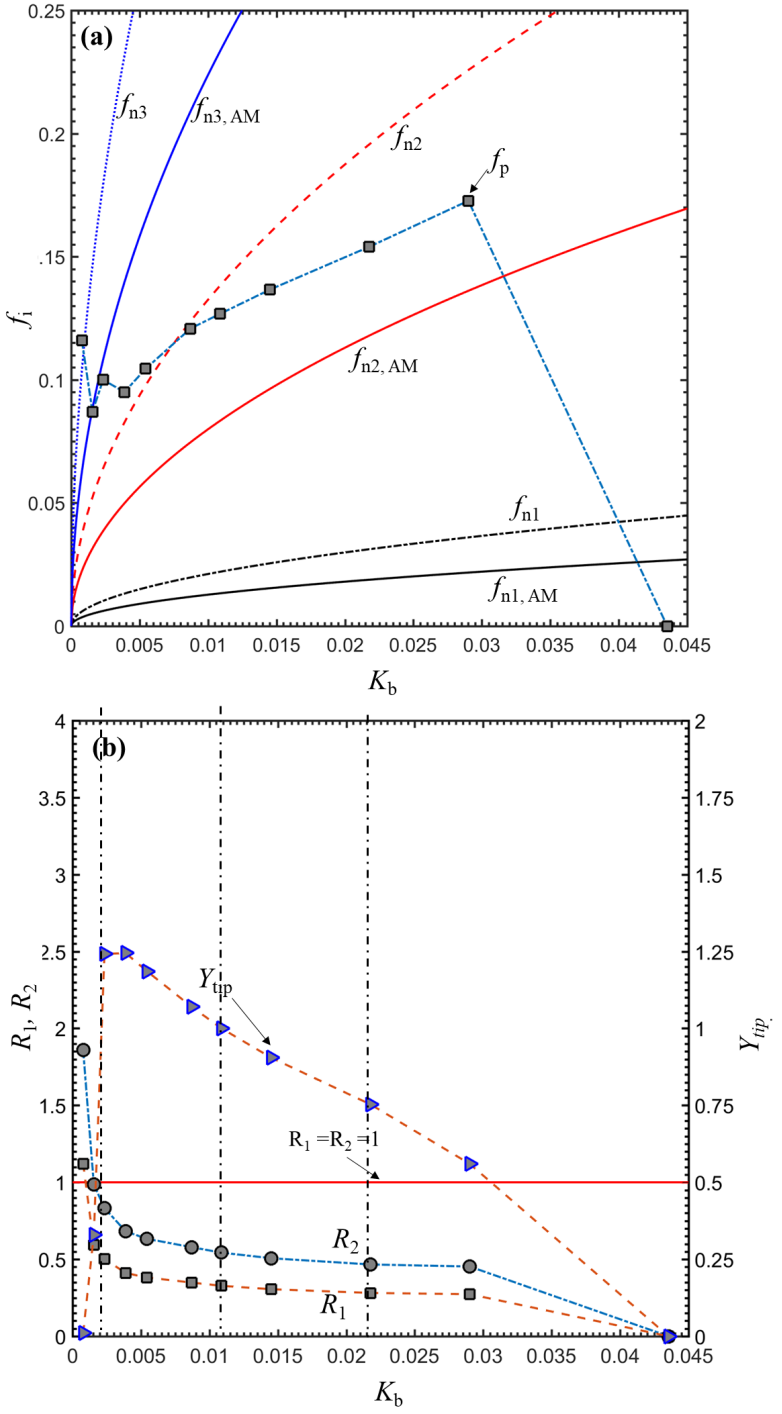

Figure 4.10: Comparison of: (a) simulated plate oscillation frequency (f_p) and plate natural frequency f_{ni} and $f_{ni,AM}$ without or with the added mass correction as a function of the stiffness K_b. Dotted and solid lines represents the f_{ni} and $f_{ni,AM}$ variations, respectively. Square symbols show results for simulated f_p; (b) plate amplitude (Y_{tip}), and frequency ratios R_1 and R_2 without or with the added mass correction as a function of the stiffness K_b. Solid square, solid circle and triangle symbols show R_1, R_2 and Y_{tip} variations, respectively. Note that $M = 0.57$ is fixed for these cases.

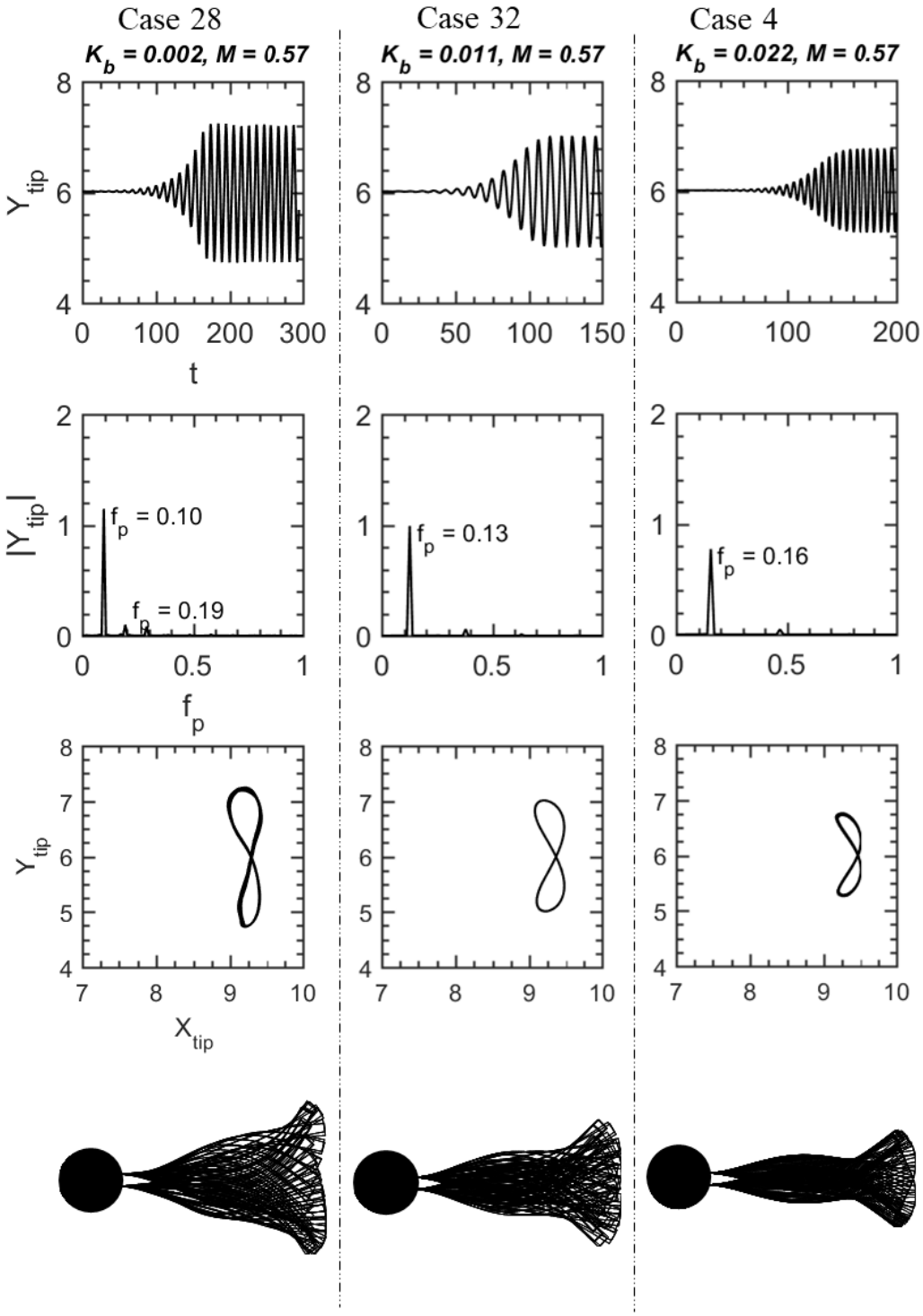

Figure 4.11: Comparison of tip displacement Y_{tip} (top row), power spectra (second row), and phase-plane plots (third row). Superimposed view of deflection mode of the splitter plate (bottom row). Note that $M = 0.038$ and $St_{n2} = 0.195$ are fixed for all cases but Young's modulus and the density ratio are different. These three cases belong to dashed vertical line in Fig. 4.10(b).

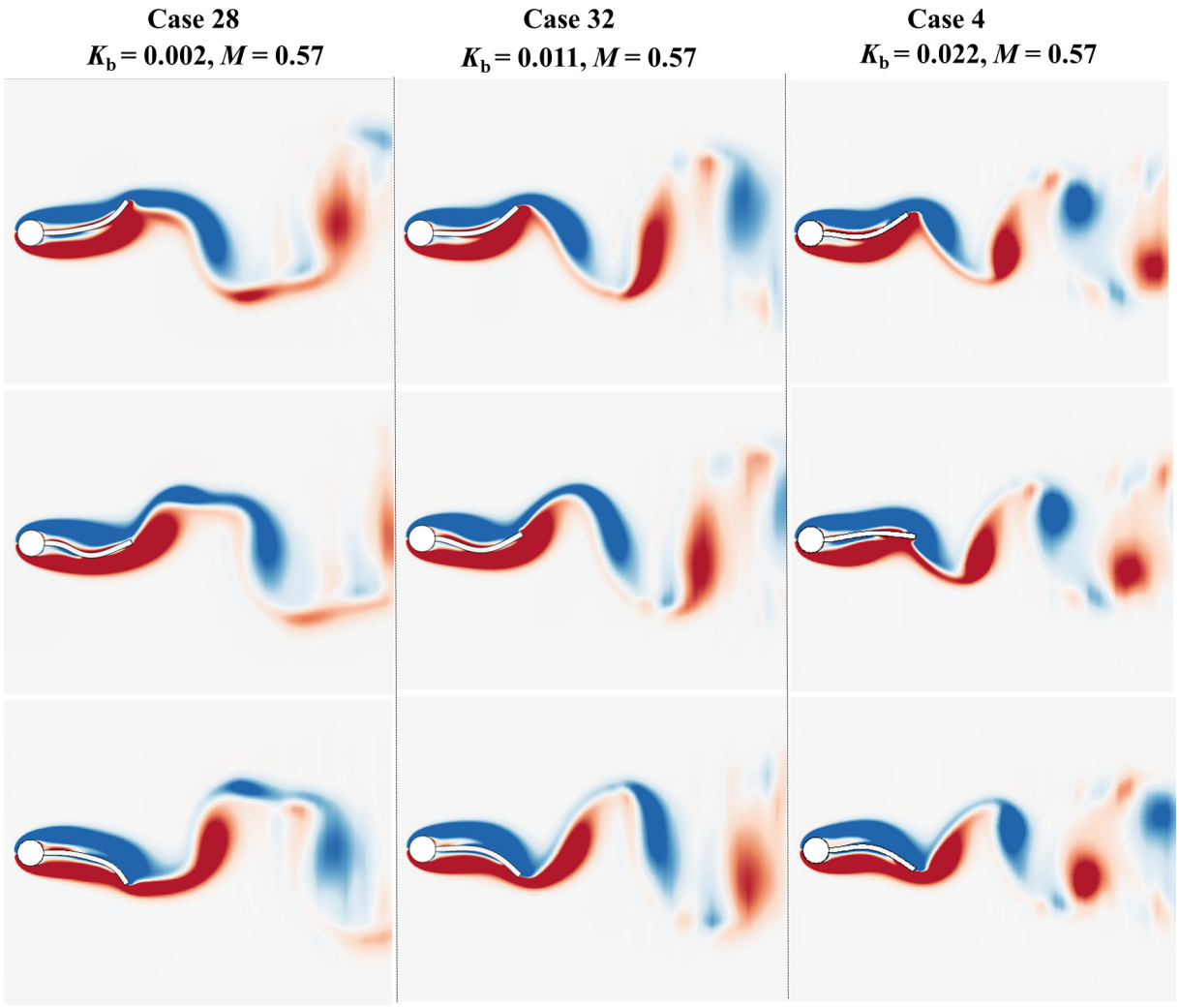

Figure 4.12: Vorticity field as a function of plate deformation for three different values of Young's modulus. The color map range is [-1, 1]; the same as shown in Fig. 5.1.

Fig. 4.11 shows Y_{tip}, FFT, phase plots and the superimposed shapes of the elastic splitter plate in the first, second, third and fourth rows, respectively. Here, Y_{tip} decreases with K_b. Fig. 4.11 (second row) shows that the plate with larger deformation at K_b = 0.0023 (case 28) vibrates with more than one frequency. The dominant frequency is closer to the second mode natural frequency and the other is the second harmonic of the dominant frequency. Fig. 4.11 (second row) shows that the phase plot is wider at K_b = 0.0023 because of the lock-in condition and large-amplitude periodic bending is exhibited at K_b = 0.0023 rather than for other values shown in fourth row. Fig. 4.12 shows the vorticity field for three cases of bending stiffness. Alternative periodic vortex shedding is observed in each case, and the vortex shedding pattern is 2S (Govardhan and Williamson (2000)) for all the cases, but the transition from the 2P to 2S mode is observed at K_b = 0.0023. The vortex structures become elongated at lower bending stiffness as compared to those for high bending stiffness due to larger plate displacement.

4.2.3 Effect of K_b and M in keeping the reduced velocity (U_R) constant

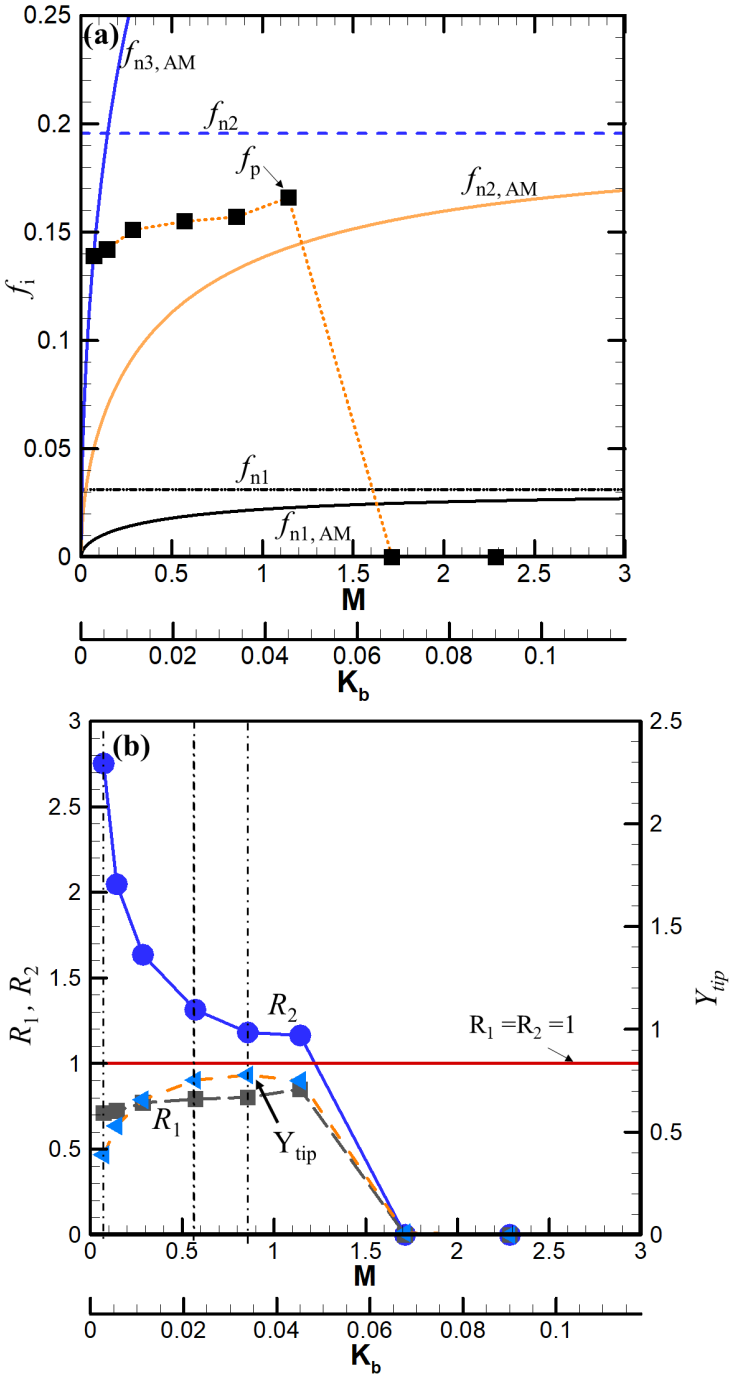

Figure 4.13: Comparison of: (a) simulated plate oscillation frequency (f_p) and plate natural frequency f_{ni} and $f_{ni,AM}$ without or with the added mass correction as a function of K_b/M ratio. Dotted and solid lines represent the f_{ni} and $f_{ni,AM}$ variations, respectively. Square symbols show results for simulated f_p; (b) plate tip amplitude (Y_{tip}) and frequency ratio R_1 and R_2 with or with the added mass correction as function of K_b/M ratio. Solid square, solid circle and triangle symbols show R_1, R_2 and Y_{tip} variations, respectively. Note that for these cases M and K_b vary but U_R is fixed.

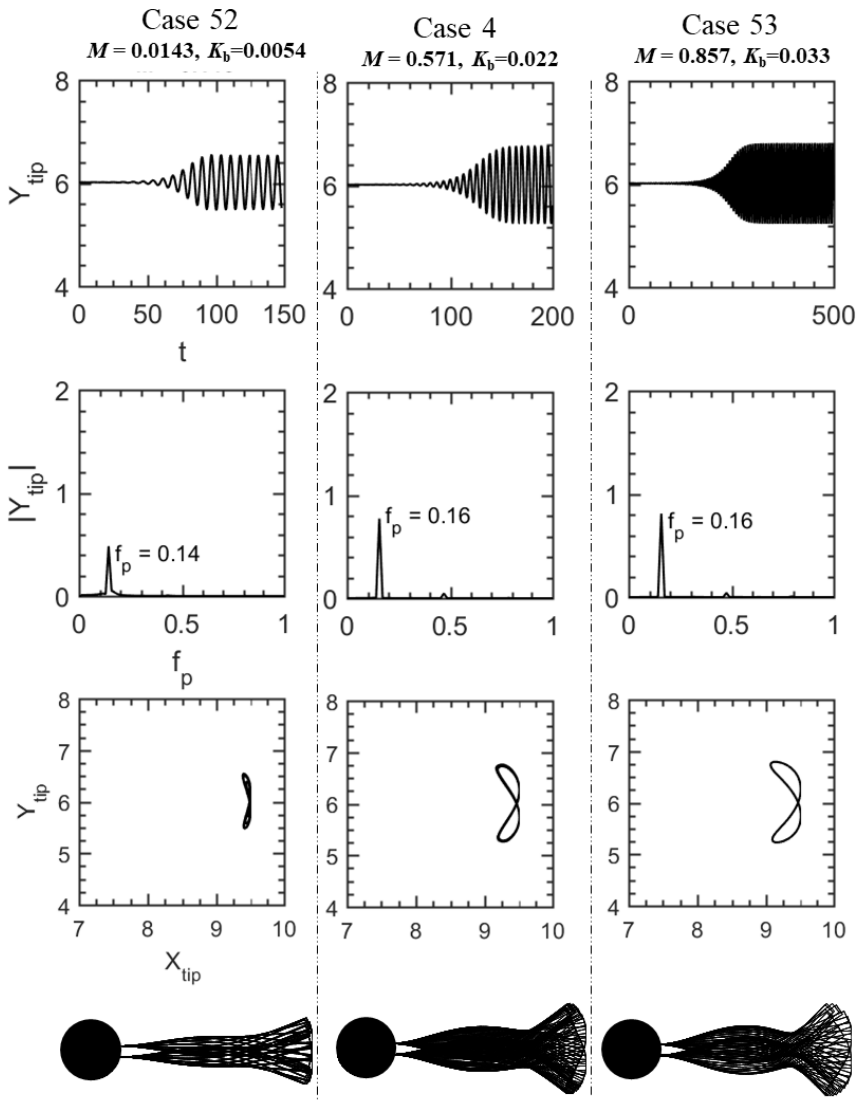

Figure 4.14: Comparison of tip displacement Y_{tip} (top row), power spectra (second row), and phase-plane plots (third row). Superimposed views of deflection mode of the splitter plate for M and K_b varying but with U_R fixed at 5.123.

The effects of K_b and M in keeping the reduced velocity (U_R) constant are discussed in this section. The simulation cases are shown in the Fig. 4.3 on the $1/M - U_R$ plane, and are listed in Table 4.5. We select K_b and M such that U_R is constant. The plate oscillation frequency f_p and plate natural frequency (f_{ni}) of first three modes with and without added mass are plotted as a function of K_b or M in the Fig. 4.13(a). Fig. 4.13(a) shows that f_p lies in between $f_{n2,AM}$ and $f_{n3,AM}$. At lower K_b or M, f_p falls on the $f_{n3,AM}$ curve. At higher values of K_b, f_p increases with M and approaches the $f_{n2,AM}$ curve. Fig. 4.13(b) shows Y_{tip}, R_1 and R_2 as a function of K_b or M. Here, R_1 increases but R_2 decreases with K_b (or M). Also, R_2 goes to a minimum at $K_b = 0.033$ ($M = 0.857$). Both R_1 and R_2 are zero at $K_b = 0.065$ ($M = 1.714$) because plate displacement is zero.

Fig. 4.13(b) shows that Y_{tip} increases with K_b (M) and reaches a maximum at $K_b = 0.033$ ($M = 0.857$). Beyond this it decreases with K_b (M). We also plot $R_1 = R_2 = 1$ for reference. The plate oscillates with larger displacement when the distance between the lock-in line and the R_2 line is a minimum.

4.2.4 Dependence of plate dynamics on K_b, U_R and M

Finally, we demonstrate that the response of the plate only effectively depends on M, K_b and U_R at a given Re. Simulation cases are listed in Table 4.6, in which the thickness (h), density ratio (ρ), and Young's modulus (E) are adjusted in such a way that M, K_b and U_R are constant. Fig. 4.15 shows that (Y_{tip}), the power spectra and the phase plots of the tip displacement are almost identical for the same K_b, M and U_R. Therefore, the plate dynamics is essentially only a function of M, K_b and U_R at a given Re.

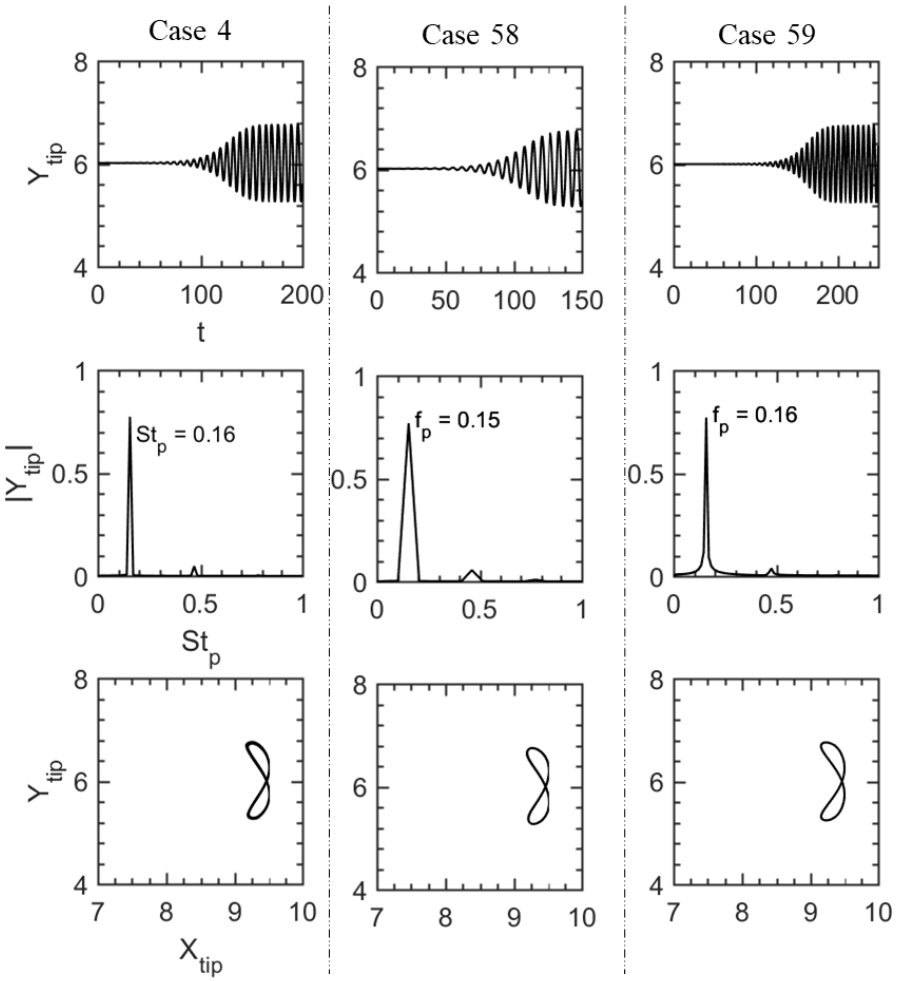

Figure 4.15: Comparison of tip displacement Y_{tip} (top row), FFT (second row), and phase-plane plots (third row) for M, K_b, U_R and L constant. The plate thickness (h), density ratio (ρ), and Young's modulus (E) are adjusted to achieve this. The values of M, K_b and U_R are given in Table 4.6.

4.2.5 Flapping map

The flapping responses for different cases as a function of M and U_R are plotted in Fig. 5.12. We also plot magnitude of Y_{tip} using a contour map for all cases. The baseline case is at $M = 0.571$ and $U_R = 5.123$, for which the material properties are the same as the benchmark problem of Turek and Hron (2006). In this map, K_b = constant and M = constant are represented by curved and vertical lines, respectively. A plot of U_R = constant is also shown in Fig. 5.12. For K_b = constant, Y_{tip} increases with M for $0.285 < M < 2.74$ and reaches maximum at $M = 2.74$ and $U_R = 11.225$. Furthermore, Y_{tip} decreases with M for $2.74 < M < 11.4$ and flapping stops at $M = 20.0$ and $U_R = 30.319$ as shown in the figure. A similar trend for Y_{tip} is noted at U_R = constant. At M = constant, Y_{tip} decreases with increasing U_R.

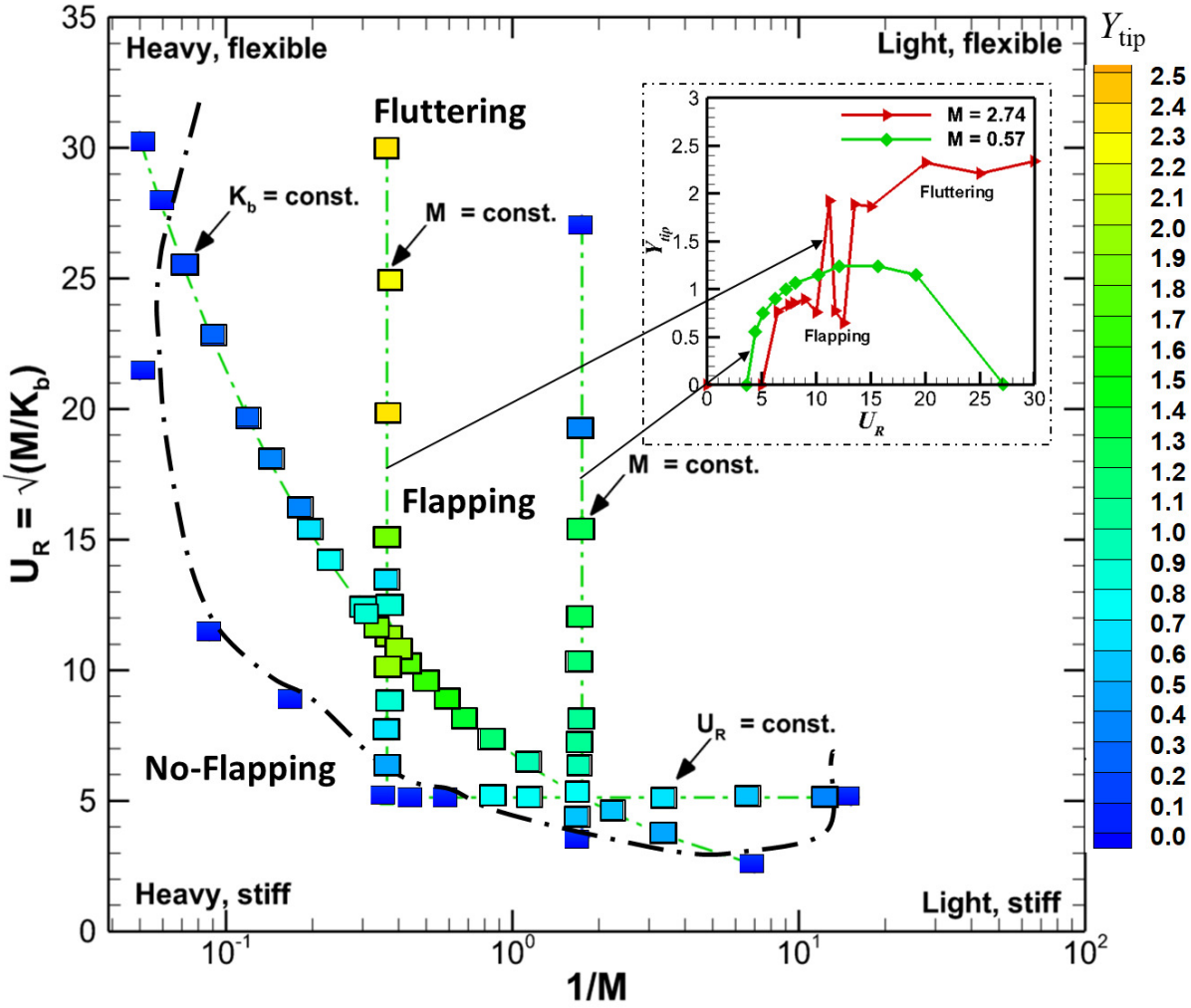

Figure 4.16: Parameter space map showing the flapping boundary as a function of the reciprocal mass ratio (M) and the reduced velocity U_R for the elastic splitter plate. Colored square points show plate oscillation amplitude (Y_{tip}), which is a function of M, K_b and U_R, as discussed in the text. Note that the present results are for an open domain.

At lower U_R, the plate displacement is also negligible. The horizontal dash-dot line represents constant U_R. On this line, Y_{tip} increases with M to reach a maximum at M = 0.857, it then decreases with M. For larger M and low U_R, no flapping is observed. Similarly, no flapping is noticed at lower U_R and M. The flapping boundary is represented by a black dash-dot line. Flapping is seen at moderate values of U_R and M. At the critical value of $M = 2.74$, a large Y_{tip} amplitude is observed. Similar characteristics (Khalak and Williamson (1999)) are observed for transverse oscillations of an elastically mounted rigid cylinder. Inset of Fig. 5.12 shows the comparison Y_{tip} with U_R for two different mass ratio. Inset of Fig. 5.12 shows that Y_{tip} increases with U_R, reaching a maximum and then decreases with U_R for $M = 0.57$. At lower U_R, the plate displacement is negligible. Similar trend is observed for $M = 2.74$ upto $U_R = 12.5$. For $U_R > 12.5$, Y_{tip} increases with increasing U_R and flutter instability occurs. As a result, plate vibrate with large amplitude.

4.3 Closure

We have employed a fluid-structure interaction (FSI) solver to simulate the dynamics of an elastic splitter plate attached to a rigid circular cylinder that is subjected to laminar flow. The FSI computational approach combines a sharp-interface immersed boundary method-based flow solver and an open-source finite-element based structure solver. In the present chapter, the effect of mass ratio (M) and bending stiffness (K_b) on the FSI response were studied at $Re = 100$. Here, Re is the Reynolds number and is based on free-stream velocity and cylinder diameter. We vary M, K_b and U_R in the ranges [0.143, 20], [0.0008, 0.0435] and [2.562, 30.0], respectively, noting that these ranges cover a high amplitude FSI response. The plate amplitude and oscillation frequency are found be a function of M and K_b. The time-varying displacement of the tip of the plate, power spectra of the displacement signal, phase plots of the plate tip displacement and the wake structure are examined in order to quantify the results. The largest amplitude of the plate was found to be for the lock-in condition at which the natural frequency of the plate in a given fluid synchronizes with the oscillation frequency of the plate. At lock-in, the oscillation frequency is lower than the natural frequency of the plate in a vacuum due to the influence of the added mass. This behavior is consistent with the classical vortex-induced vibration of a rigid cylinder at the low mass ratio. The plate exhibits a strong added mass effect at lower mass ratios and lower bending stiffness. As M and K_b increase, the oscillation frequency becomes closer to the natural frequency of the plate in a vacuum, showing the expected diminishing added-mass effect. Importantly, we determined the approximate flapping boundary on the $1/M - U_R$ plane, together with the amplitude response. Thus, the present results provide fundamental insights into flapping of an elastic splitter plate

attached to a rigid circular cylinder, which could prove useful to the design of flexible plates for energy harvesting and thermal augmentation applications.

Chapter 5

Role of Plate Thickness in Flow-Induced Dynamics of an Elastic Plate Subjected to Free-stream Flow

We investigate the effect of plate thickness on the dynamics of an elastic plate subjected to a laminar free stream. An in-house fluid-structure interaction solver is employed to understand the dynamics of the plate. We investigate the effect of thickness on the plate dynamics by taking a wide range of mass ratio and bending stiffness of the plate at Reynolds number, Re = 100. Re is based on free-stream velocity and the length of the plate. The plate dynamics depend on reduced velocity, bending stiffness and mass ratio at a given Re. Plate flapping stats at critical reduced velocity and critical mass ratio. Critical reduced velocity and critical mass ratio change with the thickness of the plate. The flapping boundary obtained from the simulations is plotted on a mass ratio-reduced velocity plane. We show the critical flapping boundary changes with plate thickness and briefly, discuss wake-structures and phase-plots for different cases of mass ratio and bending stiffness. The present results are useful to design elastic plates flapping condition in energy harvesting applications.

5.1 Introduction

The stability and nonlinear dynamics of a thin elastic flag/membrane have been investigated and found in many theoretical (Kornecki et al. (1976); Watanabe et al. (2002); Theodorsen and Mutchler (1935); Argentina and Mahadevan (2005); Eloy et al. (2008)), numerical (Zhu and Peskin (2002); Connell and Yue (2007); Huang (1995)) and experimental studies (Zhang et al. (2000); Shelley et al. (2005)). Most of the experimental studies have been carried out to investigate the flapping dynamics of a flag. In addition, the effect of flag material properties like mass and bending rigidity, flag positioning have also been examined. Theoretical and numerical studies have been accomplished for details investigation of flapping dynamic. Watanabe et al. (2002) studied the flutter phenomena of a sheet of paper numerically. They found potential flow analysis is convenient to investigate flutter behavior. Connell and Yue (2007) proposed a regime map of flag flutter which arose from their fluid-structure direct simulations. Depending on the combined effects of various factors such as mass ratio, Reynolds number and bending rigidity, flag flutter dynamics may fall into three categories: fixed-point stability, limit-cycle flapping, and chaotic flapping. Fixed-point stability is a region where the flag aligns with the flow. As the flow velocity is increased, limit-cycle flapping takes over, characterized by single-frequency repeating flag oscillations. Chaotic flapping occurs as the flow velocity is further increased. Eloy et al. (2008) addressed the linear stability of rectangular plate in uniform flow and incompressible axial flow by varying aspect ratio. Shoele and Mittal (2016b) predicted the flexible-cantilever dynamic behavior in the mass ratio and reduced velocity parameter space for length, $L = 1$ and $Re = 100$. The fluttering instability of the flag gives in a periodic or chaotic motion of the system. The chaotic regime exhibits multi-frequency, multi-amplitude, and irregular flapping behavior and violent snapping of the flag also occurs (Michelin et al. (2008); Shelley and Zhang (2011); Tian et al. (2010)).

Several previous studies defined two important dimensionless parameters that govern the dynamics of the plate - bending stiffness (K_b) and mass ratio (M) which is described in chapter 4 and the critical mass ratio for the chaotic flapping found by a linear stability analysis in Ref. Connell and Yue (2007) is given by,

$$M_{crit} = \frac{1.328{Re_L}^{-1/2} + K_b k^2}{1 - 0.65{Re_L}^{-1/2}k - 0.5K_b k^3} \tag{5.1}$$

where Re_L is Reynolds number (Re), based on the plate length and k indicates wave number. The wave number is represented by $k = 2\pi/\lambda$ with λ representing the wavelength.

The objective of the present chapter is to investigate the critical reduced velocity and critical mass ratio for plate flapping. We also examine to identify critical reduced velocity and critical mass ratio for plate flapping for different thickness of the plate. We consider

a wide range of $M = [0.9, 19.5]$, $K_b = [0.0009, 0.017]$ and $U_R = [10, 40.0]$, at $Re = 100$.

The chapter is organized as follows. We discuss the effect of M, K_b and U_R on the fluid-induced deformation of the plate in sections 5.3.1, 5.3.2 and 5.3.3, respectively. Finally, based on all simulations results, we plot a flapping map in 1/M-U_R plane in section 5.3.4.

5.2 Problem definition

We employed an in-house, validated FSI solver is described in chapter 2.

In this chapter, We also investigate the plate instability. Plate instability depends on fluid loading and inertia effect on the plate. Different angle of attack of the plate is one of most plate instability mechanism. Plate instability of the fluid-elastic plate system occurs when the reduced velocity U_R exceeds a threshold U_{Rc} in particular mass ratio (M)and $U_R < U_{Rc}$, the plate remains in a stable flat state.

In this chapter, we consider a thin, elastic plate with dimensions $1D \times 0.06D$ is kept inside an open domain, as shown in Fig. 5.1. The domain length and width are $(S_1 + S_2)$ and S_3, respectively, where S_1, S_2 and S_3 are $5L$, $20L$ and $10D$, respectively. The center of the plate is at $(S_1, S_3/2)$. The boundary conditions for the present chapter are illustrated in Fig. 5.1.

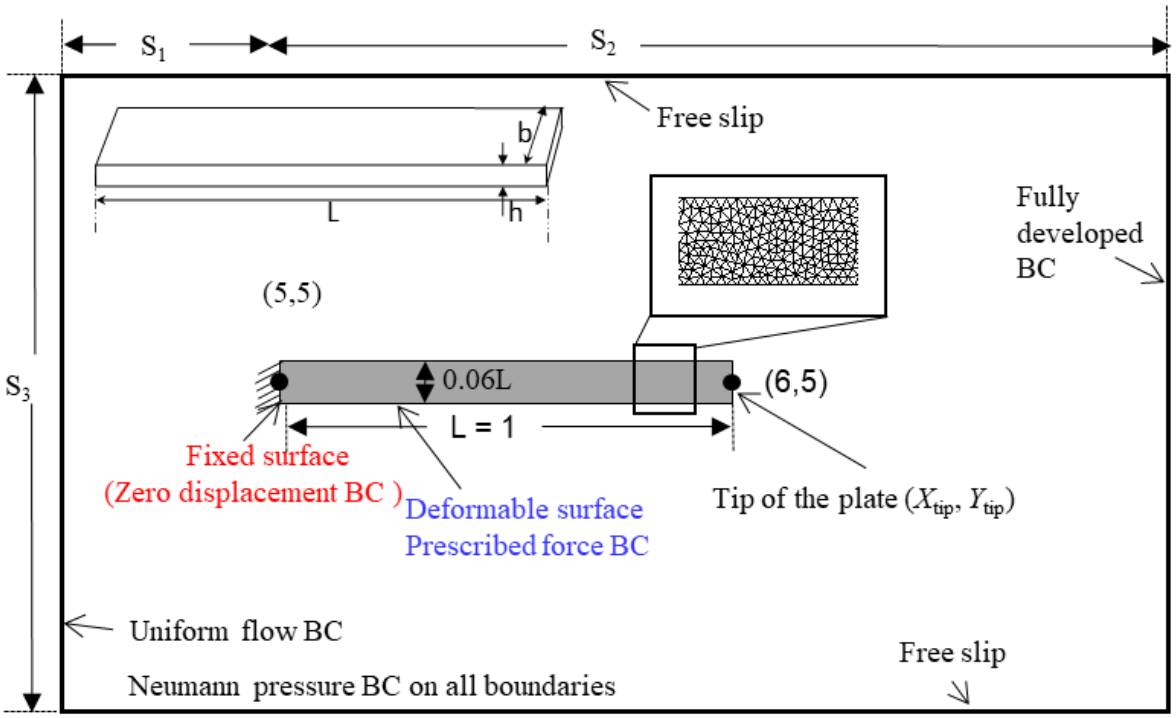

Figure 5.1: Schematic of FSI benchmark problem for a thin elastic plate

The fluid is considered to be incompressible and Newtonian. Free slip boundary condi-

tions are applied at the top and bottom of the domain. No-slip is applied at the immersed structure boundary. Fully developed flow boundary condition (BC) is applied for the velocity at the right side of the domain. At the inlet, uniform velocity is applied. The following values are considered for the simulation setup $U = 1, L = 1, Re = 100$. The time step for this unsteady simulation is set to $\Delta t = 0.01$. The Poisson ratio is taken as 0.4 in the structural solver.

5.2.1 Grid-size and domain-size independence study

We investigate grid convergence study of uniform inflow past an elastic plate in the open domain for three different grids with sizes of 360 ×160, 384 × 160, and 416 × 192. The time-step was set to $\Delta t = 0.01$. The minimum grid sizes in X and Y-direction are listed in Table 5.1, The tip deflection (Y_{tip}) signals obtained for the grids are compared in Fig. 5.2(a), with the inset showing the minor differences observed in peak amplitude for the different grids. The errors concerning the finest grid are listed in Table 5.1. Since the relative error for 360 × 160 grid, as shown in Table 5.1, is one order of magnitude smaller than for 384× 160, the 360 × 160 grid was selected for all the simulations in the present chapter. Three domains of sizes for (changing domain length and keeping domain height same), $25D \times 10D$, $30D \times$ 10D and $40D \times 10D$ are taken to address domain independent study. The tip displacement (Y_{tip}) signals obtained from three different domains are compared in Fig. 5.2(b). The inset of Fig. 5.2(b) shows the minor differences observed in peak amplitude for the different domain. The error concerning the $25D \times 10D$ domain is listed in Table 5.2 which is less than 2%.

Table 5.1: Error in the maximum plate tip deflection for different grids with respect to the finest grid examined

Cases	Grid points	Δx_{min}	Δy_{min}	Relative error in maximum Y_{tip} with respect to case 3
1	360 ×160	0.01	0.01	0.055%
2	384 ×160	0.0125	0.0125	0.062%
3	416 ×192	0.0075	0.0075	–

Table 5.2: Error in the maximum plate tip deflection for different domain sizes with respect to the lower domain size

Cases	Domain size	Relative error in maximum Y_{tip} with respect to case 3
1	25 ×10	0.016%
2	30 ×10	0.08%
3	40 ×10	–

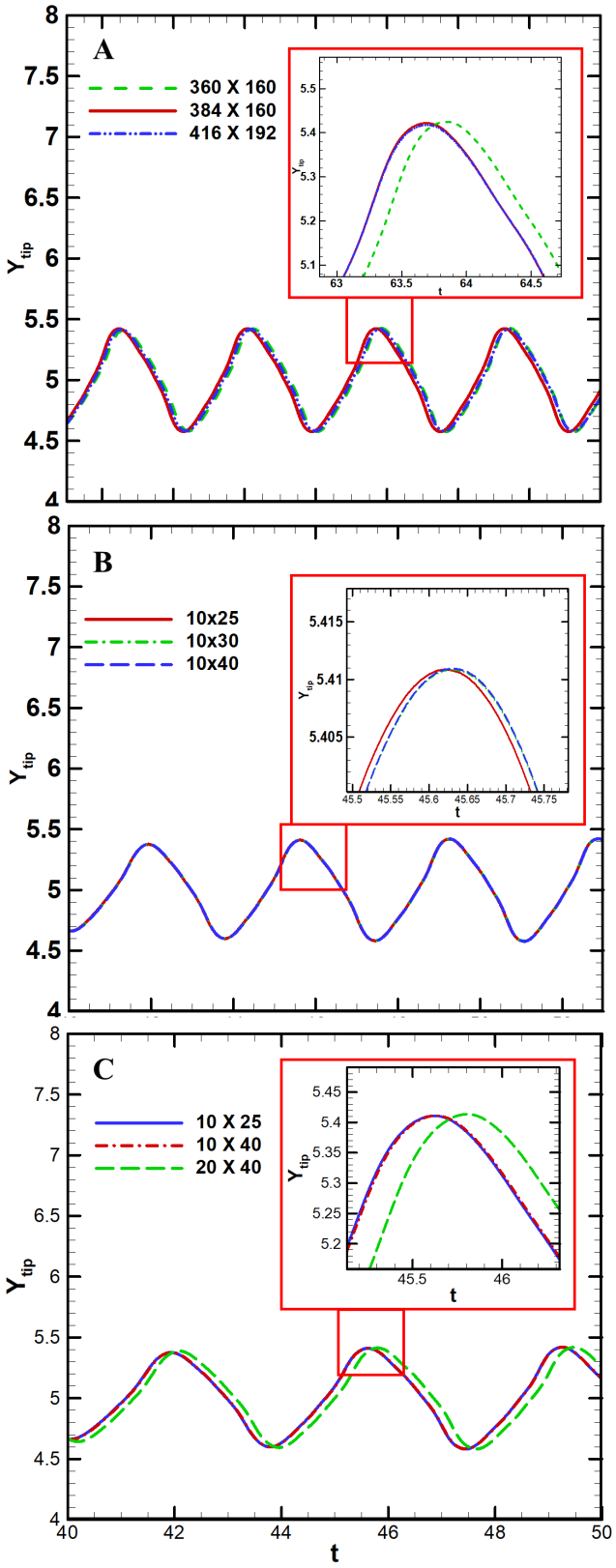

Figure 5.2: (a) Grid size convergence study: comparison of the time-varying cross-stream displacement of the plate tip (Y_{tip}) as a function of grid resolution of the immersed boundary method solver. (b) Domain size independence study: comparison of the time-varying cross-stream displacement of the plate tip (Y_{tip}) for three different domains.

Table 5.3: Error in the maximum plate tip deflection for different domain sizes with respect to case 3

Cases	Domain size	Relative error in maximum Y_{tip} with respect to case 3
1	25 ×10	0.093%
2	40 ×10	0.076%
3	40 ×20	–

We have done another domain independent study by changing the height and keeping the domain length same. Three domains of sizes for, $25D \times 10D$, $40D \times$ 10D and $40D \times 20D$ are taken to address domain independent study. The tip displacement (Y_{tip}) signals obtained from three different domains are compared in Fig. 5.2(c). The inset of Fig. 5.2(c) shows the minor differences observed in peak amplitude for the different domain. The error concerning the 25 $D \times 10D$ domain is listed in Table 5.3 which is less than 1%. Therefore, $25D \times 10D$ domain is taken for all the simulations. In the present chapter, 360×161 non-uniform Cartesian grid with $\Delta x_{min} = 0.01$ and $\Delta y_{min} = 0.01$ is considered for open domain. High resolution of a grid is incorporated into the region where the plate movement is expected. For the structural solver, a total of 568 finite quadrilateral elements for the plate is taken. The finite-element grid of the plate is shown in the inset of Fig. 5.1.

5.3 Results and Discussions

Numerical simulations were performed using the same parameters of the flexible plate as discussed in previous section 5.2 and the domain size is taken as follows; $S_1 + S_2 = 25L$ and $S_3 = 10.0L$, as shown in Fig. 5.1. The dynamics of the elastic plate as a function of a mass ratio (M), bending stiffness (K_b) and reduced velocity (U_R) of the plate are discussed. We vary M, K_b and U_R in range of [0.05, 19.5], [0.0009, 0.017] and [10, 40.0], respectively.

5.3.1 Effect of reduced velocity (U_R) keeping mass ratio (M) constant

We discuss the effect of reduced velocity (U_R) on the elastic plate displacement (Y_{tip}), oscillation fruency (f_p) and wake structures, keeping mass ratio (M) constant. We present simulations for two $M = 1$ and 10 with varying (U_R). In order to quantify the plate response, we plot data of two different mass ratio, $M = 1.0$ and 10 as represented in Fig. 5.3 and Fig. 5.5. Fig. 5.3 (first row) shows that plate deformation increases with U_R.

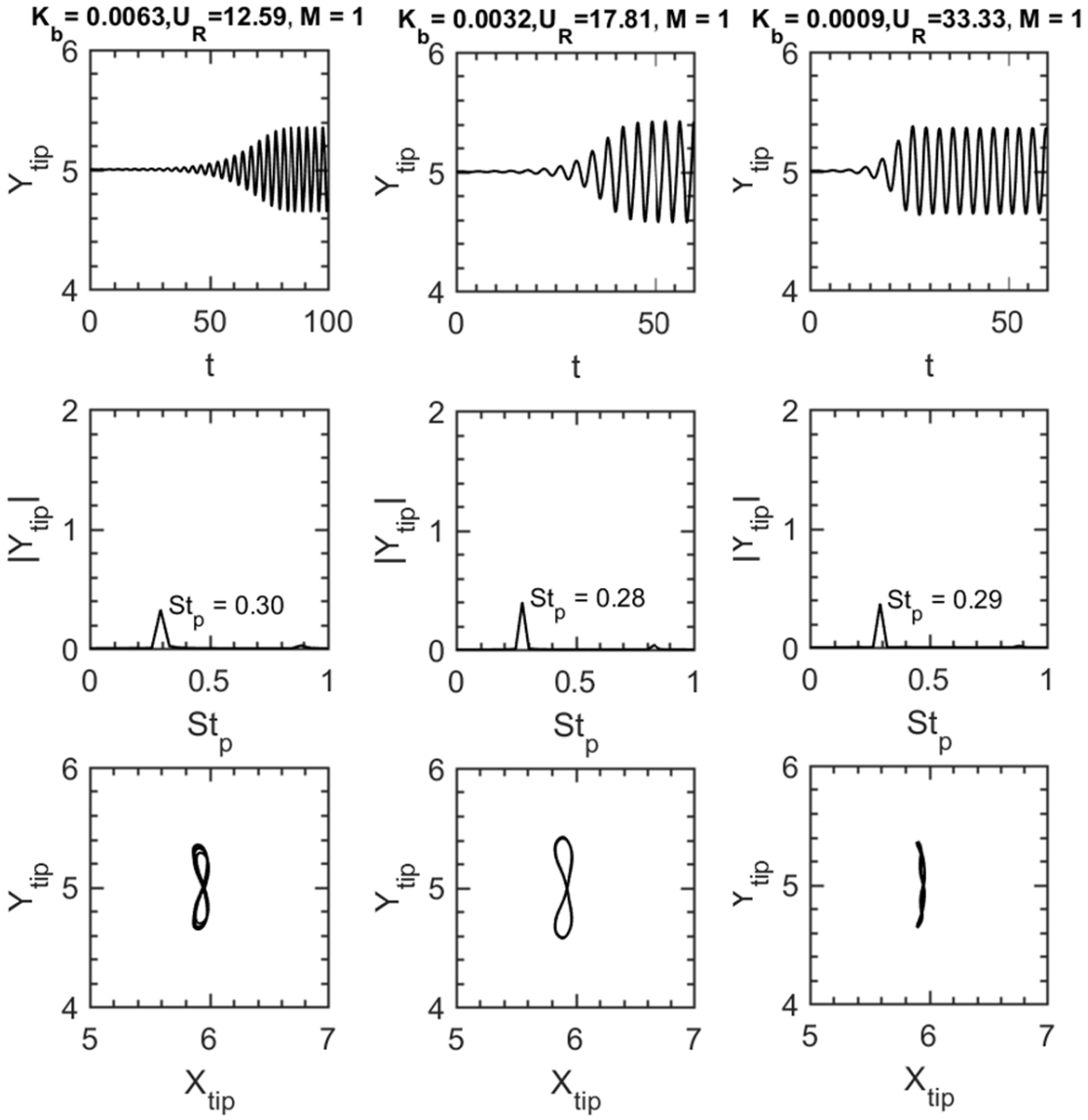

Figure 5.3: Comparison of Y_{tip} of the plate deformation, power spectra and phase plane plot are for three different U_R. Note that $M = 1.0$ is fixed for all cases.

Fig. 5.3 (second row) shows that plate deformation frequency slightly change with U_R. Fig. 5.3 (third row) shows that the the plate lateral deformation is higher at $U_R = 17.81$ for $M = 1.0$. Plate lateral deformation is lower at $U_R = 33.33$ for $M = 1.0$. Fig. 5.5 shows that the plate deformation is the function of U_R and M. Fig. 5.5 (first row) shows that plate deformation is negligible at $U_R = 20$ for $M = 10$. Plate deformation increases with U_R and amplitude of the plate deformation is nearly constant. The decrease in plate deformation frequency is not much in Fig. 5.5. Fig. 5.5 (second row) shows that the plate deformation dominant frequency slightly changes with increasing U_R.

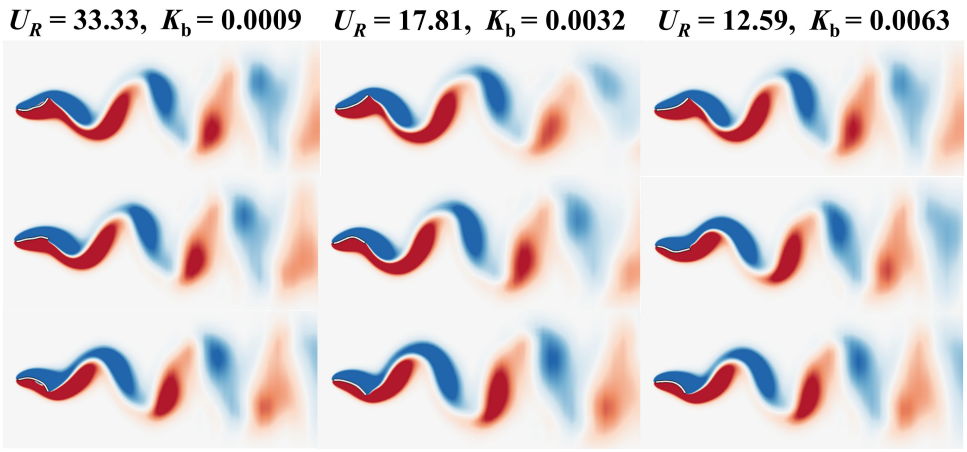

Figure 5.4: Comparison of vorticity field at different time instances for three different U_R. Note that $M = 1.0$ is fixed for all cases.

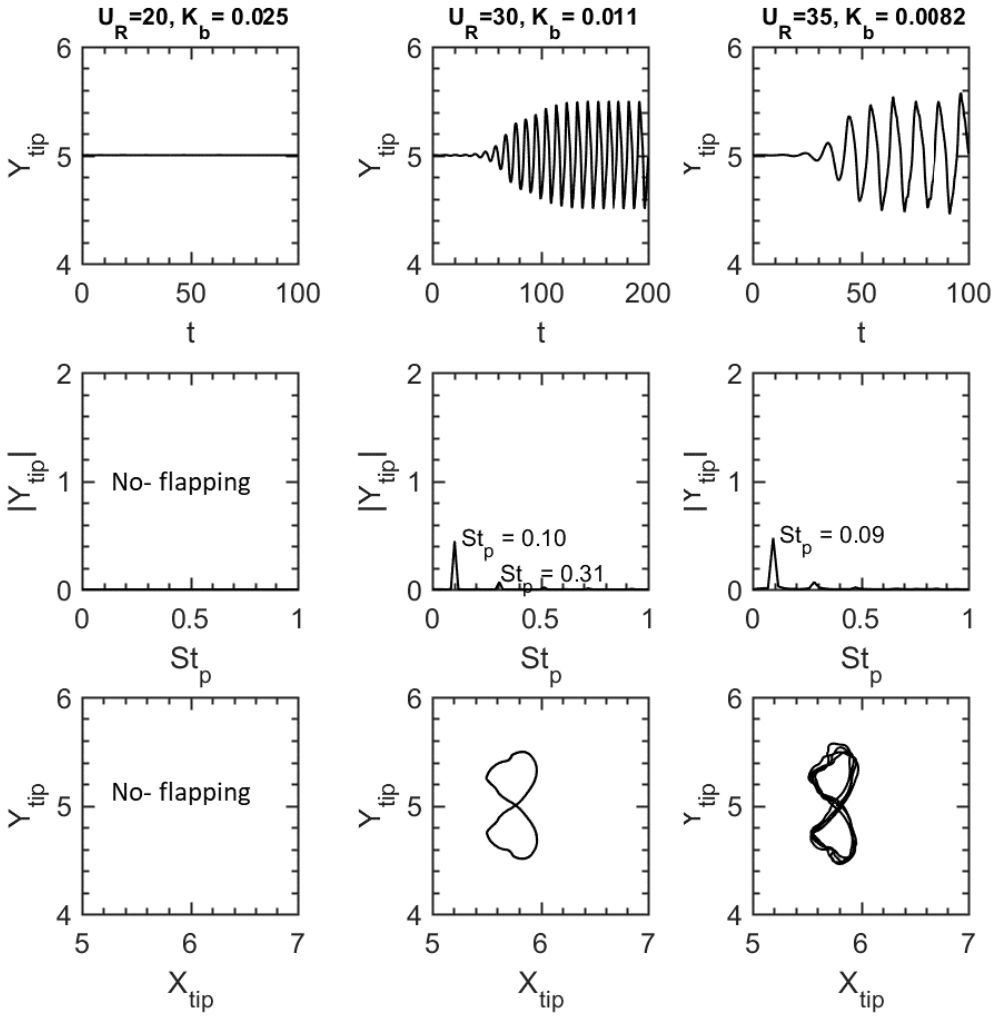

Figure 5.5: Comparison of Y_{tip} of the plate deformation, power spectra and phase plane plot are for three different U_R. Note that $M = 10$ is fixed for all cases.

Fig. 5.5 (third row) shows that the plate lateral deformation increases with U_R. So the plate deformation starts on critical M for particular U_R. Fig. 5.4 and Fig. 5.6 depicts the instantaneous vorticity fields around the plate. Three different positions like maximum, minimum and central position $6L$,$5L$) at three different instances are plotted in Fig. 5.4 and 5.6. For $M = 1$, the elastic plate is in its self-sustained oscillations state and vortices are shedding alternately (see in Fig. 5.4). For $M = 10$, the elastic plate is in its self-sustained oscillation state and one small vortex rolls with another large vortex and finally sheds alternately (see in Fig. 5.6). Vortex shedding pattern depends on the plate deformation amplitude.

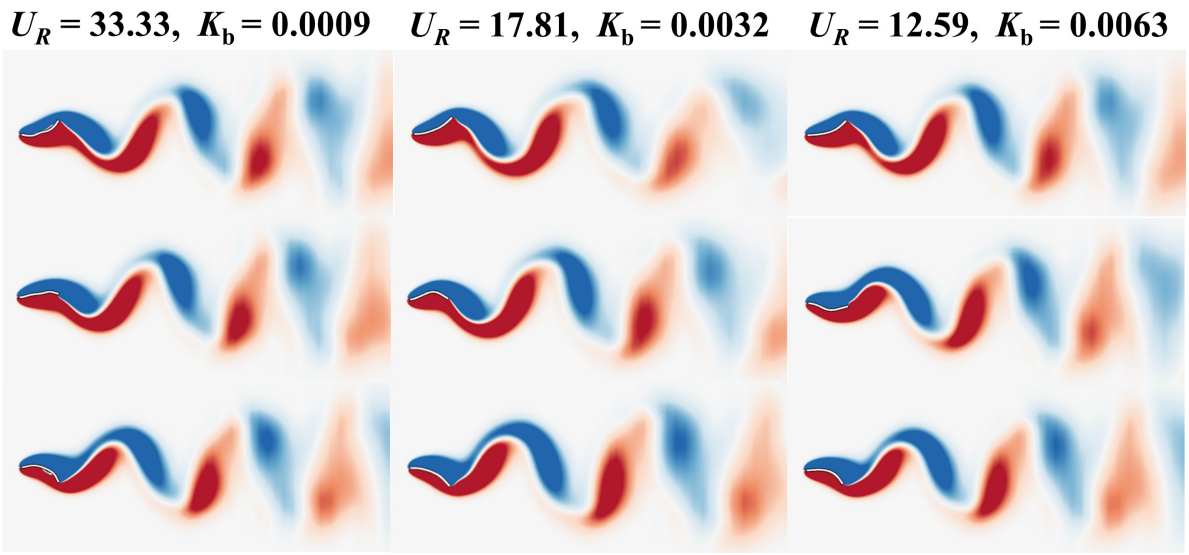

Figure 5.6: Comparison of vorticity field at different time instances for three different U_R. U_R is function of K_b and M. Here M is fixed and U_R changes with K_b. Color map range is [-1, 1].

5.3.2 Effect of reduced velocity (U_R) keeping bending stiffness (K_b) constant

The effect of reduced velocity (U_R) on the elastic plate displacement (Y_{tip}), oscillation fruency (f_p) and wake structures, keeping K_b constant is discussed. We take three different $U_R = 15$, 20, 30 and keeping mass ratio $K_b = 0.11$ constant as shown in the Fig. 5.7. U_R increases with M as K_b fixed. Fig. 5.7 shows the Y_{tip}, power spectra and phase plot of the elastic plate in the first, second and third row, respectively. Y_{tip} increases with U_R as well as M. Fig. 5.7 (first row) shows that plate deformation is negligible at $U_R = 15$ for $K_b = 0.011$. Plate flapping observes at higher $U_R(> 15)$ for $K_b = 0.011$. So plate flapping strongly depends on U_R and critical M. Fig. 5.7 (second row) shows that plate deformation decreases with U_R. Fig. 5.7 (third row) shows that phase plot is wider at higher U_R (= 30) because of lock-in condition.

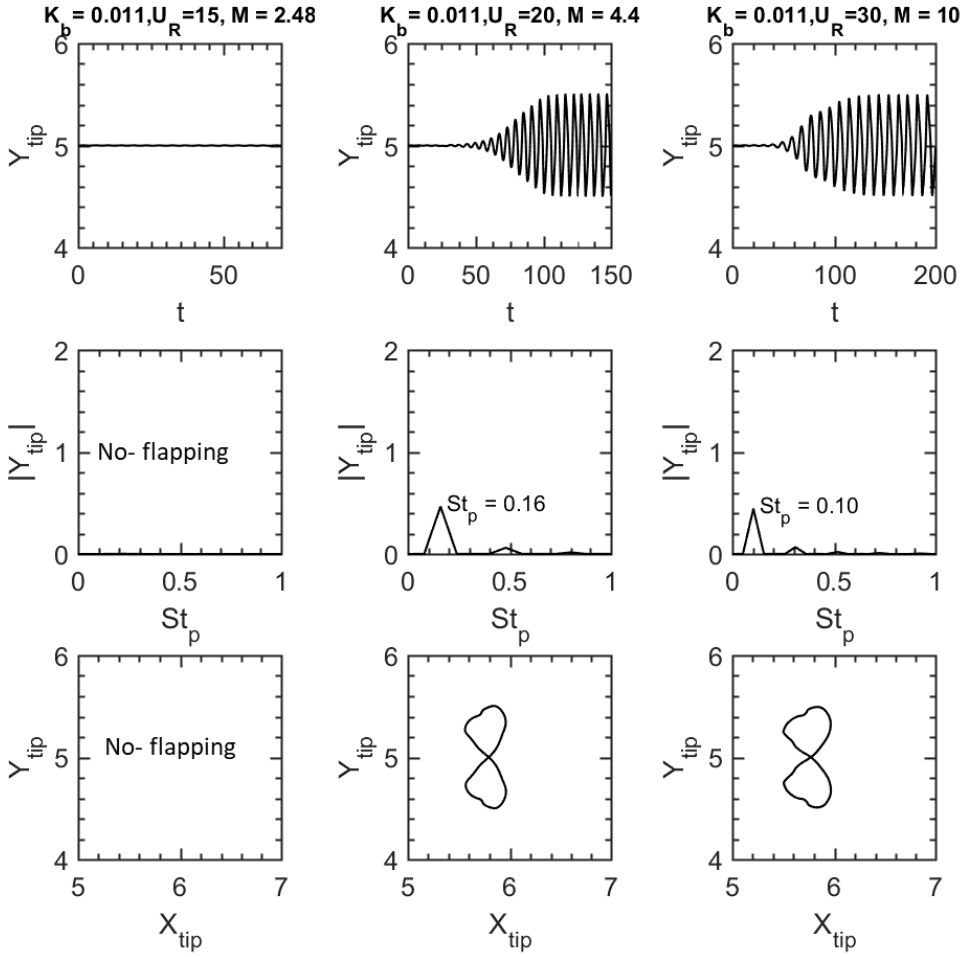

Figure 5.7: Comparison of Y_{tip} of the plate deformation, power spectra and phase plane plot are for three different U_R. Note that K_b is fixed for all cases.

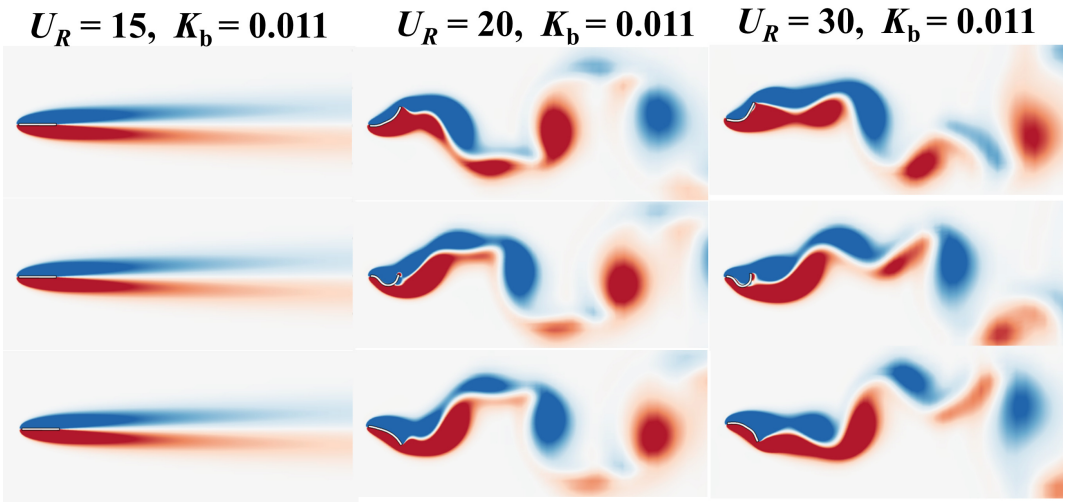

Figure 5.8: Vorticity field of plate deformation at three different U_R. Note that K_b is fixed for all cases. Color map range is [-1, 1] .

Fig. 5.8 shows the vorticity fields for three cases of U_R. For lower U_R, no flapping steady state is observed. Vortex shedding is found at a higher U_R. Vortex is becoming elongated, and shedding occurs behind the plate.

5.3.3 Effect of K_b and M keeping reduced velocity (U_R) constant

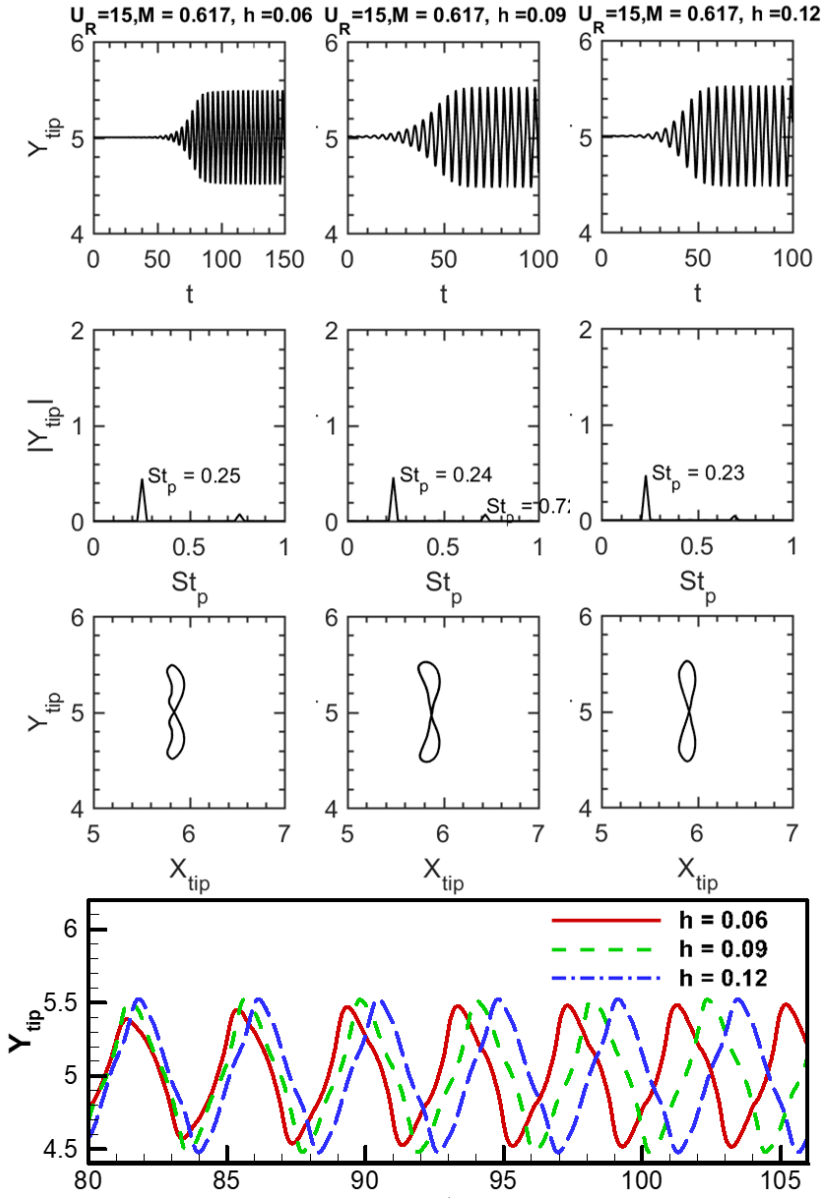

Figure 5.9: Comparison of plate deformation (Y_{tip}), FFT and phase plane plot for keeping M, K_b, U_R and L constant. Thickness (h), density ratio (ρ_s), and Young's modulus (E) are adjusted.

We also examine that the response of the plate depends on M, K_b and U_R at a given Re. Simulations are performed in which thickness (h), density ratio (ρ), and Young's modulus

(E) are adjusted in such a way that M, K_b and U_R are constant. (Y_{tip}), FFT and the phase plot of the plate are shown for same K_b, M and U_R in Fig. 5.9 and Fig. 5.11.

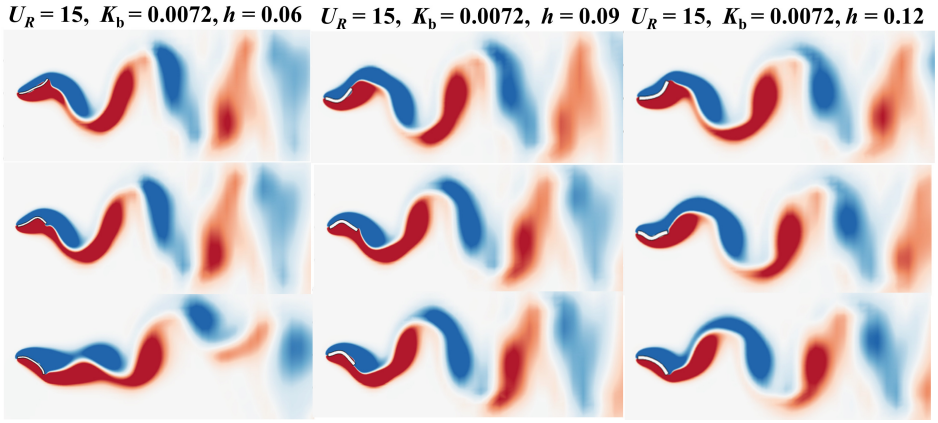

Figure 5.10: Comparison of plate deformation (Y_{tip}), FFT and phase plane plot for keeping M, K_b, U_R and L constant. Thickness (h), density ratio (ρ_s), and Young's modulus (E) are adjusted.

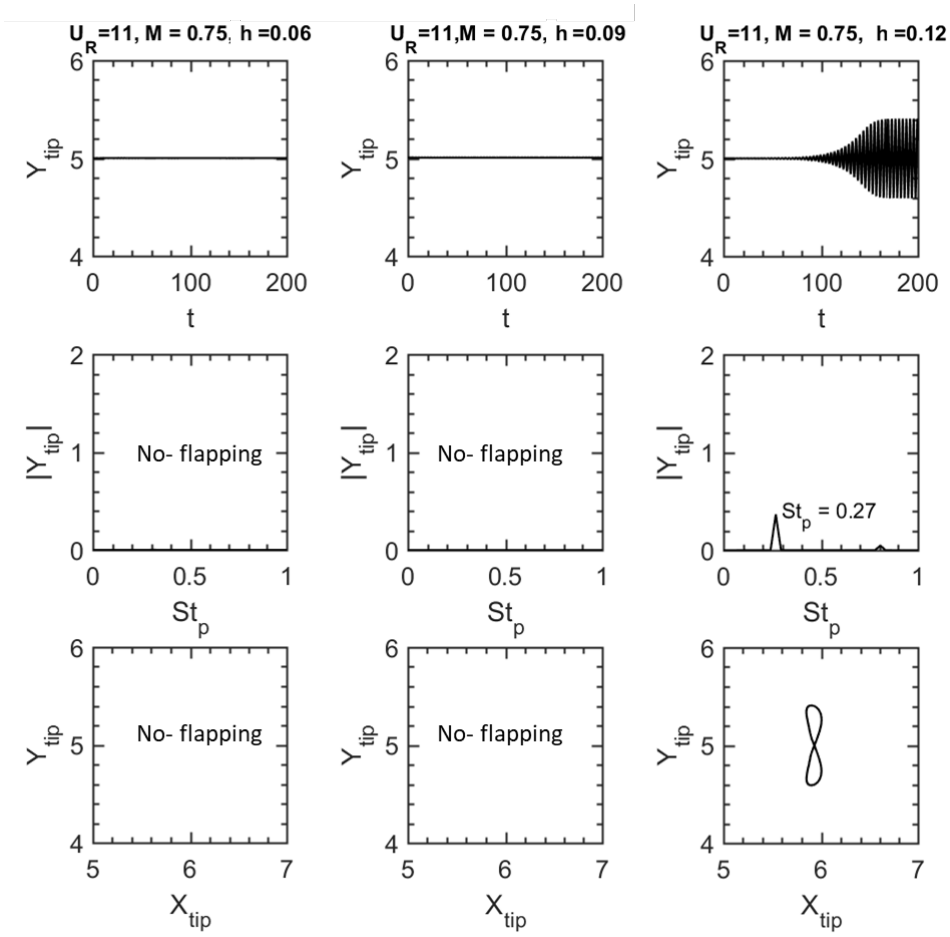

Figure 5.11: Comparison of plate deformation (Y_{tip}), FFT and phase plane plot for keeping M, K_b, U_R and L constant. Thickness(h), density ratio (ρ_s), and Young's modulus (E) are adjusted.

Two different U_R are chosen to show the effect of thickness. For $U_R = 15$ as shown in Fig. 5.9 , plate amplitude increases with plate thickness (h) but plate frequency decreases with thickness (h). As increase of thickness of plate, effective Reynolds number based on obstacle of incoming flow is increased. The instability in the shear layer as well as wake behind plate increases with thickness and acting fluid force on plate increases with thickness which causes largest deformation. Fig. 5.10 shows that the vorticity field for three cases. Three different vortex patterns are observed. For lower thickness (h), small vortex are observed and vortex is becoming elongated with thickness (h) further. For $U_R = 11$ as shown in Fig. 5.11, plate displacement is zero for thickness (h) = 0.06 and 0.09 and regular flapping is observed at thickness (h) = 0.12. Different thicknesses have different critical U_R at which flapping start.

5.3.4 Flapping map

The flapping responses for thickness (h) = 0.06 as a function of M and U_R are plotted in Fig. 5.12. Green triangle and blue diamond symbols represent the regular flapping state and steady state with no flapping shown in the Fig. 5.12, respectively. the plate flapping is distinct boundary and it is function of critical M and U_R.

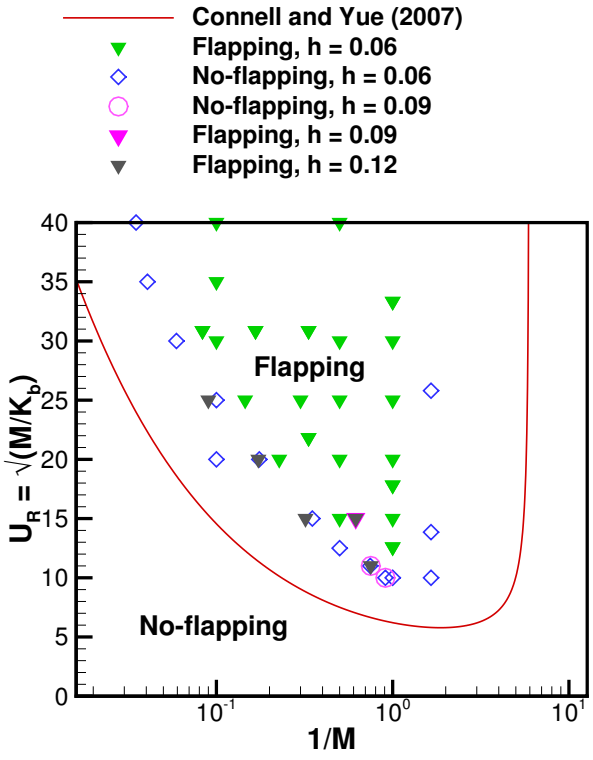

Figure 5.12: Flapping boundaries as a function of the mass ratio (M) and U_R for the elastic plate in a uniform free stream.

We also plot flapping boundary (eq. 5.1) given by Connell and Yue (2007) and compare with present simulation. We take $k = \pi$ for the first fundamental mode (Jaiman et al., 2014; Liu et al., 2014). Connell and Yue (2007) did not mention h. Very low bending rigidity is used for their simulation. They mentioned K_b which is a function of L and h. We have drawn a red line from eq. 5.1. Here Re_L is based on the length of the plate (L). In their study, They have chosen $Re = 1000$. In Our case, we used an analytical expression, and we have chosen $Re_L = 100$ which is based on the length of the plate (L). It is observed that the plate oscillates at particular U_R and critical M. The region for higher U_R and larger M is no flapping zone which is inconsistent with Connell and Yue (2007) criteria. the plate oscillation does not follow Connell and Yue (2007) criteria for plate flapping. They studied stability analysis by using potential flow theory and they showed the destabilizing effect of higher mass ratio and Reynolds number. We use viscous laminar flow and it might be reason for mismatch. For large M and low U_R, No-flapping is observed. Similarly, no flapping is noticed at lower U_R and M. Flapping is observed at the moderate value of U_R and M.

5.3.5 Effect of the presence of circular cylinder and without the presence of circular cylinder on plate deformation

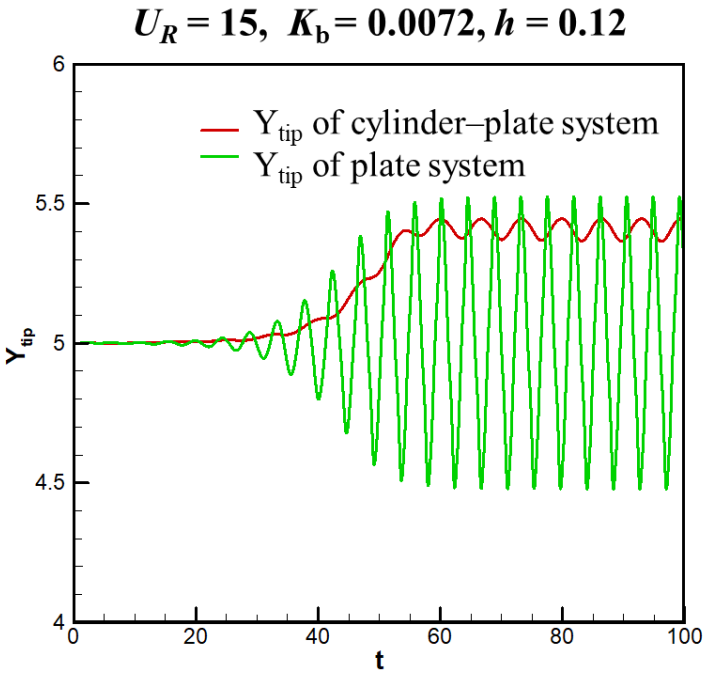

Figure 5.13: Comparison of the effect of the presence of a circular cylinder and without the presence of a circular cylinder on plate deformation.

The effect of the presence and absence of a circular cylinder on the elastic plate displacement (Y_{tip}) and wake structures, keeping K_b, U_R and M constant is discussed. Plate vibration is suppressed when the cylinder is placed in front of the elastic plate. Fig. 5.13 shows the plate deformation at two different U_R in the presence and absence of a circular cylinder. In the presence of a circular cylinder, the plate tip goes up and vibrates. No flapping is observed. For the case of absence of circular cylinder, flapping is observed with higher amplitude. Fig. 5.14 shows that the vorticity field for the presence and absence of a circular cylinder on the plate deformation. Vortex patterns are different for the two cases. Alternative periodic vortex shedding is observed in both cases and vortex shedding pattern is 2S. Shed Vortices from the plate are elongated. Due to large shear layer instability, larger Y_{tip} of plate deformation occurs. Vortex formation length is higher for plate attached to a circular cylinder. As bending rigidity is low, plate showing symmetry breaking for the second case.

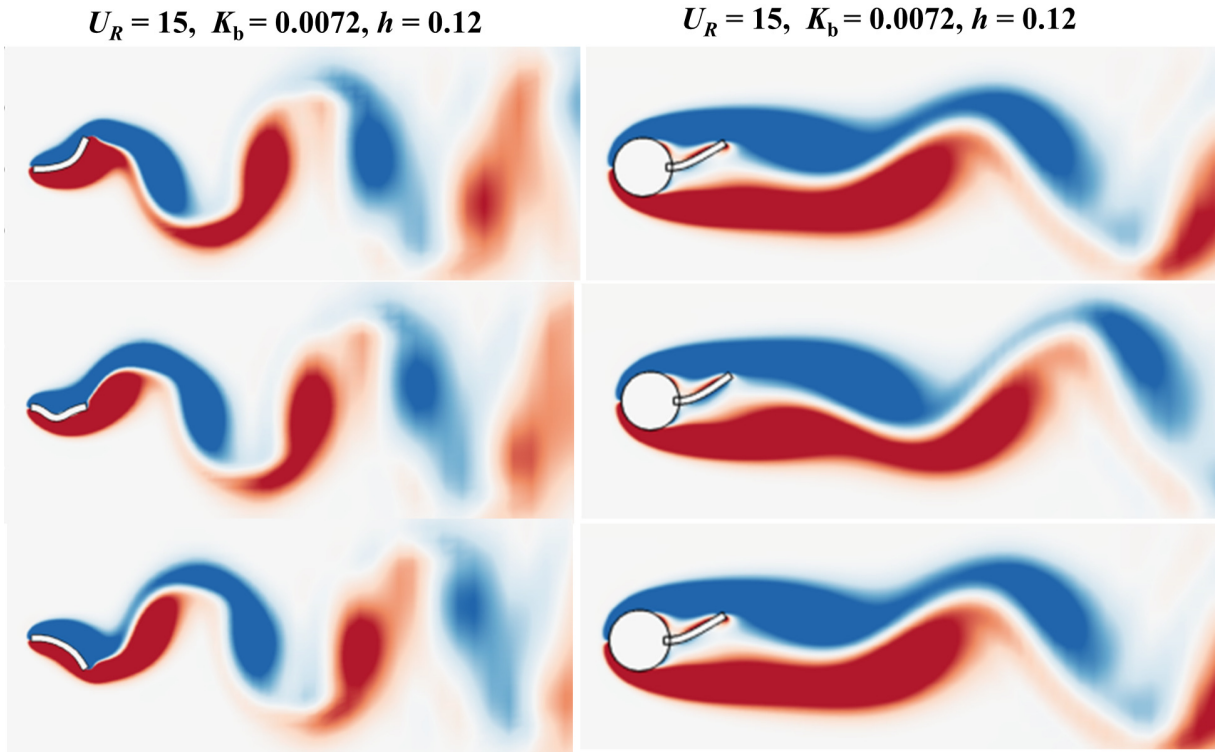

Figure 5.14: Comparison of the vorticity field of plate deformation for the presence of circular cylinder and without the presence of a circular cylinder on plate deformation. Color map range is [-1, 1] .

5.4 Closure

We have employed a fluid-structure interaction (FSI) solver to simulate the dynamics of an elastic plate and subject to laminar flow. In the present chapter, the effect of mass

ratio (M), bending stiffness (K_b) and reduced velocity U_R were studied at $Re = 100$, where Re is Reynolds number and is based on free-stream velocity and length of the plate. We vary M, K_b and U_R in range of [0.05, 19.5], [0.0009, 0.017] and [10, 40.0], respectively. The plate amplitude and oscillation frequency are found to be a function of M, K_b. We have plotted time-varying displacement of the tip of the plate, the FFT of the displacement signal, phase-plot of the plate displacement and wake structures in order to quantify the results. Plate flapping depends on critical reduced velocity and critical mass ratio. Critical reduced velocity and critical mass ratio changes with the thickness of the plate. Two types of flapping dynamics are observed: (a) fixed-point stability and (b) limit-cycle flapping. We have plotted a flapping boundary using the data of simulations on $1/M - U_R$ plane. We have found that the critical flapping boundary changes with plate thickness. The present results provide fundamental insights into the flapping of an elastic plate and could be useful to design flexible plate in energy-harvesting and thermal augmentation applications.

Chapter 6

Flow-induced Dynamics of an Inverted Elastic Plate Kept at Lee Side of a Cylinder Subjected to Free-stream Flow

We investigate the dynamics of an inverted elastic plate kept at the rear side of a circular cylinder in a uniform steady flow in the open domain at Reynolds number, Re = 100. Re is based on free-stream velocity and the cylinder diameter. In the present chapter, we investigate the effect of an upstream circular cylinder on the dynamics of an inverted elastic plate. The vortex interaction between an inverted plate and a circular cylinder is identified. Inverted flag exhibits a small deformation as well as large deformation which depends on its position and elasticity. The position of the plate affects its deformation significantly, so the gap between the inverted plate and the cylinder is the key design parameter for such flow-induced deformation of the inverted flag as energy harvesters.

6.1 Introduction

Flow-induced deformation of an elastic splitter plate with its leading edge clamped and trailing edge free to vibrate have been extensively investigated through experiment (Zhang et al. (2000); Shelley et al. (2005)), analytically (Kornecki et al. (1976); Watanabe et al. (2002); Theodorsen and Mutchler (1935); Argentina and Mahadevan (2005); Eloy et al. (2008)) and numerically (Zhu and Peskin (2002); Connell and Yue (2007)) in the recent years. In conventional plate configuration, leading is clamped and trailing edge is free, but inverted plate configuration, it is reversed and this plate configuration completely changes the behavior of plate. The FSI studies of conventional flexible structures involving large-scale flow-induced deformation by Kundu et al. (2017), Bhardwaj and Mittal (2012)

and many others showed validations of their respective solvers against the benchmark problem proposed by Turek and Hron (2006). Tian et al. (2010) studied the hydrodynamic interaction between flexible and rigid bodies in tandem arrangement. They showed that motion of flexible filament depend on gap between flexible and rigid bodies in tandem arrangement. Tian et al. (2011) performed simulation to model fish swimming. In their simulation, they kept an elastic filament behind the cylinder and they studied flapping in the Krmn gait and the entrainment regions near a cylinder. The inverted flag was recently introduced by Kim et al. (2013). In low stream velocity, inverted flag maintains straight mode. However, with increase in the stream velocity inverted flag starts flapping with large amplitude. Numerical studies have been done to investigate inverted flag dynamics and flow physics of inverted flag varying bending rigidity and the Reynolds number (Gilmanov et al. (2015); Ryu et al. (2015); Gurugubelli and Jaiman (2015)). Sader et al. (2016) theoretically studied the flapping motion of the inverted flag. They found flapping is function of aspect ratio. They investigated the divergence stability mechanism independent of the added mass parameter. Shoele and Mittal (2016a) computationally investigated on the energy harvesting performance of a piezoelectric inverted flag model by varying an initial inclination angle.

In this chapter, the inverted elastic plate kept behind certain distance from a fixed cylinder at the downstream is considered. The effect of the gap between the circular cylinder and the inverted plate on vortex shedding and its deformation are studied.

6.2 Problem definition

A rectangular computational domain as shown in Fig. 6.1 has been considered in the present computations. Computational model described in in Chapter 2 is employed. The height and width of the domain are $12D$ and $19D$, respectively. The gap between the circular cylinder and the plate has been varied such as $1D_h$, $2D_h$ and $3D_h$. D_h is horizontal distance and D_h is equal to D. The length of the plate has been fixed as $L = 2D$, and the thickness of the plate has been kept as $0.02D$. Here D is the diameter of the cylinder. Free slip boundary conditions are applied to the channel walls and No-slip boundary condition at immersed structure boundary.

At the inlet, uniform velocity is applied. In the present study, the following values are considered for the simulation setup $U = 1$, $D = 1$, $Re = 100$, $E = 1.4 \times 10^3$, $\rho_s = 10$. Here, U, D, Re, E, ρ_s are uniform velocity of the fluid at inlet, diameter of the cylinder, Reynolds number based on cylinder diameter and uniform flow at the inlet, Young's modulus and structure to fluid density ratio, respectively. The Poisson's ratio is taken as 0.4 in the structural solver.

The objectives of the present chapter are as follows:

- To investigate the effect of the gap between the circular cylinder and an inverted elastic plate on vortex shedding and find critical distance between the circular cylinder and the inverted elastic plate to obtain the maximum plate deformation.
- To study the effect of mass and Young's modulus of a flexible inverted plate keeping the fixed gap between the circular cylinder and inverted plate on the plate dynamics.

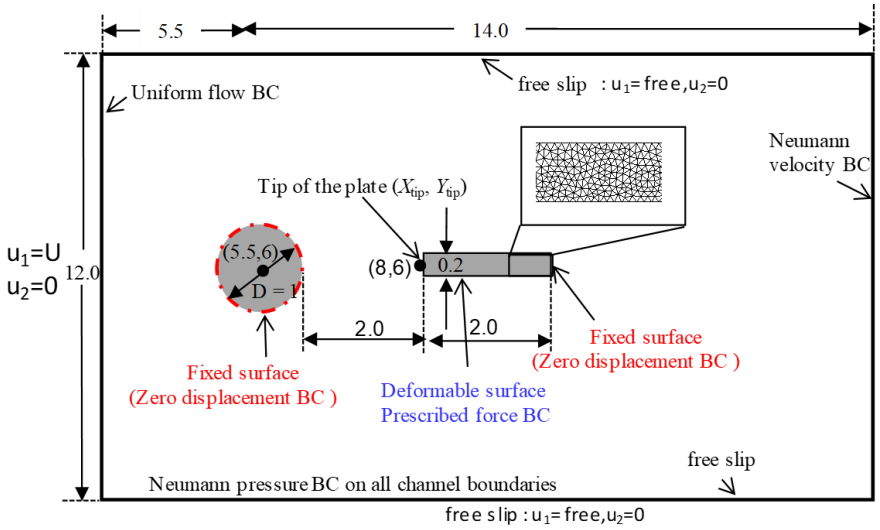

Figure 6.1: Schematic of the computational domain with boundary conditions (BC).

6.3 Results and discussion

6.3.1 Effect of gap between the cylinder and inverted elastic plate

The dynamics and deformation of the inverted elastic plate are related to vorticity structure around the plate. First, we study the dynamics of the single inverted elastic plate in uniform flow in open domain. Tip of the plate (Y_{tip}) displacement and vorticity field are shown in Fig. 6.2. single inverted elastic plate deforms one direction and makes an angle. The plate is nearly perpendicular to u-velocity. It does not regain its original position shown in Fig. 6.2 (shown at the bottom) as plate restoring force is lower than fluid X-direction force. Fig. 6.2 (top figure) shows the Y_{tip} and X_{tip} displacement of the inverted elastic plate. Y_{tip} and X_{tip} displacement are very small and alternating vortex shedding at steady state is observed. The inverted elastic plate dynamics has changed when a circular cylinder is present in front of the inverted plate and a large plate displacement is observed. The plate displacement is a function of the gap between the circular cylinder and the inverted plate. To study the effect of gap on the plate dynamics, three different cases are considered. Three different distances between the cylinder and the inverted plate

such as $1D_h$, $2D_h$ and $3D_h$ are considered to investigate the effect of the gap on vortex shedding and the plate deformation. Three distinct plate flapping have been observed: 1) inverted limit cycle oscillation for gap $1D_h$, 2) chaotic-flapping for the gap $2D_h$ and 3) deformed flapping for the gap $3D_h$. Vorticity contour and Y_{tip} plate displacement are shown in Fig. (6.2- 6.6).

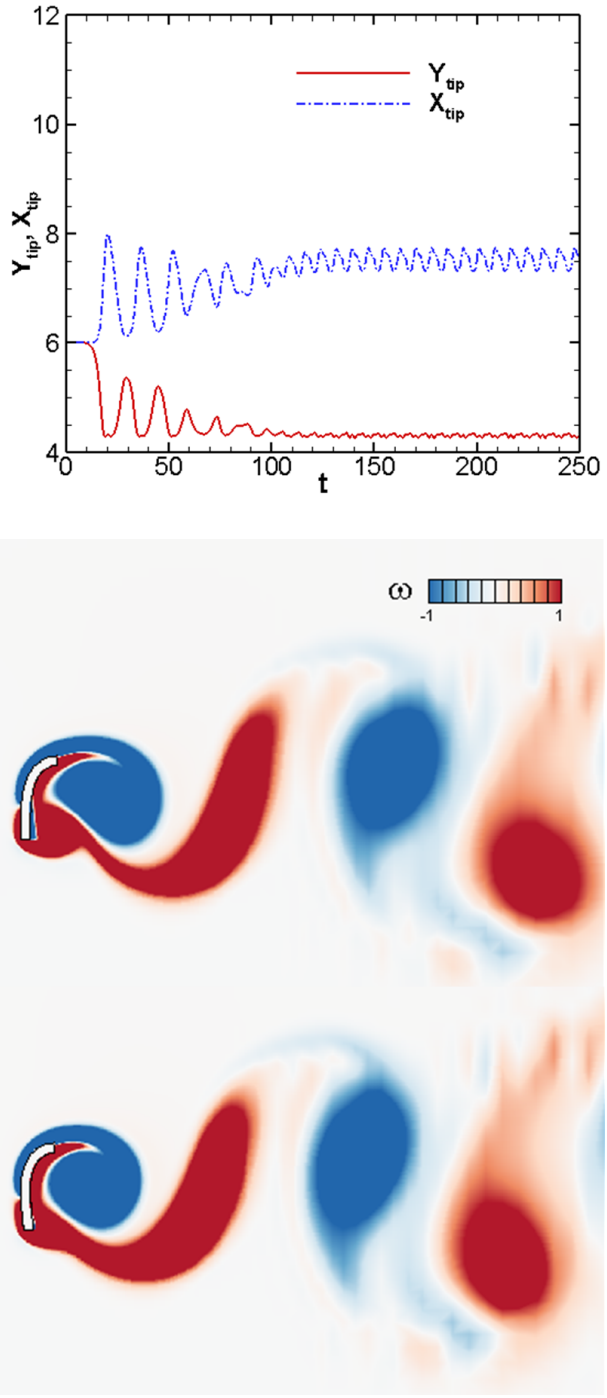

Figure 6.2: Y_{tip} displacement of an inverted elastic plate in the top row. Alternating vortex shedding is shown at middle and bottom row for two different time instances at steady state.

Fig. 6.3 shows the vorticity contour and the plate deformation for the $1D_h$ distance

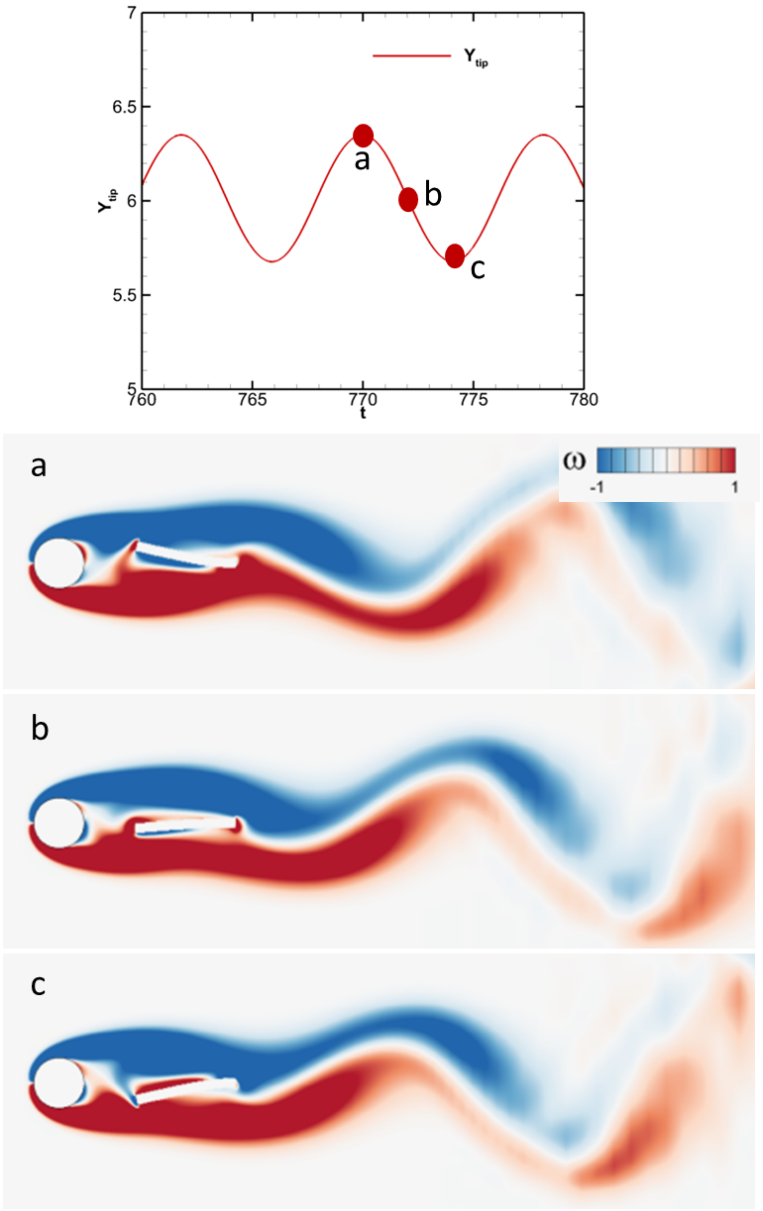

Figure 6.3: Y_{tip} displacement of an inverted elastic plate in the top row. Vorticity contour at three different positions of Y_{tip} of inverted plate. (a) vorticity contour at the maximum tip position (b) middle vorticity contour at the central tip position (c) vorticity contour at minimum tip position. Note that the distance between circular cylinder and inverted plate is $1D_h$.

between the cylinder and the inverted plate for flapping state. Fig. 6.3 (bottom three row) shows a thick shear layers over the plate. Small shear layer instability is observed. The inverted elastic plate acts like splitter plate which separates two shear layer. Vortex is shedding from the clamped end of the plate.

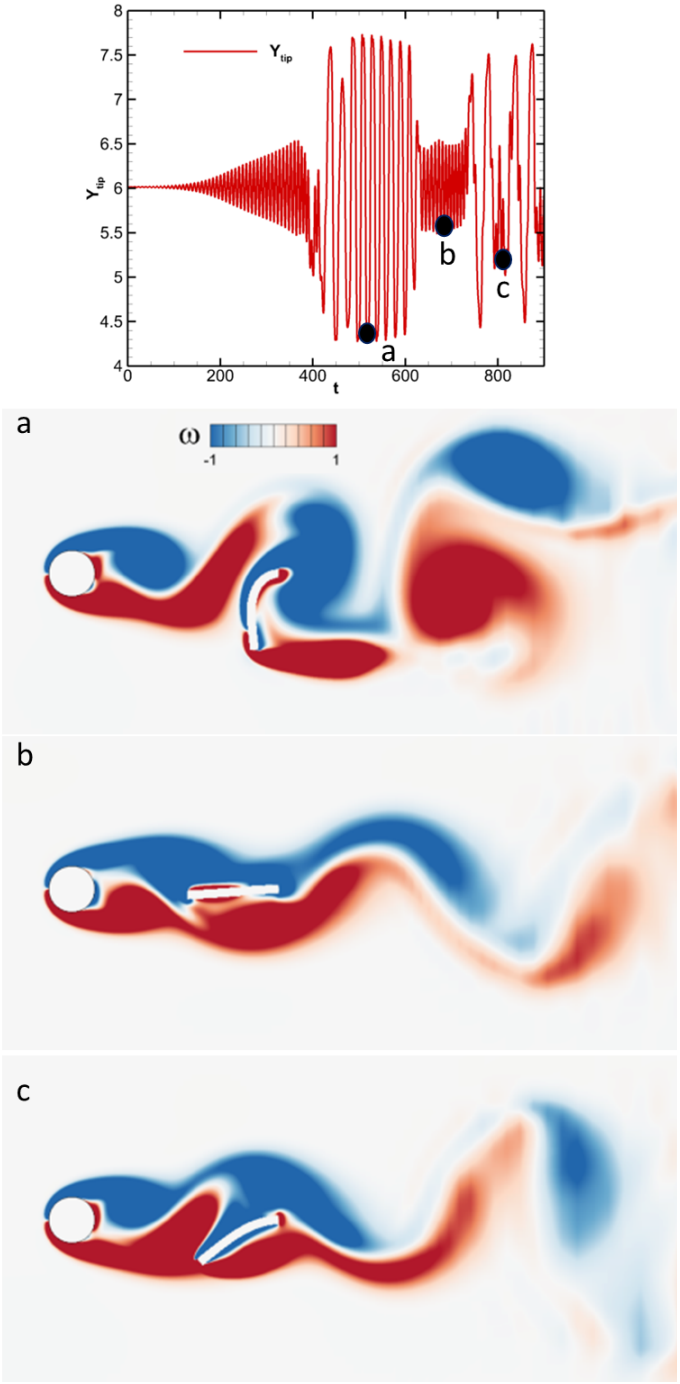

Figure 6.4: Y_{tip} displacement of an inverted elastic plate in the top row. Vorticity contour at three different positions of Y_{tip} of inverted plate. (a) vorticity contour at point(a) (b) middle vorticity contour at the central tip position (point (b)), (c) vorticity contour at point (c). Note that the distance between circular cylinder and inverted plate is $2D$.

We also plot time history of Y_{tip} displacement of an inverted elastic plate at point c of Fig. 6.4 for better understanding plate dynamics of inverted elastic plate. Fig. 6.5 shows that Time history of Y_{tip} displacement of an inverted elastic plate in the top row. Vorticity contour and positions of Y_{tip} of the inverted plate at different time instances (a-h). It is

observed that Time history of Y_{tip} displacement of an inverted elastic plate is dynamically chaos from Fig. 6.5 (top). Vortex shedding behind the plate looks regular, but it depends on plate position. Plate position depends on the timing of vortex shedding coming from the circular cylinder. Fig. 6.5 a shows maximum displacement of the plate. Fig.6 a-h shows that vortex shedding coming from the cylinder influences the plate deformation.

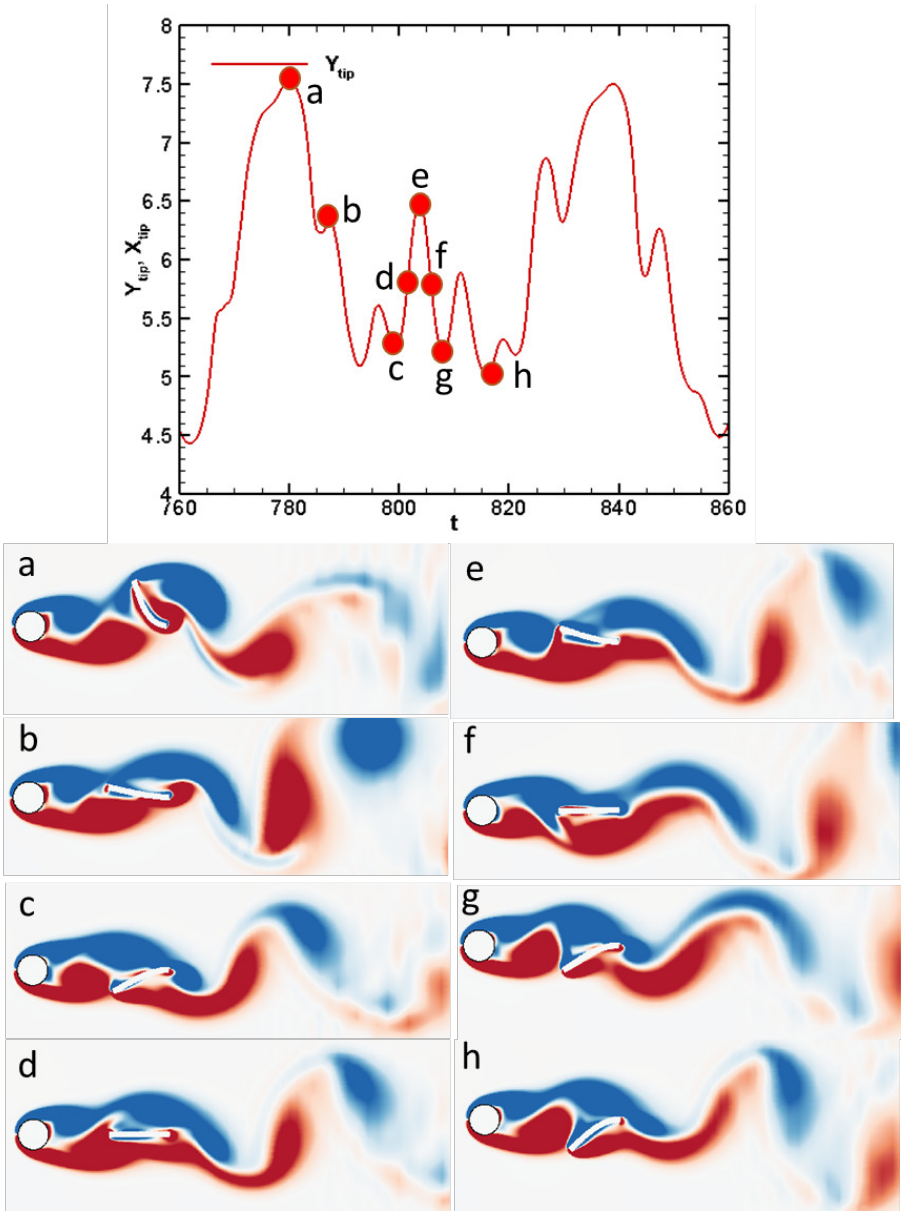

Figure 6.5: Time history of Y_{tip} displacement of an inverted elastic plate in the top row. Vorticity contour and positions of Y_{tip} of inverted plate at different time instances (a-h) Note that the distance between circular cylinder and inverted plate is $2D_h$.

Fig. 6.3 (top row) shows self sustained periodic oscillation of the inverted plate. The plate vibrates with one single dimensionless frequency of 0.128 and the plate amplitude is $0.338D$. The plate vibrates within cylinder diameter. For a cylinder without a downstream plate, one can expect vortex shedding eventually in the form of a natural

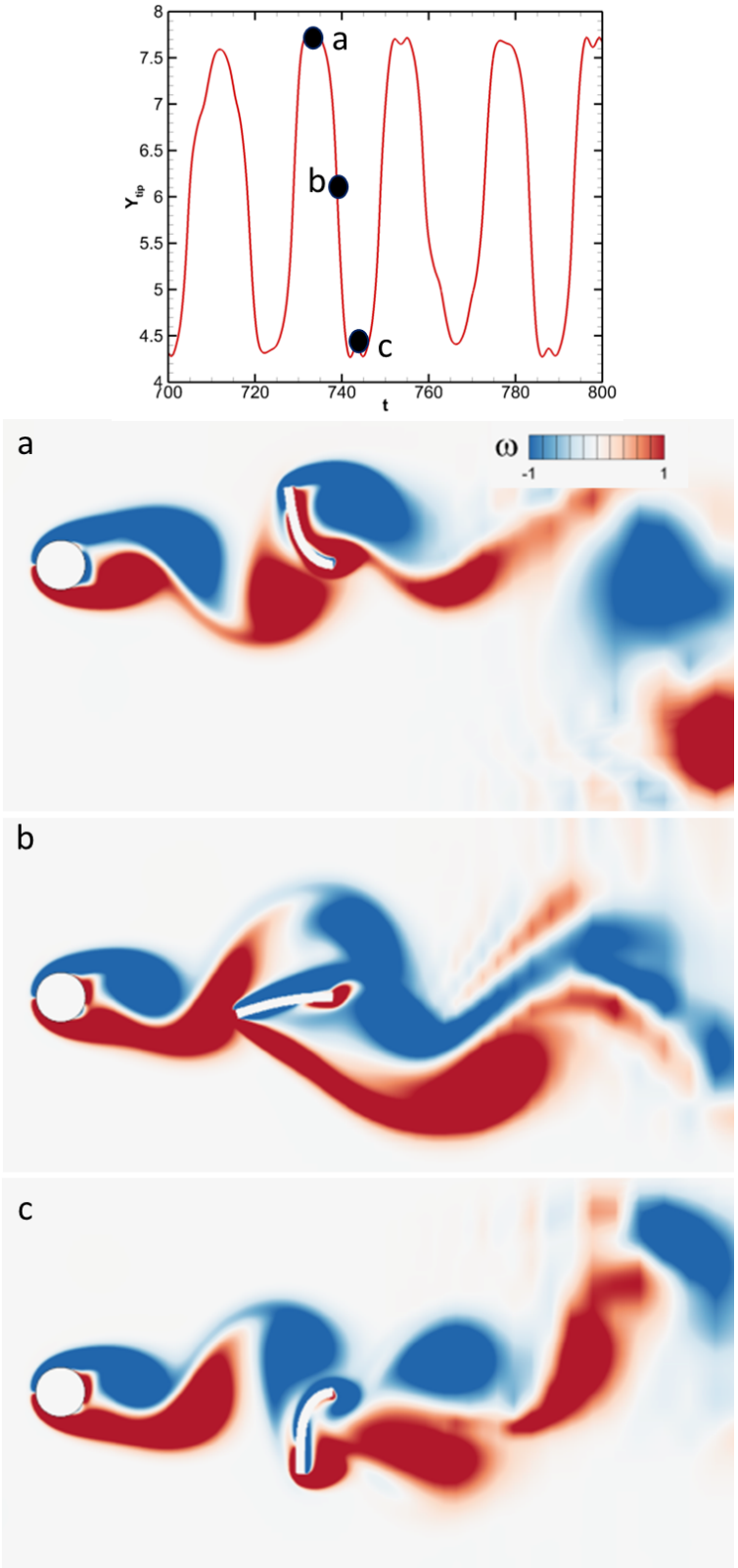

Figure 6.6: Y_{tip} displacement of an inverted elastic plate in the top row. Vorticity contour at three different positions of Y_{tip} of inverted plate. (a) vorticity contour at the maximum tip position (b) middle vorticity contour at the central tip position (c) vorticity contour at minimum tip position. Note that the distance between circular cylinder and inverted plate is $3D_h$.

von-Kármán vortex street at Reynolds number, Re =100. In this case, wavy wake structure is observed at the tailing edge of the plate. Fig. 6.4 shows the vorticity contour and the plate deformation for the $2D_h$ distance between the circular cylinder. Chaotic deflected-flapping state of inverted plate is observed in Fig. 6.4. The plate vibrates with multiple dimensionless frequencies. The plate amplitude depends on vortex shedding from circular cylinder. The instability in the shear layer is not completely taken place because of gap. As a result, The inverted plate vibrates with different amplitude. The vortices coming from cylinder shed in the gap which subsequently triggers the vibration of the plate. An alternating vortex shedding is taking place from the cylinder. When vortices shed at the tip of the plate, plate deformation occurs. Plate does not get sufficient time to deform, alternate vortices coming from opposite side as a result chaotic deformation happens. Fig. 6.6 shows the vorticity contour and the plate deformation for the $3D_h$ distance between cylinder and the inverted plate for largely deformed-flapping state. The plate vibrates with large amplitude. The instability in the shear layer is completely taken place because of gap. Shedding vortex from circular cylinder fall on the tip of the plate which gives fluid force to the plate. As a result, large plate deformation is observed. Irregular and chaotic vortex shedding observed behind the inverted plate due to the interaction of inverted plate deformation. The plate vibrates with multiple frequencies, and the maximum plate amplitude is $1.73D_h$ (see Fig. 6.6).

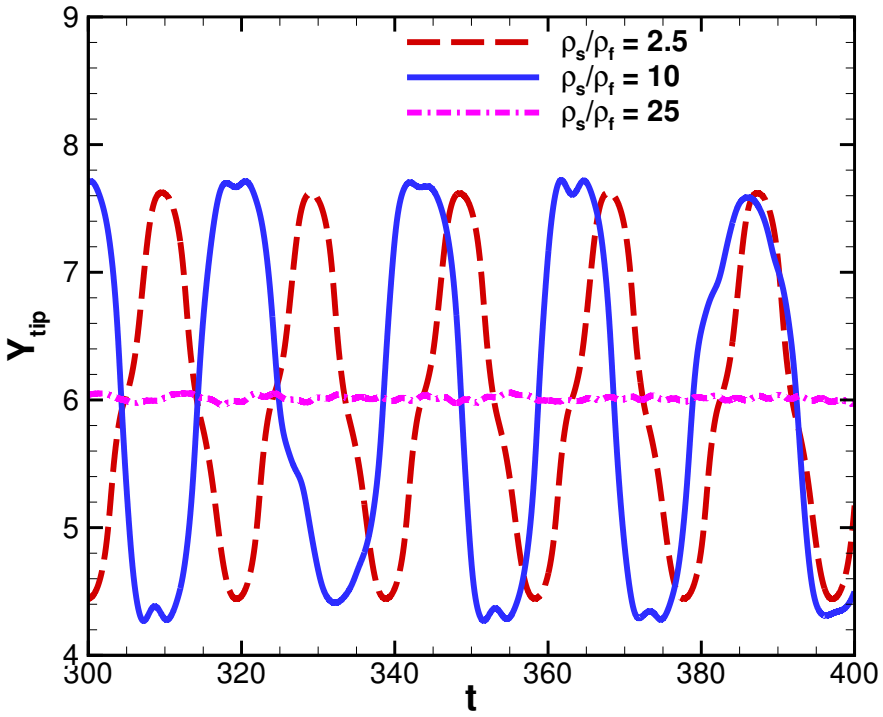

Figure 6.7: Effect of density ratio on Y_{tip} displacement of an inverted plate behind the cylinder. The distance between the cylinder and the inverted plate is $G = 3.0D_h$

6.3.2 Effect of structure density

Fig. 6.7 shows the effect of density ratio on the Y_{tip} of the inverted plate. Three different mass ratio are considered for this study. The gap between the circular cylinder and plate is fixed which is $3D$. At higher density ratio ($\rho_s = 25$), the plate displacement is negligible. At density ratio (ρ_s = 10 and 2.5), plate deformation is lager but at low density ratio, plate reaches steady state quickly. Frequency of the plate displacement is nearly same but amplitude is slightly small. There is no significant difference of plate displacement for ρ_s = 10 and 2.5.

6.3.3 Effect of Young's modulus

In this section, the effect of the structural Young's modulus on the flow-induced deformation of the inverted elastic plate is examined (see Fig. 6.8).

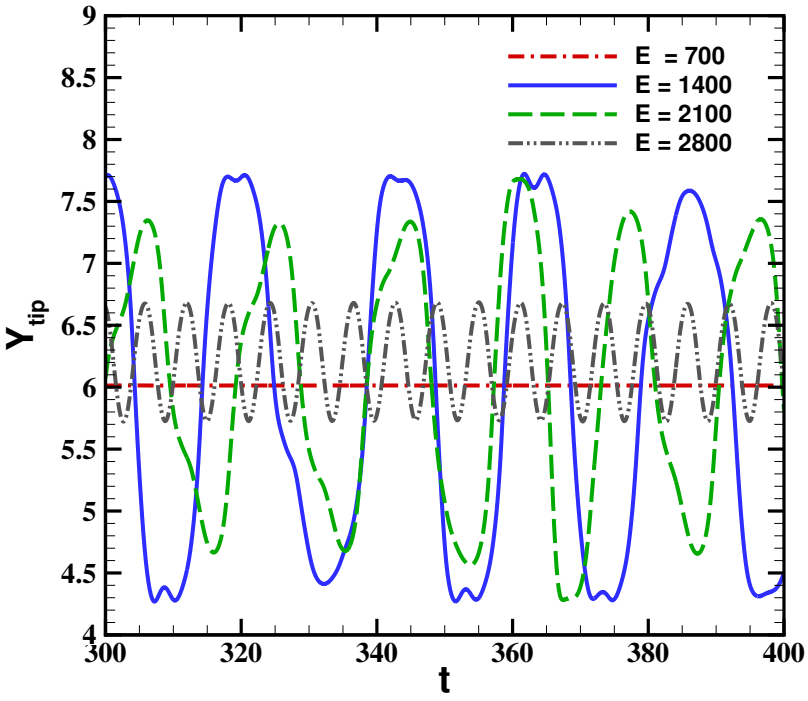

Figure 6.8: Effect of structural Young's Modulus on the Y_{tip} displacement of an inverted plate behind the cylinder. The distance between the cylinder and the inverted plate is $G = 3.0D_h$

For this purpose, the different structural Young's modulus are considered keeping ρ_s = 10 and other parameter constant. All simulations are performed in the same computational domain. For investigating the influence of the plate Young's modulus, four different values of Young's modulus, ranging from $E = 700$ to $E = 2800$ are chosen in the present

study. From the simulations, it is noticed that at Young's modulus $E = 1400$, large plate amplitude deformation is observed. The plate amplitude decreases with increase E. At low Young's modulus, the plate amplitude is low.

6.4 Closure

A FSI system consisting of a rigid circular cylinder and an inverted elastic plate placed with a gap in the downstream has been investigated numerically by using an in-house FSI solver based on sharp-interface immersed boundary method. The flow-induced deformation of the inverted elastic plate kept behind circular cylinder is our interest of study regarding the prospect of energy harvesting. Numerically, a significant increase in the amplitude of the plate oscillations has been observed at the gap of $3D_h$. The role played by the gap in this study implies that a proper choice of the gap is mandatory to control the maximum plate deformation for efficient energy harvesting. The present chapter provide understanding of interaction of rigid cylinder and inverted elastic plate. Inverted elastic plate vibrates with larger amplitude at at the gap of $3D_h$ between rigid cylinder and inverted elastic plate. Large amplitude of inverted elastic plate could be useful to the design of piezoelectric beam for energy harvesting and thermal augmentation applications.

Chapter 7

Thermal Augmentation by Flow-induced Deformation of elastic plates Subjected to Pulsatile Laminar Channel Flow

We present heat transfer enhancement by flow-induced deformation of two thin parallel elastic plates immersed in the rectangular heated channel. We employ an in-house, sharp-interface Immersed Boundary Method (IBM) based flow and heat transfer, solver. The solver is coupled with a finite element method based structural solver using an implicit coupling. In the present chapter, the large flow-induced deformation of two thin parallel insulated elastic plate in a channel with pulsating cross inflow is studied. The distance between the two elastic plates vary with position to achieve optimum heat transfer from the heated channel walls to the fluid. The interaction between twin elastic plate, flow field, and temperature field are discussed. The interaction of wake vortices between twin plates increases the mixing of the fluid in the channel and thereby the convective heat transfer from the heated channel walls to the fluid, due to a reduction in thermal boundary layer thickness. The numerical results show nearly 38% improvement of heat transfer efficiency for twin plates in rectangular channel as compare to the simple rectangular channel.

7.1 Introduction

Fluid-structure interaction can be utilized for heat transfer enhancement. The heat transfer enhancement techniques can be classified into two categories, namely: passive and active.A brief introduction to recent developments in these categories is given in Bergles (2011). In the context of passive techniques, heat transfer enhancement was demonstrated via utilizing the flow past a bluff body in a channel with different geometries of shapes

such as square cylinder (Dunne and Rannacher (2006)), wings, etc. and/or by changes in the channel geometry (Beeby et al. (2006),Fiebig et al. (1989)), in their numerical experiments, employed delta wings as vortex generators to increase heat transfer in a rectangular channel flow. Several authors have demonstrated heat transfer enhancing capabilities of different bluff bodies, like a rectangular cylinder, inclined square cylinder, and triangular cylinder, etc., inside the channel as vortex generators. Alternatively, Wang and Chen (2002) used sinusoidal wavy channel geometry to increase heat transfer. In the active techniques, The bluff bodies are oscillated to alter flow characteristics and improve the heat transfer. Increasing the strength of vortices has a positive effect on heat transfer. Transverse oscillations of a circular cylinder placed inside the channel result in enhanced heat transfer as compared to the stationary cylinder. In all studies, the heat transfer enhancement is accompanied by a cost in terms of more pressure drop. Previous numerical studies showed that structure was set in motion by an external source and motion of the flexible structures could be utilized as a heat transfer enhancement technique. For instance, Fu and Yang (2001) showed that the swinging fins in a heated channel enhance heat transfer which scales with the fin amplitude. Similarly, oscillating fins improves heat transfer from a heat sink due to enhanced convective mixing (Yang (2003)). Very few numerical studies which considered flow-induced deformation of the structure were reported. For instance, Khanafer et al. (2010) simulated a heated flexible cantilever attached to a square cylinder in a channel. However, the authors did not investigate thermal augmentation due to the motion of the cantilever. Habchi et al. (2013) studied twin elastic thin plates mounted in cross-flow configuration at a distance and subjected to the pulsatile flow. They reported that the plates oscillate in opposite-phase and in-phase for larger and smaller value of Young's modulus of the plate, respectively. Very recently, Shi et al. (2014) and Soti et al. (2015) demonstrated heat transfer enhancement via large-scale flow-induced deformation in the FSI benchmarks proposed by Turek and Hron (2006). These investigations, however, considered the flexible structure along the flow and did not consider the cross-flow configuration of the mounting structure. It is useful to examine cross-flow configuration of the mounting elastic structure to augment heat transfer in a channel. Soti et al. (2015) also demonstrated that the vortices generated due to the motion of the flexible plate drive higher sources of vorticity generated on the channel walls out into the high velocity regions, which helps in the mixing of the fluid and therby enhancing the heat transfer. Joshi et al. (2015) performed simulation of thin flexible plate involving large-scale flow-induced deformation in a rectangular channel. They found that thin flexible plate enhanced heat transfer at the channel walls by reducing thermal boundary layer thickness.

In this chapter, We employ a state-of-the-art FSI solver (section 7.2) to investigate thermal augmentation by using twin elastic plates mounted in a cross-channel flow. The

effect of many parameters such as material properties, flow parameters and geometrical configuration and convective heat transfer was not studied. The objectives of the present chapter is to investigate effect of gap between twin elastic plate on thermal augmentation in a channel with pulsating cross inflow. The interaction between twin elastic plates, flow field, and heat transfer enhancement are quantified.

7.2 Computational model

The detailed description of the FSI solver is given in Chapter 2. The convective heat transfer inside the fluid can be expressed by the following dimensionless energy equation:

$$\frac{\partial T}{\partial t} + v_i \frac{\partial T}{\partial x_i} = \frac{1}{Pe} \frac{\partial^2 T}{\partial x_j^2}, \tag{7.1}$$

where Pe is Peclet number and T is dimensionless temperature, defined in terms of dimensional temperature T^*, reference wall temperature T_w^* and reference temperature T_{ref}^*, as follows,

$$T = \frac{T^* - T_{ref}^*}{T_w^* - T_{ref}^*}, \tag{7.2}$$

T_{ref}^* is taken as inlet temperature of the fluid in all simulations unless specified otherwise. The heat transfer augmentation is characterized using instantaneous Nusselt numbers at the channel wall, which is defined as follows (Bejan (2004)):

$$Nu(x,t) = \frac{4H}{T_m - 1} \left. \frac{\partial T}{\partial y} \right|_{wall}, \tag{7.3}$$

where $4H$ is the dimensionless hydraulic diameter of the channel.

The heat transfer enhancement is quantified using the instantaneous Nusselt number given in eq. 7.3 with the definition of bulk mean temperature modified to (Guo and Sung, 1997)

$$T_m(x,t) = \frac{\int_0^H |u| T dy}{\int_0^H |u| dy}, \tag{7.4}$$

where u stands for dimensionless axial velocity component. Time-averaged Nusselt number (Nu_{avg}) over one period of oscillation, τ, for time-periodic flow is expressed as:

$$Nu_{avg}(x) = \frac{1}{\tau} \int_t^{t+\tau} Nu(x,t) dt. \tag{7.5}$$

Time- and space-averaged Nusselt number (Nu_{mean}) over surface area A is defined as:

$$Nu_{mean} = \frac{1}{A}\int\int_{A} Nu_{avg}(x)dA. \tag{7.6}$$

We define change of efficiency (η_h) for the heat transfer, defined as follows (Yang, 2003),

$$\eta_h = \frac{Nu_{mean} - Nu_{mean,\text{ channel}}}{Nu_{mean,\text{ channel}}} \times 100 \tag{7.7}$$

7.3 Problem definition

We consider twin thin parallel elastic plates immersed in a 2-D incompressible, laminar flow in the rectangular channel. The plates are fixed to the bottom wall, and the height and width of the plate are H and $0.1H$, respectively (Fig. 7.1A). The distance between the twin plates is $2H$. The rectangular channel height and width are $4H$ and $20H$. First elastic plate is placed in the rectangular channel at $4H$ distance from the inlet. At the top and bottom of the domain, no-slip boundary conditions are applied. No-slip is applied at the immersed structure boundary. Fully developed flow BC is applied for the velocity at the outlet. At the inlet, the fully developed velocity is considered which is given by:

$$u = 4U\Big(\frac{y}{4H}\Big)\Big(1 - \frac{y}{4H}\Big)\Big(\frac{1 - cos(2\pi ft)}{2}\Big) \tag{7.8}$$

where U is the maximum inlet velocity at the center of the channel, $4H$ is channel width, and f is inflow pulsation frequency. Zero Neumann boundary condition is applied for pressure at all boundaries.

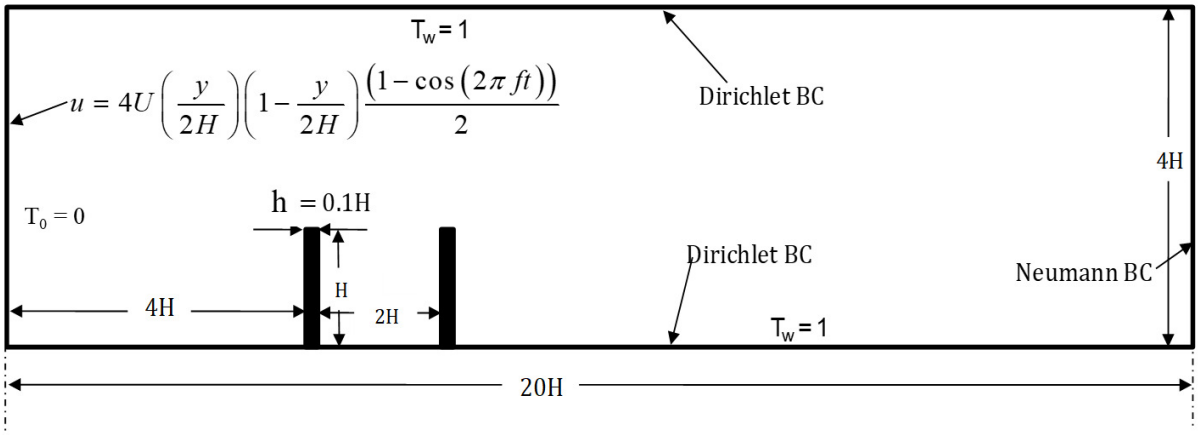

Figure 7.1: Schematic of computational domain with boundary conditions (BC) considered in the present chapter of two thin parallel elastic plate mounted in rectangular channel

The thermal boundary conditions are shown in Fig. 7.1. The temperature is considered

as uniform at the inlet. $T_0 = 0$, is considered at the channel inlet. $T_w = 1$ is prescribed at channel wall. The fluid-structure interface is insulated, and the channel walls are at constant temperature ($T_w = 1$). At channel outlet, zero Neumann temperature boundary condition is applied. The Reynolds number (based on maximum pulsation velocity U and plate height H) is 100. The dimensionless Young's modulus, structure-fluid density ratio, Poisson ratio, pulsatile frequency and Prandtl number are 1.0×10^3, 10, 0.45, 0.1 and 1 respectively.

7.4 Results and discussion

We investigate thermal augmentation by using twin elastic plates mounted in a cross-channel flow. Here we consider pulsatile inflow instead of uniform flow. Plate deforms downside of channel flow and cannot reach the original position, as shown in Fig. 7.2, for uniform flow, but plate deforms both sides for pulsatile inflow. In our studies, we are investigating flow-induced deformation, so all investigation based on flow-induced deformation. It is a passive technique to enhance heat transfer by mixing fluid in the channel. No external energy is required to move the plate. Forced oscillation for plate movement requires external energy. So, we did not consider any forced oscillation to improve heat transfer via fluid mixing.

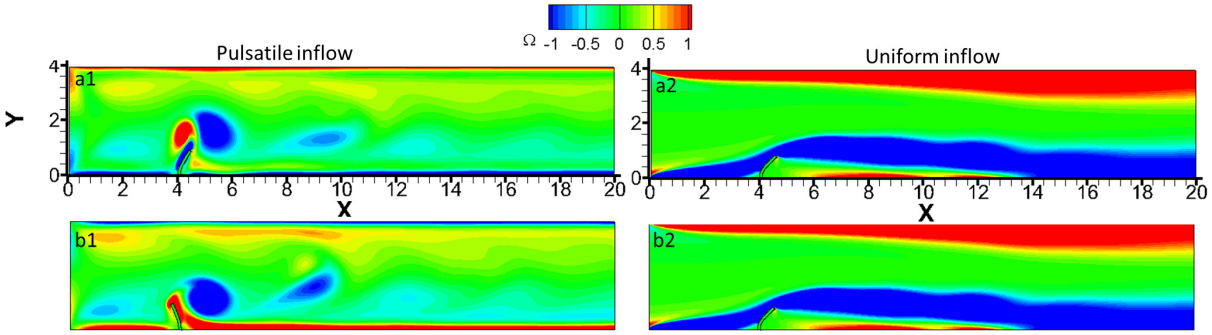

Figure 7.2: Vorticity contour at two different time instance for elastic plate in a channel with (a) pulsating cross inflow (left side (Fig. a1 and b1)) (b) without pulsating flow (right side (Fig. a2 and b2)).

To demonstrate heat transfer enhancement via fluid-structure interaction, first, we show X_{tip} and Y_{tip} position of the plate with time for twin plates in a rectangular channel. The distance between two plates is $2H$. Second, we plot vorticity contours and temperature contours at three different time instances. Third, we compare instantaneous Nusselt number at L = $5.16H$ and time-averaged Nusselt number with the channel and single plate. Finally, effect of distance between two plates on heat transfer is discussed. Fig. 7.3A shows time-varying X_{tip} signal with time for twin plates. The second plate oscillates with higher amplitude than the first plate by 29 %. Both signals show self-sustained

periodic oscillation of the plates. The dominant frequency of both signals is the same flow pulsation frequency. Fig. 7.4B shows the Y_{tip} signal with time for twin plate. We plot the phase-plot of the two plate and we observed that second plate Y_{tip} displacement is higher than the first plate. Fig. 7.4 shows vorticity contours (left column) and temperature contours (right column) at three different time instances shown in Fig. 7.4A by vertical line as well as three different positions. If the plates move in the backward X-direction, strong negative vorticity generates and at the center position, strong positive vorticity is observed behind the first elastic plates. For forward movement of the plates, positive vorticity arises at the top of the second plate. The fluid mixing is more for the forward movement of the plates as the thermal boundary thickness is lesser as compared to only channel case (see temperature contours Fig. 7.4B).

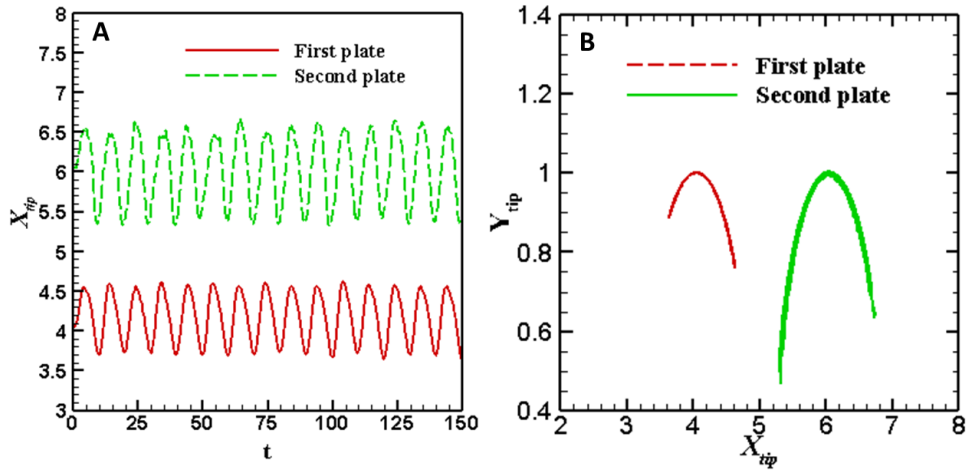

Figure 7.3: X_{tip} and Y_{tip} position of plate with time for twin plates at a rectangular channel. The distance between two plate is $2H$

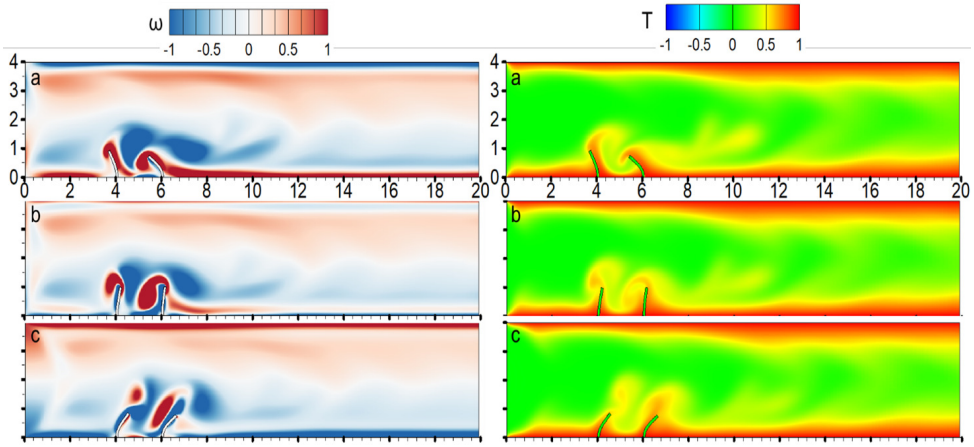

Figure 7.4: (A) Vorticity contours and (B) Temperature contours at three different time instances (a, b and c) shown in Fig. 7.3. The distance between two plates is $2H$

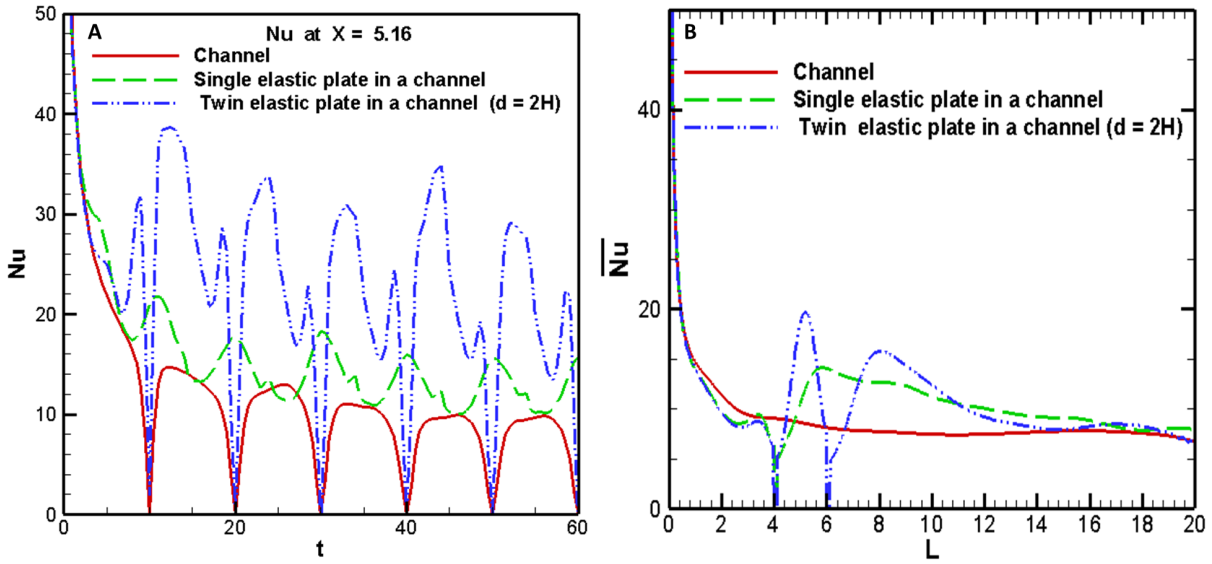

Figure 7.5: (A) Instantaneous Nusselt number at L = 5.16H (B) Time-averaged Nusselt number for three different cases.

Fig. 7.5A shows time varying Nusselt number (Nu) at L = 5.16, mid position of two plates and is compared with two different cases, only channel and channel with a single plate. Nu is largest for twin elastic plates case than the only channel and channel with a single plate. Fig. 7.5B shows time averaged Nusselt number ($\overline{Nu}$) for three cases. It is observed that $\overline{Nu}$ is highest at two specific location (L = 5 and L = 8) for twin plates.

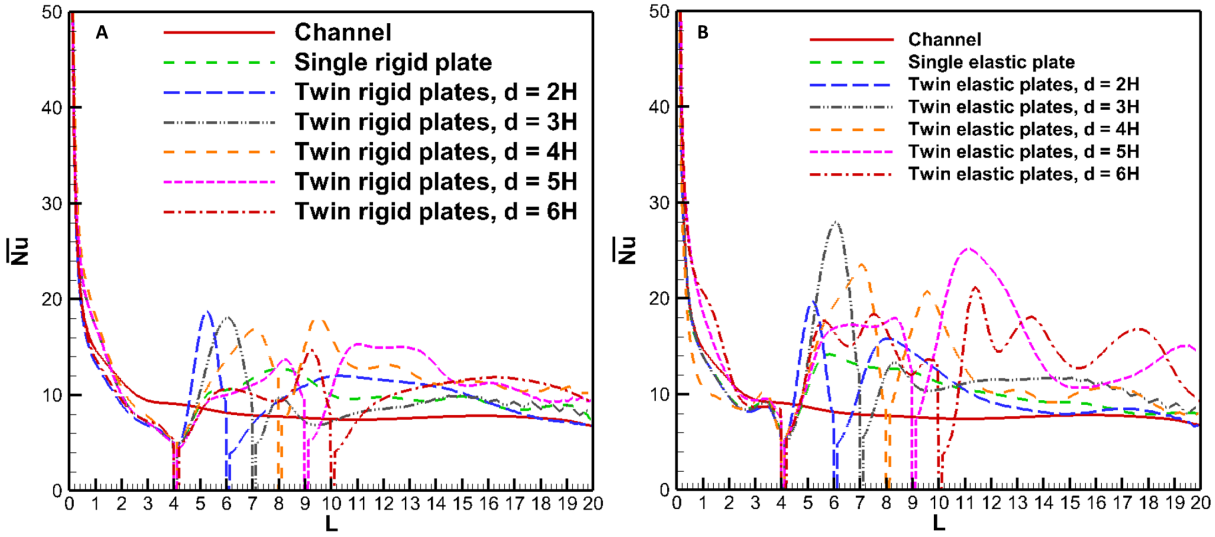

Figure 7.6: Time averaged Nusselt number ($\overline{Nu}$) for (A)rigid plate and(B) elastic plate. Note that d denotes distance between twin elastic plates.

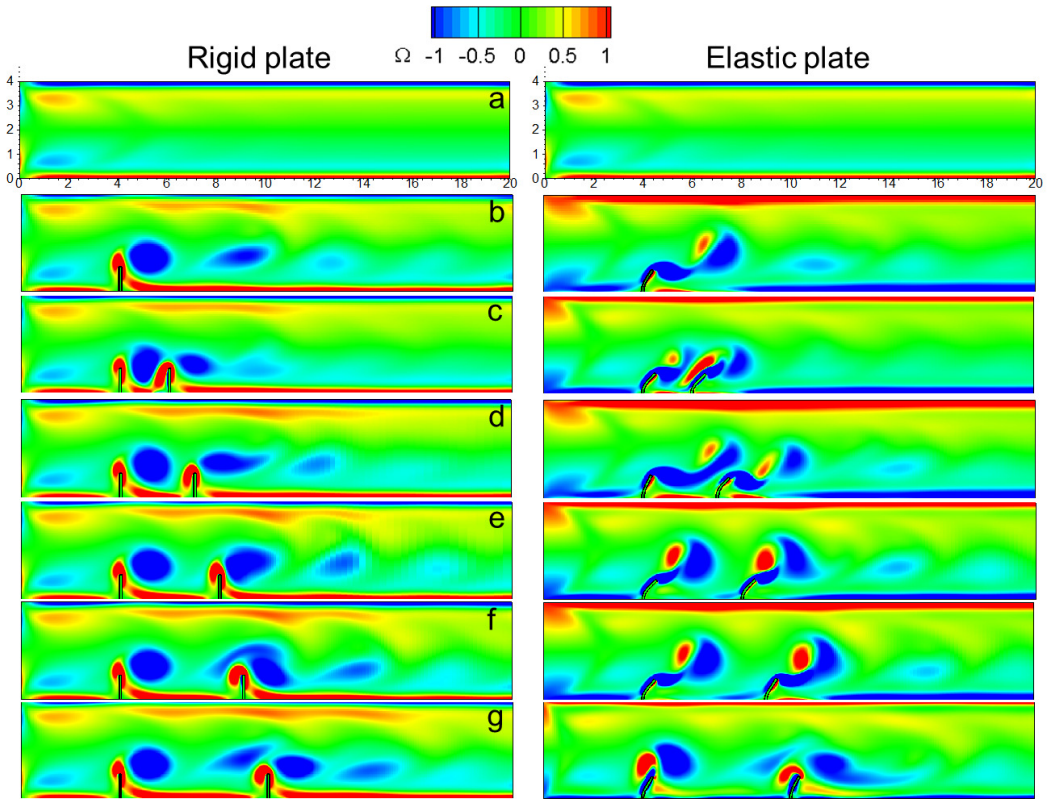

Figure 7.7: Comparison of vorticity contours for different cases: (a) rectangular channel, (b) single plate (c) twin plates, $d = H$ (d) twin plates, $d = 2H$ (e) twin plates, $d = 3H$ (f) twin plates, $d = 4H$ (g) twin plates, $d = 5H$. Note that d denotes distance between twin elastic plates.

Fig. 7.6A and B show $\overline{Nu}$ for rigid plate and elastic plate in rectangular channel. We plot more cases of distance between the two plates. For rigid plate case, $\overline{Nu}$ is nearly 20 when distance between two plates are $2H$. Peak of $\overline{Nu}$ decreases with distance of twin plates. Fig. 7.6B shows the $\overline{Nu}$ for elastic plate in rectangular channel. Peak of $\overline{Nu}$ is nearly 28 when distance between two plates is $3H$ and peak of $\overline{Nu}$ decreases with distance of twin plates. A second peak is exists in down stream for d = $5H$. Fig. 7.7 shows the vorticity contours for the rigid (left) and elastic plates (right). Five different cases are considered for twin plate both rigid as well as soft plates. The vorticity generated at the first plate interacts with second plate top edge for rigid plate cases shown in Fig. 7.7(c-g). For the case of the elastic plate in a channel, vorticity generated at the first plate and moving back and forth due to pulsatile flow. The isotherms for all configurations at steady state are plotted in Fig. 7.8, respectively. We note that the thermal boundary layer thickness of the channel wall is larger in the channel and single plate case. The thermal boundary layer thickness reduces as the strength of the vortices increases for twin plate case. It is observed from Fig. 7.8 (fifth rows) that the thermal boundary layer thickness is lowest because of the strong interaction of vortices. The interaction of wake vortices between twin plates increases the mixing of the fluid in the channel. The motion of the

plates improve convective mixing and heat transfer in bulk and near the walls by reducing thermal boundary layer thickness and it also helps to improving Nusselt number at the channel walls.

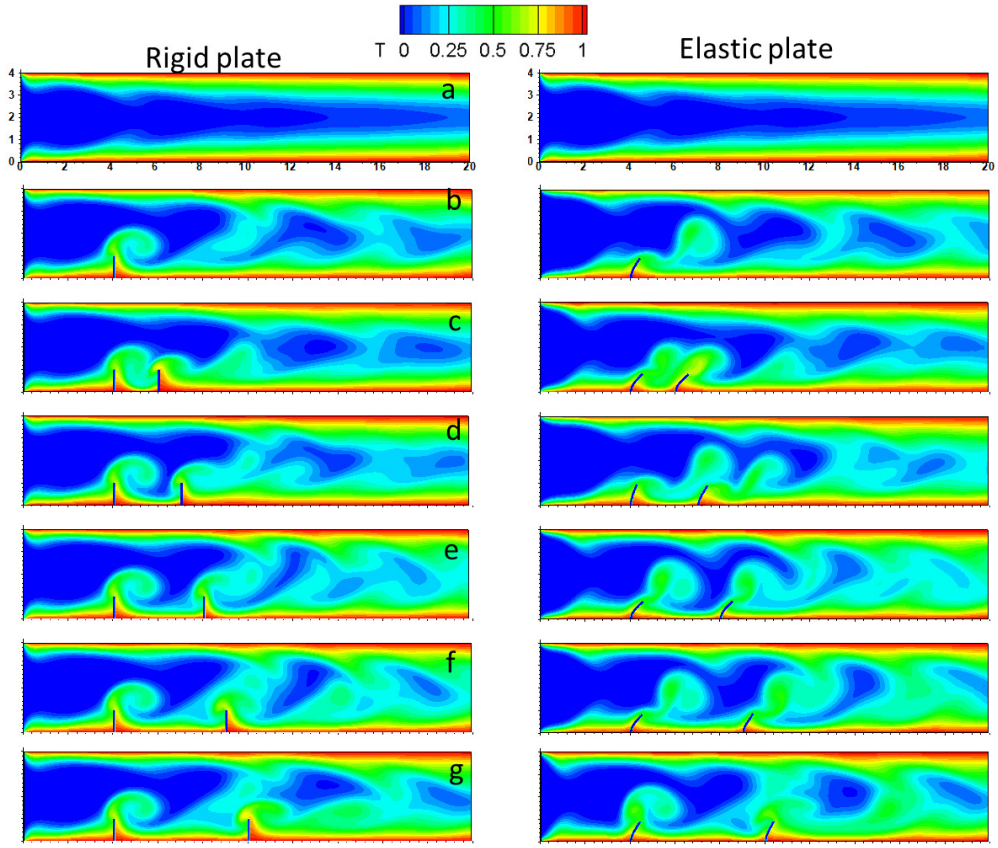

Figure 7.8: Comparison of temperature contours for for different cases: (a) rectangular channel, (b) single plate (c) twin plates, $d = H$ (d) twin plates, $d = 2H$ (e) twin plates, $d = 3H$ (f) twin plates, $d = 4H$ (g) twin plates, $d = 5H$. Note that d denotes distance between twin elastic plates.

We also calculate mean Nusselt number (Nu_{mean}) for the above cases. We observe that the Nu_{mean} is maximum for both rigid and elastic plate in a channel when the distance between plates is $4H$. We also calculate percent change of efficiency which is in Table 7.1 and Table 7.2 for rigid plates as well as elastic plates. We note that Nu_{mean} and percent change of efficiency are highest when the distance between plates is $4H$.

Table 7.1: Time-averaged Nusselt number (Nu_{mean}) and % change of efficiency for elastic plate

Configurations	Distance Between twin plates	Nu_{mean}	% change of efficiency
Channel	-	9.36	-
Single Plate	-	10.83	13.57%
Twin plate	$1H$	11.26	20.29 %
Twin plate	$2H$	12.68	35.47%
Twin plate	$3H$	11.54	23.29%
Twin plate	$4H$	12.93	38.14%
Twin plate	$5H$	12.81	36.85%
Twin plate	$6H$	12.04	28.63%

Table 7.2: Time-averaged Nusselt number (Nu_{mean}) and % change of efficiency for rigid plate

Configurations	Distance Between twin plates	Nu_{mean}	% change of efficiency
Channel	-	9.36	-
Single Plate	-	10.58	13.03%
Twin plate	$1H$	10.31	10.14
Twin plate	$2H$	10.35	10.57
Twin plate	$3H$	10.26	9.61
Twin plate	$4H$	11.67	24.67
Twin plate	$5H$	11.81	26.17
Twin plate	$6H$	10.65	13.78

7.5 Closure

We have investigated the thermal enhancement at the channel walls for two parallel elastic plates vertically mounted in a rectangular channel subjected to pulsatile inflow with respect to pulsatile channel flow without plate. The interaction of wake vortices between twin plates increases the mixing of the fluid in the channel and thereby the convective heat transfer from the heated channel walls to the fluid, due to a reduction in thermal boundary layer thickness. The distance between two plates effects the heat transfer efficiency. The obtained results for two elastic plates of distance $4H$ gives the maximum mean Nusselt number (Nu_{mean}) and change of efficiency of heat transfer is nearly 38%. Maximum time averaged Nusselt number $\overline{Nu}$ peak is observed at the mid point of twin elastic plates. Highest peak of time averaged Nusselt number $\overline{Nu}$ is noticed for twin elastic plate when the distance between two plates are $5H$.

Chapter 8

Conclusions and future work

8.1 Conclusions

In this thesis, an in-house fluid-structure interaction (FSI) solver has been benchmarked and has been employed for simulating a thin, elastic plate undergoing large-scale deformation in laminar flow. The solver couples a sharp-interface immersed boundary method for the fluid dynamics with a finite-element method to treat the structural dynamics. The two solvers are implicitly (two-way) coupled using a partitioned approach. The benchmarking of the solvers is carried out as follows. We have tested the FSI solver with the benchmark data and validate the flow and structure solvers independently as well as module of large-scale flow-induced deformation. We have qualitatively compared vortices in the wake of pulsatile flow past a circular cylinder in a channel with the published results of Al-Sumaily and Thompson (2013). Quantitatively, the flow solver is validated for predicting the lift and drag coefficients for flow past a circular cylinder under steady flow and pulsatile flow with non-zero mean velocity (Li et al. (2010); Behr et al. (1995)). For the structural solver, deflection of a cantilever beam under uniformly distributed impulse load is compared with the published results of Tian et al. (2010). The FSI solver was validated against an benchmark problem in which a thin elastic splitter plate is attached to (a) a square cylinder, and (b) a circular cylinder and in both the cases, the plate attains self-sustained oscillation. The former was proposed by Turek and Hron (2006) and was validated by Bhardwaj and Mittal (2012) using the in-house solver used in the present thesis. In Ref. Bhardwaj and Mittal (2012), St_p was in excellent agreement while the difference in Y_{tip} was around 11%, as compared to the benchmark data of Turek and Hron (2006). The results in the present thesis show reduction in the error of Y_{tip} to around 1%. Overall, the St_p and Y_{tip} are excellent agreement with published results for both FSI benchmarks.

The effect of the pulsatile inflow on the flow-induced deformation of an elastic plate inside a channel is simulated numerically. In the case of the pulsatile inflow, the plate

experiences strong forcing from vortices that form from the separating shear layers from the cylinder and subsequently advect downstream over the surfaces of the plate. Despite the tendency of the vortices to form and shed symmetrically because of the applied longitudinal forcing, the coupling with the allowable cross-stream oscillation mode of the plate leads to substantially increased cross-stream oscillation amplitude relative to the unforced case in general. The maximum plate displacement is observed when the applied oscillation frequency is twice the natural plate frequency in a particular mode ($St_f \cong 2St_{ni}$), corresponding to the resonant or lock-in case. The mode of the natural frequency depends upon the plate length. For applied frequencies away from this condition, beating is observed due to the superposition of the applied and natural oscillatory signals. The plate deformation response, and drag of the plate and its components, are quantified for forcing flow amplitudes $K \leq 1$, and for forcing frequencies, $St_f \leq 1$. The total drag on the plate is found to be significantly larger relative to the steady inflow, at forcing frequencies equal or larger than lock-in frequency, at a given flow amplitude. For lock-in cases, the plate displacement, total drag, pressure as well as skin friction drag increases with the forcing flow amplitude.

The dynamics of an elastic splitter plate attached to a rigid circular cylinder and is subjected to laminar flow has been studied. In this configuration, the effect of mass ratio (M) and bending stiffness (K_b) are studied at $Re = 100$, where Re is Reynolds number and is based on free-stream velocity and cylinder diameter. We vary M, K_b and U_R in range of [0.143, 20], [0.0008, 0.0435] and [2.562, 30.0], respectively. The plate amplitude and oscillation frequency are found to be a function of M and K_b. We plot time-varying displacement of the tip of the plate, FFT of the displacement signal, phase-plot of the plate displacement and wake structures in order to quantify the results. The largest amplitude of the plate is found to be in the lock-in condition at which the natural frequency of the plate in a given fluid synchronizes itself with the oscillation frequency of the plate. At lock-in, the oscillation frequency is lower than the natural frequency of the plate in a vacuum due to added mass effect. These findings are consistent with those for classical vortex-induced vibration of a rigid cylinder at the low mass ratio. The plate exhibits a strong added mass effect at the lower mass ratio and lower bending stiffness. As M and K_b increases, the oscillation frequency becomes closer to the natural frequency of the plate in a vacuum, showing the diminishing added mass effect. We plot a flapping boundary using the data of simulations on mass ratio-reduced velocity plane, and it is found to be consistent with previous available theories and data.

The role of the plate thickness in determining flapping dynamics of an elastic thin plate is numerically investigated. We vary mass ratio (M), bending stiffness (K_b) and reduced velocity U_R for different cases of plate thickness h at $Re = 100$, where Re is Reynolds number and is based on free-stream velocity and length of the plate. The range

of variation of M, K_b and U_R are [0.05, 1.1], [0.0009, 0.017] and [10, 40.0], respectively. The plate amplitude and oscillation frequency are found to be a function of M, K_b and h. We plot time-varying displacement of the tip of the plate, FFT of the displacement signal, phase-plot of the plate displacement and wake structures in order to quantify the plate flapping dynamics. As a function of M and U_R, two types of flapping are observed: (a) fixed-point stability and (b) limit-cycle flapping. We plot the flapping boundary using the data of simulations on $1/M - U_R$ plane. The plate flapping occurs at a critical U_R and critical M. The plate flapping boundary changes with thickness of the plate because critical U_R and critical M change with the plate thickness. We tested another configuration of a FSI system consisting of a rigid cylinder and a flexible inverted plate placed with a gap in the downstream. A significant increase in the amplitude of the plate oscillations has been observed at a critical gap.

Finally, we have investigated thermal enhancement at the walls of a heated channel subjected to pulsatile inflow and two parallel elastic plates are vertically mounted in this channel. The distance between two plates influences the heat transfer. The interaction between twin elastic plates, flow field, and temperature field as function of distance between the plates are discussed. Numerical simulations show that the time- and space-averaged Nusselt number (Nu_{mean}) is maximum for two elastic plates of a distance $4H$. In this case, we have found nearly 38 % improvement in Nu_{mean} with using twin elastic plates respect to a channel without a bluff body. The maximum time averaged Nusselt number $\overline{Nu}$ peak is observed at the midpoint of twin elastic plates in this case. The interaction of wake vortices between the deforming plates increases the mixing of the fluid in the channel and thereby increase the convective heat transfer from the heated channel walls due to reduction in thermal boundary layer thickness.

The dynamics of an elastic plate under periodic fluid loading is useful for energy harvesting. Energy harvesting depends on plate vibration amplitudes for the piezoelectric plate and its increases with plate vibration amplitudes. When the piezoelectric elastic plate placed in the wake of a bluff body, the maximum voltage from piezoelectric plates has been found at lock-in condition where the periodic vortex shedding frequency of the plate matches with the natural frequency of the plate (Akaydın et al., 2010). Plate oscillates with maximum amplitude at lock-in condition. This condition is most important for energy harvesting and also a design criterion for energy harvesting applications.

The findings of the present thesis provide fundamental insights into the interaction of an elastic plate with laminar flow and useful for several applications such as designing energy-harvesting devices, cooling microelectronics by thin flexible plates and cardiovascular flows.

8.2 Future work

The following research directions could be investigated in future:

- The in-house FSI solver can be further developed to tackle FSI of a thin elastic plate together with VIV of the cylinder.
- The pitching and heaving of flapping plates for propulsion applications could be explored.
- Flow-induced dynamics of an inverted elastic plate kept at the rear side of a cylinder can be studied numerically to achieve heat transfer augmentation.
- Thermal augmentation by utilizing FSI of multiple plates can be investigated numerically.

Appendix A

Effect of shape of bluff-body on flow-induced deformation of an elastic Plate

Numerical simulations were performed using three different bluff body. The following values are considered for the simulation setup: U_m=1, $D = 1$, $Re = 100$, $E = 175$, ρ_s=10 where U_m, L, Re E and ρ_s are mean velocity , plate length, Reynolds number based on plate length and mean velocity of fluid, Young's modulus and fluid to structure density ratio, respectively. Dimensionless thickness of the plate is 0.2. The Poisson's ratio is taken as 0.4 in the structural solver.

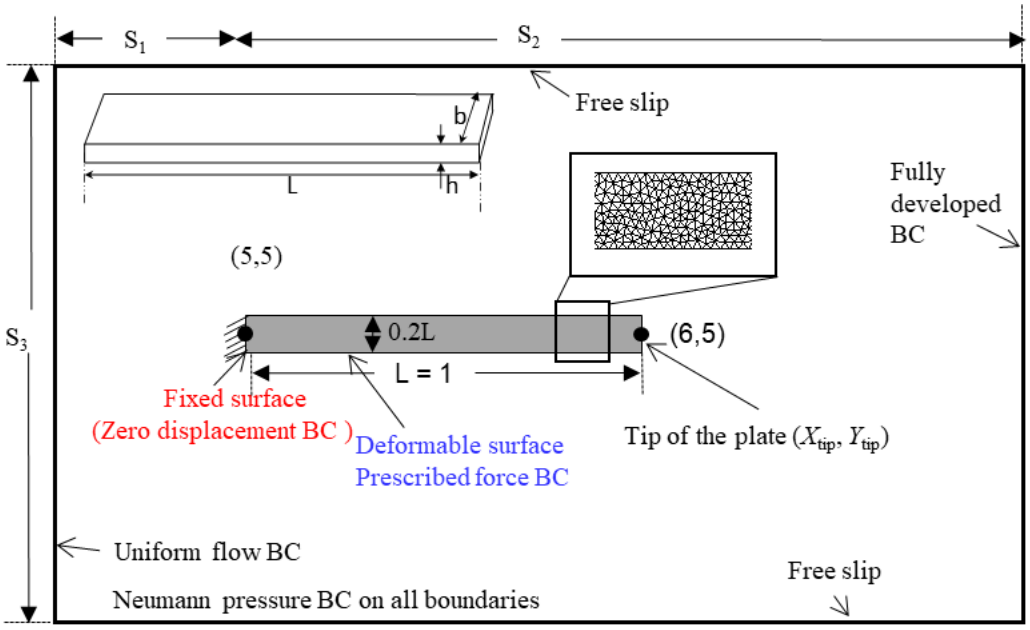

Figure A.1: Computational domain for examining the effects of bluff body on the dynamics of a flexible structure.

The domain size is taken as follows; $S_1 + S_2 = 25L$ and $S_3 = 10.0L$, as shown in Fig. A.1. Note that Fig. A.1 shows only plate configuration. The plate will be attached to bluff bodies for other configuration. The leading edge of the plate is clamped, and tailing is free. Force boundary condition is applied in the deformable plate surface. The fluid is taken to be Newtonian and incompressible. The plate is considered to consist of Saint Venant-Kirchhoff material, which accounts for geometric nonlinearity for a linear elastic material. The boundary conditions for the present problem are illustrated in Fig. A.1. Neumann boundary condition is applied at the top and bottom boundary of the open domain. No-slip boundary condition is applied in immersed structure boundary. Zero Neumann boundary condition is applied for the velocity at the channel outlet. At the inlet, uniform velocity is applied.

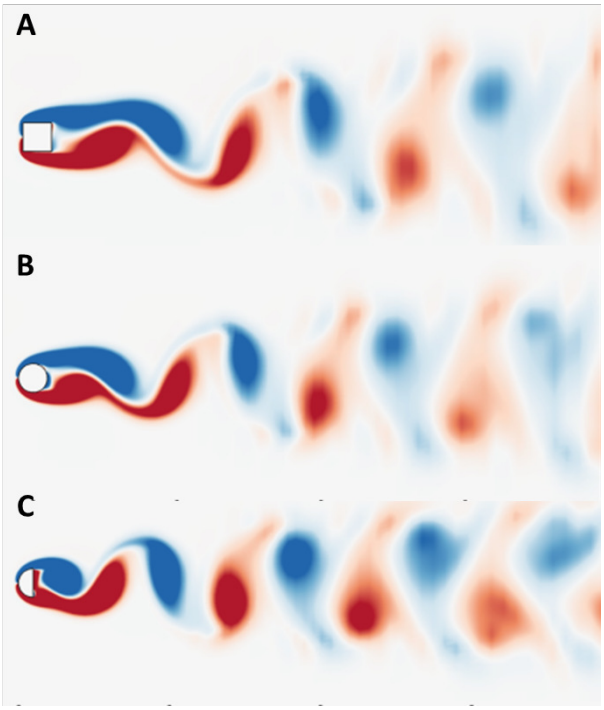

Figure A.2: Vortical wake structures for flow past three different bluff body; (A) square cylinder (B) circular cylinder (C) half circular cylinder. Color map range is [-1, 1].

Table A.1: Comparison of vortex shedding Strouhal number (St_f) for different bodies

Case	**Re**	St_f
Plate	100	0
Circular cylinder	100	0.169
Half circular cylinder	100	0.198
Square circular cylinder	100	0.153

We compare vortex shedding Strouhal number (St_f) and vortical wake structures for

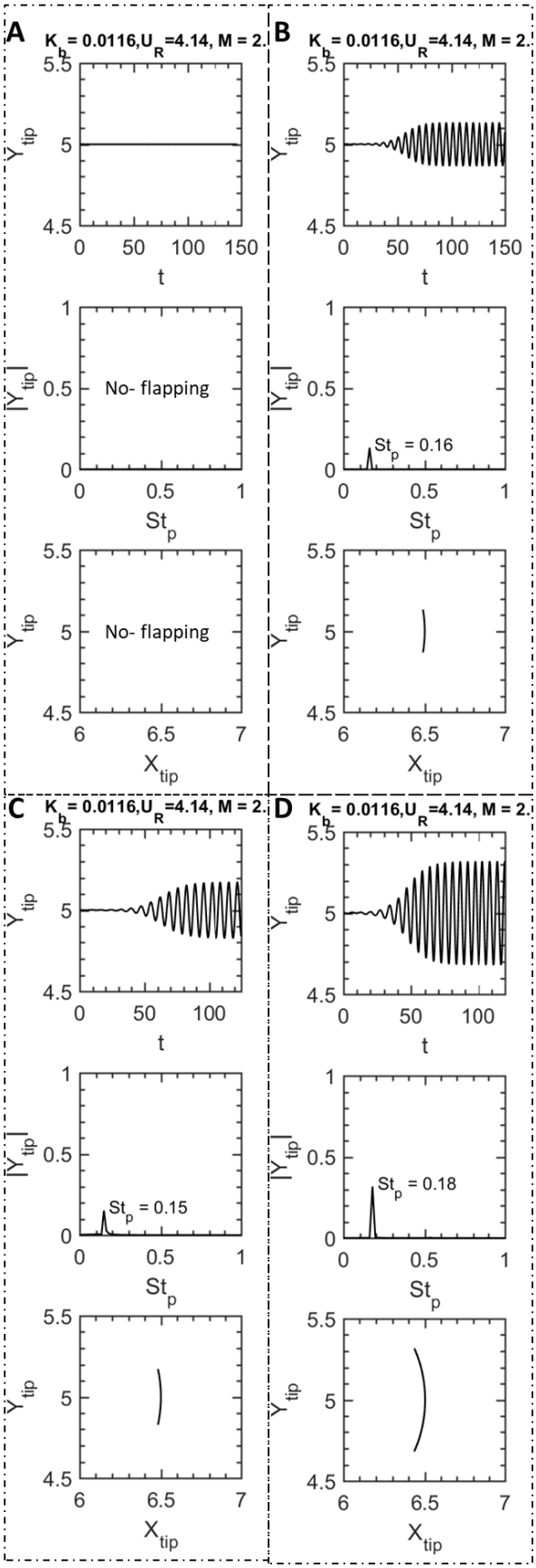

Figure A.3: Comparison of Y_{tip} of the plate deformation, power spectra and phase plane plot are for four different cases:(A) only plate (B) circular cylinder (C) square cylinder (D) half circular cylinder D-shaped. Color map range is [-1, 1].

flow past three different bluff body placed in a open domain shown in Fig. A.2. Fig. A.2A is flow past square cylinder where vortex formation length is higher than Fig. A.2B. Vortex formation length of half circular cylinder shown in Fig. A.2C is smaller than other two cases. Periodic Von-karman vortex shedding are observed for three cases but shedding vortices are smaller for half circular cylinder. We also examine vortex shedding Strouhal number (St_f) for three case which is shown in Table A.1. St_f is higher for half circular cylinder and lower for square cylinder. No vortex shedding is observed for the case of only plate. Now, we discuss flexible plate oscillation behind bluff bodies. Shedding vortex coming from the bluff body gives the periodic force to the an elastic plate attached behind the bluff body and elastic plate deformation occurs. The plate reaches self-sustained periodic oscillation at steady state. The elastic plate oscillation responses for four different cases are examined. Fig. A.3 shows the Y_{tip}, power spectra, phase plot and superimposed shapes of the elastic splitter plate in the first, second, and third row, respectively for each case. No plate deformation is observed for the only plate shown in Fig. A.3A. Fig. A.3D (second row) shows that plate with larger deformation for plate behind half cylinder vibrates with a larger frequency than other cases. The dominant frequency is closer to the vortex shedding frequency of respectively attached cylinder. Fig. A.3D (third row) shows that the phase plot is larger for half cylinder case.

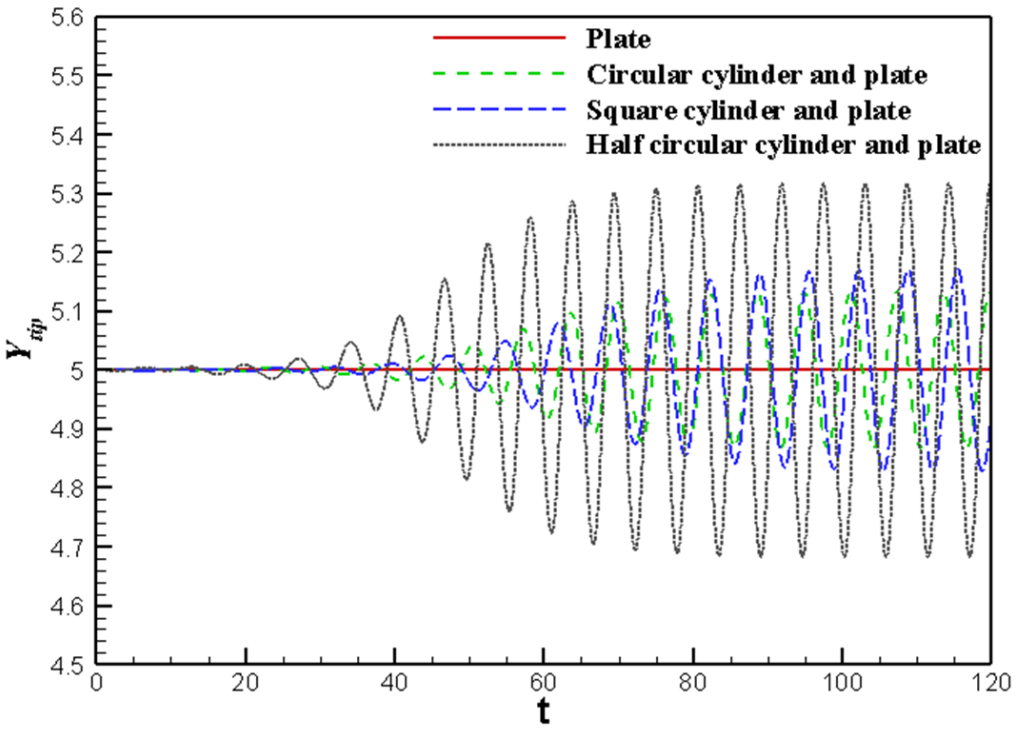

Figure A.4: Comparison of Y_{tip} of the plate deformation for four different cases.

Fig. A.4 shows the comparison of Y_{tip} of plate deformation signal. Y_{tip} is higher for

half

Table A.2: Comparison of flexible plate frequency and Y_{tip} plate deformation

Case	f_p	Y_{tip}
Flexible Plate	0	0
Flexible Plate behind Circular cylinder	0.16	0.12
Flexible Plate behind Half circular cylinder	0.18	0.32
Flexible Plate behind Square circular cylinder	0.15	0.17

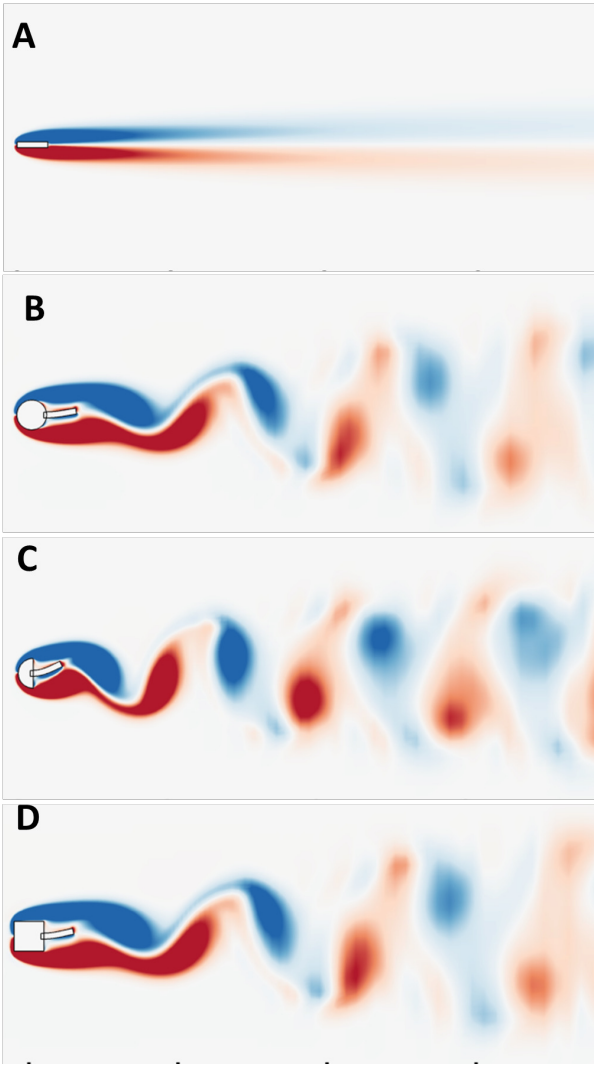

Figure A.5: Comparison of vorticity field for four different cases :(A) only plate and elastic plate attached to (B) circular cylinder (C) square cylinder (D) half circular cylinder D-shaped. Color map range is [-1, 1].

cylinder case shown in Fig. A.4. The details of plate oscillation frequency and amplitude of Y_{tip} of plate deformation for four different cases are shown in Table A.2. Fig. A.5

shows that the vorticity field for four cases. Alternative periodic vortex shedding is observed in the last three cases, and vortex shedding pattern is 2S for all the cases. Shed Vortices from half circle D-shaped bluff body rolls on the tip of the flexible plate. As a result, larger Y_{tip} of plate deformation occurs. As vortex formation length is higher for circular and rectangular cylinder, acting force on the flexible plate is lower than half circle D-shaped bluff body case.

A.1 Closure

We employ a fluid-structure interaction (FSI) solver to simulate the dynamics of an elastic plate attached behind the bluff body and is subjected to laminar flow. The FSI combines a sharp interface immersed boundary method based flow solver and an open source finite-element based structure solver. In the present chapter, the effect of the bluff body is studied at $Re = 100$, where Re is Reynolds number and is based on free-stream velocity and length of the plate. The oscillation amplitude and frequency of the plate tip were examined as affected by the bluff body. The oscillation amplitude and frequency of the plate tip are strongly affected by the vortex shedding coming from the bluff body. The present results provide fundamental insights into the flapping of an elastic plate and could be useful to design the elastic plate in energy-harvesting and thermal augmentation applications.

Appendix B

Non-dimensional form of 2-D Navier-Stokes equations

The 2-D Navier-Stokes equations of dimensional form at the x-direction component:

$$\rho\Big(\frac{\partial u_x^*}{\partial t^*} + u_x^*\frac{\partial u_x^*}{\partial x} + u_y^*\frac{\partial u_x^*}{\partial y^*}\Big) = -\frac{\partial p^*}{\partial x^*} + \mu\Big(\frac{\partial^2 u_x^*}{\partial x^{*2}} + \frac{\partial^2 u_x^*}{\partial y^{*2}}\Big) \tag{B.1}$$

Assume no additional body forces. The components of the velocity field u^* are denoted by subscripts (x,y,z). The pressure is given by p^* and ρ is the density.

First we divide by the density ρ in order to simplify the equation.

$$\rho\Big(\frac{\partial u_x^*}{\partial t^*} + u_x^*\frac{\partial u_x^*}{\partial x} + u_y^*\frac{\partial u_x^*}{\partial y^*}\Big) = -\frac{1}{\rho}\frac{\partial p^*}{\partial x^*} + \nu\Big(\frac{\partial^2 u_x^*}{\partial x^{*2}} + \frac{\partial^2 u_x^*}{\partial y^{*2}}\Big) \tag{B.2}$$

Now in order to obtain the non-dimensional equation we make the following substitutions.

$u_x^* = u_x u_0^*$
$p^* = p u_0^{*2}\rho$
$t^* = tL/u_0^*$
$x^* = xL$
$y^* = yL$
$z^* = zL$

u_0^* is reference velocity and L is reference length. Using the above substitutions we end up with the following equation:

$$\frac{\partial u_x u_0^*}{\partial tL/u_0^*} + u_x u_0^*\frac{\partial u_x u_0^*}{\partial xL} + u_y u_0^*\frac{\partial u_x u_0^*}{\partial y^* L} = -\frac{1}{\rho}\frac{\partial p u_0^{*2}\rho}{\partial xL} + \nu\Big(\frac{\partial^2 u_x u_0^*}{\partial x^2 L^2} + \frac{\partial^2 u_x u_0^*}{\partial y^2 L^2}\Big) \tag{B.3}$$

We simplify above equation by dividing u_0^{*2}/L.

$$\frac{\partial u_x}{\partial t} + u_x \frac{\partial u_x}{\partial x} + u_y \frac{\partial u_x}{\partial y} = -\frac{1}{\rho}\frac{\partial p}{\partial x} + \nu \frac{1}{u_0^* L}\left(\frac{\partial^2 u_x}{\partial x^2} + \frac{\partial^2 u_x}{\partial y^2}\right) \tag{B.4}$$

Here $\frac{\nu}{u_0^* L}$ is inverse Reynolds number ($\frac{1}{Re}$).

$$\frac{\partial u_x}{\partial t} + u_x \frac{\partial u_x}{\partial x} + u_y \frac{\partial u_x}{\partial y} = -\frac{1}{\rho}\frac{\partial p}{\partial x} + \frac{1}{Re}\left(\frac{\partial^2 u_x}{\partial x^2} + \frac{\partial^2 u_x}{\partial y^2}\right) \tag{B.5}$$

similarly we can get the y-direction component.

$$\frac{\partial u_y}{\partial t} + u_x \frac{\partial u_y}{\partial x} + u_y \frac{\partial u_y}{\partial y} = -\frac{1}{\rho}\frac{\partial p}{\partial x} + \frac{1}{Re}\left(\frac{\partial^2 u_y}{\partial x^2} + \frac{\partial^2 u_y}{\partial y^2}\right) \tag{B.6}$$

Appendix C

Non-dimensional form of Navier's Equations for structure

The governing equations for the structure, Navier equations (momentum balance equation in Lagrangian form) in dimensional form, are written as follows,

$$\rho_s \frac{\partial^2 d_i^*}{\partial t^{*2}} = \frac{\partial \sigma_{\mathbf{ij}}^*}{\partial x_j^*} + \rho_s f_i^* \tag{C.1}$$

where i and j range from 1 to 3, ρ_s is the structure density, d_i is the displacement component in the i direction, t is the time, σ_{ij} is the stress tensor and f_i is the body force component in the i direction. The displacement vector $\mathbf{d}(\mathbf{x}, t)$ describes the motion of each point in the deformed solid as a function of space $\mathbf{x}$ and time t.

The second Piola-Kirchhoff stress tensor $\sigma_{\mathbf{ij}}$ is related to the Green Lagrangian strain tensor $\mathbf{E}$:

$$\sigma_{\mathbf{ij}} = 2\mu_s \mathbf{F}\mathbf{E} + \lambda_s tr(\mathbf{E})\mathbf{F} \tag{C.2}$$

$\mathbf{F}$ is the deformation gradient tensor given by:

$$\mathbf{F}_{\mathbf{ik}}^* = \delta_{ik} + \frac{\partial d*_i}{\partial x_k^*}, \tag{C.3}$$

The Green-Lagrangian strain tensor $\boldsymbol{E}$ is defined as

$$\mathbf{E} = \frac{1}{2}(\mathbf{F}^{\mathbf{T}}\mathbf{F} - 1), \tag{C.4}$$

here $\mathbf{tr}$ is the tensor trace, λ_s and μ_s are Lam constants which are characteristics of the elastic material. They are related to the Young modulus (E^*) and Poissons coefficient (ν_s) by:

$$\lambda_{\mathbf{s}} = \frac{\nu_s E^*}{(1+\nu_s)(1-2\nu_s)} \tag{C.5}$$

and

$$\mu_{\mathbf{s}} = \frac{E^*}{2(1+\nu_s)} \tag{C.6}$$

putting λ_s and μ_s in Eq.(C.7) which gives following equation:

$$\sigma_{\mathbf{s}} = \frac{E^*}{(1+\nu_s)}\mathbf{FE} + \frac{\nu_s E^*}{(1+\nu_s)(1-2\nu_s)} tr(\mathbf{E})\mathbf{F} \tag{C.7}$$

Now in order to obtain the non-dimensional equation, we make the following substitutions.

$d_i^* = d_i L$

$t^* = tL/u_0^*$

$x_j{}^* = x_j L$

$h^* = HL$

u_0^* is reference velocity and L is reference length.

We simplify above equation by dividing ρ_s.

$$\frac{\partial^2 d_i^*}{\partial t^{*2}} = \frac{1}{\rho_s}\frac{\partial \sigma_{ij}^*}{\partial x_j^*} + f_i^* \tag{C.8}$$

Using the above substitutions we end up with the following equation:

$$\frac{\partial^2 d_i L}{\partial t^{*2} L/u_0^{*2}} = \frac{1}{\rho_s}\frac{\partial \sigma^*{}_{ij}}{\partial x_j L} + f_i^* \tag{C.9}$$

$$\frac{\partial^2 d_i}{\partial t^{*2}} = \frac{L}{u_0^{*2}\rho_s}\frac{\partial \sigma^*{}_{ij}}{L\partial x_j} + \frac{L}{u_0^{*2}} f_i^* \tag{C.10}$$

$$\frac{\partial^2 d_i}{\partial t^{*2}} = \frac{h^*}{u_0^{*2} M\rho_f L}\frac{\partial \sigma^*{}_{ij}}{\partial x_j} + \frac{L}{u_0^{*2}} f_i^* \tag{C.11}$$

Here $\mathbf{FE}$ and $tr(\mathbf{E})\mathbf{F}$ are dimensionless.

$$F_{ik}^* = \delta_{ik} + \frac{\partial d*_i}{\partial x_k^*}, \tag{C.12}$$

$$F_{ik} = \delta_{ik} + \frac{\partial d_i L}{\partial x_k L}, \tag{C.13}$$

$$F_{ik} = \delta_{ik} + \frac{\partial d_i}{\partial x_k}, \tag{C.14}$$

$$\frac{\partial^2 d_i}{\partial t^2} = \frac{h^*}{u_0^{*2} M\rho_f L}\frac{\partial}{\partial x_j}\Big(\frac{E^*}{(1+\nu_s)}\mathbf{FE} + \frac{\nu_s E^*}{(1+\nu_s)(1-2\nu_s)} tr(\mathbf{E})\mathbf{F}\Big) + \frac{L}{u_0^{*2}} f_i^* \tag{C.15}$$

$$\frac{\partial^2 d_i}{\partial t^2} = \frac{h^*}{u_0^{*2} M \rho_f L} \frac{E^*}{(1+\nu_s)} \frac{\partial}{\partial x_j}(\mathbf{FE}) + \frac{h^*}{u_0^{*2} M \rho_f L} \frac{\nu_s E^*}{(1+\nu_s)(1-2\nu_s)} \frac{\partial}{\partial x_j}\big(tr(\mathbf{E})\mathbf{F}\big) \quad \text{(C.16)}$$

$$+ \frac{L}{u_0^{*2}} f_i^* \quad \text{(C.17)}$$

$$\frac{\partial^2 d_i}{\partial t^2} = \frac{E^* h^{*3}}{12 \rho_f u_0^{*2} L^3 M h^{*2}} \frac{12 L^2}{(1+\nu_s)} \frac{\partial}{\partial x_j}(\mathbf{FE}) + \frac{E^* h^{*3}}{12 \rho_f u_0^{*2} L^3 M h^{*2}} \frac{12 L^2 \nu_s}{(1+\nu_s)(1-2\nu_s)} \frac{\partial}{\partial x_j}\big(tr(\mathbf{E})\mathbf{F}\big)$$

$$+ \frac{L}{u_0^{*2}} f_i^*$$

$$\frac{\partial^2 d_i}{\partial t^2} = K_b \frac{12 L^2}{M h^{*2} (1+\nu_s)} \frac{\partial}{\partial x_j}(\mathbf{FE}) + K_b \frac{12 L^2 \nu_s}{M h^{*2} (1+\nu_s)(1-2\nu_s)} \frac{\partial}{\partial x_j}\big(tr(\mathbf{E})\mathbf{F}\big) + \frac{L}{u_0^{*2}} f_i^* \quad \text{(C.18)}$$

$$\frac{\partial^2 d_i}{\partial t^2} = \frac{12 K_b}{M H^2} \frac{1}{(1+\nu_s)} \frac{\partial}{\partial x_j}(\mathbf{FE}) + \frac{12 K_b}{M H^2} \frac{\nu_s}{(1+\nu_s)(1-2\nu_s)} \frac{\partial}{\partial x_j}\big(tr(\mathbf{E})\mathbf{F}\big) + \frac{L}{u_0^{*2}} f_i^* \quad \text{(C.19)}$$

$$\frac{\partial^2 d_i}{\partial t^2} = \frac{K_b 12}{M H^2} \frac{1}{(1+\nu_s)} \frac{\partial}{\partial x_j}(\mathbf{FE}) + \frac{K_b 12}{M H^2} \frac{\nu_s}{(1+\nu_s)(1-2\nu_s)} \frac{\partial}{\partial x_j}\big(tr(\mathbf{E})\mathbf{F}\big) + \frac{L}{u_0^{*2}} f_i^* \quad \text{(C.20)}$$

$$\frac{\partial^2 d_i}{\partial t^2} = \Big(\frac{1}{{U_R}^2}\Big) \frac{12}{H^2} \frac{1}{(1+\nu_s)} \frac{\partial}{\partial x_j}(\mathbf{FE}) + \Big(\frac{1}{{U_R}^2}\Big) \frac{12}{H^2} \frac{\nu_s}{(1+\nu_s)(1-2\nu_s)} \frac{\partial}{\partial x_j}\big(tr(\mathbf{E})\mathbf{F}\big) + \frac{L}{u_0^{*2}} f_i^* \quad \text{(C.21)}$$

Here $K_b = \frac{E^*}{\rho_f^* u_0^{*2}} \frac{h^{*3}}{12 L^3}$, $M = \frac{\rho_s h^*}{\rho_f L}$, $U_R = \sqrt{\frac{M}{K_b}}$ and $F_i = \frac{L}{u_0^{*2}} f_i^*$

Bibliography

Akaydın, H., Elvin, N., and Andreopoulos, Y. (2010). Wake of a cylinder: a paradigm for energy harvesting with piezoelectric materials. *Experiments in Fluids*, 49(1):291–304.

Akcabay, D. T. and Young, Y. L. (2012). Hydroelastic response and energy harvesting potential of flexible piezoelectric beams in viscous flow. *Physics of Fluids (1994-present)*, 24(5):054106.

Al-Sumaily, G. F. and Thompson, M. C. (2013). Forced convection from a circular cylinder in pulsating flow with and without the presence of porous media. *International Journal of Heat and Mass Transfer*, 61:226–244.

Alben, S. (2015). Flag flutter in inviscid channel flow. *Physics of Fluids*, 27(3):033603.

Alben, S. and Shelley, M. J. (2008). Flapping states of a flag in an inviscid fluid: bistability and the transition to chaos. *Physical review letters*, 100(7):074301.

Argentina, M. and Mahadevan, L. (2005). Fluid-flow-induced flutter of a flag. *Proceedings of the National academy of Sciences of the United States of America*, 102(6):1829–1834.

Armstrong, B., Barnes, F., and Grant, I. (1986). The effect of a perturbation on the flow over a bluff cylinder. *The Physics of fluids*, 29(7):2095–2102.

Bagheri, S., Mazzino, A., and Bottaro, A. (2012). Spontaneous symmetry breaking of a hinged flapping filament generates lift. *Physical review letters*, 109(15):154502.

Balaras, E. (2004). Modeling complex boundaries using an external force field on fixed cartesian grids in large-eddy simulations. *Computers & Fluids*, 33(3):375–404.

Barbi, C., Favier, D., Maresca, C., and Telionis, D. (1986). Vortex shedding and lock-on of a circular cylinder in oscillatory flow. *Journal of Fluid Mechanics*, 170:527–544.

Beeby, S. P., Tudor, M. J., and White, N. (2006). Energy harvesting vibration sources for microsystems applications. *Meas. Sci. Technol.*, 17(12):175–195.

Behr, M., Hastreiter, D., Mittal, S., and Tezduyar, T. (1995). Incompressible flow past a circular cylinder: dependence of the computed flow field on the location of the lateral boundaries. *Computer Methods in Applied Mechanics and Engineering*, 123(1-4):309–316.

Bejan, A. (2004). *Convection Heat Transfer*. Wiley.

Bergles, A. E. (2011). Recent developments in enhanced heat transfer. *Heat and mass transfer*, 47(8):1001.

Bhardwaj, R. and Mittal, R. (2012). Benchmarking a coupled immersed-boundary-finite-element solver for large-scale flow-induced deformation. *AIAA*, 50(7):1638–1642.

Bhardwaj, R. and Sharma, A. (2017). *Immersed boundary methods, in CRC Handbook of Thermal Engineering(Editor: R. P. Chhabra)*. Number ISBN 9781498715270. CRC Press (Taylor Francis).

Çevik, G., Akşit, M. F., and Şabanoviç, A. (2011). Piezoelectric wind power harnessing–an overview.

Choi, Y. J., Vedula, V., and Mittal, R. (2014). Computational study of the dynamics of a bileaflet mechanical heart valve in the mitral position. *Annals of biomedical engineering*, 42(8):1668–1680.

Connell, B. S. and Yue, D. K. (2007). Flapping dynamics of a flag in a uniform stream. *Journal of fluid mechanics*, 581:33–67.

Deivasigamani, A., McCarthy, J., John, S., Watkins, S., Trivailo, P., and Coman, F. (2013). Flutter of cantilevered interconnected beams with variable hinge positions. *Journal of fluids and structures*, 38:223–237.

Dunne, T. and Rannacher, R. (2006). Adaptive finite element approximation of fluid-structure interaction based on an eulerian variational formulation. In *Fluid-structure interaction*, pages 110–145. Springer.

Dunnmon, J., Stanton, S., Mann, B., and Dowell, E. (2011). Power extraction from aeroelastic limit cycle oscillations. *Journal of Fluids and Structures*, 27(8):1182–1198.

Eloy, C., Lagrange, R., Souilliez, C., and Schouveiler, L. (2008). Aeroelastic instability of cantilevered flexible plates in uniform flow. *Journal of Fluid Mechanics*, 611:97–106.

Eloy, C., Souilliez, C., and Schouveiler, L. (2007). Flutter of a rectangular plate. *Journal of Fluids and Structures*, 23(6):904–919.

Fadlun, E., Verzicco, R., Orlandi, P., and Mohd-Yusof, J. (2000). Combined immersed-boundary finite-difference methods for three-dimensional complex flow simulations. *Journal of computational physics*, 161(1):35–60.

Fiebig, M., Brockmeier, U., Mitra, N., and Gü termann, T. (1989). Structure of velocity and temperature fields in laminar channel flows with longitudinal vortex generators. *Numer. Heat Transfer*, 15(3):281–302.

Fu, W.-S. and Yang, S.-J. (2001). A numerical study of effects of the swinging amplitude of fins on heat transfer characteristics in a flow. *Heat Mass Transfer*, 38(1):55–63.

Fung, Y.-c. (1965). *Foundations of solid mechanics*. Prentice Hall.

Furquan, M. and Mittal, S. (2015). Flow past two square cylinders with flexible splitter plates. *Computational Mechanics*, 55(6):1155–1166.

Garg, H., Soti, A. K., and Bhardwaj, R. (2018). A sharp interface immersed boundary method for vortex-induced vibration in the presence of thermal buoyancy. *Physics of Fluids*, 30(2):023603.

Ghias, R., Mittal, R., and Dong, H. (2007). A sharp interface immersed boundary method for compressible viscous flows. *Journal of Computational Physics*, 225(1):528–553.

Gibou, F., Fedkiw, R. P., Cheng, L.-T., and Kang, M. (2002). A second-order-accurate symmetric discretization of the poisson equation on irregular domains. *Journal of Computational Physics*, 176(1):205–227.

Gilmanov, A., Le, T. B., and Sotiropoulos, F. (2015). A numerical approach for simulating fluid structure interaction of flexible thin shells undergoing arbitrarily large deformations in complex domains. *Journal of Computational Physics*, 300:814–843.

Goldstein, D., Handler, R., and Sirovich, L. (1993). Modeling a no-slip flow boundary with an external force field. *Journal of Computational Physics*, 105(2):354–366.

Gordnier, R. E. (2009). High fidelity computational simulation of a membrane wing airfoil. *Journal of Fluids and Structures*, 25(5):897–917.

Govardhan, R. and Williamson, C. (2000). Modes of vortex formation and frequency response of a freely vibrating cylinder. *Journal of Fluid Mechanics*, 420:85–130.

Griffin, O. M. and Hall, M. (1991). Vortex shedding lock-on and flow control in bluff body wakes. *Journal of fluids engineering*, 113(4):526–537.

Guilmineau, E. and Queutey, P. (2002). A numerical simulation of vortex shedding from an oscillating circular cylinder. *Journal of Fluids and Structures*, 16(6):773–794.

Guo, Z. and Sung, H. J. (1997). Analysis of the nusselt number in pulsating pipe flow. *Int. J. Heat Mass Transfer*, 40(10):2486–2489.

Gurugubelli, P. and Jaiman, R. (2015). Self-induced flapping dynamics of a flexible inverted foil in a uniform flow. *Journal of Fluid Mechanics*, 781:657–694.

Gurugubelli, P. S., Jaiman, R. K., and Khoo, B. C. (2014). Flexible flapping dynamics of parallel elastic plates in a uniform flow: application to energy harvesting devices. In *33rd International Conference on Ocean, Offshore and Arctic Engineering, OMAE*.

Habchi, C., Russeil, S., Bougeard, D., Harion, J.-L., Lemenand, T., Ghanem, A., Della Valle, D., and Peerhossaini, H. (2013). Partitioned solver for strongly coupled fluid–structure interaction. *Computers & Fluids*, 71:306–319.

Hilber, H. M., Hughes, T. J., and Taylor, R. L. (1977). Improved numerical dissipation for time integration algorithms in structural dynamics. *Earthquake Engineering & Structural Dynamics*, 5(3):283–292.

Huang, L. (1995). Flutter of cantilevered plates in axial flow. *Journal of Fluids and Structures*, 9(2):127–147.

Hughes, T. J. (1987). The finite element method prentice-hall. *New Jersey (USA)*.

Jaiman, R. K., Parmar, M. K., and Gurugubelli, P. S. (2014). Added mass and aeroelastic stability of a flexible plate interacting with mean flow in a confined channel. *Journal of Applied Mechanics*, 81(4):041006.

Joshi, R. U., Soti, A. K., and Bhardwaj, R. (2015). Numerical study of heat transfer enhancement by deformable twin plates in laminar heated channel flow. *Comput. Therm. Sci.: Int. J.*, 7(5-6).

Khalak, A. and Williamson, C. (1997). Fluid forces and dynamics of a hydroelastic structure with very low mass and damping. *Journal of Fluids and Structures*, 11(8):973–982.

Khalak, A. and Williamson, C. (1999). Motions, forces and mode transitions in vortex-induced vibrations at low mass-damping. *J. Fluids & Struct.*, 13(7-8):813–851.

Khanafer, K., Alamiri, A., and Pop, I. (2010). Fluid–structure interaction analysis of flow and heat transfer characteristics around a flexible microcantilever in a fluidic cell. *International Journal of Heat and Mass Transfer*, 53(9-10):1646–1653.

Kim, D., Cossé, J., Cerdeira, C. H., and Gharib, M. (2013). Flapping dynamics of an inverted flag. *Journal of Fluid Mechanics*, 736.

Kim, J., Kim, D., and Choi, H. (2001). An immersed-boundary finite-volume method for simulations of flow in complex geometries. *Journal of Computational Physics*, 171(1):132–150.

Konstantinidis, E., Balabani, S., and Yianneskis, M. (2003). The effect of flow perturbations on the near wake characteristics of a circular cylinder. *Journal of Fluids and Structures*, 18(3-4):367–386.

Kornecki, A., Dowell, E., and O'brien, J. (1976). On the aeroelastic instability of two-dimensional panels in uniform incompressible flow. *Journal of Sound and Vibration*, 47(2):163–178.

Kumar Soti, A. (2018). *Computational and experimental investigation of fluid-structure interaction with applications in energy harvesting and thermal augmentation*. PhD dissertation, Indian Institute of Technology Bombay.

Kundu, A., Soti, A. K., Bhardwaj, R., and Thompson, M. C. (2017). The response of an elastic splitter plate attached to a cylinder to laminar pulsatile flow. *Journal of Fluids and Structures*, 68:423–443.

Lācis, U., Brosse, N., Ingremeau, F., Mazzino, A., Lundell, F., Kellay, H., and Bagheri, S. (2014). Passive appendages generate drift through symmetry breaking. *Nature communications*, 5:5310.

Lee, J., Kim, J., Choi, H., and Yang, K.-S. (2011). Sources of spurious force oscillations from an immersed boundary method for moving-body problems. *Journal of computational physics*, 230(7):2677–2695.

Lee, J. and You, D. (2013a). An implicit ghost-cell immersed boundary method for simulations of moving body problems with control of spurious force oscillations. *Journal of Computational Physics*, 233:295–314.

Lee, J. and You, D. (2013b). Study of vortex-shedding-induced vibration of a flexible splitter plate behind a cylinder. *Phys. Fluids*, 25(11):110811.

Lee, J. H., Huang, W.-X., and Sung, H. J. (2014). Flapping dynamics of a flexible flag in a uniform flow. *Fluid Dynamics Research*, 46(5):055517.

Leontini, J. S., Jacono, D. L., and Thompson, M. C. (2013). Wake states and frequency selection of a streamwise oscillating cylinder. *Journal of Fluid Mechanics*, 730:162–192.

Li, S. and Lipson, H. (2009). Vertical-stalk flapping-leaf generator for wind energy harvesting. In *ASME 2009 Conference on Smart Materials, Adaptive Structures and Intelligent Systems*, pages 611–619. American Society of Mechanical Engineers.

Li, T., Zhang, J. Y., and Zhang, W. H. (2010). Numerical simulation of oscillating flows over a circular cylinder. In *Applied Mechanics and Materials*, volume 29, pages 414–419. Trans Tech Publ.

Liao, J. C., Beal, D. N., Lauder, G. V., and Triantafyllou, M. S. (2003). Fish exploiting vortices decrease muscle activity. *Science*, 302(5650):1566–1569.

Liu, J., Jaiman, R. K., and Gurugubelli, P. S. (2014). A stable second-order scheme for fluid–structure interaction with strong added-mass effects. *Journal of Computational Physics*, 270:687–710.

Marella, S., Krishnan, S., Liu, H., and Udaykumar, H. (2005). Sharp interface cartesian grid method i: An easily implemented technique for 3d moving boundary computations. *Journal of Computational Physics*, 210(1):1–31.

Meneghini, J. and Bearman, P. (1995). Numerical simulation of high amplitude oscillatory flow about a circular cylinder. *Journal of Fluids and Structures*, 9(4):435–455.

Meschini, V., De Tullio, M., Querzoli, G., and Verzicco, R. (2018). Flow structure in healthy and pathological left ventricles with natural and prosthetic mitral valves. *Journal of fluid mechanics*, 834:271–307.

Michelin, S., Smith, S. G. L., and Glover, B. J. (2008). Vortex shedding model of a flapping flag. *Journal of Fluid Mechanics*, 617:1–10.

Mittal, R., Dong, H., Bozkurttas, M., Najjar, F., Vargas, A., and von Loebbecke, A. (2008). A versatile sharp interface immersed boundary method for incompressible flows with complex boundaries. *J. Comput. Phys.*, 227(10):4825–4852.

Mittal, R. and Iaccarino, G. (2005). Immersed boundary methods. *Annu. Rev. Fluid Mech.*, 37:239–261.

Mittal, R., Seo, J. H., Vedula, V., Choi, Y. J., Liu, H., Huang, H. H., Jain, S., Younes, L., Abraham, T., and George, R. T. (2016). Computational modeling of cardiac hemodynamics: Current status and future outlook. *Journal of Computational Physics*, 305:1065–1082.

Mittal, R., Zheng, X., Bhardwaj, R., Seo, J. H., Xue, Q., and Bielamowicz, S. (2011). Toward a simulation-based tool for the treatment of vocal fold paralysis. *Frontiers physiol.*, 2:19.

Negrut, D., Rampalli, R., Ottarsson, G., and Sajdak, A. (2007). On an implementation of the hilber-hughes-taylor method in the context of index 3 differential-algebraic equations of multibody dynamics (detc2005-85096). *Journal of computational and nonlinear dynamics*, 2(1):73–85.

Olivier, M., Dumas, G., and Morissette, J. (2009). A fluid-structure interaction solver for nano-air-vehicle flapping wings. In *Proceedings of the 19th AIAA computational fluid dynamics conference, San Antonio, USA*, pages 1–15.

Orrego, S., Shoele, K., Ruas, A., Doran, K., Caggiano, B., Mittal, R., and Kang, S. H. (2017). Harvesting ambient wind energy with an inverted piezoelectric flag. *Applied Energy*, 194:212–222.

Park, K.-H., Min, J. K., Kim, J.-K., Park, S.-H., and Ha, M. Y. (2013). A study on a flexible wing with up–down vibration in a pulsating flow of cooling air to improve heat transfer efficiency. *Heat Mass Transfer*, 49(10):1459–1470.

Peskin, C. S. (1972). Flow patterns around heart valves: a numerical method. *Journal of computational physics*, 10(2):252–271.

Razzaq, M., Damanik, H., Hron, J., Ouazzi, A., and Turek, S. (2012). Fem multigrid techniques for fluid–structure interaction with application to hemodynamics. *Applied Numerical Mathematics*, 62(9):1156–1170.

Razzaq, M., Turek, S., Hron, J., Acker, J., Weichert, F., Grunwald, I., Roth, C., Wagner, M., and Romeike, B. (2010). Numerical simulation and benchmarking of fluid-structure interaction with application to hemodynamics. *Fundamental Trends in Fluid–Structure Interaction, GP Galdi and R. Rannacher, eds., World Scientific*, pages 171–199.

Rogers, A. L., Manwell, J. F., and Wright, S. (2006). Wind turbine acoustic noise. *Renewable Energy Research Laboratory, University of Massachusetts at Amherst*.

Rostami, A. B. Energy harvesting by hydro/aero elastic phenomena in small scale.

Ryu, J., Park, S. G., Kim, B., and Sung, H. J. (2015). Flapping dynamics of an inverted flag in a uniform flow. *Journal of Fluids and Structures*, 57:159–169.

Sader, J. E., Cossé, J., Kim, D., Fan, B., and Gharib, M. (2016). Large-amplitude flapping of an inverted flag in a uniform steady flow–a vortex-induced vibration. *Journal of Fluid Mechanics*, 793:524–555.

Saiki, E. and Biringen, S. (1996). Numerical simulation of a cylinder in uniform flow: application of a virtual boundary method. *Journal of Computational Physics*, 123(2):450–465.

Seo, J. H. and Mittal, R. (2011). A sharp-interface immersed boundary method with improved mass conservation and reduced spurious pressure oscillations. *J. Comput. Phys.*, 230(19):7347–7363.

Shelley, M., Vandenberghe, N., and Zhang, J. (2005). Heavy flags undergo spontaneous oscillations in flowing water. *Physical review letters*, 94(9):094302.

Shelley, M. J. and Zhang, J. (2011). Flapping and bending bodies interacting with fluid flows. *Annu. Rev. Fluid Mech.*, 43:449–465.

Shi, J., Hu, J., Schafer, S. R., and Chen, C.-L. C. (2014). Numerical study of heat transfer enhancement of channel via vortex-induced vibration. *Appl. Therm. Eng.*, 70(1):838–845.

Shoele, K. and Mittal, R. (2014). Computational study of flow-induced vibration of a reed in a channel and effect on convective heat transfer. *Phys. Fluids*, 26(12):127103.

Shoele, K. and Mittal, R. (2016a). Energy harvesting by flow-induced flutter in a simple model of an inverted piezoelectric flag. *Journal of Fluid Mechanics*, 790:582–606.

Shoele, K. and Mittal, R. (2016b). Flutter instability of a thin flexible plate in a channel. *Journal of Fluid Mechanics*, 786:29–46.

Shukla, S., Govardhan, R., and Arakeri, J. (2013). Dynamics of a flexible splitter plate in the wake of a circular cylinder. *Journal of Fluids and Structures*, 41:127–134.

Soti, A. K., Bhardwaj, R., and Sheridan, J. (2015). Flow-induced deformation of a flexible thin structure as manifestation of heat transfer enhancement. *Int. J. Heat Mass Transfer*, 84:1070–1081.

Tahoe. An open source c++ finite element solver, which was developed at Sandia National Labs, CA. http://sourceforge.net/projects/tahoe/.

Tang, D., Yamamoto, H., and Dowell, E. (2003). Flutter and limit cycle oscillations of two-dimensional panels in three-dimensional axial flow. *Journal of Fluids and Structures*, 17(2):225–242.

Tang, L., Paı, M. P., et al. (2007). On the instability and the post-critical behaviour of two-dimensional cantilevered flexible plates in axial flow. *Journal of Sound and Vibration*, 305(1):97–115.

Tang, L., Païdoussis, M. P., and Jiang, J. (2009). Cantilevered flexible plates in axial flow: energy transfer and the concept of flutter-mill. *Journal of Sound and Vibration*, 326(1):263–276.

Terracol, M., Manoha, E., Herrero, C., Labourasse, E., Redonnet, S., and Sagaut, P. (2005). Hybrid methods for airframe noise numerical prediction. *Theoretical and Computational Fluid Dynamics*, 19(3):197–227.

Tetlow, G. and Lucey, A. D. (2009). Motions of a cantilevered flexible plate in viscous channel flow driven by a constant pressure drop. *International Journal for Numerical Methods in Biomedical Engineering*, 25(5):463–482.

Theodorsen, T. and Mutchler, W. (1935). General theory of aerodynamic instability and the mechanism of flutter.

Thomson, W. (1996). *Theory of vibration with applications*. CRC Press.

Tian, F.-B. (2013). Role of mass on the stability of flag/flags in uniform flow. *Applied Physics Letters*, 103(3):034101.

Tian, F.-B., Luo, H., Zhu, L., Liao, J. C., and Lu, X.-Y. (2011). An efficient immersed boundary-lattice boltzmann method for the hydrodynamic interaction of elastic filaments. *Journal of computational physics*, 230(19):7266–7283.

Tian, F.-B., Luo, H., Zhu, L., and Lu, X.-Y. (2010). Interaction between a flexible filament and a downstream rigid body. *Physical Review E*, 82(2):026301.

Turek, S. and Hron, J. (2006). Proposal for numerical benchmarking of fluid-structure interaction between an elastic object and laminar incompressible flow. In *Fluid-structure interaction*, pages 371–385. Springer.

Udaykumar, H., Mittal, R., and Shyy, W. (1999). Computation of solid–liquid phase fronts in the sharp interface limit on fixed grids. *Journal of computational physics*, 153(2):535–574.

Van Kan, J. (1986). A second-order accurate pressure-correction scheme for viscous incompressible flow. *SIAM J. Sci. Statist. Comput.*, 7(3):870–891.

Vigmostad, S. C., Udaykumar, H. S., Lu, J., and Chandran, K. B. (2010). Fluid–structure interaction methods in biological flows with special emphasis on heart valve dynamics. *Int. J. Numer. Methods Biomed. Eng.*, 26(3-4):435–470.

Wall, W. A. and Ramm, E. (1998). *Fluid Structure Interaction Based Upon a Stabilized (ALE) Finite Element Method*. SFB 404, Geschäftsstelle.

Wang, C.-C. and Chen, C.-K. (2002). Forced convection in a wavy-wall channel. *Int. J. Heat Mass Transfer*, 45(12):2587–2595.

Watanabe, Y., Isogai, K., Suzuki, S., and Sugihara, M. (2002). A theoretical study of paper flutter. *Journal of Fluids and Structures*, 16(4):543–560.

Wu, J., Qiu, Y., Shu, C., and Zhao, N. (2014). Flow control of a circular cylinder by using an attached flexible filament. *Physics of Fluids*, 26(10):103601.

Xu, M., Wei, M., Yang, T., and Lee, Y. S. (2016). An embedded boundary approach for the simulation of a flexible flapping wing at different density ratio. *European Journal of Mechanics-B/Fluids*, 55:146–156.

Yang, J. and Balaras, E. (2006). An embedded-boundary formulation for large-eddy simulation of turbulent flows interacting with moving boundaries. *Journal of Computational Physics*, 215(1):12–40.

Yang, J., Preidikman, S., and Balaras, E. (2008). A strongly coupled, embedded-boundary method for fluid–structure interactions of elastically mounted rigid bodies. *Journal of Fluids and Structures*, 24(2):167–182.

Yang, J. and Stern, F. (2012). A simple and efficient direct forcing immersed boundary framework for fluid–structure interactions. *Journal of Computational Physics*, 231(15):5029–5061.

Yang, S.-J. (2003). Numerical study of heat transfer enhancement in a channel flow using an oscillating vortex generator. *Heat Mass Transfer*, 39(3):257–265.

Ye, T., Mittal, R., Udaykumar, H., and Shyy, W. (1999a). An accurate cartesian grid method for viscous incompressible flows with complex immersed boundaries. *J. Comput. Phys.*, 156(2):209–240.

Ye, T., Mittal, R., Udaykumar, H., and Shyy, W. (1999b). A cartesian grid method for viscous incompressible flows with complex immersed boundaries. In *14th Computational Fluid Dynamics Conference*, page 3312.

You, D., Mittal, R., Wang, M., and Moin, P. (2003). Study of rotor tip-clearance flow using large-eddy simulation. In *41st Aerospace Sciences Meeting and Exhibit*, page 838.

Zhang, J., Childress, S., Libchaber, A., and Shelley, M. (2000). Flexible filaments in a flowing soap film as a model for one-dimensional flags in a two-dimensional wind. *Nature*, 408(6814):835–839.

Zheng, X., Xue, Q., Mittal, R., and Beilamowicz, S. (2010). A coupled sharp-interface immersed boundary-finite-element method for flow-structure interaction with application to human phonation. *J. Biomech. Eng.*, 132(11):111003.

Zhu, L. and Peskin, C. S. (2002). Simulation of a flapping flexible filament in a flowing soap film by the immersed boundary method. *Journal of Computational Physics*, 179(2):452–468.

Publications under the candidature

Journal publications

1. **A. Kundu**, AK Soti, R Bhardwaj, MC Thompson, (2017),"The response of an elastic splitter plate attached to a cylinder to laminar pulsatile flow," Journal of Fluids and Structures, Vol. 68, pp. 423-443.

2. **A. Kundu**, AK Soti, R Bhardwaj, MC Thompson, "Flow-induced Dynamics of an Elastic Splitter Plate attached to a Cylinder in a Free-stream Laminar Flow," Journal of Computers & Fluids (**Submitted**).

3. **A. Kundu**, R Bhardwaj, MC Thompson, "Effect of thickness on flow-induced flapping of an elastic plate in a free-stream laminar flow," Journal of Fluids and Structures (**Under preparation**).

4. **A. Kundu**, R Bhardwaj, MC Thompson, "Dynamics of an inverted plate in front of a circular cylinder," Journal of Fluids and Structures (**Under preparation**).

5. **A. Kundu**, AK Soti, R Bhardwaj, MC Thompson, "Heat transfer enhancement via twin leaflet," International Journal of Heat and Mass Transfer (**Under preparation**).

Conferences

1. **Anup Kundu**, AK Soti, Rajneesh Bhardwaj, Effect of Plate Thickness on Flow-Induced Flapping of an Elastic Plate in a Free-stream Laminar Flow,' Proceedings of the 7th International and 45th National Conference on Fluid Mechanics and Fluid Power (FMFP) conference at IIT Bombay from 10 - 12, December 2018.

2. **Anup Kundu**, AK Soti, Rajneesh Bhardwaj, Effect of Bluff-body on Flow-induced Deformation of an Elastic Plate in a Free-stream Laminar Flow,' Proceedings of the 7th International and 45th National Conference Fluid Mechanics and Fluid Power (FMFP) conference at IIT Bombay from 10 - 12, December 2018 .

3. **Anup Kundu**, Rajneesh Bhardwaj, "Dynamics of an elastic splitter plate attached to a cylinder," Proceedings of the 44th National Conference on Fluid Mechanics and Fluid Power, at Amrita University, Amritapuri Campus, Kollam, Kerala from December 14-16, 2017.

4. **Anup Kundu**, Rajneesh Bhardwaj, "Dynamics of an inverted plate in front of a circular cylinder," Proceedings of the 44th National Conference on Fluid Mechanics and Fluid Power, at Amrita University, Amritapuri Campus, Kollam, Kerala from December 14-16, 2017.

5. **Anup Kundu**, Rajneesh Bhardwaj, "Fluid-Structure Interaction (FSI) validations and its application to heat transfer," Proceedings of the 6th International and 43rd National Conference on Fluid Mechanics and Fluid Power, MNNITA, Allahabad, U.P., India, 15 December 2016.

6. **A Kundu**, AK Soti, R. U. Joshi, R. Bhardwaj, "Effect of Pulsatile flow on flow-induced deformation of an elastic plate," 5th International and 41st National Conference on Fluid Mechanics and Fluid Power (NCFMFP) at IIT Kanpur December 12-14, 2014.

7. **Anup Kundu**, Rajneesh Bhardwaj, "Effect of Flow Pulsation on Vortex Induced Vibration," 2nd Mechanical Engineering Graduate Research Symposium (MEGRES), IIT Bombay, Mumbai, India, 21 March 2015.